Doctoral Dissertation

Galaxy Merger Identification Methods and Investigations of the Role of Mergers in Galaxy Evolution

（衝突銀河の分類方法と銀河進化における銀河衝突の役割の研究）

OMORI, Kiyoaki Christopher

Nagoya University

Graduate School of Physics

Division of Particle and Astrophysical Science

Laboratory of Galaxy Evolution (Ω)

STUDENT ID 462101014

Expected Date of Completion: March 2024

March 25, 2024

Abstract

Galaxies are an astronomical object composed of stars, gas, dust, and dark matter, which evolve throughout their lifetime. In the currently accepted Λ-dominated cold dark matter (ΛCDM) framework for structure formation and evolution in the Universe, the main pathway for structure evolution is considered to be through hierarchical merging, or the process in which multiple smaller objects merge and combine into one larger object. In the context of galaxies, this process is galaxy interactions or mergers, where multiple galaxies merge into a single larger galaxy. As such, galaxy mergers and interactions are a fundamental process to consider when studying galaxy evolution.

Further, galaxy interactions and mergers are considered to be associated with numerous processes that are related to galaxy evolution. When galaxies interact and merge, gas inflows towards the circumnuclear region of the involved galaxies, which can trigger processes such as enhancement of star formation or starbursts, chemical evolution, gas accretion onto supermassive black holes and the subsequent ignition of active galactic nuclei, and quasars. The connection between merger activity and these processes make galaxy mergers an important and unique laboratory for galaxy evolution studies. However, our understanding of the relative role of mergers in galaxy evolution is still far from complete, one of the reasons being due to the difficulty of accurate identification of mergers in observational data.

In this research, I identify mergers in observational data using multiple approaches, in an attempt to achieve improved completeness (less misses) and precision (less contamination). First, I combined the use of optical images with spatially resolved stellar kinematic information to identify galaxies within the SDSS-MaNGA survey. The use of spatially resolved kinematics allows us to identify merging systems that could be missed by other methods, such as galaxies with no visual merger signatures but with merger-induced kinematic disturbances. Next, I used a convolutional neural network (CNN) to identify galaxy mergers within the HSC-SSP. In this work, a deep representation learning model pretrained on galaxy images and labels is fine-tuned using observation-realistic synthetic images of hydrodynamical simulations. This method is able to identify mergers at various mass ratios and merger stages, as well as differentiate between mergers and projections.

With our identified mergers, I conduct various investigations on the role of mergers in galaxy evolution. First, I investigated the spatially resolved relationship between stellar mass and gas phase metallicity (MZR) in merging galaxies. I find that in merging systems, there is a bimodality in the spatially resolved MZR that is not existent in non-merging systems. I find that the dilution is occurring in the central region of close galaxy pairs, a result consistent with chemical evolution in galaxy merger simulations. The gas inflows caused by mergers causes the metallicity dilutions. In addition, using the machine-learning based merger identifications, I investigated the connection between merger activity and local environment, as well as the connection between merger activity and AGN activity. In the first investigation, I find that mass underdense environments are more likely to harbour merger activity. These results were consistent with the results of N-body simulations, but did not align with numerous observational studies. In the second investigation, I find that mergers are not necessarily the trigger for AGN activity, but also that AGNs are more likely to reside in merging systems than non-merging systems.

Through my identification methods and followup investigations, it was made clear that galaxy mergers trigger metallicity dilutions in the central regions of galaxies, galaxy mergers have greater incidence in mass underdense regions, and that AGN activity is not necessarily caused by mergers. As such, this research was able to make clarifications on the role of mergers within galaxy evolution from multiple angles.

Acknowledgements

First and foremost, I would like to express my gratitude towards my supervisor, Professor Tsutomu Takeuchi. Ever since I joined his research group, the Laboratory of Galaxy Evolution Omega Lab, as a third year undergraduate student, he has been an excellent supervisor for me, providing endless and unwavering support and guidance, and offering encouraging advice during hardships. He has always been supportive of my research path, granting me great freedom in pursuing independent and collaborative research projects, and giving me his blessings to take advantage of many domestic and international opportunities. It is because of his supervision that I have been able to take steps forward in becoming an independent and autonomous researcher. Thank you.

I would like to thank all of my collaborators, Tsutomu Takeuchi, Connor Bottrell, John Silverman, Andy Goulding, Mike Walmsley, Hassen Yesuf, Xuheng Ding, Yoshiki Toba, and Gergö Popping for their assistance in conducting my research. Through the many fruitful discussions with all of you, I was able to considerably enrich my knowledge and insight. The major backbones of this thesis could not have been developed without each of your contributions. I would also like to thank my co-researchers Shenli Tang and Juan Alfonzo for the valuable discussions I was able to have with them. Thank you.

I would like to thank my professors at Nagoya University, especially Shu-ichiro Inutsuka, Kiyotomo Ichiki, John Wojdylo, Bernard Gelloz, See Kit Foong, and Marc Humblet, for helping develop my knowledge and enthusiasm for all things physics, as well as science, to where they are now. I would also like to extend these thanks to my science subject teachers at London Central Secondary School in Canada, especially my high school physics teachers Mike Embree and Dave Gilbert. Your guidance and teachings were integral to my academic success. Thank you.

I thank all of my colleagues both within Omega Lab and in the Division of Particle and Astrophysical Science, as well as my colleagues in the G30 School of Science Program. Thank you to Kazuki Nishida, Chikako Nishihara, Kai Kono, Moe Yoda, Shuntaro Yoshida, Sayaka Nagasaki, Katsuya Abe, Daisei Abe, Ryunosuke Maeda, Hiroto Kondo, Suchetha Cooray, Adrien Levacic, Siri Bhagavatula, Shu Nishimoto, Zhang Tingyu, Nguyen Son Thai, Hibiki Shimoyama,

Chihiro Kondo, Tae Hojo, Yuichi Yoshioka, Hai-Xia Ma, Wen Shi, Emi Fujitani, Ayumi Wakida, Erina Kawamoto, Sena Matsui, Daiki Iwasaki, Dillon Loh, Guozhang Lin, Yuta Kimura, Reiji Moriguchi, Shunya Uchida, Taisei Yamagata, Taiga Yamamoto, and Sota Osaki. I was able to have many discussions, both science and non-science related, with all of you. My experiences with you made my time at Nagoya University fruitful and memorable. Thank you.

I owe extreme gratitude to my family for their overwhelming amount of support and encouragement during my life. I would not have been able to pursue academics and knowledge without your support and blessings. Thank you.

Finally, one last thanks to everybody who has been involved in, influenced, or played a role in my life up to this point, be it in Canada, Japan, or anywhere else. You are all amazing. Thank you.

Contents

List of Figures

List of Tables

Chapter 1

Introduction

Galaxies are astronomical objects composed of stars, gas, interstellar medium (ISM) and dark matter. Galaxies form and evolve within a complicated aggregation of processes, some caused internally (in-situ) and others externally (ex-situ). A fundamental ex-situ process is galaxy interaction and merging. Galaxy interactions and mergers are an important process to understand when discussing galaxy evolution, and considered to be one of the fundamental pathways of structure growth in the context of galaxies. Despite the importance of the process, the relative role of galaxy mergers on galaxy evolution is heavily contested, and quantitative conclusions are yet to be made. We discuss what galaxy interactions and mergers are in Section 1.1. Section 1.2 discusses the various galaxy evolutionary processes believed to be associated with merger activity, and the various conclusions. Section 1.3 highlights the difficulty of conducting galaxy merger studies, and the methods taken to create galaxy merger samples.

1.1 Background

Galaxies are an astronomical object composed of stars, gas, dust, and dark matter. In the early early, homogeneous, and expanding Universe, there are small density fluctuations. These density perturbations grow over time, and in overdense regions where the density difference becomes large compared to the underdense regions, gravitational collapse occurs creating protogalaxies. Gas in these protogalaxies forms stars to shape the first galaxies, which will further evolve from

internal star formation events or external accretion events.

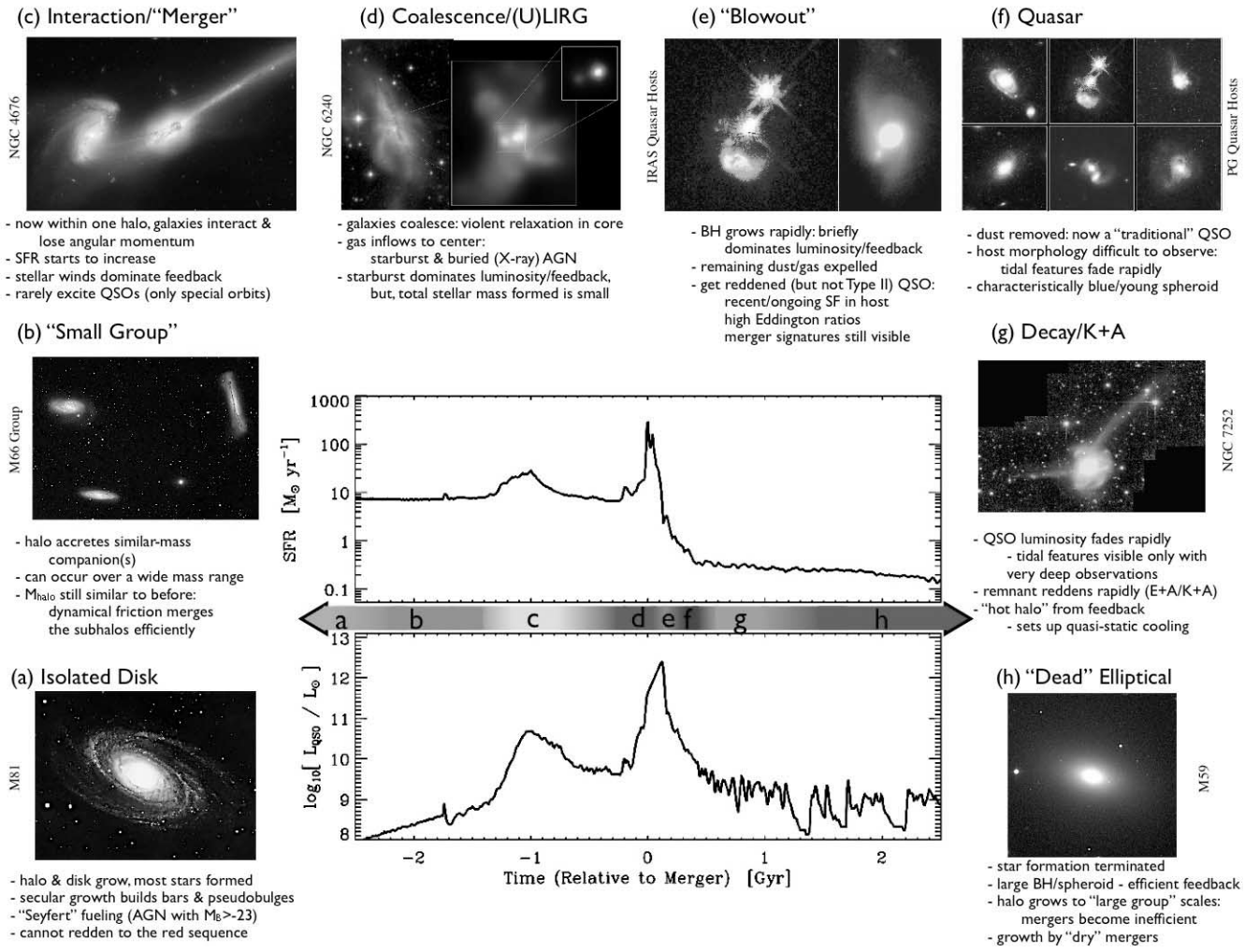

Fig. 1.1: From Hopkins et al. (2008b), an outline of the phases of a galaxy merger.

One way galaxies undergo such external accretion is through galaxy interaction and mergers. The hierarchical growth of galaxies (Press & Schechter, 1974) via merging is a commonly accepted pathway of galaxy evolution in the current Λ cold dark matter (ΛCDM) framework for structure formation in the Universe (White & Rees, 1978; Peebles, 1982; Blumenthal et al., 1984; White & Frenk, 1991; Lacey & Cole, 1994). Galaxy interactions and mergers occur when galaxies come into close contact. A detailed picture of the galaxy interaction process can be seen in Figure 1.1 taken from Hopkins et al. (2008b). First, there are multiple isolated galaxies (**a)**), all within separate halos. These then become a small group (**b)**), where external mass accretion starts. In step **c)**, the galaxies start the interaction process, becoming one halo. It is this step

when star formation rates starts to enhance. The next step is coalescence (**d)**), where the two galaxies coalesce into a single galaxy. In this step, gas inflows towards the circumnuclear regions, fueling star formation and active galactic nuclei (AGN) activity. As star formation and accretion onto supermassive black holes continue, feedback occurs, and dust and gas are "blown out" (**e)**) . The fuel for further star formation and accretion are expelled from the galaxy, so star formation activity decreases after this point, leading to the quasar stage (**f)**). Eventually, with the loss of fuel, the quasar decays off (**g)**), before finally relaxing to a quenched elliptical (**h**)). This several gigayear process, as illustrated, encompasses a large number of processes pertaining to galaxy evolution.

1.2 Processes Triggered by Galaxy Mergers

As stated previously, galaxy mergers and interactions are associated with numerous processes pertaining to galaxy evolution, primarily due to the inflow of gas to the nuclear regions of the galaxies. However, a definitive conclusion on the relative role of mergers in these processes is yet to be made, and the importance of mergers with regards to these processes is still contested. We discuss a number of such processes and the studies investigating them.

1.2.1 Star formation enhancement

Galaxy mergers are considered to be associated with enhancement of star formation activity (Beckman et al., 2008; Saitoh et al., 2009; Barnes, 2004; Ellison et al., 2008; Patton et al., 2011, 2013; Hopkins et al., 2013; Moreno et al., 2015; Sparre & Springel, 2016; Thorp et al., 2019), as can be seen in Fig. 1.2. Hydrodynamical simulations show that during galaxy-galaxy interactions, the resulting tidal inflows can compress and shock gas, inducing enhanced star formation, or starburst activity.

Indeed, observations show that many Ultra-Luminous Infrared Galaxies (ULIRGs), some of the most luminous infrared objects, and some of the most actively starforming objects in the Universe are considered a product of galaxy mergers (Sanders & Mirabel, 1996). However, in other observational studies, it is found that not all merging systems have enhanced star formation,

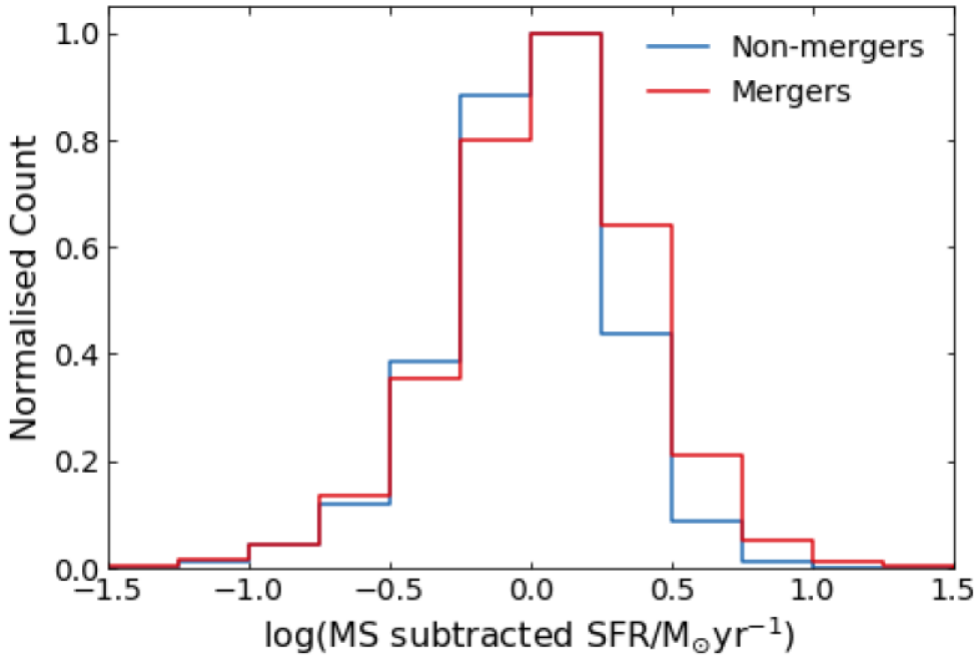

Fig. 1.2:

From Pearson et al. (2019), a comparison between star formation rate offset from the starforming main sequence between mergers and non-mergers. Mergers show an increased star formation rate.

such as in Pearson et al. (2019). Others show that galaxy mergers can suppress or shut down star formation activity (Robotham et al., 2013). As such, the role of mergers in shaping a galaxy's star formation history is debated.

One reason for such contested conclusions lie in the sample selection of galaxy mergers. Different merger selection methods can find widely varying merger samples, some with very little overlap (De Propris et al., 2007). The expectation is that gas inflows and activity during the merger process is a catalyst for star formation. However, if gas-poor mergers, in which stars do not form, are selected during sample selection for merger studies, then a star formation rate increase among the sample may not be observed.

1.2.2 Chemical evolution

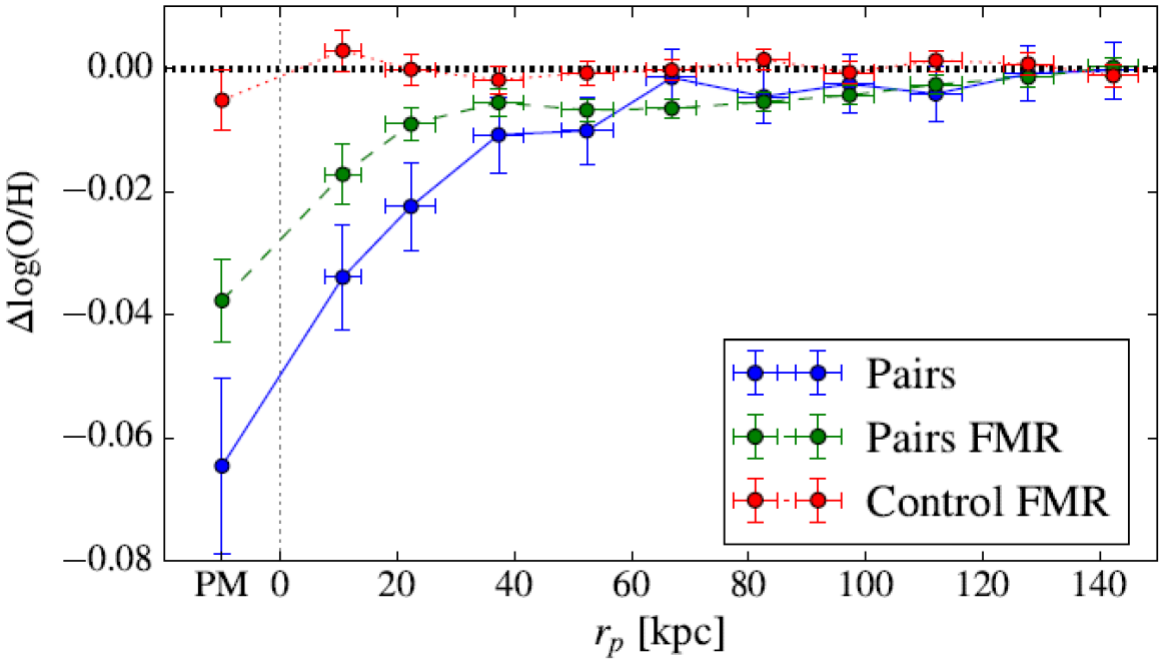

Fig. 1.3:

Modified from Bustamante et al. (2020), a comparison of metallicity offset from the fundamental metallicity relation between mergers and non-mergers. Mergers show a diluted gas phase metallicity.

The gas activity associated with galaxy mergers can also affect the chemical composition of

galaxies. When galaxies gravitionally interact, low-metallicity gases in the outskirt regions of the merging galaxy radially inflow into the circumnuclear regions of the host galaxy (Ellison et al., 2008; Rupke et al., 2010; Montuori, M. et al., 2010; Sol Alonso et al., 2010; Perez et al., 2011; Torrey et al., 2012; Sparre & Springel, 2016; Thorp et al., 2019). As such, dilutions of the gas phase metallicities in the central regions of interacting galaxies are observed in both simulations and observations (Rupke et al., 2010; Montuori, M. et al., 2010; Bustamante et al., 2018). As a result of such dilutions, merging galaxy pairs have an offset from two fundamental galaxy scaling relations. These are the mass-metallicity relation (MZR), which is the relationship between stellar mass and gas phase metallicity, and the fundamental metallicity relation (FMR), the three-dimensional plane relationship between stellar mass, star formation rate, and gas phase metallicity. Namely, the gas phase metallicity of merging galaxies show a dilution from these relations, as can be seen in Fig. 1.3. However, during the gigayear-scale long merging process, complex chemical evolution including both dilution and enhancement of metallicities can occur (Torrey et al., 2012), and further investigations will be required to fully understand the role of mergers in chemical evolution.

1.2.3 Active galactic nuclei (AGN) activity

Galaxy mergers are also considered to be associated with AGN activity (Keel et al., 1985; Sanders et al., 1988; Matteo et al., 2005; Koss et al., 2010; Ellison et al., 2011; Satyapal et al., 2014; Ellison et al., 2015; Goulding et al., 2018; Ellison et al., 2019) When two galaxies interact and merge, gas will inflow towards the center of the host galaxy, and accrete onto the central supermassive black hole (SMBH). Such accretions can be a fuel for AGN activity, and it can be observed in high AGN luminosities over multiple wavelengths.

However, the relative impact of mergers in AGN activity is still not a concrete conclusion. While some studies find that the AGN incidence increases in merger galaxies (Ellison et al., 2011; Silverman et al., 2011; Lackner et al., 2014; Satyapal et al., 2014; Weston et al., 2017; Goulding et al., 2018), or that mergers are more likely to harbour AGNs (Treister et al., 2012; Santini et al., 2012; Kocevski et al., 2015; Ellison et al., 2019), for example in Fig. 1.4, but others find negligible difference (Grogin et al., 2005; Gabor et al., 2009; Cisternas et al., 2011;

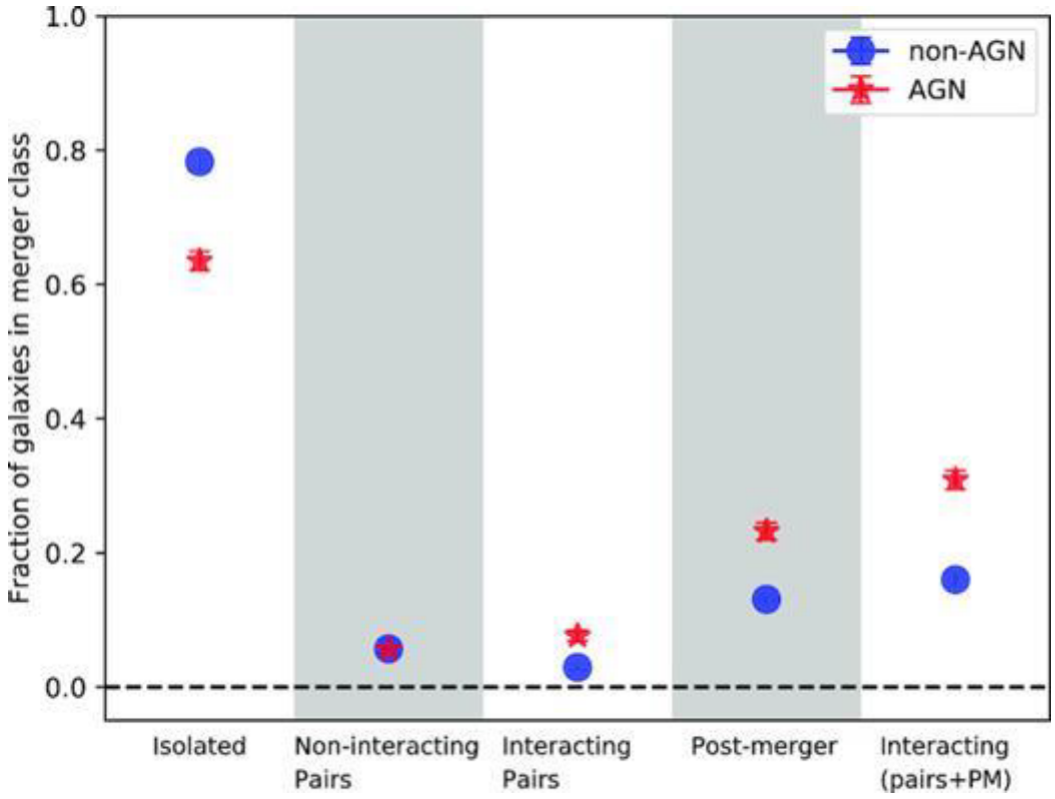

Fig. 1.4:

From Ellison et al. (2019), a comparison of merger fraction between AGNs and non-AGNs for isolated galaxies, non-interacting pairs, interacting pairs, post-mergers, and all interacting galaxies. Merger incidence is increased among AGNs that are interacting.

Kocevski et al., 2012; Villforth et al., 2014; Mechtley et al., 2016; Gao et al., 2020; Silva et al., 2021). One key reason for disagreements is believed to lie in AGN identification methods, as different studies will identify AGNs using different methods, which can lead to AGNs at different stages of their lifetime (Sanders et al., 1988). Some studies will identify AGNs using emission line diagnostics such as Baldwin, Phillips and Terlevich (BPT) diagrams Baldwin et al. (1981), others through full spectral fitting (Thorne et al., 2022). Coming to a definite conclusion about the role of mergers in AGN growth will require an understanding of how to correctly identify not just mergers, but also AGNs.

1.3 Merger identification methods

A major reason for the many disagreements of the role that galaxy mergers plays in galaxy evolution is the difficulty in creating a complete, precise sample of galaxy mergers. There have been many different methods used to identify a merger sample in galaxy surveys, and each method can produce widely different merger samples, as they can be sensitive to different types of merger signatures. We list some of the methods used in previous studies to identify merger galaxies, and the advantages and disadvantages associated with each method.

1.3.1 Spectroscopic pair matching

Spectroscopic pair matching is a method where close galaxy pairs are searched for in the sky, and a merger sample is created based on projected distance and redshift separation (e.g., Lin et al., 2004; Soares, 2007). A strength of this method is that since the pairs are identified and confirmed spectroscopically, chance projections are more likely to be eliminated. An example of a close pair identified through this method from Mantha et al. (2019) is shown in Fig. 1.5.

However, as the method searches primarily for galaxy pairs, mergers in the post-coalescence or post-merger phase can be missed. This method is also heavily affected by spectroscopic incompleteness, as finding pairs requires spectroscopic redshifts (Zepf & Koo, 1989; Burkey et al., 1994; Carlberg et al., 1994; Yee & Ellingson, 1995; Woods et al., 1995; Patton et al., 1997; Wu & Keel, 1998). Spectroscopic completeness has been achieved in later studies, but

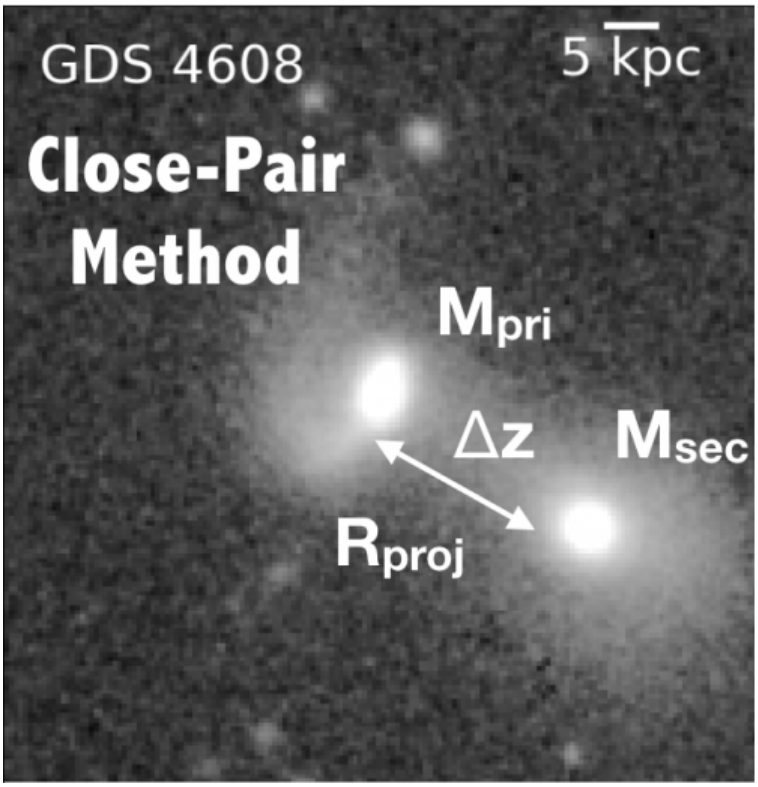

Fig. 1.5: From https://info.umkc.edu/galaxy-evolution-group/mcintosh/, modified from Mantha et al. (2019), an example of a galaxy pair identified through spectroscopic pair matching.

is still observationally expensive (Barton et al., 2000; De Propris et al., 2005; Ellison et al., 2008; Rodrigues et al., 2018; Duncan et al., 2019). Also, the criteria for pair selection, such as velocity offsets and projected separation, can vary between studies, and such discrepancies can create incompleteness or interlopers in merger samples. Further, merger pairs that have projected separations larger than the maximum adopted in each study can go undetected.

1.3.2 Nonparametric statistics

As stated in the previous section, galaxy mergers and interactions can disturb the visual morphologies of galaxies (Toomre & Toomre, 1972; Toomre, 1977; Negroponte & White, 1983; Hernquist, 1992; Naab & Burkert, 2003; Hopkins et al., 2008a; Berg et al., 2014). Such morphological disturbances can be quantified in the form of non-parametric morphological statistics. These include, but are not limited to, the following parameters.

The first set are the concentration-asymmetry-smoothness (CAS) parameters (Bershady et al., 2000; Conselice et al., 2000; Conselice, 2003).

Concentration: a parameter quantifying the concentration of stellar light in the central region of a galaxy. Parametrized by

$$C = \log(\frac{r_{80}}{r_{20}}),$$

where r_{80} is the circular radius containing 80 % of the total luminosity and r_{20} the radius containing 20%. This value tends to hold a higher value for elliptical galaxies which usually hold more light in the central regions.

Asymmetry: a parameter quantifying how asymmetric the galaxy is. This parameter is obtained through the following computation:

$$A = \min[\frac{\sum |I_0 - I_\phi|}{\sum |I_0|}] - \min[\frac{\sum |B_0 - B_\phi|}{\sum |B_0|}],$$

where I_0 is each pixel, I_ϕ is the pixel rotated by ϕ degrees (in many cases 180), B_0 the pixels of the background image, and B_ϕ the background image pixels rotated by ϕ degrees. Interacting galaxies that have structures such as tidal tails and disturbances tend to have a higher value of A.

Smoothness: also referred to as clumpiness. This parameter quantifies the existence of high

frequency patches of light in a galaxy. Galaxies with clumps of star formation have a high smoothness parameter.

$$S = 10 \sum_{x,y=1,1}^{N,N} \frac{(I_{x,y} - I^{\sigma}_{x,y}) - B_{x,y}}{I_{x,y}},$$

where $I_{x,y}$ is each pixel, $I^{\sigma}_{x,y}$ is each pixel smoothed, $B_{x,y}$ each background pixel, and N the total number of pixels in a galaxy. Areas undergoing star formation, such as star-forming regions in mergers, have a patchy/clumpy light distribution therefore have a high S.

Examples of the above parameters are shown in Fig. 1.6, from Conselice (2003).

Gini coefficient (Lotz et al., 2004): This parameter was originally used in economics to measure various inequalities such as wealth, income, and consumption, among a population. In the context of galaxy morphology studies, this parameter is used to quantify the inequality of light distribution within a galaxy.

$$G = \frac{1}{|\bar{x}|n(n-1)} \sum_{i}^{n} (2i - n - 1)|x_i|,$$

where n is the number of pixels in a galaxy image, x_i is the flux of pixel i, and $|\bar{x}|$ is the average flux across n pixels. A value of 0 means that the galaxy light is distributed equally among all pixels, and a value of 1 means that all light belongs to a single pixel.

M_{20} (Lotz et al., 2004): This parameter M_{tot} quantifies the total second-order moment. This is the summation of flux of each pixel in a galaxy f_i multiplied by the squared distance to the galaxy center.

$$M_{tot} = \sum_{i}^{N} M_i = \sum_{i}^{N} f_i((x_i - x_c)^2 + (y_i - y_c)^2),$$

where M_i is the second-order moment of a pixel, and x_c and y_c are the coordinates of the galaxy center, computed by finding the point minimizing M_{tot}. Similarly, M_{20} is the second-order moment of the pixels containing 20% of a galaxy's light, or in other words the brightest regions such as bright nuclei, bar regions, and spiral arms. M_{20} is computed by ordering all galaxy pixels by flux, then taking only the pixels accounting for the brightest 20% of the galaxy, the normalizing by M_{tot}.

$$M_{20} = \log_{10}\left(\frac{\sum_i M_i}{M_{tot}}\right), \quad \text{while} \quad \sum_i f_i < 0.2 f_{tot},$$

where M_i is the second-order moment of a pixel, M_{tot} is the total galaxy second-order moment, f_{tot} is the total flux identified by a segmentation map, and f_i the flux for each pixel, with f_1 the flux for the brightest pixel, f_2 the flux for the second brightest, and so on. This parameter is similar to concentration C as it measures the light in the presumed brightest regions, but M_{20} is dependent on the spatial distribution of the pixels, and the center of the galaxy is a free parameter independent of aperture, unlike C. This value is more sensitive to merger features such as double nuclei.

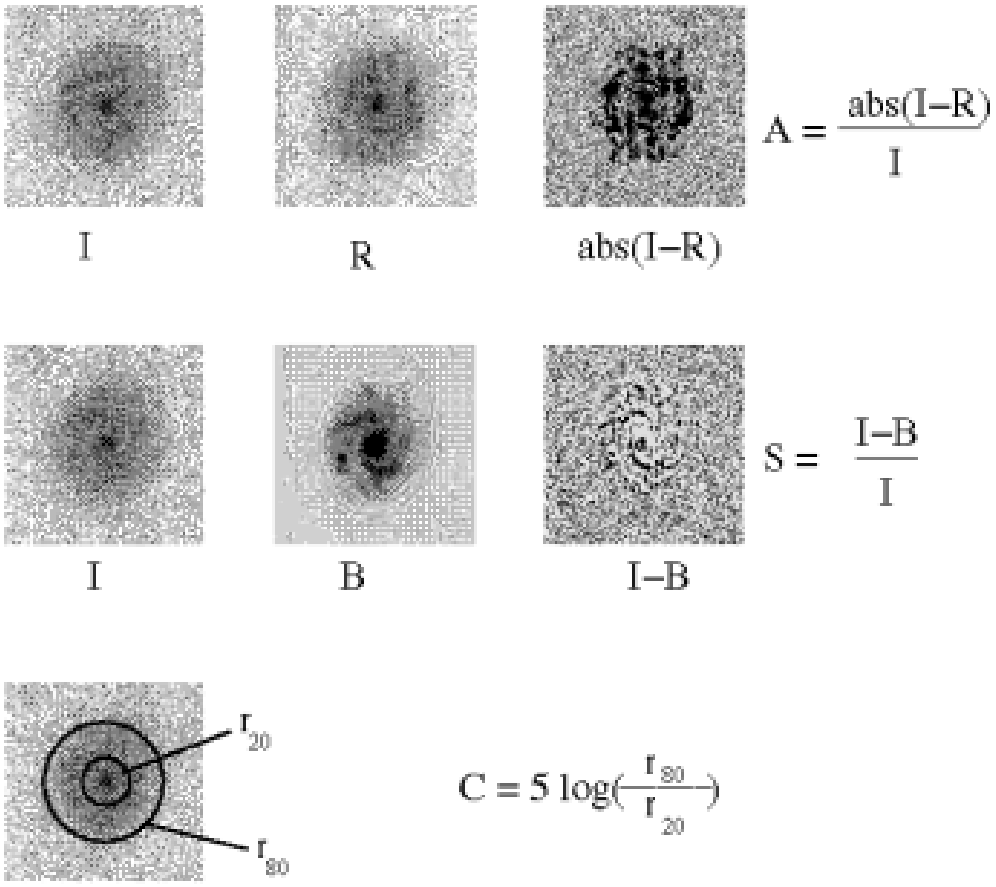

Fig. 1.6: From Conselice (2003), an illustration showing the CAS parameters and how they are obtained.

Combining an n number of these parameters can create a merger classification criteria in an

n-dimensional feature space, in forms such as random forest classifiers (e.g., Goulding et al., 2018; Snyder et al., 2019; Rose et al., 2023; Thibert et al., 2021; Guzmán-Ortega et al., 2023). The use of these parameters and the n-dimensional feature spaces is a form of dimensionality reduction, as such a smaller sample size is required as a training dataset compared to image-based classification methods.

A major limitation with the parametrizing of image-base morphologies lies in the imaging quality, particularly for merger classification. Many merger signatures are faint, low surface brightness features, and require high resolution and depth of images to resolve (Conselice et al., 2000; Bottrell et al., 2019a; Thorp et al., 2021; Wilkinson et al., 2022). Using image data from modern day imaging surveys, such as the Hyper Suprime-Cam Subaru Strategic Program can overcome such limitations. However, even with high quality images, the use of non-parametric statistics still has issues. First, the morphological disturbances and associated parameters may not necessarily be merger-driven, and could be a result of in-situ activity. Also, these statistics do not completely capture the complexity existing in imaging data, thus there are limitations in the amount of information that can be extracted from them and the associated n-dimensional feature spaces.

1.3.3 Visual classification

Visual identification and classification, both by expert scientists and citizen science, is a very commonplace approach in galaxy morphology studies. This approach is able to incorporate human knowledge of what is a merger, and can also purify classification results used in other methods, such as those from the non-parametric statistics above, and machine learning methods. Visual classification can extract a larger amount of information from imaging compared to the above methods, and are not restricted to summary statistics and n-dimensional spaces.

However, this method is not without its limitations either. First, even for expect scientists, the criteria for merger classification can vary greatly between individuals, as such, the same galaxy may be classified differently by different people. Next, the visual classification process can be very time- and human-resource consuming, making it inefficient and unrealistic in modern day galaxy surveys which can contain up to several million targets. These issues can be partially

resolved through citizen science, such as the Galaxy Zoo Project (Lintott et al., 2011, hereinafter referred to as GZ1), and the ensuing Galaxy Zoo 2 (Willett et al., 2013, hereinafter referred to as GZ). GZ1 and GZ2 are morphology catalogue containing morphological probabilities and labels for over 1 million galaxies in the Sloan Digital Sky Survey (SDSS, York et al. 2000). Each galaxy is given a classification by multiple citizen scientists. In GZ1, the classification is made from one of six morphologies. In GZ2, a multi-step decision tree is used to determine a morphology, as shown in Fig. 1.7. In each case, the choices made by the scientists are summarized in a single value weighted by the 'correctness' of each scientist. Since its publication, Galaxy Zoo probabilities have been used in many merger related sciences (Darg et al., 2010; Holincheck et al., 2016). However, while citizen science allows for classification of larger galaxy catalogues, there still exists a tradeoff in accuracy compared to expert scientists.

1.3.4 Galaxy morphological classification using machine learning

Recent advances made in machine and deep learning technology have also had effects in galaxy morphological classification. The visual classification process in the previous section can become far less time- and human-resource consuming through machine learning methods, through methods such as convolutional neural networks (CNNs). Instead of having to visually assign labels to entire galaxy catalogues, a smaller training dataset can be selected and visually classified, and a machine learning model can be trained based on the training sample. The remaining galaxies can then be inputted into the trained model, and each be given morphological labels. The use of CNNs can achieve performances greater than other computational methods (Krizhevsky et al., 2017), and can even surpass the performance of some human classifications (He et al., 2015), which was formerly the gold standard. CNNs have been used in both morphological classification as a whole (Dieleman et al., 2015; Domínguez Sánchez et al., 2018; Jacobs et al., 2019; Zhu et al., 2019; Ghosh et al., 2020; Cheng et al., 2021; Domínguez Sánchez et al., 2022; Walmsley et al., 2022a; Cavanagh et al., 2023; Huertas-Company & Lanusse, 2023), and for the specific task of merger classification (Walmsley et al., 2019; Pearson et al., 2019; Bottrell et al., 2019b; Bickley et al., 2021; Ćiprijanović et al., 2020; Ferreira et al., 2020; Ćiprijanović et al., 2021; Bickley et al., 2022; Bottrell et al., 2022; Pearson et al., 2022; Ferreira et al., 2022).

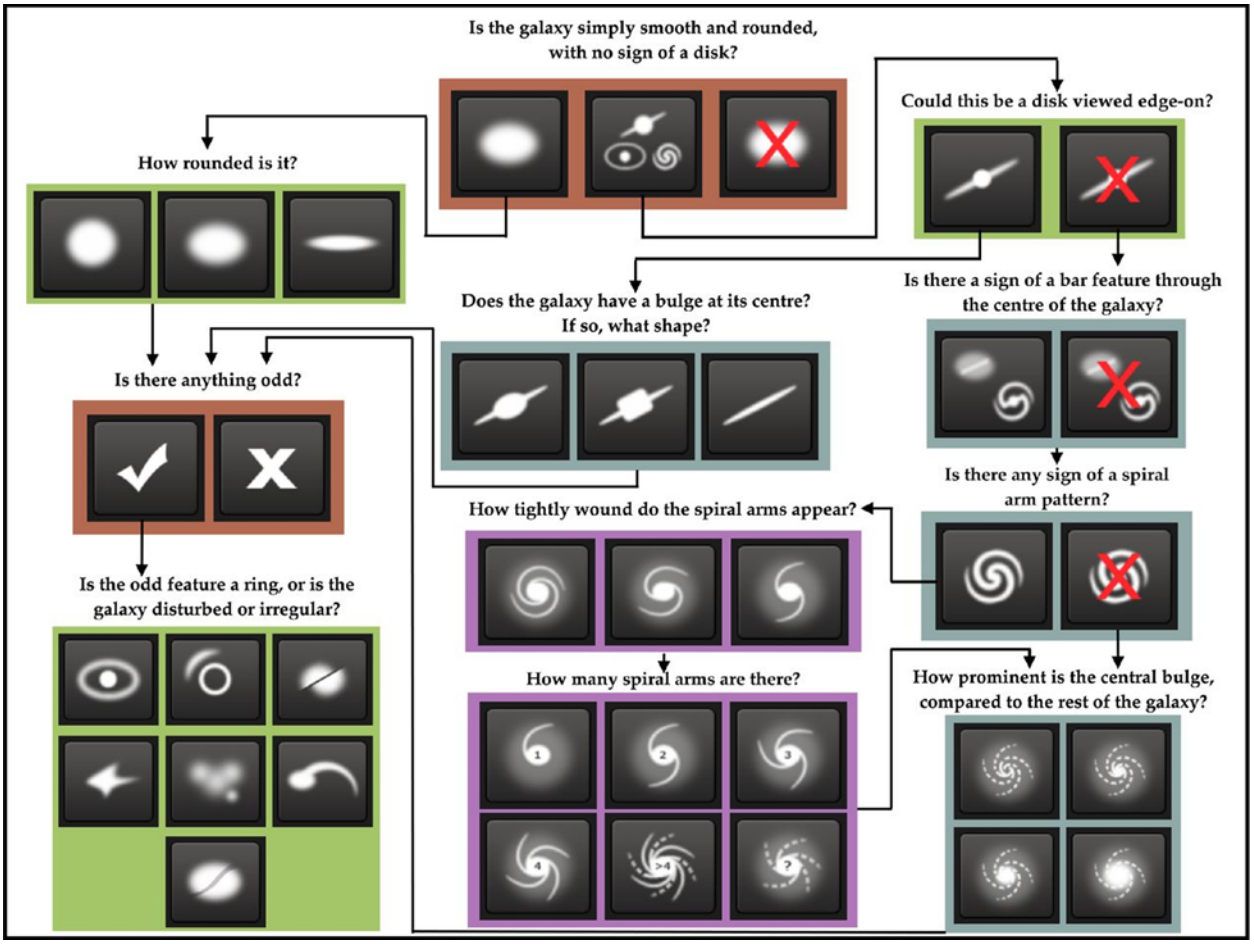

Fig. 1.7: From Willett et al. (2013), a flowchart of the multi-step decision tree used in GZ2 for determining galaxy morphologies. Questions are colour-coded by the depth in the decision tree, and brown-coded questions are asked for all galaxies. Each choice in each question corresponds to a response. For example, the top question "Is the galaxy simply smooth and rounded, with no sign of a disk?" can be answered "Smooth" (left), "Features or disk" (center), or "Star or artifact" (right).

However, similar issues as those of previously mentioned methods can also arise with machine learning methods. As mentioned earlier, many galaxy merger features are faint and of low surface brightness. As such, it is ideal that high quality images are used both for training the model and for making predictions. In addition, preparing the training sample still requires a heavy amount of time and human resources, as an ideal model will require several thousand samples. Finally, if the training samples are given inaccurate labels, for example chance projections, the resulting model will also output inaccurate merger probabilities. There have been many different methods taken to ensure accurate training data, such as use of simulation-based (Pearson et al., 2019) or citizen science-based labels (Gharat & Dandawate, 2022), but creating a perfectly accurate model is still a very complex science given the complexity of galaxy mergers.

1.4 Outline of this thesis

This thesis summarizes my approaches over my graduate school studies for galaxy merger identification within observational image data, and galaxy evolution related investigations conducted using each method. These studies are in chronological order, and follow my different ideas developed through numerous surveys and the types of data they offer. At first, I was primarily interacting with SDSS data, and conducting image-based identification, both through direct visual classification and basic machine learning models. However, I quickly realized the limitations of pure reliance on visual identification, especially with the catalogue size of SDSS, as well as the lower depth and resolution of SDSS optical images. I then started to look at other methods and surveys.

The first approach incorporated spatially resolved spectroscopic follow-ups of SDSS observations, from the integral-field spectroscopic survey Mapping Nearby Galaxies at Apache Point Observatory (MaNGA) survey. The MaNGA survey includes spatially resolved spectroscopic information, which allows for the mapping of stellar and gaseous kinematics of galaxies to be mapped. The spatially resolved kinematics can hold information about galaxy evolution processes not visible in optical image data, including merger-induced disturbances. Combining spatially resolved spectroscopic information with optical images would enable not only for iden-

tification of previously missed mergers, but also rule out chance projections and spectroscopic overlaps. However, this approach had multiple limitations. Not all kinematically disturbances are merger driven, and there would be a difficulty distinguishing between merger-induced kinematic disturbances and disturbances caused by in-situ events. Furthermore, visually identifying the many stellar and gaseous kinematics in addition to the optical images would be more resource consuming than identifying optical images alone, and the current state of the MaNGA survey would not consist of a sufficient galaxy sample for training of machine learning models. Finally, investigations made by other researchers during this time (Nevin et al., 2021; Bottrell et al., 2022) showed that while the addition of kinematic information did increase the accuracy of merger identification, the enhancement was small.

The next approach reverted back to optical image-based machine learning methods. The imaging data used for this approach is observed using the Subaru telescope, specifically from the HyperSuprime Cam Subaru Strategic Program (HSC-SSP). Images from the HSC-SSP are of much greater depth and resolution than previous surveys such as SDSS, and can show much fainter merger features. The HSC-SSP also contains tens of millions of target galaxies, and can be used as a sample for numerous future galaxy studies, including investigations on galaxy mergers. To avoid the above mentioned issues associated with machine learning methods, we conduct a transfer learning fine-tuning based approach to train our model. A pretrained model is fine-tuned for a specific task, in this case galaxy merger identification. This method requires a smaller dataset compared to training a model from scratch. Further, to ensure an accurate training sample, observation-realistic images from the TNG simulations were used to fine-tune the model. The final model was one that could accurately differentiate between mergers and chance projections, and also correctly predict mergers at varying mass ratios and merger stages. This model will be used as a starting point for future studies I will conduct related to mergers in the HSC-SSP.

This thesis is structured as follows. Chapter 2 shows the combined kinematic-optical image approach for merger identification in the MaNGA survey, and a followup investigation on the spatially resolved MZR in merger galaxies. Chapter 3 introduces the machine learning approach for merger identification in the HSC-SSP, and an investigation on the environment in which

merger incidence is high. Chapter 4 continues the use of the machine learning methodology used in Chapter 3, this time investigating the relationship within AGNs and mergers in the HSC-SSP. Final conclusions, summaries, and future prospects are indicated in Chapter 5. Appendix A is a reference work where we used a kinematic approach to identify galaxies with a kinematically disturbed core (KDC) in SDSS-MaNGA.

Chapter 2

The Spatially Resolved Mass-Metallicity Relation in Mergers

Based on "*The bimodality in the mass-metallicity relation in SDSS-MaNGA galaxy pairs*" by Kiyoaki Christopher Omori and Tsutomu T. Takeuchi, 2022, Astronomy & Astrophysics, Article Number 145, Volume 660, April 2022

2.1 Abstract

Interacting galaxies show a metallicity dilution compared to isolated galaxies of similar masses in the mass-metallicity space at the global scale. We investigate the spatially resolved mass-metallicity relation (MZR) of galaxy pairs in the SDSS-MaNGA survey to investigate the local relation between the stellar mass surface density, Σ_*, and the metallicity, and whether there exists a difference between merging and non-merging systems. We investigate the spatially resolved relationship between the stellar mass surface density and the metallicity abundance, 12 + log (O/H), for star-forming spaxels belonging to 298 galaxy pairs identified using visual and kinematic indicators in the SDSS-MaNGA survey. We also investigate if **a)** the location of a spaxel relative to the galaxy centre and **b)** the galaxy pair separation have any effect on the local MZR, to understand where chemical evolution may occur in interacting galaxy systems. We find that the correlation between mass and metallicity holds for interacting galaxies at the local level.

However, we find two peaks in spaxel distribution, one peak with enriched metallicity and the other with diluted metallicity. We find that the spaxels belonging to the galaxy central regions (i.e. at lower $R/R_{\rm eff}$) are concentrated close to the two peaks. We also find that the metallicity-diluted spaxels belong to galaxy pairs with closer projected separations and that spaxels with enriched metallicity belong to galaxy pairs with greater projected separations.

2.2 Introduction

In the current Λ-dominated cold dark matter (ΛCDM) framework for structure formation in the Universe, the hierarchical growth of galaxies through merging is the commonly agreed upon pathway for galaxy evolution. Despite galaxy interactions and mergers being a major driver of galaxy evolution, we are yet to make many quantitative conclusions on the process, and our understanding of galaxy interactions and mergers is far from complete. One such example is the chemical evolution of interacting galaxy systems. While the chemical evolution of isolated galaxies has been extensively studied, there have been comparatively fewer studies done on the topic for interacting galaxies.

We can improve our understanding of chemical evolution in interacting galaxies by examining the relationship between two fundamental properties of galaxies: stellar mass (M_*) and gas phase metallicity (hereinafter referred to as 'metallicity'). Stellar mass can be an indicator of the amount of gas converted into stars during a galaxy's lifetime. Metallicity can be a tracer of gas reprocessed into stars or accreted due to external processes and can be a reflection of the state of galaxy evolution. Both of these properties can change as a consequence of star formation events. The relationship between these two properties is called the mass-metallicity relation (MZR; Lequeux et al. 1979). This relationship indicates that the metallicity, in particular the oxygen abundance, of galaxies increases with increasing stellar mass (Tremonti et al., 2004; Foster, C. et al., 2012). Lower-mass galaxies are more greatly affected by blowouts due to galactic winds or outflows from galactic processes; this results in metal content leaving the galaxy, which in turn dilutes the gas phase metallicity. On the contrary, higher-mass galaxies are more chemically enriched. This could be due to higher-mass galaxies being less affected by the above processes

and having the ability to retain their metal content, or it could be a consequence of 'chemical downsizing' (Somerville & Davé, 2015). At larger stellar masses, the relation bends and flattens off towards an asymptotic value. This behaviour indicates some sort of saturation value for gas phase metallicity, possibly due to the galactic outflow, which regulates metallicity (Tremonti et al., 2004).

This relation has been shown to also hold true at a local, or spatially resolved, scale. Studies of HII regions for a small number of galaxies have shown that a relationship exists between stellar mass density and metallicities, with denser regions exhibiting a greater metallicity (Edmunds & Pagel, 1984; Vila-Costas & Edmunds, 1992). Later, Moran et al. (2012) found a local correlation between stellar mass density and metallicity using long-slit spectra of galaxies in the Galactic All Sky Survey (GASS; McClure-Griffiths et al. 2009). The advancement in integral-field-spectroscopy (IFS) techniques has allowed for detailed analyses on the spatially resolved properties of a larger sample of galaxies. Studies using spatially resolved spectra have confirmed that the relation between the stellar mass density and metallicity is a locally scaled version of the global MZR (Rosales-Ortega et al., 2012; Sánchez et al., 2013; Barrera-Ballesteros et al., 2016).

Recent studies have shown that the metallicity of galaxy mergers falls below the MZR, or in other words, interacting galaxies have lower nuclear metallicities than those of isolated galaxies of similar masses (Ellison et al., 2008; Scudder et al., 2012; Cortijo-Ferrero et al., 2017). In particular, close galaxy pairs show an offset from the MZR. A likely explanation for this is gas inflow to galaxy core regions during a merger event (Rupke et al., 2010; Montuori, M. et al., 2010; Perez et al., 2011). The dilution in metallicity due to this inflow event occurs at a galaxy-wide scale and is not just a local phenomenon occurring at the galaxy centre (Rowlands et al., 2018). Accreted lower-metallicity gas from a galaxy merger will flow into a higher-metallicity central region, resulting in a lower gas phase metallicity.

In this paper we investigate the spatially resolved MZR of galaxy pairs in the IFS survey Mapping Nearby Galaxies at Apache Point Observatory (MaNGA; Bundy et al. 2015) to study the effects of interaction on a local scale. We compare the loci of the spaxels of our sample to the MZR curve derived from all star-forming spaxels in the MaNGA survey to confirm if metallicity dilutions occur for galaxy pairs. We also investigate if the distribution of spaxels of the paired

sample is affected by other parameters.

For this paper, we adopt a ΛCDM model with the following cosmological parameters: $H_0 = 70$ km s $^{-1}$ Mpc^{-1}, $\Omega_\Lambda = 0.7$, $\Omega_M = 0.3$.

The paper is structured as follows. Section 2.3 describes our sample and methods to obtain our properties. We highlight our results in Sect. 2.4. We discuss our results in Sect. 2.5, and our conclusions are presented in Sect. 2.6.

2.3 Data and analysis

2.3.1 Sample

For this work we used data from the IFS survey MaNGA, one of the three core projects of Sloan Digital Sky Survey IV (SDSS-IV; Blanton et al. 2017). It uses the 2.5 meter telescope at the Apache Point Observatory (Gunn et al., 2006) and aimed to map and acquire spatially resolved spectroscopic observations of ∼10,000 local galaxies in a redshift range of $0.01 < z < 0.15$, with an average redshift of 0.037 (Law et al., 2016), by 2020. MaNGA spectra cover a wavelength range of 3,600Å–10,000Å at a resolution of R ∼ 2,000.

The MaNGA target selection is optimised in such a way that galaxies are selected based only on their SDSS *i*-band absolute magnitude and redshift, and the sample is unbiased based on their sizes or environments. The methodology and extensive efforts taken for this optimisation are highlighted in Wake et al. (2017). We used data from SDSS Data Release 16 (DR16), which includes the spatially resolved maps of 4675 unique MaNGA targets.

2.3.2 Selection

We selected our sample of galaxy pairs using a method that combines visual identification of MaNGA cutout images, visual inspection of 2D kinematic maps, and relative velocity differences.

First, we visually investigated the 2D stellar kinematic maps of MaNGA galaxies. The stellar kinematic maps were obtained from the output of the data analysis pipeline (DAP) in MaNGA (Westfall et al., 2019). In the DAP, the Voronoi binning method of Cappellari & Copin (2003)

is used to bin, stack, and average the spectra of adjacent spaxels such that the target minimum signal-to-noise ratio (S/N) to obtain accurate stellar kinematics is met, which in this case is 10. The stellar continuum of each binned spectrum was fitted using the penalised pixel-fitting method by Cappellari (2017) and hierarchically clustered Medium-resolution Isaac Newton Telescope library of empirical spectra stellar library (MILES stellar library: Sánchez-Blázquez et al. 2006). The stellar kinematic information (velocity and velocity dispersion) was obtained through this fitting process. From the 2D kinematic maps, we visually identified 1569 galaxies with disturbed stellar kinematics.

We next inspected whether or not these 1569 galaxies were galaxy pairs or isolated galaxies through visual confirmation of their optical images and SDSS galaxy pair data. We investigated the MaNGA image cutouts of the galaxies and considered the galaxy a galaxy pair if it met one of the following two criteria: a) a secondary galaxy was within the cutout and b) a secondary galaxy exists within the range of the SDSS Neighbours Table.

We confirmed that these galaxy pairs were within a physically connected range and not projections following the redshift difference range adopted in Patton et al. (2000). After these steps, our final sample consisted of 298 galaxy pairs lying in the redshift range $0.013 < z < 0.15$.

2.3.3 Obtaining physical properties

After the sample selection, the next step was to extract the physical properties from the spaxels of our sample galaxies. The properties of interest in this work are the stellar surface mass densities and gas phase metallicities.

Stellar surface mass densities

The spatially resolved stellar surface mass densities were obtained by finding the ratio between the stellar mass and surface area of each spaxel.

To obtain the stellar mass, we referred to the MaNGA FIREFLY Value Added Catalogue (MaNGA FIREFLY VAC; Goddard et al. 2017), which provides spatially resolved stellar population properties for MaNGA galaxies. The MaNGA FIREFLY VAC summarises the results of running the full spectral-fitting code FIREFLY (Wilkinson et al., 2017) on spatially resolved

MaNGA spectra that are binned using the Voronoi binning method with a S/N of 10 per pixel. Details on the fitting process and how the stellar population properties are obtained are detailed in Goddard et al. (2017).

After the stellar masses for each spaxel were obtained, the surface mass densities were obtained. In MaNGA data, each spaxel has a size of 0.5 arcsec. We used the small angle approximation to estimate the physical scale of the spaxel:

$$\theta = \tan^{-1}\left(\frac{d}{D}\right) \approx \frac{206,625\ [\text{arcsec}]}{1\ [\text{radian}]}\frac{d}{D}, \tag{2.1}$$

with θ the angular size of the spaxel in arcseconds, D the angular diameter distance, and d the diameter of the spaxel.

We approximated the distance using the Hubble law,

$$D \approx \frac{cz}{H_0}, \tag{2.2}$$

with the redshift information for each galaxy available through the DAP catalogue. We obtained the physical scale, $\frac{d}{\theta}$, of each spaxel using the small angle approximation and then converted the spaxel size from arcseconds to parsecs to obtain the spaxel area.

We found the ratio between the stellar mass and spaxel area to obtain the surface mass density. We corrected for any projection effects and inclination by multiplying the stellar mass surface density by the value b/a, with b and a representing the projected semi-major and semi-minor axes of the galaxy, respectively. This value was obtained from the DAP:

$$\Sigma_* = \frac{M_*}{pc^2}\frac{b}{a}. \tag{2.3}$$

Gas phase metallicities

For this work we adopted the O3N2 metallicity calibrator from Marino et al. (2013) since it is also used in Barrera-Ballesteros et al. (2016), a work that handles the spatially resolved MZR for

MaNGA galaxies;

$$12 + \log(\mathrm{O/H}) = 8.533[\pm 0.012] - 0.214[\pm 0.012] \times \mathrm{O3N2}. \tag{2.4}$$

The O3N2 calibrator was determined by taking the logarithmic differences between the line ratios log(OIII/Hβ) and log([NII]/Hα):

$$\mathrm{O3N2} = \log\left(\frac{[\mathrm{O\ III}]\lambda 5007}{\mathrm{H}\beta} \times \frac{\mathrm{H}\alpha}{[\mathrm{N\ II}]\lambda 6585}\right). \tag{2.5}$$

We note that diffused ionised gas (DIG) can significantly affect emission line fluxes and, consequently, the emission line ratios obtained from these fluxes (Reynolds, 1985, 1987; Walterbos & Braun, 1994; Hoopes et al., 1996; Greenawalt et al., 1998; Hoopes & Walterbos, 2003; Madsen et al., 2006; Voges & Walterbos, 2006). When using the O3N2 calibrator to calculate metallicity, DIG can cause a scatter in metallicity measurements, with the metallicity appearing higher in some galaxies and lower in others (Zhang et al., 2017). However, offsets introduced by DIG are cancelled out when the sample size is sufficiently large (Zhang et al., 2017), an observation that we adopt in this paper.

Once the surface mass densities and gas phase metallicities of all spaxels were obtained, we selected only the star-forming spaxels of each galaxy as gas phase metallicity calibrators are only accurate for star-forming spaxels. The selection was done by comparing the [OIII]/Hβ and [NII]/Hα line ratios in a Baldwin-Phillips-Terlevich diagram (BPT diagram; Baldwin et al. 1981). Next, the S/N was obtained for the star-forming spaxels by multiplying each spaxel's flux by the square root of its inverse variance. Details on the process used to obtain the inverse variance are given in Westfall et al. (2019). Of the star-forming spaxels, we left out spaxels with a S/N < 3 in both N[II]6585 and Hα, as well as any other spaxels that lacked coverage, had unreliable measurements, or were otherwise considered in the MaNGA catalogue to be unusable for science. We show the spaxels used in our study in Fig. 2.1. We note that the majority of our spaxels (99%) have an Hα equivalent width > 6Å, an additional threshold for classifying star-forming spaxels (Cid Fernandes et al., 2010).

2.4 Results

Figure 2.2 plots the oxygen abundance of the star-forming spaxels of our galaxy pair samples as a function of stellar mass surface density within 1.5 $R_{\rm eff}$. The same plot for all star-forming spaxels in the MaNGA survey, which we used to plot the red line in Fig. 2.2, is available in Fig. 2.3 as reference.

We find a bimodality in the metallicity distribution at higher stellar masses, which indicates that two populations of spaxels exist. Such a discrete bimodality is not present in the MaNGA population as a whole, however, as seen in Appendix 2.3.

One of the peaks agrees with the MZR, meaning that higher stellar masses exhibit higher metallicity. This indicates that for some galaxies pairs, the MZR at the local level is in agreement with that of the global level.

There is a secondary peak located below the fit curve for all MaNGA galaxies, albeit in agreement with the contour lines, indicating that there are spaxels with lower metallicities than those with similar stellar masses. These diluted spaxels are in relative accordance with the conclusions of studies that investigated the MZR for galaxy pairs at a global level (e.g. Rupke et al. 2010; Bustamante et al. 2020), which find that galaxy pairs show a metallicity decrement compared to isolated galaxies of similar stellar mass.

2.5 Discussion

In this section we discuss the properties and possible origins of the bimodality.

There have been a number of works that discuss the MZR in interacting galaxies (Michel-Dansac et al., 2008; Rupke et al., 2010) and a further few that include the star formation rate and discuss the fundamental metallicity relation (FMR) in interacting galaxies (Mannucci et al., 2010; Robotham et al., 2014; Grønnow et al., 2015; Bustamante et al., 2020). In particular, Morales-Vargas et al. (2020) conducted a thorough study on the spatially resolved MZR in star-forming regions of perturbed galaxies in the Calar Alto Legacy Integral Field Area (CALIFA; García-Benito et al. 2015) survey. They find that tidally perturbed galaxies show lower oxygen abundances compared to similar-mass non-perturbed galaxies. We compared our findings with

these results. Our results in Fig. 2.2 show that while some spaxels in galaxy pairs show a dilution in gas phase metallicity, which is in agreement with the above-mentioned works that investigate the MZR for galaxy pairs, there are also spaxels that do not show diluted metallicities. This bimodality in distribution is not present in Morales-Vargas et al. (2020). We looked to see if there were any properties that may show a close relation with the loci of the spaxels. In this work we focus on two properties: **a)** the effective radius of each spaxel and **b)** the separation of the galaxy pair each spaxel belongs to.

2.5.1 Spaxel distribution by effective radius

Figure 2.4 shows the spaxels colour-coded by $R_{\rm eff}$, extending out to 1.5 $R_{\rm eff}$. We find that the two peaks in Fig. 2.2 are similar in loci with the core regions of the galaxy. This indicates that the central regions of galaxies contribute to the bimodality. This bimodality indicates that there are two populations of galaxies in the sample, one population with enriched metallicity and one with a dilution of metallicity. The dilution in the latter population is likely a consequence of the galaxy interactions. In a galaxy interaction, strong inflows of gas from the paired galaxy occur, and the accreted gas flows towards the circumnuclear regions of the primary galaxy, fuelling star formation (Iono et al., 2004). If the paired galaxy has outer regions that are metal poor, such as in local galaxies (Shields, 1990), the accreted gas will also be metal poor, resulting in lower-metallicity gas diluting the metallicity in the core region of the primary galaxy (Montuori, M. et al., 2010).

The former population, or the higher-mass, higher-metallicity spaxels belonging to galaxy core regions, can be explained by the inside-out galaxy evolution model (Kepner, 1999). In this model, a negative metallicity gradient is observed, with the greatest metallicity values in the galaxy cores (Vilchez et al., 1988; Vila-Costas & Edmunds, 1992).

While the effective radius indicates that there are both higher-metallicity and lower-metallicity cores in our sample, it does not give us a sufficient understanding of the nature of the galaxies in the sample.

2.5.2 Galaxy pair separation

Previous studies investigating the MZR or FMR for interacting galaxies have found that close galaxy pairs have a lower metallicity compared to galaxy pairs with a greater projected separation (Michel-Dansac et al., 2008; Bustamante et al., 2020). It should be noted that metallicity will have a scatter as at any given distance a galaxy pair can be at a number of different stages of the merger process.

Figure 2.5 plots all spaxels within 1.5 $R_{\rm eff}$ colour-coded by the projected separation of the galaxy pair the spaxel belongs to. We find that spaxels that have a gas phase metallicity consistent with that of the MZR, with increased stellar mass resulting in increased metallicity, likely belong to a galaxy pair with a greater projected separation. We also find that spaxels with diluted metallicity belong to galaxies with lower projected separation. In other words, closer galaxy pairs are more diluted, particularly in their nuclear regions, as can be seen from the previous section. The closest galaxy pairs experiencing a dilution in metallicity is consistent with previous works that studied the MZR or FMR for galaxy pairs (Rupke et al., 2010; Bustamante et al., 2020; Garduño et al., 2021).

Galaxy pairs with a close separation ($<$ 5 kpc separation) can indicate a merger at a number of different stages. Galaxies can be near the first pericentre passage or approaching coalescence. At both of these stages, galaxies are experiencing metallicity dilution in circumnuclear regions. In the first case, the primary galaxy experiences an inflow of low-metallicity gas from the secondary galaxy, and the gas phase metallicity abundance is diluted (Tremonti et al., 2004; Torrey et al., 2012; Montuori, M. et al., 2010). In the second case, when galaxies are approaching coalescence, strong gas inflows are observed, resulting in a dilution of nuclear metallicities (Torrey et al., 2012). Close galaxy pairs can also be post-coalescence and experience enrichment from supernova ejecta (Montuori, M. et al., 2010).

Galaxy pairs with a projected separation of $>$ 20 kpc can be at the first encounter, before the first pericentre passage. At this stage, little metallicity evolution is observed (Rupke et al., 2010; Torrey et al., 2012), so the metallicity abundance would be expected to be in accordance with the MZR. The pair can also be in a state after the first pericentre passage, where star formation events enhance the nuclear metallicity (Torrey et al., 2012). However, the pair could also be in a

period after the first pericentre passage and in the midst of separation before final coalescence, when inflow events will dilute the circumnuclear metallicity (Montuori, M. et al., 2010).

We note that the majority of our galaxies are within 20 kpc in projected separation; as such, they would all be classified under the general term 'close pairs' and commonly placed in a single bin in previous literature. However, we find that there is a possible bimodality dependent on projected separation even with this upper limit of separation. This bimodality is consistent with the metallicity evolution in a galaxy merger.

2.5.3 Possible selection effects

Figure 2.6 shows the contours of the redshift distribution of our sample. We find that spaxels that belong to galaxies with $z > 0.1$ show a metallicity enrichment, whereas spaxels that belong to galaxies with $z < 0.1$ are more scattered throughout the MZR. We note that the lack of metallicity-diluted galaxies at $z > 0.1$ is possibly due to selection effects. Following the luminosity-metallicity relation (Skillman et al., 1989; Pilyugin, 2001; Guseva et al., 2009), lower-metallicity galaxies have lower intrinsic luminosities, resulting in observational limits of their detection. Additionally, merger classifications are incomplete at higher redshifts (Huertas-Company et al., 2015).

2.6 Conclusions

In this work we have investigated the gas phase metallicity (12 + log(O/H)) as a function of stellar mass, or the MZR, of star-forming spaxels in MaNGA galaxy pairs identified using visual and kinematic features. Our main findings include the following:

1. We find a bimodality – two peaks in the distribution of spaxels in the mass-metallicity space for galaxy pairs – a feature that is not present in the MaNGA sample as a whole. This bimodality was not observed in the study by Morales-Vargas et al. (2020), a previous spatially resolved study on perturbed galaxies.

2. The spaxels at the peaks correspond to spaxels in the cores of the galaxy pairs, indicating both metallicity enrichment and dilution in circumnuclear regions.

3. Galaxy pairs with closer separations showed a tendency to display metallicity dilution, whereas galaxy pairs with greater separations showed a metallicity enrichment. This is likely an indicator of metallicity evolution during the galaxy merger process.

Previous studies on the global MZR of interacting galaxies have found that there is a metallicity dilution present for interacting galaxies compared to isolated galaxies of similar stellar masses. Our results show that a metallicity dilution can be observed for interacting galaxies at the local level; however, there is a bimodality that is likely attributable to galaxy separation.

In future works, we plan to investigate the star formation rate of this galaxy sample and investigate the effects of galaxy interaction on the FMR for MaNGA galaxy pairs.

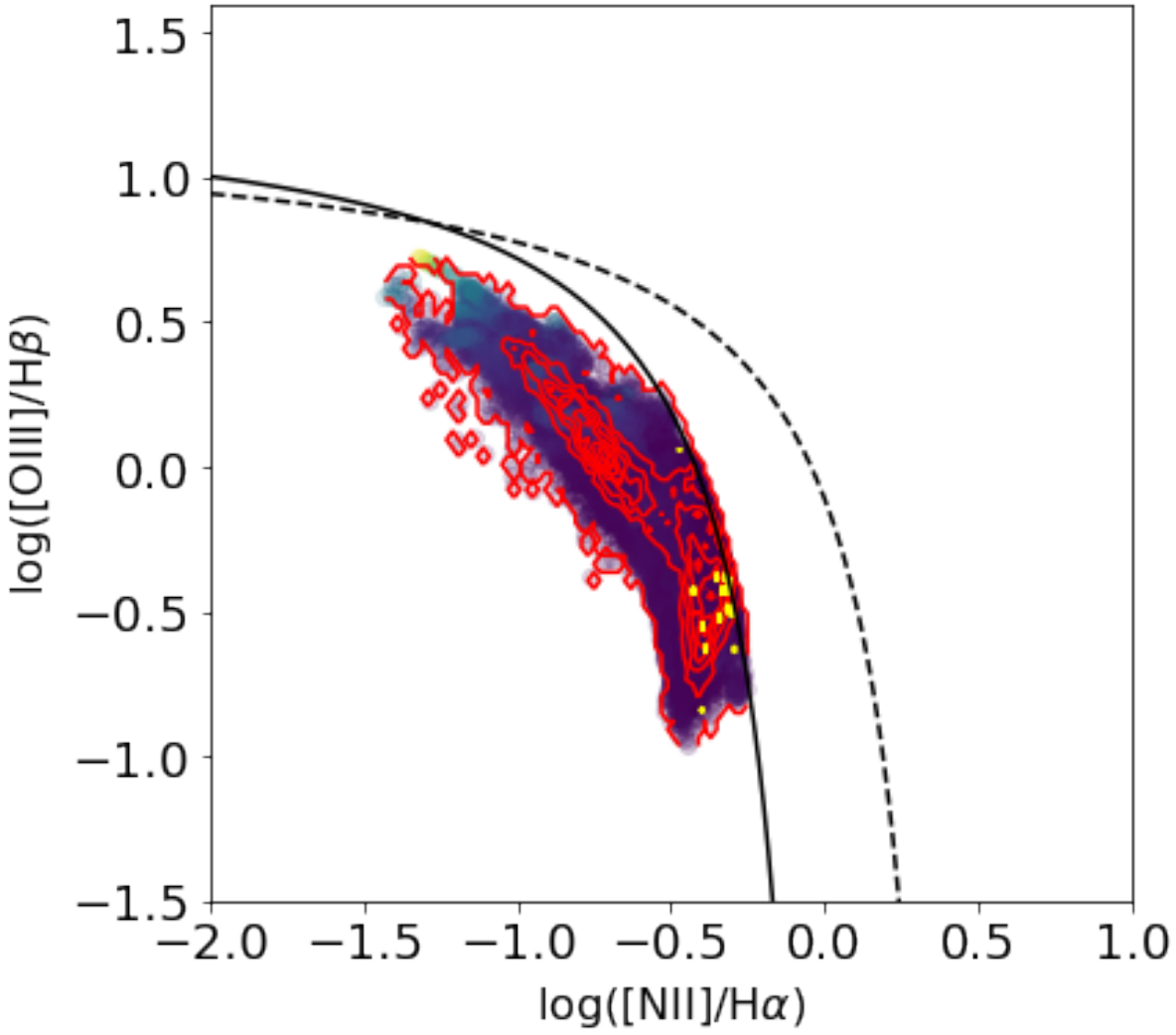

Fig. 2.1: /

Hβ and [NII]/Hα diagnostic diagram.] Distribution of the spaxels of our sample of galaxy pairs shown in an [OIII]/Hβ and [NII]/Hα diagnostic diagram. The solid and dotted black lines are the star-forming and composite classification lines, respectively, defined in Kewley et al. (2006). The red and yellow contours represent the distribution of spaxels with Hα equivalent width greater than or less than 6Å, respectively.

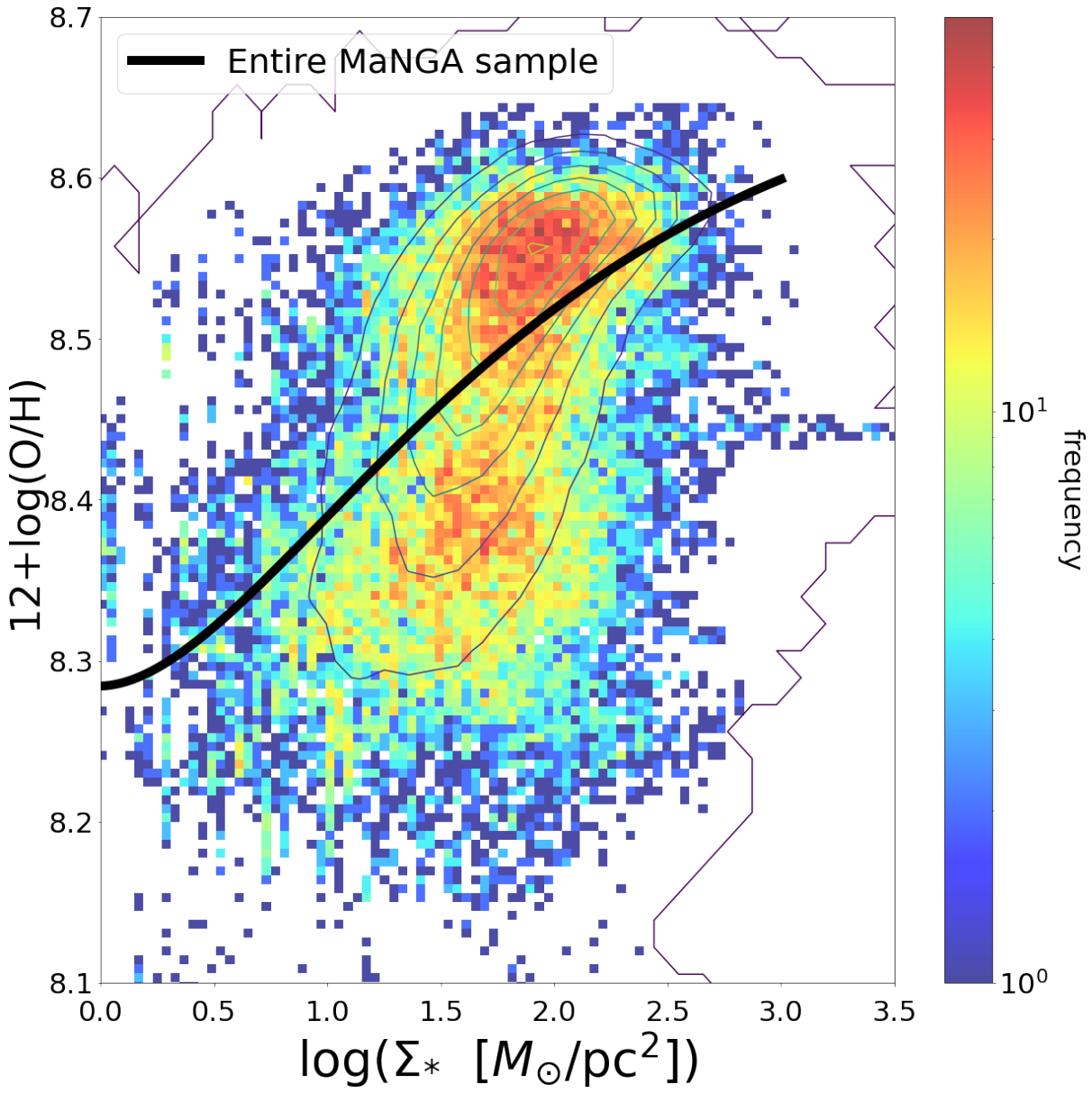

Fig. 2.2: Distribution of oxygen abundance as a function of stellar mass surface density for all star-forming spaxels in the 298 galaxy pairs in the MaNGA survey. The colour bar indicates the number of spaxels per bin in the $\Sigma_* - Z$ space. The black curve is the best-fit line found from the entire MaNGA sample. The contours indicate the distribution of all MaNGA spaxels.

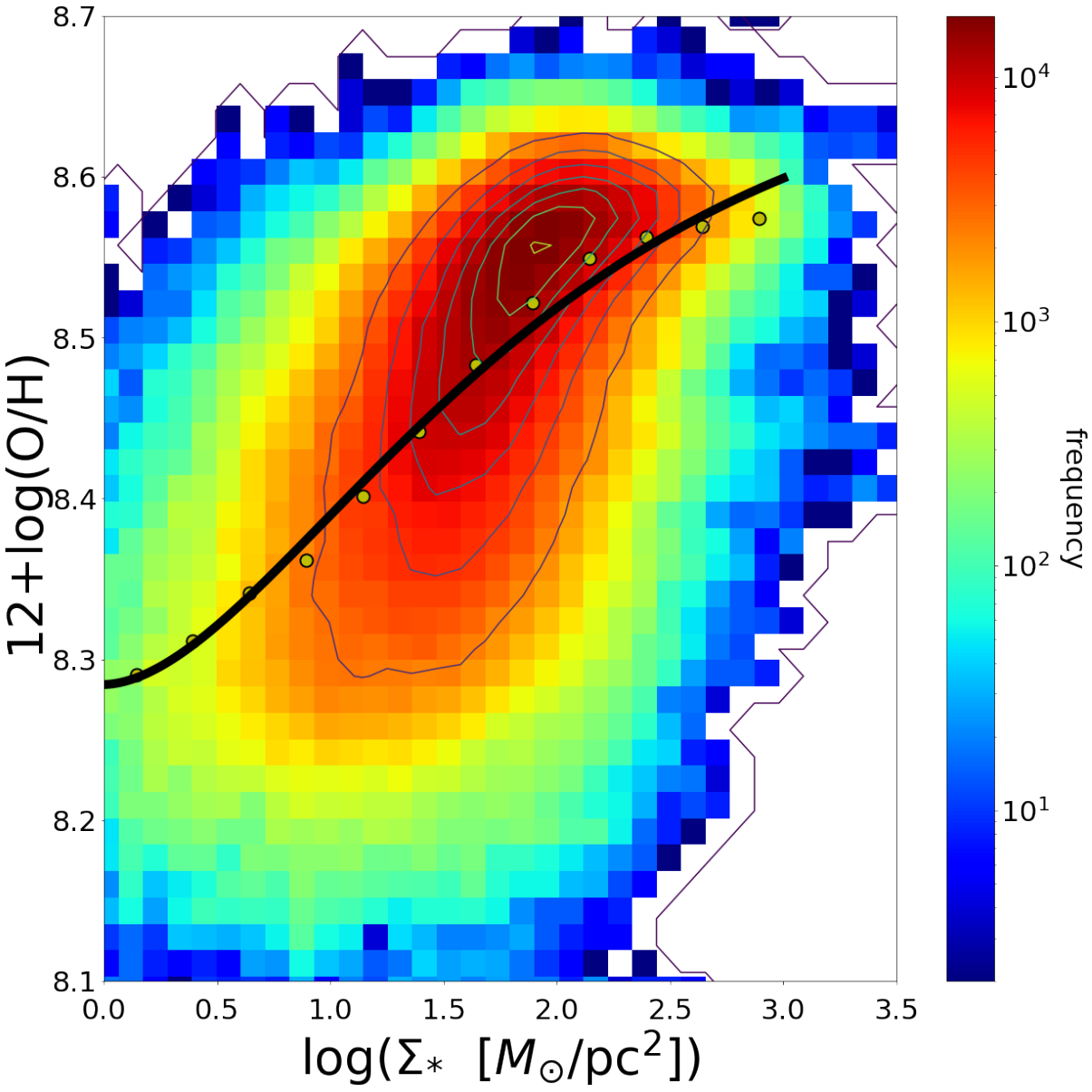

Fig. 2.3: Distribution of oxygen abundance as a function of stellar mass surface density for all star-forming spaxels from all galaxies in the MaNGA survey. The colour bar indicates the number of spaxels per bin in the $\Sigma_* - Z$ space. The black curve is the best-fit line following Sánchez et al. (2013).

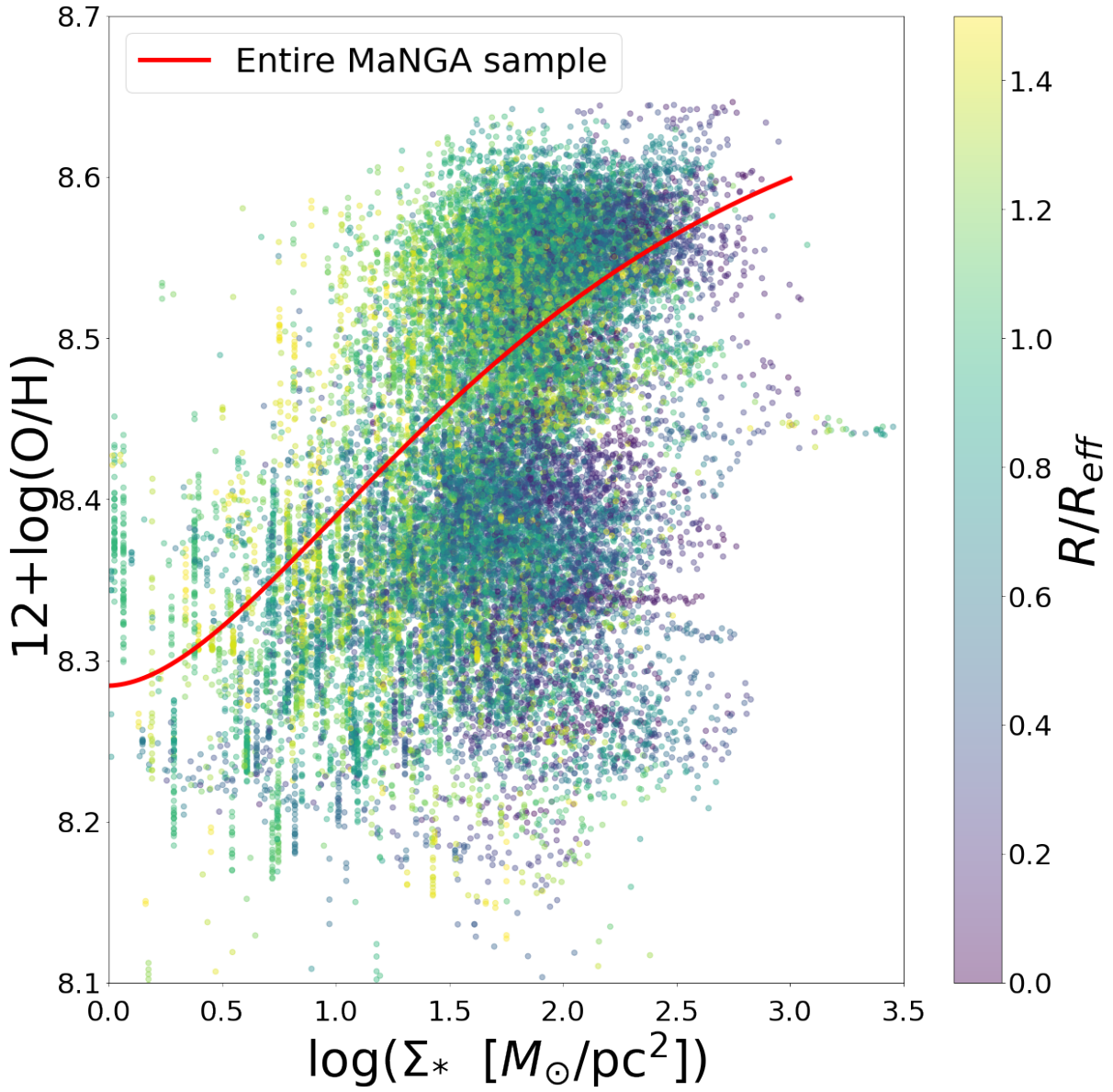

Fig. 2.4: Distribution of oxygen abundance as a function of stellar mass surface density for all star-forming spaxels in the 298 galaxy pairs in the MaNGA survey, colour-coded by effective radius. All spaxels over 1 $R_{\rm eff}$ are masked.

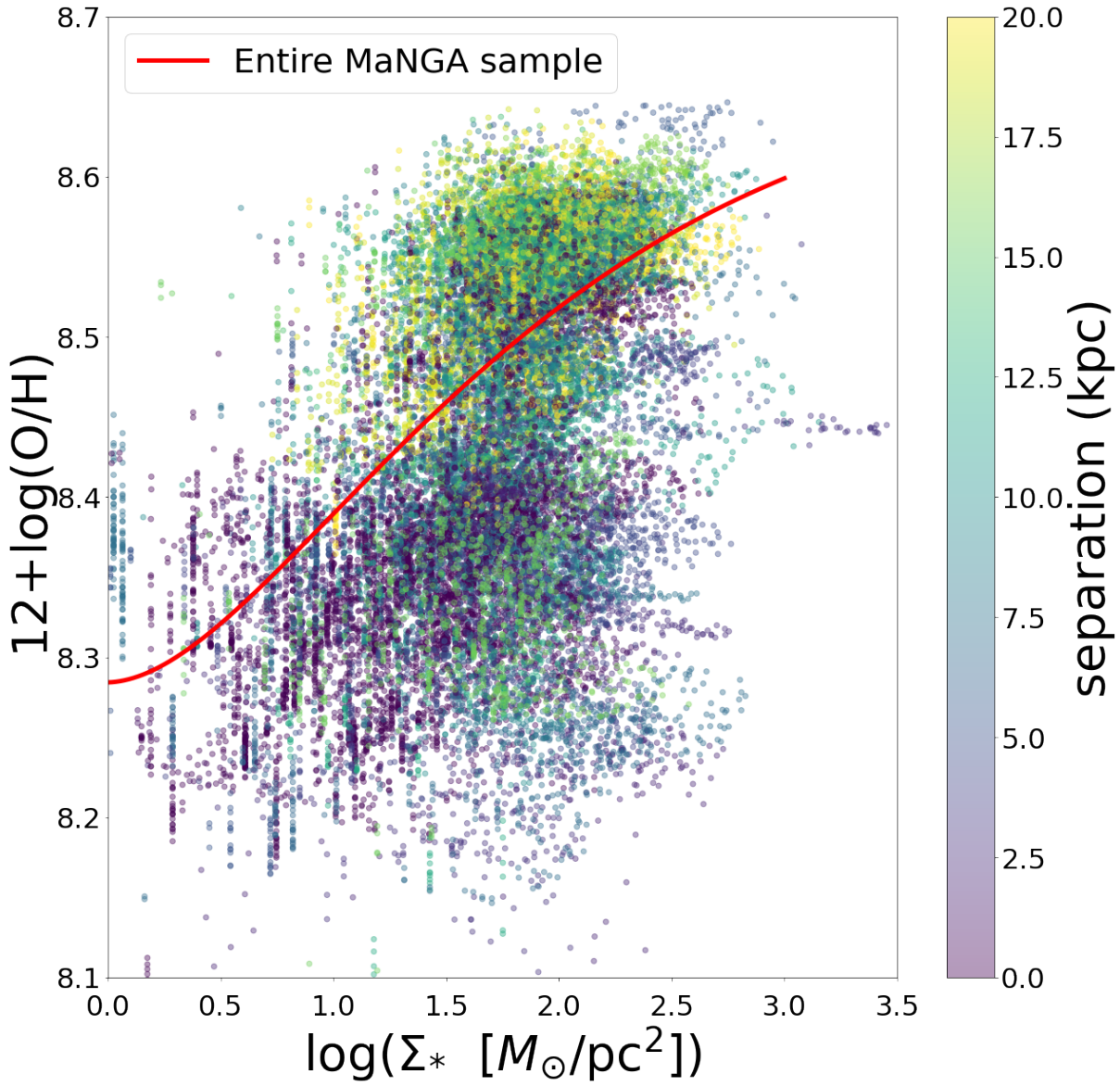

Fig. 2.5: Distribution of oxygen abundance as a function of stellar mass surface density for all star-forming spaxels in the 298 galaxy pairs in the MaNGA survey, colour-coded by galaxy pair separation. All spaxels over 1 $R_{\rm eff}$ are masked.

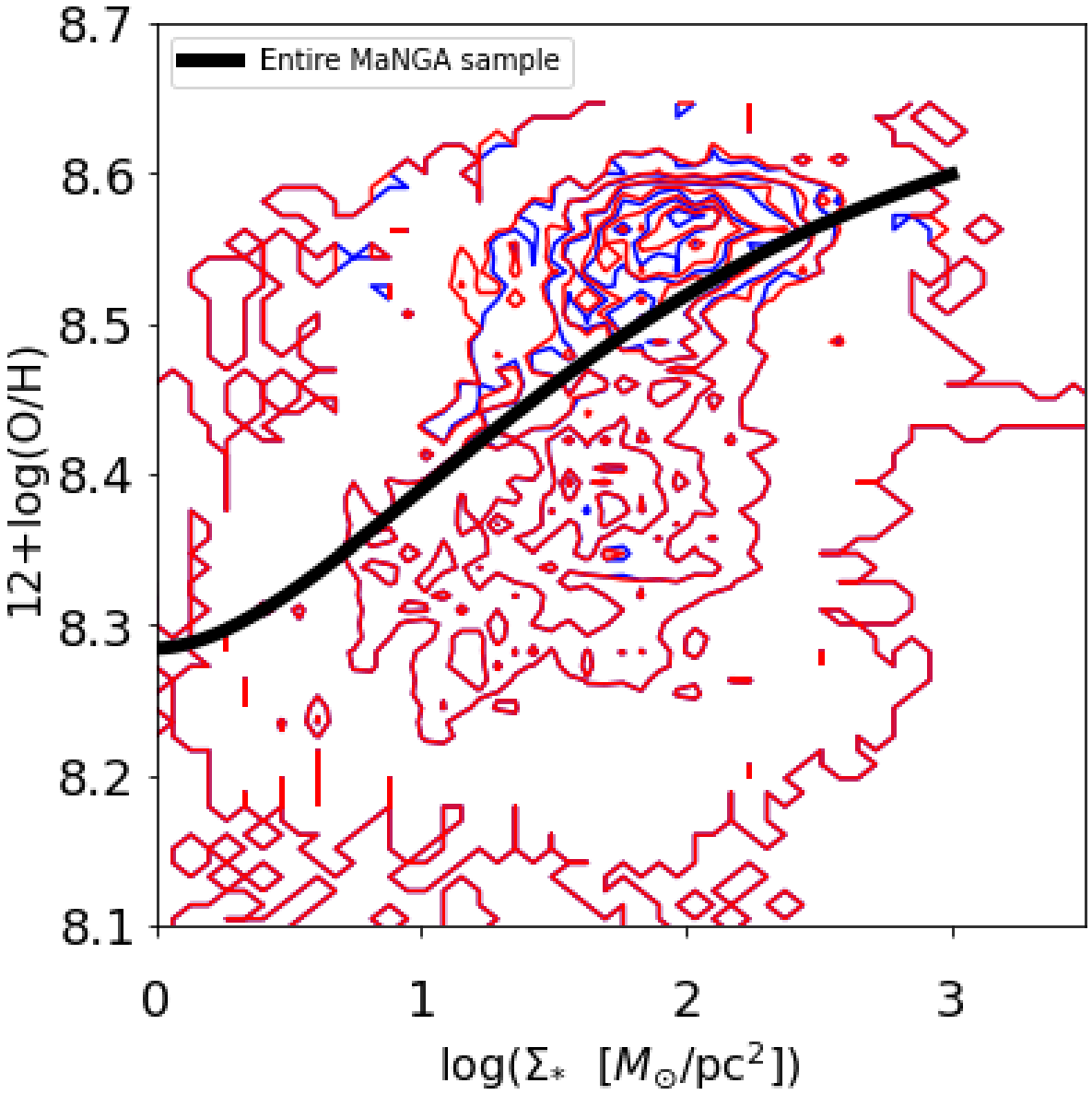

Fig. 2.6: Contours of the redshift distribution of our sample. The red and blue contours represent spaxels below and above redshift 0.1.

Chapter 3

The effect of environment in galaxy merger incidence

Based on "*Galaxy mergers in Subaru HSC-SSP: a deep representation learning approach for identification and the role of environment on merger incidence*" by Kiyoaki Christopher Omori, Connor Bottrell, Mike Walmsley, Hassen M. Yesuf, Andy D. Goulding, Xuheng Ding, Gergö Popping, John D. Silverman, Tsutomu T. Takeuchi, and Yoshiki Toba, 2023, Astronomy & Astrophysics, Article Number 142, Volume 679, November 2023

3.1 Abstract

Galaxy mergers and interactions are an important process within the context of galaxy evolution, however, there is still no definitive method which identifies pure and complete merger samples . A method for creating such a merger sample is required so that studies can be conducted to deepen our understanding of the merger process and its impact on galaxy evolution. We used Zoobot, a deep learning representation learning model pretrained on citizen science votes on Galaxy Zoo DeCALS images. We fine-tuned Zoobot using $\sim$ 1200 synthetic HSC-SSP images of galaxies from the TNG simulation. We find that our fine-tuned model returns an accuracy on the synthetic validation data of $\sim$ 76%. This number is comparable to those of previous studies in which convolutional neural networks were trained with simulation images, but with our work

requiring a far smaller number of training samples. For our synthetic data, our model is able to achieve completeness and precision values of $\sim 80\%$. In addition, our model is able to correctly classify both mergers and non-mergers of diverse morphologies and structures, including those at various stages and mass ratios, while distinguishing between projections and merger pairs. We then used the fine-tuned model to make merger probability predictions on galaxies from HSC-SSP public data release 3, and compiled them to a publicly available catalogue. Using our merger probabilities, we examined the relationship between merger activity and environment. For the relation between galaxy mergers and environment, we find two distinct trends. Using stellar mass overdensity estimates for TNG simulations and observations using SDSS and GAMA, we find that galaxies with higher merger scores favor lower mass density environments on scales of 0.5 to 8 h^{-1}Mpc. However, below these scales in the simulations, we find that galaxies with higher merger scores favor higher density environments.

3.2 Introduction

Galaxy evolution involves many processes that can affect the physical properties of the involved galaxies. Galaxy interactions and mergers are considered to be an important driver of physical phenomena and evolution in galaxies. For example, galaxy interactions and mergers can drive inflow of gas toward the centers of galaxies (Hernquist, 1989; Barnes & Hernquist, 1992; Mihos & Hernquist, 1996; Naab & Burkert, 2001; Hopkins & Quataert, 2010; Blumenthal & Barnes, 2018). These inflows can enhance star formation activity (Beckman et al., 2008; Ellison et al., 2008; Patton et al., 2011, 2013; Hopkins et al., 2013; Moreno et al., 2015; Sparre & Springel, 2016; Thorp et al., 2019), dilute central gas phase metallicities (Ellison et al., 2008; Rupke et al., 2010; Montuori, M. et al., 2010; Sol Alonso et al., 2010; Perez et al., 2011; Torrey et al., 2012; Sparre & Springel, 2016; Thorp et al., 2019), trigger accretion onto supermassive black holes (Keel et al., 1985; Sanders et al., 1988; Matteo et al., 2005; Koss et al., 2010; Ellison et al., 2011; Satyapal et al., 2014; Ellison et al., 2015; Goulding et al., 2018; Ellison et al., 2019), and trigger quasars (Urrutia et al., 2008). More broadly, in the Λ-dominated cold dark matter framework for structure formation in the Universe, accretion of stellar material though galaxy mergers (ex situ

assembly) is a key process by which massive galaxies grow their stellar mass.

Despite their importance, we do not have a full understanding of galaxy interactions and mergers. While studies have been able to quantify the role of mergers as a driver of stellar mass growth (Robotham et al., 2014; Rodriguez-Gomez et al., 2016), the specific role of mergers in driving stellar mass growth, enhancement of star formation and active galactic nucleus activity, and morphological transformations is still contentious. Even the type of environment in which galaxy mergers are prevalent does not have a definitive conclusion. Some dark matter halo simulations predict that mergers are more likely to happen in lower-mass, lower-density regions (Ghigna et al., 1998); however other simulation results (Fakhouri & Ma, 2009; Hester & Tasitsiomi, 2010), and observational studies (Jian et al., 2012) do not necessarily agree with this prediction, stating that mergers occur in denser environments. A major reason for the lack of a clear understanding of the role of mergers and interactions in galaxy evolution or their environments is the difficulty in precisely identifying merger galaxies in observational data.

There have been numerous studies employing several different methods for merger identification, each with strengths and limitations. One approach is the close-pairs method. This method searches for binary pairs in the sky using imaging and photometry or spectroscopy (e.g., Lin et al., 2004; Soares, 2007). The use of spectroscopy allows for more accurate redshift information than photometric redshifts. However, this method has a number of issues. First, it misses galaxies in the post-coalescence phase of a merger, as there is only access to single-galaxy characteristics. Second, it requires spectroscopic redshifts, which may also be impacted by spectroscopic incompleteness. Third, merger rates in observations may be overestimated compared to those in simulations, even if the same criteria are used, due to, for example, chance projections or the difficulty of obtaining accurate merging timescales (Kitzbichler & White, 2008). The criteria for pair selection, such as exact velocity and separation cuts, have undergone significant refinement, resulting in fewer interlopers in merging pair samples being registered (Zepf & Koo, 1989; Burkey et al., 1994; Carlberg et al., 1994; Yee & Ellingson, 1995; Woods et al., 1995; Patton et al., 1997; Wu & Keel, 1998). Also, some mergers may not be detected by this method, as there may be merging galaxy pairs with a pair distance greater than the maximum projected distance adopted for a study.

Other methods rely on galaxy imaging data and their morphologies. Galaxy interactions can cause disturbances to the morphology of a galaxy (Toomre & Toomre, 1972; Toomre, 1977; Negroponte & White, 1983; Hernquist, 1992; Naab & Burkert, 2003; Hopkins et al., 2008a; Berg et al., 2014), which can be quantified into non-parametric statistics. An example of these statistics are the concentration-asymmetry-smoothness (CAS) parameters (Bershady et al., 2000; Conselice et al., 2000; Conselice, 2003), Gini, and M_{20} (Lotz et al., 2004). An n number of these parameters can be combined to create a criteria for merger classification in the n-dimensional feature space (e.g., Goulding et al., 2018; Snyder et al., 2019; Rose et al., 2023; Thibert et al., 2021; Guzmán-Ortega et al., 2023). Using these statistics can reduce the dimensionality of data being used. As a result, the required number of training samples can be reduced compared to image classification methods such as convolutional neural networks. In addition, congregating these parameters into an n-dimensional space will not constrain merger classification within a specific parameter, but instead a combination of parameters. However, this method is also not without limitations, the greatest being that merger-driven morphological disturbances are low surface brightness features (Conselice et al., 2000; Bottrell et al., 2019a; Thorp et al., 2021; Wilkinson et al., 2022) requiring high quality imaging, both in terms of depth and resolution, to identify. Modern-day imaging surveys, such as the multitiered, wide-field, multiband imaging survey Hyper Suprime-Cam Subaru Strategic Program (HSC-SSP; Aihara et al. 2018, see Section 3.1), can enable for such imaging where these features are visible. However, the issue still remains that these non-parametric statistics do not capture the complexity in high-quality imaging data provided by modern wide-field galaxy surveys, and as such, not all information from images can be extracted from these statistics and the n-dimensional feature spaces using them, especially as dimensionality reduction inevitably leads to loss of information.

There have also been methods relying on visual inspection of galaxy images. When conducting morphological studies, visual classification by experts is largely considered the gold standard (Nair & Abraham, 2010). Most notably, the visual approach can incorporate domain-specific human knowledge in the classification of galaxies, i.e., merger classification results can be purified through human intuition of what is visually a merger, particularly in classifications done by machine learning methods. Indeed, visual follow-ups by human classifiers is often employed

to purify merger 'candidate' samples produced by automated and quantitative approaches (e.g., Bickley et al., 2022; Pearson et al., 2022). The visually distilled samples yield more robust scientific outcomes on merger properties. Therefore, it is clear that domain knowledge provided by human classifiers is valuable. Second, visual classifications, in principle, use all of the morphological information encoded in high-quality galaxy images, and is not restricted to a set of summary statistics (Blumenthal et al., 2020). However, this method also has its weaknesses. First, the criteria for what is considered a merger can differ depending on the individual carrying out the visual inspection: so the same galaxy may be assigned a different label by different people. Additionally, visual inspection by humans can be very time-consuming, and not realistic for large data-sets in modern-day galaxy surveys, many of which contain several million targets. The Galaxy Zoo Project (Lintott et al., 2008, 2011, hereinafter referred to as GZ1) overcame these issues to an extent. GZ1 is a catalog (Darg et al., 2010a) offering morphology probabilities for over 1 million Sloan Digital Sky Survey (SDSS) galaxies, with citizen scientists assigning labels for morphological features. The labels assigned in this catalog are summarized into a single weighted statistic depending on the 'correctness' of the scientists. Merger probabilities are part of this catalog, and have been used in many merger-related studies, such as Holincheck et al. (2016); Weigel et al. (2017). However, while citizen science can be more time efficient than classifications made by expert scientists, it may not be as reliable.

Recent advents in deep learning technology for image-based galaxy characterization have made the visual inspection process less time- and human-resource consuming. Convolutional neural networks (CNNs) and deep learning models have achieved performances greater than other computer imaging methods (Krizhevsky et al., 2017), even surpassing the performance of some human classifications (He et al., 2015). CNNs have already been used in a number of studies, both in galaxy morphology classification as a whole (e.g., Dieleman et al., 2015; Domínguez Sánchez et al., 2018; Jacobs et al., 2019; Zhu et al., 2019; Ghosh et al., 2020; Cheng et al., 2021; Domínguez Sánchez et al., 2022; Walmsley et al., 2022a; Cavanagh et al., 2023; Huertas-Company & Lanusse, 2023), and the specific task of galaxy merger classification, with varying levels of accuracy (e.g., Walmsley et al., 2019; Pearson et al., 2019; Bottrell et al., 2019b; Bickley et al., 2021; Ćiprijanović et al., 2020; Ferreira et al., 2020; Ćiprijanović et al., 2021;

Bickley et al., 2022; Bottrell et al., 2022; Pearson et al., 2022; Ferreira et al., 2022).

In this work, we investigate a particular approach of the training process in CNNs, in the form of transfer learning. Training a CNN from scratch requires a very large labeled training set, and preparing such a data-set for any classification task presents similar issues as those highlighted in visual inspection above, such as the high time- and human-resource costs. This step can be potentially streamlined and made more efficient through transfer learning, or transferring the knowledge from a previous study and adapting it to a new data-set. The approach of using transfer learning for galaxy merger identification was conducted by Ackermann et al. (2018), who find that transfer learning using the diverse ImageNet data-set can lead to improvements over conventional machine learning methods. In Domínguez Sánchez et al. (2019), transfer learning and fine-tuning using astronomical data was conducted. This study found that knowledge can be transferred between astronomical surveys, and that combining transfer learning and fine-tuning can boost model performance and reduce training sample size. This work will combine the approaches of the above works. We use the techniques of transfer learning and fine-tuning, through the use of the pretrained model Zoobot (Walmsley et al., 2023). Zoobot is a pretrained model trained on diverse astronomical images, using human knowledge in its pretrained weights as a foundation. In Walmsley et al. (2022b), ring galaxies were correctly classified using a fine-tuning sample size of $\sim$ 100, finding that galaxy morphological classification problems can be solved through a transfer-learning and fine-tuning approach. Our approach is to use the weights of Zoobot as a foundation, and fine-tuned the model for the purpose of galaxy merger identification. The model is fine-tuned to classify HSC-SSP images, using a small sample of survey-realistic HSC-SSP images from the TNG50 cosmological magneto-hydrodynamical simulation (Pillepich et al., 2019; Nelson et al., 2019) and corresponding ground truth merger status labels. This approach is able to construct a model combining **a)** human domain knowledge on galaxy morphology and **b)** ground truth merger labels accessible only from simulations.

This work is broadly divided into two portions. In the first portion, encompassing from Section 3.3 to Section 3.5, we introduce our machine-learning based approach for classification, and evaluate the performance of our classifier. In the second portion of this work, composed of Section 3.6 and Section 3.7, we conduct investigations using the merger and non-merger galaxies

we identified using our fine-tuned model, particularly the relationship between galaxy mergers and environment. Specifically, we investigate whether mergers are found more frequently in higher density or lower density environments. We study the relationship between galaxy merger probability and their mass overdensities by using multiscale environmental parameters, ranging from 0.05 Mh^{-1}Mpc to 8 h^{-1}Mpc, computed by Yesuf (2022). We compare the findings of the relationship found in the observational galaxies with those in simulations, and discuss the results.

3.3 Method

In this section, we describe the Zoobot deep representation model from (Walmsley et al., 2022a,b; Walmsley et al., 2023). We then describe our approach to fine-tuning Zoobot using observation realistic synthetic HSC-SSP images constructed from galaxies from the TNG50 cosmological hydrodynamical simulation.

3.3.1 Zoobot

Zoobot (Walmsley et al., 2023) is a publicly available pretrained model that can be fine-tuned for use in galaxy morphology classification problems. The initial deep learning model is trained with the methods written in Walmsley et al. (2022a), using data and labels from Galaxy Zoo DECaLS (hereinafter referred to as GZ DECaLS). GZ DECaLS is a project where galaxy images in the deep, low-redshift Dark Energy Camera Legacy Survey (DECaLS, Dey et al., 2019) are given morphological identifications by citizen science volunteers. Zoobot uses DECaLS imagery due to its superior depth and seeing compared to that in the imagery used in previous GZ projects. For example, in GZ 2 (Darg et al., 2010a), which is often used for machine learning architecture in astronomical imaging classification (e.g., Banerji et al., 2010; Ackermann et al., 2018), SDSS images are used. This imaging survey has a median 5σ point source depth of r = 22.7 mag with a median seeing of 1.4 arcseconds and a plate scale of 0.396 arcseconds per pixel (York et al., 2000). The DeCALS survey has a median 5σ point source depth of r = 23.6 mag, and seeing better than 1.3 arcseconds, and a plate scale of 0.262 arcseconds per pixel (Dey et al., 2019), offering improved imaging quality. This not only allows for fainter and low surface brightness

merger features to be revealed, but also is closer to the depth of the images we conduct training and make predictions from, which we explain in Section 3.4.

The classifications made in the GZ DECaLS data-set were for galaxy features such as bars, bulges, spiral arms, and merger indicators. A total of 96 milion clicks gives approximately 7.5 million classifications were given for over 310,000 galaxies in GZ DeCALS. These classifications were then used to train a deep representation learning model. Predictions made by the trained model achieved 99% accuracy when measured against confident volunteer classification for a variety of features, such as spiral arms, bars, and merger status. The results of Walmsley et al. (2022b) showed that this trained model was able to find similar galaxies and anomalies without any modification, even for tasks that it was never trained for. Further, the model can be fine-tuned for specific morphological classification tasks.

The technique of fine-tuning consists of training an initial model (usually with a large amount of data), then adapting the model to a different task (usually with a smaller amount of training data). Once the initial model is trained and representations learned, the 'head' layer, or the upper layer, is removed, and the weights of the remaining layers, or 'base' layers, frozen. A 'new head' model with outputs appropriate for the different task is added, then trained with data and labels for the new task. The characteristic of this method is that a far smaller training sample for the specific task is required compared to training a model from scratch.

Walmsley et al. (2022b) found that when using a small training sample (~1000 samples), this fine-tuning approach can yield higher accuracies compared to training a data-set from scratch. Further, fine-tuning using a 'base' model trained on generic galaxy morphology data and labels (Zoobot) yielded higher accuracies than fine-tuning a model trained with a generic terrestrial set of representations (ImageNet). Further detailed descriptions and methods used in Galaxy Zoo DeCALS and Zoobot are available in Walmsley et al. (2022a), Walmsley et al. (2022b), and Walmsley et al. (2023).

3.3.2 Fine-tuning Zoobot using simulation images

Training data

Training a classifier, whether it be from scratch or through transfer learning, requires training data consisting of image data and corresponding ground truth labels. For this work, we require galaxy image data with labels of either merger or non-merger. We obtain images with ground-truth merger labels by using synthetic HSC-SSP images of galaxies from the TNG50 simulation. The use of simulations gives us access to information about a galaxy that is generally unavailable in observations, such as when the galaxy underwent or will undergo its previous or next merger, as well as properties of the merger activity itself, such as the mass ratio between the galaxies involved.

IllustrisTNG50

We use data available from simulation data to acquire galaxy samples for mergers and non-mergers. Specifically, we use a suite of large-volume cosmological magneto-hydrodynamical simulation data in the form of IllustrisTNG simulation data. The IllustrisTNG simulations (Springel et al., 2018; Pillepich et al., 2018a; Naiman et al., 2018; Nelson et al., 2018; Marinacci et al., 2018), performed with with the moving mesh code AREPO (Springel, 2010), includes a comprehensive model for galaxy formation (Weinberger et al., 2017; Pillepich et al., 2018b). This model includes treatments for stellar formation and evolution, black hole growth, magnetic fields, stellar and black hole feedback, and radiative cooling. TNG simulations track the evolution of dark matter, gas, stars, and supermassive black holes ranging from the very early universe up to redshift $z = 0$. TNG simulations include three runs spanning a range of volume and resolution, TNG50, TNG100 and TNG300, in order of ascending volume and descending resolution. For this work we use simulation data from TNG50 (Pillepich et al., 2019; Nelson et al., 2019), which offers the highest resolution, with evolving 2×2160^3 dark matter particles and gas cells in a 50 Mpc box.

We use survey-realistic synthetic HSC images from the TNG50 data, with the imaging to come in Bottrell et al. (2023). The galaxies from the TNG simulations go through a multiple steps to produce these synthetic images.

First, the images are forward-modeled into idealized synthetic images in HSC *grizy* bands (Kawanomoto et al., 2018) using the Monte Carlo Radiative transfer code SKIRT (Camps & Baes, 2020). For each galaxy in our sample, stellar and gaseous particle data taken from its friends-of-friends (FoF) group within a spherical volume is used to run the radiative transfer simulation. The radius captured within this spherical volume is sufficiently large that extended structures, satellites, and nearby groups and clusters are included in the transfer simulations.

SKIRT models the spectral energy distribution (SED) of stellar populations using the Bruzual & Charlot (2003) template spectra and Chabrier (2003) initial mass function for stellar populations older than 10 Myr, and with the MAPPINGS III SED photoionization code (Groves et al., 2008) for younger stellar populations (<10 Myr). The MAPPINGS III library accounts for emission from HII regions, surrounding photodissociation regions, gas and dust absorptions in birth clouds around young stars, nebular and dust continuum and line emission.

Next, as TNG simulations do not explicitly track dust evolution, a dust model is required to account for the relationship between dust and gas properties. The model used follows Popping et al. (2022), which takes into account the empirical scaling relation between the dust-to-metal mass ratio (DTM) and metallicity within gas (Rémy-Ruyer et al., 2014). Following the empirical broken power law, Rémy-Ruyer et al. (2014), the metallicity in each gas cell can be converted in to a dust-to-gas mass density ratio, which then in turn can be used to compute the dust density (abundances). As in Schulz et al. (2020) and Popping et al. (2022), the dust abundances is set to zero for cells that are not star forming or temperatures greater than 75000 K. Dust self-absorption is not accounted for in the transfer simulations.

Finally, RealSim (Bottrell et al., 2019b) in conjunction with HSC Data Access Tools, is used for **a)** assignment of insertion location within HSC and flux calibration, **b)** spatial rebinning to HSC angular scale, and **c)** reconstruction of a HSC PSF and convolusion of the idealized image, and the final injection into HSC-SSP. The full-color images created using these steps visually resemble those of real galaxies in the HSC-SSP (Eisert et al. in prep). Detailed descriptions on the synthetic images and how they are processed will be provided in Bottrell et al. (2023). We use synthetic images at 3 snapshots, 78, 84, and 91, corresponding to redshifts z = 0.3, 0.2, and 0.1, respectively. We also constrain the subhalo stellar mass to be $\log(M_*/M_\odot) > 9$, which is

approximately the lowest limit for stellar structures in TNG data to be well resolved.

Merger and non-merger selection

We select galaxy mergers based on the time to the closest merger event, either the most recent merger event or the next merger event. We define a merger event to be the snapshot within a simulation galaxy's merger tree where two halos from the previous snapshot merge and become a single halo. The observability timescale for galaxy interaction signatures in imaging data is difficult to constrain, as it can depend on a wide range of properties. These range from the method used for merger identification (pair identification, nonparametric statistics), physical properties of the interacting galaxies themselves (gas mass, pair mass ratio, dust) to the properties of the observations (wavelength, viewing angle, resolution). Studies have been conducted using hydrodynamical simulations (Lotz et al., 2008, 2010a,b) to constrain the observability timescale for various merger identification methods and merger properties. Timescales found from these works can be as low as 0.2 – 0.4 Gyr, and can exceed 1 Gyr, depending on the signature used, such as galaxy asymmetry or Gini - M_{20} metric, as well as the physical properties of the galaxies themselves.

For this work, we apply a 0.5 Gyr cut since or until the closest merger event to select a merger sample. This cutoff will allow for most merger signatures to be detected. As we would like to make the model agnostic to a diverse scope of mergers, we do not place any constraints on the physical properties of the galaxies such as gas mass or star formation rate, and include mergers of varying mass ratios: major (mass ratio <1:4), minor (mass ratio <1:10), and mini (mass ratio <1:20). Mass ratios are defined comparing the maximum stellar masses of the composing galaxies of the merger pair. These restrictions leave us with 291 mergers, with 104 at snapshot 78, 111 at snapshot 84, and 76 at snapshot 91.

For non-merger selection, we adopt a cutoff so that visual merger signatures should not be visible in the images. For this work, the non-mergers have the most recent or next merger event to be > 3 Gyr, sufficiently greater than the observability timescales found in the works above. These cutoffs give us 1472 non-mergers. We do not use all of these non-mergers, as it is preferable that the size of classes are balanced when training models. Further, to ensure that we

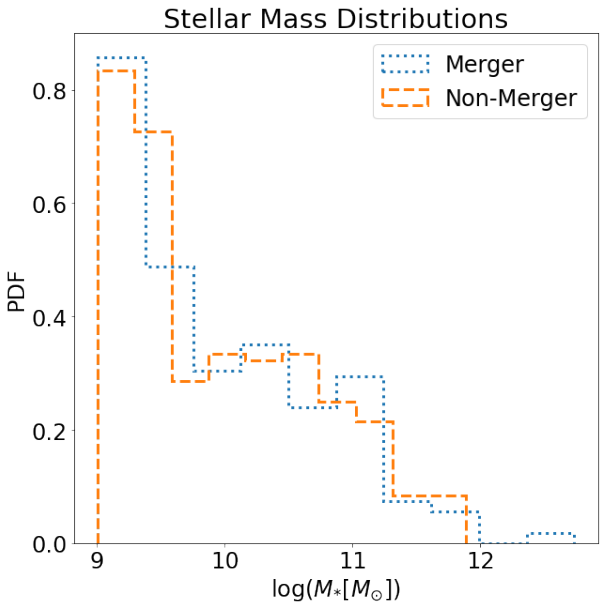

Fig. 3.1: Stellar mass distributions for the simulated TNG50 merger and non-merger galaxies used for fine-tuning Zoobot. There are 291 each of mergers and non-mergers, with 104 at $z = 0.3$. 111 at $z = 0.2$, and 76 at $z = 0.1$. Each merger galaxy used in the fine-tuning process has a corresponding non-merger galaxy at the same snapshot with a stellar mass within 0.1 dex.

do not have stellar mass and redshift biases between the merger and non-merger samples, for each merger galaxy we select a non-merger galaxy with the same snapshot (redshift) and a stellar mass within 0.1 dex. The stellar mass distributions of the merger and non-merger galaxies are shown in Fig 3.1. Conducting a two-sample KS test on the merger and non-merger stellar mass distribution returns a statistic of 0.01, and a p-value of 0.99. The sample used for fine-tuning includes 291 mergers and non-mergers of similar stellar mass distribution, and as each galaxy in the image catalog is processed by SKIRT along four lines of sight, we have ~1200 synthetic HSC *gri* images each for mergers (assigned with a class label of 1) and non-mergers (assigned with a class label of 0). A sample size of this order can achieve greater accuracies through fine-tuning using Zoobot as opposed to training a model from scratch, or from transfer learning using ImageNet, as shown in Walmsley et al. (2022b). We note that while our merger sample includes mergers at varying mass ratios and stages, they are all given the same class label. As such, the output of our model will only predict whether or not a galaxy is a merger, and will not make classifications on merger mass ratio or stage.

Cutouts are made for the ~ 2400 galaxy images as a final preprocessing step. These cutouts

Layer (type)	Output Shape	Num. Parameters
GlobalAveragePooling2D	(None, 1280)	0
Dropout	(None, 1280)	0
Dense	(None, 64)	81984
Dropout	(None, 64)	0
Dense	(None, 64)	4160
Dropout	(None, 64)	0
Dense	(None, 64)	1

Table 3.1: Architecture of the new 'head' model we attach to the Zoobot 'base' model. The output shape and the number of free parameters are also shown.

encompass 10× Sersic $R_{\rm eff}$ of each galaxy, and are resized to 300 × 300 pixels for input into the model.

Training procedure

As highlighted in the previous sections, the 'head' trained on GZ DeCALS is removed, and the 'base' model is frozen. Detailed architecture of the Zoobot 'base' model are available in Walmsley et al. (2022a). We summarize the newly added 'head' layer for the merger identification task in Table 3.1.

We train our new head using binary cross-entropy loss, with a maximum of 150 epochs available for training. However this maximum number of epochs may not necessarily be reached, as we follow Walmsley et al. (2022b) and adopt an early stopping algorithm, which ends training when the validation loss stops decreasing. The training time is dependant on the data-set size. For the small data-sets used in this work, each epoch takes about 50 seconds, with the longest training taking 48 epochs and the shortest 18 epochs.

Before we conduct tests on observational data, we first evaluate the performance of the model

Class	Precision	Recall	F1-Score
Non-merger	0.74	0.83	0.75
Merger	0.80	0.70	0.80

Table 3.2: Means of metrics of ten individual Zoobot fine-tuning runs, assuming a complete binary class split (non-merger class (class 0): merger probability <0.5, merger class (class 1): merger probability >0.5). Each run split the TNG50 data-set into different 63% training, 27% validation, and 10% testing data-sets. The metrics are based on the validation data-set.

on simulation data alone. We split the TNG50 data-set into training, validation, and testing data-sets. To prevent contamination between the training and testing sample, we make sure that all four viewing angles of a single galaxy are contained in a single data-set. For example, if a galaxy with viewing angle 1 is included in the training data-set, the other three viewing angles are also included in the training data-set, and no angles of the same galaxy are in the testing or validation data-sets. We create ten independent training/validation/testing subsets through ten-fold cross validation so that each galaxy will be assigned a merger probability. The split for each data-set is 63% training, 27% validation, and 10% testing. We record the accuracy, loss, validation accuracy and validation loss of each run.

Table 3.2 reports the mean precision, recall, and f1-score for each class (merger and non-merger). A summary of the confusion matrices for each run are available in Figure 3.2. We note a stochasticity in validation accuracy and validation loss in the confusion matrices, likely resulting from the variation in the training/validation/testing data-set splits.

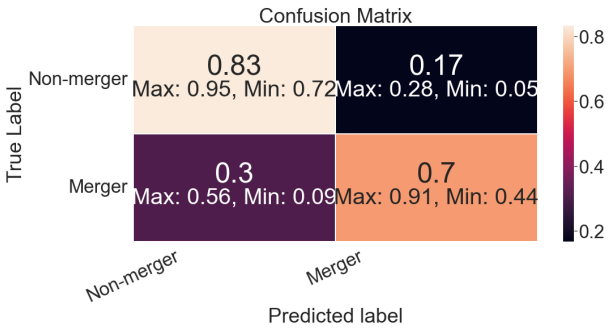

Fig. 3.2: Total combined confusion matrix for the 10 runs of our Zoobot fine-tuning process. Each run fine-tuned a new model on a different set of training/validation data, and the confusion matrices are on 10 different sets of testing data.he stellar mass distributions for merger and non-merger galaxies used for fine-tuning Zoobot. The maximum and minimum values for each cell are also indicated.

The mean accuracy obtained from the ten runs is 76%. These results are comparable to or greater than previous works that trained CNNs from scratch using simulation images of galaxy mergers (e.g., Pearson et al., 2019), with this work using a far smaller set of training data. For example, Pearson et al. (2019) uses ~ 7000 images to train their simulation network, and achieves an accuracy of 65.2%. We can expect a further increase in training data by incorporating mergers and non-mergers from more TNG snapshots when the images become available, which should further improve accuracies.

Making predictions on galaxies returns a merger probability between 0 and 1, with 0 indicating a non-merger galaxy and 1 indicating a merger galaxy, independent of merger mass ratio or merger stage. Figure 3.3 shows histograms of the merger probabilities for the combined 10 runs. In Fig. 3.3a we see that the probabilities are peaked in a range between 0.4 - 0.5, indicating that many galaxies have unclear classifications, and not as many galaxies are "confidently" labeled mergers or non-mergers. However, we find that more mergers are given a probability >0.5, and more non-mergers are given a probability <0.5. We further investigate what type of mergers are given unclear merger probabilities. Figure 3.3b shows the merger probability distributions on ground truth pre-merger (within 0.5 Gyr until the merger event) and post-merger (within 0.5 Gyr since the merger event) galaxy images. We find that while the model most frequently gives pre-mergers a probability >0.8, post-mergers are found to be most frequently given a probability between 0.4 - 0.5. Figure 3.3c shows the merger probability distributions on ground truth major merger (mass ratio >1:4), minor merger (1:4 >mass ratio >1:10), and mini merger (1:10 >mass ratio >1:20) images. We find that while the model is able to give high merger probabilities to mergers of all mass ratios, more minor and mini mergers are given lower probabilities (0.5 <merger probability <0.8) compared to major mergers. As such, the galaxies given unclear merger probabilities are likely to be minor and mini post-mergers.

We next evaluated the model's performance at various thresholds using an ROC curve. The ROC curve plots the true positive ($\frac{TP}{TP+FN}$) against the false positive ($\frac{FP}{FP+TN}$) rates at all probability thresholds between 0 and 1. Figure 3.4 shows the ROC curve. The area under the ROC curve (AUC) measures the ability of the model, returning a value between 0 and 1. This value is the probability that a randomly selected merger has a merger probability greater than that of a

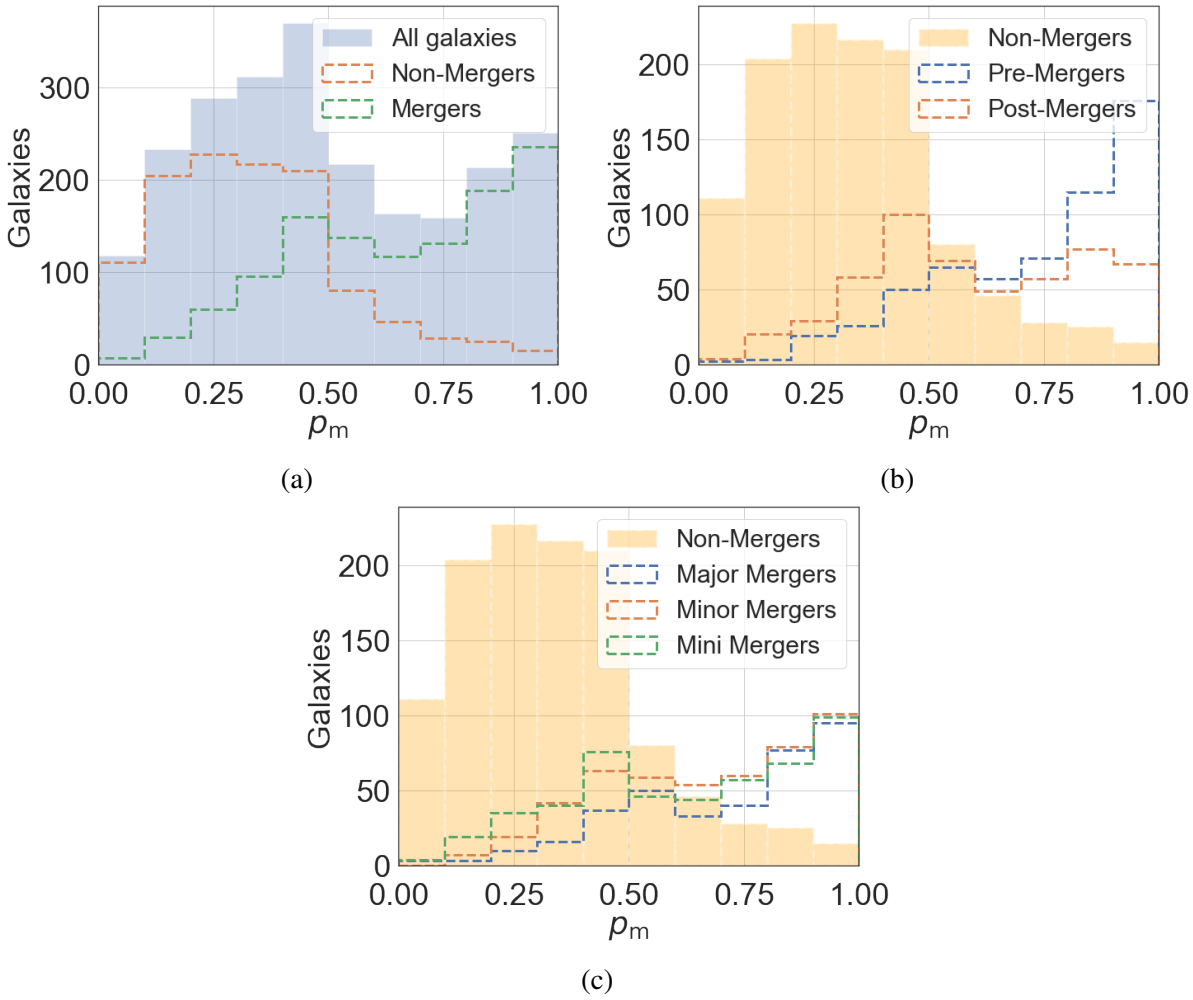

Fig. 3.3: Merger probability distributions for TNG50 synthetic galaxy images predicted using our fine-tuned model. We used ten-fold cross-validation during training for ten independent testing samples to find probabilities for all galaxies, so that each galaxy was given one probability during the process. Each subfigure shows the merger probability distributions for different types of ground-truth mergers. a) All galaxies, mergers, and non-mergers. b) Non-mergers, pre-mergers (0.5 Gyr >time until merger >0 Gyr), and post-mergers (0.5 Gyr >time since merger >0 Gyr). c) Non-mergers, major mergers (mass ratio >1:4), minor mergers (1:4 >mass ratio >1:10), mini mergers (1:10 >mass ratio >1:20).

randomly selected non-merger. An AUC of 1 indicates a perfect classifier. Our AUC is 0.84.

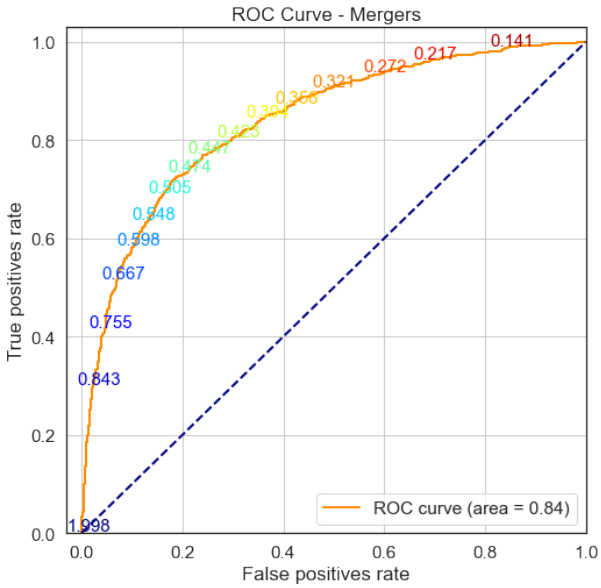

Fig. 3.4: Trained model's ROC curve. The numbers overlayed on the curve indicate thresholds where the false positive and true positive rates along the curve are recorded. The dotted diagonal line is the performance of a completely random model that outputs a random probability for any image. An ROC curve is preferred to be above this dotted diagonal, and the curve generated from our model is above this line. We also find an AUC value of 0.84.

We further show the model's performance as a function of merger probability in Fig. 3.5a, in the form of mean completeness and precision curves of the combined 10 runs. The completeness is obtained by the dividing the number of ground truth mergers with a greater merger probability than the probability bin, by the total number of ground truth mergers in the testing data-set:

$$\text{Completeness}(p_{\text{merg}}) = \frac{(\text{Num. GT Mergers} > p_{\text{merg}}) - \text{Total GT Mergers}}{\text{Total GT Mergers}}, \quad (3.1)$$

where GT means ground truth. The precision is obtained by the dividing the number of ground truth mergers with a greater merger probability than the probability bin by the total number of

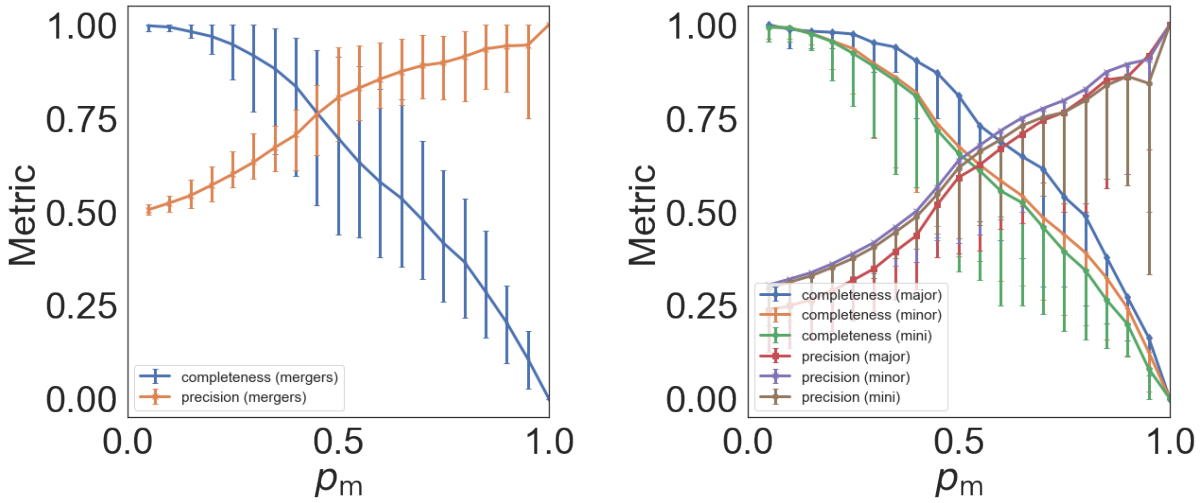

(a) (b)

Fig. 3.5: Precision and completeness curves of the TNG images, with mean completeness and prevision as a function of merger probability. Figure 3.5a (left panel) shows the curves assuming a complete binary split. The blue curve indicates completeness, and the orange curve indicates precision. Vertical error bars indicate the maximum and minimum values for the metric from the ten runs at each probability bin. Figure 3.5b (right panel) investigates the curves taking into consideration differing merger mass ratios (major, minor, mini). We find mini and minor mergers are predicted at an equivalent, if not greater precision compared to major mergers. We also find that the completeness at any fixed merger probability decreases with decreasing merger mass ratio.

objects with a greater merger probability than the probability bin:

$$\text{Precision}(p_{\text{merg}}) = \frac{\text{Num. GT Mergers} > p_{\text{merg}}}{\text{Num. Objects} > p_{\text{merg}}}. \quad (3.2)$$

The model has values of 80% for both completeness and precision for mergers on the testing data-set if we adopt a complete binary split, that is, any galaxy with a merger probability > 0.5 is classified as a merger, and any < 0.5 is classified as a non-merger. This accuracy can be considered a reasonable result (> 80%). However, if we adopt a merger and non-merger split based on "confident" predictions, or merger probability > 0.8, our mean accuracy increases to 91%.

We further investigated the role of the mass ratio in the completeness and precision curves. Fig. 3.5b shows the mean precision and completeness as a function of the same merger probabilities; however, this time separating the major, minor, and mini mergers. We find that the mean precision at a binary split is 59% for major mergers, 63% for minor mergers, and 62% for mini mergers. These metrics increase to 80% for major mergers, 82% for minor mergers, and 79% for mini mergers for "confident" merger probabilities. The precision values are lower when the mergers are split by mass ratio as opposed to a two-class split due to the method of computing the metrics. There are an equal number of overall mergers and non-mergers; however, the respective numbers of major, minor, and mini mergers are lower than the number of non-mergers in each test data-set. As a result while the numerator in Equation 3.2 accounts only for mergers of the labeled mass ratio, the denominator includes all non-mergers and mergers regardless of mass ratio. As such, our findings with respect to the precisions shown in Fig. 3.5b are more relevant in a qualitative manner rather than quantitative. Noting the gradients for the metric curves, we find that the completeness curve for major mergers drops off most gradually, indicating that our model is most confident in classifying major mergers. We also note that the precision for mini mergers (mass ratio <1:20) is the highest between the three mass ratios at a binary split, and remains the highest at the "confident" probabilities, indicating that the model is able to predict mini mergers at an equivalent or greater precision compared to major and minor mergers. This

precision will allow for studies using large, precise samples of sub-major mergers, which have adverse effects on galaxy properties such as size growth (Bédorf & Portegies Zwart, 2013; Lang et al., 2014; Martin et al., 2018; Bottrell et al., 2023).

We provide some examples of true positive, true negative, false positive, and false negative galaxy classifications from the 10 runs in Figures 3.6 - 3.9, respectively, adopting a completely binary split. With this split, the model seems to be able to identify mergers of diverse morphologies, ranging from interacting pairs to merger remnants with visual signatures. We also find that the model is able to identify non-mergers of diverse morphologies, including projections, overlaps, and isolated galaxies, as shown in the varying appearances of true negative predictions in Fig. 3.7. The model seems to have mixed results on galaxy projections, as there are examples in both Fig. 3.8 (false positives) and Fig. 3.7 (true negatives). For incorrectly classified mergers (false negatives), many of the mergers with low probabilities (merger probability < 0.3) are those with large mass ratios ($\mu < 0.25$) whose times since or until the nearest merger event are close to the selection threshold of 0.5 Gyr (> 0.3 Gyr), meaning that potential merger indicators may not be visible, for example 84-569599_v0 (merger probability 0.05) in row 4, column 5 of Fig. 3.9 is a mini merger that is 0.31 Gyr until its merger event, and look visually very similar to non-mergers. Many of these galaxies would also likely not be classified as mergers by human-based visual classification methods. However, we also note there are also misclassifications with major mergers, for example 84-577873_v0 (merger probability 0.40) in row 3, column 4 of Fig. 3.9 is a major merger that is 0.49 Gyr until its merger event, which would likely be labeled as a merger by human-based methods. For misclassified non-mergers (false positives), galaxies with high merger probabilities (>0.8) are likely to be classified as merging by human-based methods, as they show merger-like disturbances, and may also have projections. As such, our machine-learning based approach may encounter similar issues as previous human-based visual approaches. Nevertheless, even with its misclassifications, we find that the model is able to correctly classify mergers and non-mergers of diverse morphologies, which should be useful for merger galaxy sciences.

3.4 Predictions from observations

In this section, we describe the work we do to make predictions from observational images using the fine-tuned model. For the work conducted in this section, we trained a new head model using

a 70% training and 30% validation split of the simulation data-set used in the previous section, and no further split of testing data, and attached it to the original Zoobot base model. Armed with our fine-tuned Zoobot model, we apply it to SDSS and GAMA spectroscopically confirmed galaxies in the HSC-SSP public data release 3 (Aihara et al., 2022).The training with this split lasted 37 epochs, with a duration of 23 minutes using GPU (NVIDIA Quadro P400).

The HSC-SSP is a multi-tiered, wide-field, multi-band imaging survey on the Subaru 8.2 m telescope on Maunakea in Hawaii. Detailed information about the survey, its instrumentation, and its techniques are available in Aihara et al. (2018) and relevant papers (Bosch et al., 2018; Miyazaki et al., 2018; Komiyama et al., 2018; Furusawa et al., 2018). We use data from HSC-SSP due to its wide field of observation and exceptional ground-based depth and resolution. In its widest component (Wide layer), HSC-SSP covers about 600 deg^2 of the sky in five broad band filters (*grizy*), with observations from 330 nights coadded. The depth of the HSC survey is $r \approx 26$ mags (5σ, point source) for the Wide layer. The coverage and depth of HSC-SSP will give us access to high quality imaging data, both in terms of depth and resolution, of several million galaxies. We plan to make merger probabilities for all of HSC-SSP Wide in future works, a catalog of which will be made publicly available for the benefit of the galaxy astronomy community. This merger probability catalog is expected to be one of the largest catalogs of its kind.

For the work conducted in Section 3.6, we use a subsample of galaxies from the HSC-SSP Wide internal data release S21A catalog to conduct predictions on with our trained model. To select a galaxy sample, we cross-match HSC-SSP S21A galaxies to SDSS Data Release 17 (Abdurro'uf et al., 2022) and Galaxy And Mass Assembly Data Release 4 (GAMA DR4, Driver et al., 2022) galaxies within 1 sky arcsec. We are left with 145,544 matches in SDSS and 156,604 matches in GAMA, for a total of 302,148 galaxies. All galaxies matched have spec-z measurements from their respective catalogs. We only use spectroscopic redshifts, due to photometric redshift errors. The galaxies have a magnitude limit of r <17.7 mag for SDSS galaxies and r <19.8 for GAMA galaxies. The galaxies lie within a redshift range of $z = 0.01 - 0.35$ and have $M_* = 3 \times 10^9 - 3 \times 10^{11} M_\odot$. M_* values are obtained following Chen et al. (2012) for the SDSS galaxies and its own catalog for the GAMA galaxies. The SDSS

galaxy stellar masses, using a principal component analysis method on SDSS spectra. First, a model spectra is created based on Bruzual & Charlot (2003) stellar population synthesis model. Next, principal components are identified from the model library. Finally, the SDSS spectra are fitted to the model and physical properties estimated. The masses obtained are consistent with the GALEX-SDSS-WISE Catalog (Salim et al., 2016, 2018). The GAMA galaxy stellar masses are obtained using the SED fitting code MAGPHYS (Driver et al., 2018). MAGPHYS also uses a library based on Bruzual & Charlot (2003). Sets of optical and infrared spectra are regressed toward flux measurements and errors to find a best-fit SED and physical parameters, including stellar mass.

Each galaxy in the catalog also has several environmental parameters related to its local mass density, studied in Yesuf (2022). The stellar mass overdensities within radii of 0.5, 1, and 8 h^{-1}Mpc, as well as within the radii determined by the projected distance to the fifth nearest neighbor are calculated. Only galaxies within $|\Delta v| < 1000\mathrm{kms}^{-1}$ relative to the primary source are considered in this calculation. This cutoff prevents unrelated foreground or background galaxies from being included. The densities are normalized by the median densities of all galaxies within a given mass range and redshift bin, making them overdensities relative to the median in the redshift bin. Details on how the densities are calculated are written in Yesuf (2022) and the papers referenced within.

We make predictions on *gri* images for each HSC galaxy, with the images having the same dimensions as the synthetic HSC images of the TNG50 galaxies - cutouts encompassing $10\times R_{\rm eff}$, re-sized to 300×300 pixels. For each input image, our model will output a merger probability between 0 and 1, with 0 indicating non-merger and 1 indicating a merger, again independent of merger mass ratio or merger stage.

We note that some HSC galaxy identifications are susceptible to "bright galaxy shredding", discussed in Aihara et al. (2018). Bright ($i < 19$) galaxies, especially of late-type, are deblended into multiple objects, with the debelending seen even after cross-matching with a spectroscopic catalog. An inspection of the non-cropped image of objects affected by shredding reveals that that it is part of the spiral arm of a larger galaxy. As much as 15% of bright galaxies in HSC-SSP suffer from shredding, so it is expected that there are galaxies suffering from similar effects in our

classified samples. However, these issues are expected to be resolved when making predictions on future HSC-SSP public data releases. For this work, as we are using the SDSS/GAMA coordinates and their petrosian radii to make our cutouts, we should not be as affected by shredding compared to HSC data.

3.5 Results

3.5.1 Prediction results

HSC ID	ra	dec	z	$\log M_*$	$R_{\rm eff}$	$p_{\rm m}$
40976904286657178	135.21693	-0.21783	0.13429	9.943	0.9441	0.7748
40976904286655515	135.22422	-0.25286	0.26773	10.694	1.3761	0.7483
40976899991693591	135.15696	-0.35011	0.25953	10.821	0.9325	0.3731
40976899991692475	135.17823	-0.37379	0.19826	10.504	0.6889	0.3613
40976899991691083	135.20912	-0.40034	0.26186	10.743	1.0057	0.5251
40976899991693989	135.26473	-0.34614	0.24198	10.705	1.6524	0.0672
40976899991696732	135.18206	-0.29366	0.29414	10.836	1.1030	0.3663
40976899991691777	135.18733	-0.38641	0.19540	10.144	1.1781	0.1652
40976899991691430	135.21054	-0.39348	0.28980	10.759	1.0949	0.5085
40976899991694631	135.15008	-0.33319	0.05939	8.866	2.6338	0.7436
40976899991693794	135.15210	-0.34947	0.26207	10.340	1.4300	0.4818
40976899991696948	135.17852	-0.29013	0.27716	9.994	1.0920	0.5929
40976899991691991	135.24448	-0.38132	0.24180	10.305	2.5256	0.7694
40976899991695733	135.25520	-0.30936	0.18415	10.020	1.2535	0.46
40976762552736285	135.30275	-0.40450	0.05354	9.133	4.5769	0.3163
40976762552740451	135.37273	-0.31733	0.19510	10.929	2.2518	0.8324
40976762552740452	135.37037	-0.31746	0.25747	10.715	0.5802	0.5953
40976766847703396	135.37322	-0.23766	0.16621	10.811	1.5467	0.2116
40976766847703397	135.37279	-0.24190	0.16573	10.506	1.6312	0.9555

HSC ID	ra	dec	z	$\log M_*$	$R_{\rm eff}$	$p_{\rm m}$
40976766847703399	135.37344	-0.24142	0.16594	10.615	1.9264	0.9908
40976762552738449	135.28666	-0.33515	0.26827	11.320	2.2055	0.3459
40976766847702646	135.30618	-0.25849	0.29045	10.707	1.6513	0.5657
40976762552736933	135.30769	-0.39226	0.22278	10.529	1.1481	0.2732
40976762552740515	135.30821	-0.31517	0.24312	9.896	0.8089	0.4699
40976762552738409	135.33213	-0.36124	0.25705	10.751	1.0680	0.9826
40976762552736294	135.33828	-0.40318	0.26815	11.329	2.2871	0.5786
40976762552742253	135.36727	-0.28019	0.25275	10.934	2.1941	0.4373
40976766847702611	135.39386	-0.25755	0.25260	10.640	0.8993	0.1903
40976762552741814	135.39651	-0.28928	0.19703	10.545	0.3985	0.3219
40976766847701731	135.39655	-0.27429	0.22804	10.465	1.9479	0.6111
40976762552742193	135.28365	-0.28082	0.17447	9.971	2.6430	0.4646
40976762552739290	135.31943	-0.34077	0.26830	9.983	0.7235	0.5471
40976762552736240	135.37890	-0.40896	0.05313	9.096	6.0766	0.7281
40976762552740286	135.39585	-0.31716	0.29559	10.575	1.4935	0.4666
40976766847703322	135.31126	-0.24207	0.25290	10.410	2.1315	0.3007
40976762552741545	135.44065	-0.29678	0.26180	10.837	0.6233	0.5643
40976625113785130	135.48564	-0.38518	0.05395	9.457	2.6896	0.8668
40976629408751687	135.51163	-0.21064	0.22986	10.424	0.7680	0.7198
40976629408751688	135.51255	-0.21012	0.22967	10.248	0.4214	0.4831
40976629408750797	135.54671	-0.22893	0.19659	10.894	1.4055	0.1699
40976629408750382	135.54730	-0.23722	0.19644	11.146	4.4098	0.053
40982126966885668	135.55857	-0.25699	0.22170	10.944	1.5032	0.3568
40976766847701828	135.43250	-0.27151	0.25743	10.809	2.0530	0.7592
40976762552737937	135.43958	-0.37213	0.26135	10.987	1.4061	0.3925
40976762552739879	135.44235	-0.32958	0.27184	10.685	0.5545	0.3653
40976762552738863	135.44374	-0.34980	0.15155	10.078	0.5537	0.419
40976762552740471	135.44444	-0.31185	0.25232	10.659	1.6281	0.4699

HSC ID	ra	dec	z	log M_*	$R_{\rm eff}$	$p_{\rm m}$
40976766847702501	135.46048	-0.25834	0.24422	11.006	1.8693	0.5078
40976625113785151	135.50582	-0.38393	0.25171	10.411	1.2218	0.4472
40976629408750193	135.51633	-0.24125	0.22140	10.408	0.9475	0.4726
40976629408751398	135.51787	-0.21498	0.19656	10.337	0.5552	0.4349
40976625113784193	135.53078	-0.40043	0.26279	10.723	0.8274	0.6342
40976629408749210	135.54732	-0.26064	0.24385	10.739	0.8131	0.5196
40976629408751447	135.48590	-0.21248	0.16618	10.596	3.1214	0.1834
40976625113785220	135.52434	-0.38658	0.26165	10.910	1.7522	0.4662
40976625113786795	135.46829	-0.34921	0.05241	8.494	3.0910	0.9335
40976629408748869	135.50342	-0.26874	0.19726	10.279	0.9728	0.9893
40976762552736784	135.41781	-0.39603	0.26117	10.492	1.4752	0.4339
40976762552741365	135.42152	-0.29802	0.26824	10.426	1.6294	0.8903
40976629408749351	135.53904	-0.26022	0.22074	10.385	1.6815	0.0493
40981989527934944	135.67194	-0.21819	0.05997	9.083	2.7364	0.9566
40982126966885854	135.59505	-0.25632	0.19317	11.438	2.0676	0.165
40982122671928018	135.59930	-0.27767	0.19637	11.068	1.8879	0.8561
40982122671927271	135.60395	-0.29491	0.19825	11.270	2.1408	0.4805
40981989527934844	135.65505	-0.22233	0.10273	9.903	2.0060	0.6676
40981985232969061	135.69097	-0.32358	0.17740	10.485	1.1327	0.5548
40981985232967672	135.70058	-0.36116	0.08788	9.074	0.9949	0.278
40981985232968570	135.71434	-0.33538	0.17808	10.853	1.1405	0.4262
40982122671927716	135.57639	-0.28623	0.19606	10.474	1.4490	0.8206
40981985232968612	135.65165	-0.33686	0.19772	10.611	2.1617	0.41
40981989527933177	135.67603	-0.25484	0.25129	10.530	0.8201	0.425
40982122671927680	135.61961	-0.28783	0.19702	10.328	2.5378	0.5472
40982122671926097	135.61658	-0.33138	0.26120	10.592	1.4494	0.5626
40982122671926870	135.62705	-0.30860	0.19963	9.708	1.0420	0.7633
40981985232969647	135.69227	-0.31079	0.13356	9.451	1.1420	0.4742

HSC ID	ra	dec	z	$\log M_*$	$R_{\rm eff}$	$p_{\rm m}$
40981985232968813	135.70288	-0.32925	0.09314	9.776	2.7844	0.1154
40981985232970463	135.71027	-0.29308	0.26066	10.791	2.7758	0.5786
40981985232969151	135.71490	-0.32117	0.17706	9.706	1.7172	0.3195
40982126966884814	135.57342	-0.27512	0.19628	10.336	2.0398	0.3492
40982126966885055	135.59256	-0.27102	0.19540	10.134	1.6839	0.4856
40981985232951981	135.68154	-0.27986	0.26193	10.297	1.0504	0.3029
40981985232967477	135.73078	-0.36489	0.22454	10.771	0.4270	0.4251
40981985232970109	135.74972	-0.30242	0.26085	11.215	1.3032	0.4513
40981989527934384	135.79851	-0.22982	0.17606	9.926	1.0072	0.1477
40981989527934170	135.80072	-0.23603	0.17599	9.716	1.2900	0.4016
40981985232969326	135.81074	-0.31340	0.20760	10.413	1.3809	0.6139
40981852088978835	135.83511	-0.23642	0.17413	9.905	0.5537	0.208
40981847794016226	135.83749	-0.34008	0.14554	10.713	2.1392	0.2231
40981985232950349	135.73741	-0.32388	0.22417	10.421	0.8955	0.3653
40981989527934397	135.76746	-0.23007	0.20488	10.620	0.9891	0.344
40981985232965887	135.82071	-0.40762	0.28682	10.947	3.1291	0.4036
40981989527933501	135.82308	-0.24959	0.22550	11.049	2.5445	0.8067
40981847794016125	135.84895	-0.33965	0.29843	10.822	1.2614	0.5855
40981985232967693	135.73292	-0.36045	0.22426	10.444	1.0980	0.319
40981985232968436	135.74714	-0.34237	0.22599	9.543	0.7074	0.3162
40981989527934007	135.77253	-0.24174	0.05335	8.667	2.8426	0.9708
40981847794015190	135.83250	-0.36627	0.19668	10.505	1.8821	0.5068
40981985232969760	135.75180	-0.30706	0.26428	10.626	1.7436	0.0223
40981985232969103	135.75098	-0.32218	0.26209	10.410	1.3062	0.1162
40981852088978960	135.87131	-0.23098	0.17344	10.756	1.5608	0.0463
40981852088978562	135.87701	-0.24709	0.07045	9.897	2.4559	0.2487
40981847794013081	135.88012	-0.41601	0.20618	11.197	2.4952	0.1114
40981852088978765	135.88627	-0.24478	0.11626	10.053	1.5032	0.3452

HSC ID	ra	dec	z	$\log M_*$	$R_{\rm eff}$	$p_{\rm m}$
40981852088978766	135.88613	-0.24206	0.24474	10.638	0.6579	0.4592
40981847794018431	135.88837	-0.28318	0.22097	10.606	1.3980	0.8443
40981852088978464	135.88945	-0.24604	0.11599	9.128	1.5107	0.9017
40981847794017340	135.90251	-0.30801	0.20497	10.255	0.6966	0.5503
40981852088979170	135.90373	-0.22666	0.02753	8.075	1.3228	0.3781
40981847794016363	136.00019	-0.33316	0.06118	9.713	3.7256	0.8857
40981847794013129	135.89255	-0.41416	0.19866	11.010	5.2362	0.3495
40981847794015308	135.90247	-0.36129	0.24516	10.429	0.7885	0.3501
40981852088978051	135.90370	-0.26032	0.28277	10.789	0.7917	0.3431
40981852088979653	135.91716	-0.21178	0.29830	11.053	1.3312	0.3079
40981852088977394	135.95344	-0.27492	0.28278	10.715	0.7636	0.3306
40981852088978907	135.97436	-0.23236	0.10133	10.191	2.5446	0.4643
40981847794018119	135.99632	-0.29402	0.29913	10.604	0.6031	0.4682
40981847794016776	135.93059	-0.32284	0.25760	10.124	2.6254	0.4407
40981847794014333	136.00503	-0.39139	0.20464	10.368	2.1277	0.6403
40981710355060082	136.03456	-0.39216	0.13068	10.223	3.0902	0.096
40981714650028094	136.06114	-0.21669	0.19492	10.021	0.3262	0.378
40981710355062162	136.06953	-0.36011	0.18600	10.705	0.9990	0.6745
40981710355064096	136.10309	-0.31839	0.17288	10.775	2.6697	0.1513
40981714650028161	136.11893	-0.21877	0.19512	10.777	1.5408	0.1589
40981710355064378	136.14023	-0.31481	0.02752	8.940	2.7519	0.6419
40981710355064289	136.02206	-0.31579	0.29827	10.790	1.1696	0.2407
40981710355065024	136.04558	-0.29793	0.28277	10.717	0.6261	0.4212
40981710355064709	136.05189	-0.30551	0.29893	10.925	0.5419	0.5634
40981710355060130	136.09631	-0.40863	0.29579	11.032	1.0084	0.36
40981714650027586	136.10349	-0.22912	0.25270	10.604	0.5467	0.4787
40981710355060976	136.07947	-0.38972	0.20789	10.442	1.4764	0.0372
40981710355065904	136.20063	-0.27818	0.19727	10.317	1.7864	0.1112

HSC ID	ra	dec	z	$\log M_*$	$R_{\rm eff}$	$p_{\rm m}$
40981710355059800	136.18560	-0.41130	0.17309	10.023	1.5663	0.9854
40981710355059801	136.18447	-0.41159	0.17240	9.681	1.7232	0.9935
40981577211080834	136.24242	-0.21019	0.12337	9.500	1.4331	0.2654
40981572916111911	136.25013	-0.31091	0.17285	10.015	1.5878	0.5259
40981714650026645	136.20023	-0.25288	0.23678	10.547	0.6091	0.6009
40981572916112889	136.29457	-0.28684	0.29735	11.012	1.0322	0.2886
40981572916111127	136.30446	-0.33314	0.29972	11.209	1.4737	0.1421
40981572916110161	136.30652	-0.35008	0.29746	10.982	1.3044	0.2321
40981577211078717	136.25842	-0.24671	0.12860	10.024	1.8408	0.4079
40981572916110056	136.30153	-0.35638	0.29845	10.739	1.3044	0.6164
40981572916110403	136.34247	-0.34742	0.10060	10.100	0.9891	0.1316
40981572916110041	136.34440	-0.35868	0.19759	10.547	1.9729	0.2738
40981577211077430	136.36572	-0.26922	0.21000	9.681	0.5527	0.3744
40981435477158027	136.39208	-0.35561	0.19717	10.994	1.3322	0.2616
40981435477160441	136.40599	-0.29473	0.18525	10.561	1.3473	0.4004
40981435477159465	136.40932	-0.31837	0.18524	11.197	2.1935	0.5015
40981435477158589	136.41360	-0.34316	0.18565	10.355	1.2898	0.6629
40981439772120527	136.42277	-0.26524	0.20525	10.046	0.9058	0.3614
40981435477157667	136.43139	-0.36128	0.09659	10.485	3.2623	0.2952
40981439772120766	136.43437	-0.25707	0.17261	10.756	2.2285	0.053
40981435477156478	136.44881	-0.39046	0.25250	10.643	0.5673	0.4057
40981435477161073	136.45242	-0.28332	0.09753	10.198	2.8080	0.5396
40981572916110529	136.33691	-0.34519	0.19752	10.412	0.5349	0.4029
40981572916110949	136.34863	-0.33599	0.19766	10.783	1.4658	0.6506
40981577211077859	136.38494	-0.26104	0.29186	10.934	1.2153	0.4431
40981435477157494	136.40392	-0.36386	0.26047	10.190	1.0188	0.477
40981435477157213	136.41406	-0.37183	0.25925	10.798	1.0672	0.4377
40981439772120338	136.43036	-0.26927	0.21010	10.192	0.7013	0.5752

HSC ID	ra	dec	z	$\log M_*$	$R_{\rm eff}$	$p_{\rm m}$
40981435477161234	136.43199	-0.28058	0.17237	10.297	0.4906	0.6069
40981435477155169	136.44326	-0.41231	0.21927	10.620	1.1089	0.1955
40981572916107498	136.36066	-0.40744	0.17254	10.476	1.9771	0.0308
40981435477156961	136.44411	-0.37745	0.25249	10.421	1.1418	0.5026
40981435477156527	136.44818	-0.38558	0.25237	10.377	1.1168	0.3056
40981572916110266	136.37397	-0.35157	0.20526	10.050	0.9338	0.3272
40981577211080780	136.37971	-0.21177	0.10080	9.430	0.8620	0.1981
40981435477157831	136.39500	-0.35782	0.21044	9.869	1.7190	0.6759
40981439772120186	136.41590	-0.27182	0.17286	9.645	1.3542	0.6551
40981572916112108	136.38104	-0.30549	0.12826	9.364	1.9114	0.149
40981439772121514	136.42582	-0.24081	0.29212	10.514	1.5747	0.434
40981435477157654	136.44495	-0.36326	0.19984	10.282	2.6409	0.105
40981302333169252	136.60418	-0.23777	0.09503	10.856	2.4992	0.4861
40981439772120716	136.52107	-0.26037	0.03988	9.903	4.3280	0.4375
40981435477155212	136.57536	-0.41517	0.17204	10.925	2.7321	0.1815
40981302333169905	136.59523	-0.22197	0.09473	9.720	2.4096	0.9601
40981302333167967	136.61303	-0.26201	0.09577	9.496	0.6662	0.2686
40981435477155625	136.49334	-0.40326	0.20831	10.751	5.0494	0.9046
40981435477154826	136.56583	-0.41733	0.28316	10.769	0.3331	0.3648
40981298038201512	136.60125	-0.37568	0.28458	10.625	0.6051	0.3997
40981302333169537	136.61009	-0.23055	0.21551	10.370	0.8046	0.5816
40981298038202582	136.61398	-0.35390	0.27952	10.871	1.0088	0.5183
40981298038201295	136.59981	-0.38262	0.28442	10.684	1.1173	0.5346
40981435477157755	136.48670	-0.36251	0.23226	10.491	1.7665	0.4564
40981435477157374	136.50500	-0.36764	0.21975	10.457	3.0445	0.0238
40981298038205006	136.68191	-0.29762	0.28412	10.368	1.4587	0.8621
40981302333170072	136.74931	-0.21714	0.19995	10.407	1.5826	0.5231
40981298038203480	136.61652	-0.33181	0.19715	9.878	1.5063	0.2077

HSC ID	ra	dec	z	$\log M_*$	$R_{\rm eff}$	$p_{\rm m}$
40981298038200699	136.66129	-0.39341	0.21970	11.438	6.4774	0.2268
40981298038200700	136.66179	-0.39581	0.22079	9.393	0.5343	0.5946
40981298038200701	136.66424	-0.39522	0.22107	10.362	1.1333	0.4185
40981298038199798	136.66611	-0.41376	0.06984	10.036	2.0992	0.1537
40981298038200518	136.67796	-0.39644	0.20899	10.206	0.4990	0.4569
40981302333169297	136.69562	-0.23238	0.28470	10.837	1.2988	0.4465
40981298038203192	136.62169	-0.33924	0.28659	11.007	0.8706	0.5678
40981298038202399	136.62930	-0.35898	0.28506	11.240	4.3573	0.2308
40981298038202400	136.63034	-0.36014	0.28316	11.457	7.2489	0.3515
40981298038200031	136.63695	-0.40901	0.28074	10.587	0.3735	0.3607
40981298038202631	136.63886	-0.35202	0.28177	10.856	0.9550	0.6153
40981298038201255	136.64377	-0.38454	0.22187	10.508	0.5906	0.4235
40981298038202553	136.64567	-0.35563	0.28435	10.740	2.1072	0.7774
40981298038200904	136.67076	-0.39060	0.21904	10.606	0.3661	0.4149
40981298038200278	136.67357	-0.40168	0.21859	10.561	0.9076	0.3018
40981298038201130	136.67919	-0.38760	0.22204	10.795	2.1214	0.4523
40981302333169296	136.68966	-0.23227	0.28038	10.670	0.6001	0.4808
40981298038201384	136.71117	-0.37944	0.22045	10.838	1.3014	0.0223
40981298038201418	136.66053	-0.38115	0.21923	10.563	1.6723	0.4221
40981298038203867	136.69047	-0.32547	0.29386	10.504	1.0442	0.5039
40981302333169298	136.69254	-0.23204	0.28088	10.937	2.6833	0.6184
40981298038204037	136.68846	-0.32019	0.20919	9.981	1.2159	0.7034
40981298038199749	136.68391	-0.41443	0.21857	10.533	1.8105	0.4787
40981160599244842	136.88259	-0.41026	0.07056	9.198	1.5311	0.9784
40981164894212984	136.77490	-0.22480	0.12699	9.773	1.2191	0.3982
40981160599248951	136.77866	-0.31758	0.22081	11.029	1.1940	0.1718
40981160599246901	136.78518	-0.37154	0.10098	9.989	1.1034	0.2023
40981160599249519	136.81239	-0.30372	0.20990	10.908	2.0451	0.4765

HSC ID	ra	dec	z	$\log M_*$	$R_{\rm eff}$	$p_{\rm m}$
40981160599249520	136.81473	-0.30467	0.20944	10.352	0.8492	0.8537
40981160599246274	136.81804	-0.38431	0.28130	10.929	0.9232	0.3802
40981164894211482	136.85074	-0.25989	0.07757	9.855	4.3522	0.7451
40981160599249853	136.79349	-0.29973	0.20928	10.097	0.5680	0.272
40981160599247644	136.84761	-0.35294	0.18979	9.638	0.6974	0.3366
40981164894212309	136.87056	-0.23742	0.28108	10.951	1.8864	0.3028
40981160599245493	136.76710	-0.39688	0.21942	10.142	1.7783	0.74
40981160599246215	136.77879	-0.38241	0.29745	10.572	1.9615	0.9366
40981160599247169	136.83194	-0.36316	0.26165	10.379	1.7707	0.4471
40981160599244954	136.85659	-0.41001	0.29830	10.796	4.2189	0.8424
40981160599250431	136.93203	-0.28326	0.18161	10.257	0.9700	0.3998
40981023160293227	136.96731	-0.37416	0.28286	11.330	2.0150	0.811
40981027455262404	136.99584	-0.22313	0.18525	10.441	0.7495	0.3685
40981023160294322	136.99797	-0.35192	0.22182	11.023	1.4881	0.2362
40981027455260821	137.01211	-0.25731	0.18428	10.725	2.6531	0.3106
40981027455260331	137.01942	-0.26833	0.20443	11.070	2.3793	0.141
40981160599248105	136.92592	-0.34065	0.22160	10.756	2.3475	0.605
40981023160295909	136.96652	-0.32165	0.29882	10.224	0.7685	0.4749
40981023160295205	136.97517	-0.33557	0.28120	10.926	0.8219	0.474
40981023160293277	136.97873	-0.37021	0.21042	10.471	1.8593	0.8752
40981023160293276	136.97895	-0.37448	0.19950	10.478	1.1121	0.4148
40981023160293565	136.98910	-0.36594	0.19850	10.395	1.8949	0.3472
40981023160297847	136.99323	-0.28213	0.20301	10.480	0.6076	0.3969
40981023160295259	136.99933	-0.33425	0.27968	10.629	1.2224	0.486
40981027455260231	137.03183	-0.27105	0.20408	10.249	0.6581	0.4123
40986520718430481	137.04736	-0.39633	0.28459	10.996	1.2874	0.8983
40986520718434277	137.05533	-0.31679	0.20504	10.733	2.6350	0.689
40981160599245729	136.92352	-0.39404	0.23939	10.034	1.1595	0.4964

HSC ID	ra	dec	z	$\log M_*$	$R_{\rm eff}$	$p_{\rm m}$
40981027455262025	136.97573	-0.23145	0.05562	8.846	3.7770	0.4742
40981023160298050	137.01395	-0.27732	0.09413	9.053	1.5281	0.4672
40986525013400199	137.04384	-0.23300	0.22004	10.061	1.7538	0.4784
40986520718429917	137.04614	-0.40856	0.21292	9.833	1.4141	0.32
40986520718432226	137.05151	-0.36369	0.20487	9.696	1.4211	0.5315
40981023160295602	136.96663	-0.32664	0.28120	10.707	2.4363	0.0278
40981027455260929	136.97649	-0.25632	0.18423	10.318	2.1361	0.4698
40986383279482086	137.20752	-0.31274	0.21853	11.208	3.1959	0.7179
40986525013399362	137.06518	-0.25760	0.22018	10.637	1.2207	0.2852
40986520718434003	137.07836	-0.32479	0.23906	10.539	1.1378	0.4785
40986383279478755	137.13275	-0.38235	0.22634	10.266	0.7390	0.3712
40986383279479124	137.13290	-0.37505	0.28262	10.690	1.2086	0.4377
40986383279479384	137.17325	-0.36907	0.27785	11.030	1.9048	0.4766
40986383279478870	137.18173	-0.38014	0.28262	10.558	0.5813	0.43
40986383279481468	137.19737	-0.32558	0.18660	10.042	0.7001	0.17
40986387574443743	137.20600	-0.26708	0.23914	10.172	0.4921	0.4161
40986387574424727	137.15369	-0.25314	0.29525	10.579	1.3507	0.3266
40986387574443360	137.18185	-0.27462	0.16418	10.018	3.0667	0.3649
40986387574446143	137.26860	-0.21165	0.13450	10.066	1.6487	0.8842
40986383279477229	137.30523	-0.41789	0.13433	9.902	1.9742	0.9692
40986387574446179	137.24537	-0.21335	0.18448	10.105	1.7100	0.5916
40986387574446180	137.24485	-0.21352	0.29506	10.931	1.0320	0.64
40986383279481240	137.27003	-0.32889	0.21934	10.996	2.0092	0.4027
40986383279477845	137.28174	-0.40480	0.28680	10.571	0.0032	0.7679
40986383279479746	137.29472	-0.35351	0.21891	10.897	0.9899	0.3991
40986383279479747	137.30256	-0.35492	0.21960	11.127	3.8967	0.307
40986383279479748	137.29868	-0.35232	0.21930	10.815	1.3548	0.4018
40986245840527031	137.34893	-0.30703	0.16068	10.959	2.6630	0.0978

HSC ID	ra	dec	z	$\log M_*$	$R_{\rm eff}$	$p_{\rm m}$
40986387574445791	137.24055	-0.22006	0.29552	10.805	1.0128	0.2122
40986383279481611	137.28082	-0.32111	0.20429	10.400	0.5376	0.402
40986245840526280	137.31370	-0.32515	0.20431	10.678	1.1210	0.3429
40986250135490042	137.32700	-0.26774	0.29416	10.944	0.8846	0.6664
40986245840524318	137.35596	-0.36603	0.29810	10.899	1.5179	0.6518
40986383279479465	137.22892	-0.36702	0.28119	10.638	1.2589	0.5013
40986245840524478	137.36183	-0.36237	0.21926	10.499	1.3590	0.2969
40986383279480715	137.24884	-0.34178	0.29961	10.215	1.8967	0.5054
40986383279477531	137.26409	-0.41042	0.16955	10.043	1.8897	0.3351
40986245840525149	137.34664	-0.34949	0.21879	9.790	1.5721	0.619
40986245840524037	137.35083	-0.37591	0.15178	10.220	4.2463	0.4224
40986250135492280	137.36380	-0.21677	0.21926	10.776	1.0235	0.3701
40986245840528105	137.38553	-0.28686	0.15165	11.056	4.4491	0.4552
40986250135492448	137.45255	-0.21316	0.21932	10.819	1.0869	0.4535
40986250135491682	137.46178	-0.22848	0.24757	11.009	0.8025	0.5396
40986108401572511	137.49997	-0.38137	0.22037	11.083	1.8831	0.8841
40986108401572513	137.50266	-0.38334	0.21947	10.036	0.6594	0.154
40986245840528359	137.37963	-0.28549	0.16083	10.239	2.8011	0.6539
40986245840506460	137.43486	-0.37316	0.27487	10.471	1.1209	0.3842
40986250135491255	137.47616	-0.23873	0.21242	10.104	0.7166	0.4045
40986250135492632	137.48344	-0.21036	0.16909	10.397	0.9715	0.5908
40986245840527168	137.36794	-0.30730	0.24736	10.484	1.2970	0.722
40986250135492400	137.44808	-0.21502	0.23745	10.493	1.2173	0.0955
40986112696539287	137.50740	-0.25693	0.20466	10.303	1.5072	0.4905
40986245840524612	137.38984	-0.35932	0.21912	10.109	1.4196	0.4682
40986250135491857	137.46601	-0.22514	0.16089	9.678	2.8810	0.1739
40986245840525709	137.46932	-0.33907	0.20500	9.839	1.4077	0.9114
40986245840523814	137.40576	-0.37590	0.16851	9.799	1.5329	0.4209

HSC ID	ra	dec	z	$\log M_*$	$R_{\rm eff}$	$p_{\rm m}$
40986108401575716	137.53116	-0.31982	0.16814	10.975	1.4564	0.8316
40986112696542291	137.58893	-0.21679	0.09339	9.908	3.6819	0.3232
40986112696542123	137.60546	-0.21788	0.01893	8.037	1.6248	0.5158
40986108401577859	137.62798	-0.28849	0.16843	10.311	1.2041	0.5685
40986108401573878	137.58412	-0.35622	0.26061	10.539	0.5791	0.6176
40986112696541092	137.59642	-0.23240	0.19350	10.615	1.0814	0.1403
40986108401572965	137.59917	-0.37583	0.26195	10.725	1.5849	0.8776
40986108401576894	137.52502	-0.30407	0.24480	10.188	1.5081	0.4676
40986112696542054	137.55427	-0.21730	0.16855	9.769	2.5578	0.256
40986112696538378	137.67380	-0.26795	0.08002	9.492	0.7613	0.2142
40985970962618907	137.81188	-0.34645	0.17050	9.362	1.4954	0.1842
40985970962619757	137.74911	-0.33093	0.13566	10.271	1.9666	0.7272
40985970962615920	137.79088	-0.41302	0.05459	8.375	0.5741	0.302
40985975257586553	137.79990	-0.23483	0.05435	9.708	4.4920	0.3648
40985970962617286	137.79831	-0.38107	0.19360	10.239	0.8768	0.2041
40985970962621017	137.80557	-0.30349	0.24468	10.749	1.9999	0.6215
40985970962622013	137.78507	-0.28430	0.24787	10.224	1.0871	0.329
40985975257584651	137.74201	-0.26371	0.29519	10.706	2.0715	0.0822
40985970962620837	137.77342	-0.30526	0.26387	9.970	2.5253	0.7285
40985970962616611	137.79874	-0.39458	0.24619	10.272	1.0308	0.6312
40985975257586074	137.85084	-0.23939	0.07027	9.584	2.4961	0.9088
40985833523665117	137.87489	-0.37457	0.24599	11.138	1.0438	0.3856
40985837818632240	137.88213	-0.20995	0.16762	10.439	0.8377	0.317
40985833523664006	137.92199	-0.39578	0.15051	10.269	1.4285	0.2413
40985837818632067	137.93822	-0.21446	0.14554	9.967	1.6736	0.6548
40985837818630772	137.94520	-0.24600	0.24618	11.387	2.7265	0.0953
40985970962617610	137.86153	-0.37393	0.29298	11.207	2.6617	0.5562
40985970962618254	137.86332	-0.35850	0.29229	11.199	0.5813	0.6

HSC ID	ra	dec	z	$\log M_*$	$R_{\rm eff}$	$p_{\rm m}$
40985970962618255	137.86291	-0.35904	0.28996	10.408	1.9901	0.4483
40985833523664778	137.87351	-0.37939	0.24526	11.154	3.2575	0.1082
40985833523665383	137.87692	-0.36773	0.29046	10.448	1.3737	0.5193
40985837818630270	137.89274	-0.25334	0.28084	10.948	1.8282	0.558
40985837818631081	137.93580	-0.23651	0.16692	9.893	1.3993	0.5861
40985837818631536	137.94569	-0.22889	0.24585	10.745	1.1813	0.3906
40985833523665594	137.88138	-0.35977	0.29108	10.601	1.0342	0.216
40985970962615626	137.83339	-0.41796	0.26422	10.379	1.4512	0.2172
40985833523664213	137.93011	-0.39298	0.15115	9.346	1.2161	0.0704
40985837818630193	137.96933	-0.25677	0.16834	10.750	2.7973	0.4778
40985837818630164	137.99765	-0.25786	0.24585	9.663	0.8465	0.4405
40985833523666762	138.01758	-0.33837	0.15634	10.288	0.5402	0.392
40985837818629672	138.03084	-0.27033	0.19948	10.834	1.6756	0.3107
40985700379677893	138.09474	-0.21073	0.16689	9.634	0.7422	0.2486
40985837818630554	137.98379	-0.24736	0.24439	10.878	2.5516	0.233
40985837818629376	138.03466	-0.27527	0.16853	10.221	0.3804	0.4931
40985833523645587	138.03713	-0.38818	0.15161	9.792	1.1580	0.2046
40985700379678100	138.07415	-0.21079	0.22494	10.986	3.2627	0.3581
40985700379677520	138.06895	-0.22046	0.22519	10.025	1.3196	0.353
40985833523666891	137.98322	-0.33538	0.28134	10.589	1.3697	0.5525
40985833523666091	137.98540	-0.35505	0.29600	10.607	2.0964	0.1335
40985700379676659	138.21060	-0.23988	0.16428	10.973	6.0364	0.5222
40985700379675621	138.22037	-0.26268	0.16567	10.692	1.3201	0.6291
40985700379675619	138.22490	-0.26139	0.16560	10.982	2.4150	0.9169
40985700379675620	138.22331	-0.26394	0.16588	10.666	1.1444	0.4625
40985700379677477	138.11179	-0.22368	0.20368	10.676	1.2772	0.1911
40985696084709646	138.13279	-0.39603	0.28422	10.882	2.1633	0.6348
40985700379677412	138.13742	-0.21773	0.27659	10.996	2.0763	0.5182

HSC ID	ra	dec	z	$\log M_*$	$R_{\rm eff}$	$p_{\rm m}$
40985696084713669	138.17392	-0.29410	0.16584	10.168	0.6009	0.4993
40985696084713670	138.17385	-0.29230	0.29026	10.391	1.6692	0.5024
40985696084711363	138.19089	-0.35596	0.15604	10.193	1.1211	0.4215
40985558645761717	138.24639	-0.30614	0.29825	10.523	0.9134	0.1882
40985696084711352	138.22650	-0.35602	0.28595	10.971	1.6854	0.6132
40985700379676857	138.16418	-0.23738	0.27675	10.170	0.8775	0.7135
40985558645762639	138.24728	-0.28980	0.29768	10.099	0.9204	0.4086
40985696084709253	138.22934	-0.40447	0.22538	10.324	2.3692	0.0462
40985558645762395	138.32698	-0.28948	0.16760	10.134	1.6751	0.2805
40985558645763226	138.28455	-0.27779	0.16454	10.329	0.5904	0.3395
40985562940724413	138.28582	-0.22765	0.10313	10.074	2.8581	0.3107
40985558645762582	138.34123	-0.28867	0.22109	10.934	1.3678	0.217
40985558645762447	138.28907	-0.29497	0.22066	10.363	1.3326	0.4357
40985558645759696	138.34311	-0.34856	0.29564	10.786	0.7788	0.3497
40985558645762583	138.34589	-0.29008	0.22133	10.762	0.9635	0.3211
40985558645763198	138.34708	-0.27901	0.27782	10.382	1.0815	0.3929
40985562940724390	138.27140	-0.22860	0.12260	9.342	2.1272	0.5959
40985558645761796	138.28677	-0.30461	0.13921	9.654	1.9758	0.2667
40985558645761952	138.34800	-0.30127	0.20162	9.855	1.3305	0.4393
40985562940724980	138.40785	-0.21955	0.17091	9.749	1.0752	0.4869
40985558645763121	138.30894	-0.28031	0.29827	10.435	1.4502	0.1739
40985558645758613	138.31601	-0.36670	0.27989	10.263	0.9109	0.1191
40985558645759300	138.42250	-0.35441	0.12259	10.081	2.6362	0.405
40985425501769840	138.43706	-0.24387	0.17020	10.316	0.5310	0.3844
40985425501769754	138.44113	-0.24362	0.17072	10.326	0.5614	0.3009
40990918764942757	138.53247	-0.36075	0.16639	9.698	0.8428	0.3714
40985558645762160	138.41195	-0.29805	0.29856	10.877	0.7042	0.3947
40985562940723630	138.41461	-0.24233	0.23498	10.684	0.7504	0.4748

HSC ID	ra	dec	z	$\log M_*$	$R_{\rm eff}$	$p_{\rm m}$
40985562940722587	138.42069	-0.25864	0.29843	11.245	1.7539	0.5966
40985425501769342	138.43865	-0.25383	0.24748	10.813	1.2841	0.4763
40985421206807358	138.51455	-0.35685	0.29190	10.707	0.4577	0.5417
40990918764942582	138.52655	-0.36386	0.16729	10.367	0.9501	0.1401
40985421206804340	138.44648	-0.40512	0.29088	10.734	0.9716	0.1523
40985558645759027	138.42910	-0.35724	0.16736	10.202	2.0275	0.4914
40985421206809919	138.45399	-0.30901	0.13713	9.092	1.9495	0.9927
40985421206805942	138.46706	-0.38111	0.16693	9.897	2.1516	0.103
40990918764946278	138.55025	-0.27858	0.08646	8.858	1.8239	0.3287
40990923059909072	138.51982	-0.26490	0.09981	9.329	2.6609	0.5553
40990918764940508	138.59223	-0.41057	0.07067	9.742	1.4411	0.4495
40990918764945982	138.60493	-0.28843	0.20855	10.923	1.3666	0.1428
40990781325993107	138.63993	-0.34991	0.13561	9.546	0.4188	0.4687
40990785620954891	138.69033	-0.22222	0.16564	11.082	2.8777	0.9837
40990918764940604	138.57163	-0.40562	0.22134	10.455	0.5471	0.4457
40990923059912516	138.57942	-0.21432	0.24775	10.923	0.8884	0.327
40990918764946404	138.59065	-0.28236	0.26094	10.379	0.9368	0.5134
40990918764946232	138.59508	-0.28526	0.16698	9.712	0.8290	0.3338
40990923059910498	138.59777	-0.24613	0.22187	10.705	1.1045	0.4518
40990781325996692	138.64553	-0.27742	0.22052	10.377	0.4302	0.4694
40990785620955349	138.69506	-0.21551	0.16462	10.045	0.3183	0.6053
40990781325996310	138.65198	-0.28479	0.22188	10.123	1.5892	0.8421
40990918764943882	138.58378	-0.33597	0.07007	9.304	2.8307	0.458
40990781325995338	138.60922	-0.30393	0.29661	10.339	1.5405	0.8997
40990781325991452	138.61412	-0.38250	0.22035	10.230	2.3017	0.874
40990785620954073	138.67890	-0.24045	0.26026	10.301	1.0910	0.3375
40990781325992667	138.69782	-0.35595	0.05578	9.110	4.2933	0.6081
40990643887039801	138.85525	-0.30188	0.02846	8.713	3.1721	0.603

HSC ID	ra	dec	z	$\log M_*$	$R_{\rm eff}$	$p_{\rm m}$
40990785620953336	138.71928	-0.26252	0.16596	10.350	0.5640	0.504
40990785620952834	138.72165	-0.26833	0.16544	10.392	1.5498	0.7344
40990785620952950	138.72546	-0.26552	0.16532	10.544	0.8113	0.4366
40990785620953274	138.72922	-0.26047	0.13586	9.942	1.4863	0.7943
40990785620955310	138.74820	-0.21469	0.16603	10.924	1.1709	0.1888
40990648182001174	138.81110	-0.21015	0.20555	10.472	1.9116	0.7688
40990643887036010	138.85654	-0.38869	0.16442	10.593	2.5520	0.665
40990781325996503	138.72304	-0.27770	0.27239	10.888	0.9446	0.5813
40990785620954303	138.75194	-0.23957	0.29761	10.717	1.0028	0.4001
40990785620954123	138.75736	-0.24104	0.29614	10.855	0.6126	0.5426
40990643887035681	138.79309	-0.39678	0.22160	10.149	1.7155	0.6287
40990648182000322	138.79752	-0.22814	0.20577	10.244	0.9567	0.7185
40990648182000321	138.80129	-0.22817	0.20567	10.243	0.6341	0.4048
40990781325989822	138.71394	-0.41661	0.29297	10.359	1.2559	0.3978
40990781325972643	138.78834	-0.37178	0.20154	9.893	1.8367	0.1706
40990648182000393	138.85962	-0.22859	0.29064	10.580	1.5222	0.6303
40990781325991196	138.78198	-0.39071	0.20147	9.958	1.6231	0.1023
40990643887037421	138.82261	-0.36185	0.16592	10.457	2.4827	0.0681
40990643887040165	138.88488	-0.29264	0.16501	10.203	1.3506	0.3439
40990643887035726	138.97183	-0.39907	0.25945	10.783	1.4328	0.5057
40990648182000673	138.87066	-0.22071	0.18735	10.090	1.0963	0.0824
40990648181998500	138.89829	-0.27094	0.14469	9.868	1.9263	0.9153
40990648181999364	138.91215	-0.25183	0.29579	10.905	1.0045	0.3639
40990643887040267	138.92969	-0.28943	0.20600	10.439	0.8459	0.5889
40990648182001205	138.93037	-0.21204	0.29345	10.873	0.9986	0.3783
40990643887039411	138.94155	-0.31037	0.24881	10.646	1.7217	0.3915
40990648182000306	138.94498	-0.22906	0.20593	10.528	0.6141	0.3783
40990648181998374	138.94974	-0.27467	0.24412	10.509	0.6994	0.5022

HSC ID	ra	dec	z	$\log M_*$	$R_{\rm eff}$	$p_{\rm m}$
40990506448085619	139.00179	-0.28945	0.08883	9.770	2.6104	0.2623
40990643887036211	138.88716	-0.38565	0.08801	9.383	2.7554	0.3711
40990643887038976	138.95013	-0.32259	0.16551	9.394	1.8738	0.7291
40990506448082043	138.98359	-0.37515	0.25109	10.216	1.5198	0.0819
40990510743047053	139.00104	-0.24453	0.24712	10.370	1.8028	0.2687
40990648181998901	138.88733	-0.26217	0.29122	10.607	1.1303	0.2621
40990643887038431	138.94320	-0.33472	0.20659	10.177	1.5407	0.2109
40990506448085674	139.01452	-0.29074	0.08767	9.523	0.8670	0.299
40990506448085137	139.05349	-0.30278	0.16343	10.649	1.1512	0.3243
40990506448080213	139.10339	-0.40890	0.25985	10.417	0.7390	0.5773
40990506448084239	139.13756	-0.32550	0.21189	10.816	0.9633	0.4552
40990506448086016	139.14964	-0.28586	0.20707	11.068	2.2383	0.0969
40990506448080134	139.03635	-0.40257	0.24560	9.973	0.6832	0.4073
40990506448080135	139.03698	-0.40263	0.24614	9.621	1.4301	0.9332
40990506448083209	139.03675	-0.34800	0.14449	9.997	2.4488	0.1359
40990506448081511	139.04478	-0.38575	0.25959	10.728	0.8497	0.7764
40990506448083100	139.05267	-0.35128	0.29108	11.408	2.2678	0.9349
40990506448080534	139.07692	-0.40276	0.16298	10.111	1.7325	0.1076
40990506448084647	139.14182	-0.31560	0.29060	10.941	0.7094	0.7578
40990506448081188	139.04376	-0.39311	0.24595	10.226	0.9787	0.7386
40990510743030195	139.05099	-0.22607	0.29185	10.458	0.8643	0.4071
40990506448082848	139.08449	-0.35821	0.29161	10.504	0.9567	0.1571
40990510743047801	139.14581	-0.22862	0.10200	9.848	5.2669	0.0395
40990369009132834	139.19152	-0.37695	0.22124	10.914	1.5197	0.192
40990369009131007	139.19535	-0.40939	0.14099	10.111	1.2733	0.3364
40990373304092136	139.29127	-0.26977	0.15446	10.068	1.9609	0.3983
40990369009137539	139.17927	-0.29952	0.16533	9.769	1.3976	0.1133
40990373304093410	139.22638	-0.24544	0.29108	10.026	0.6504	0.3394

HSC ID	ra	dec	z	log M_*	$R_{\rm eff}$	$p_{\rm m}$
40990373304094572	139.28208	-0.21886	0.26272	10.811	0.9331	0.3748
40990369009136659	139.28615	-0.31631	0.26540	10.661	0.6491	0.5517
40990373304094092	139.29778	-0.22929	0.26249	10.723	1.1700	0.3916
40990373304095073	139.30633	-0.20999	0.26085	10.841	1.3561	0.2143
40990369009135736	139.30671	-0.33078	0.21599	10.439	0.7618	0.3674
40990369009135737	139.30466	-0.32939	0.21572	9.939	1.5337	0.446
40990369009131367	139.29336	-0.40331	0.22172	10.092	0.8547	0.0961
40990373304093048	139.30066	-0.25229	0.08944	9.251	1.5614	0.3316
40990369009131379	139.25355	-0.40233	0.26263	10.213	1.4674	0.3824
40990369009137850	139.27469	-0.29214	0.10190	9.655	2.5374	0.8158
40990369009130700	139.33374	-0.41542	0.22178	10.654	0.6247	0.405
40990369009136489	139.33209	-0.31649	0.21801	9.659	0.9413	0.5053
40990369009136703	139.33773	-0.31281	0.21874	10.285	1.1761	0.5445
40990369009131772	139.34410	-0.39556	0.22130	10.245	1.1460	0.7141
40990373304093658	139.31888	-0.23899	0.27993	11.024	1.2015	0.3761
40990231570178556	139.36089	-0.35262	0.16314	10.014	1.5002	0.5218
40990231570175686	139.36646	-0.41391	0.22081	10.589	1.2105	0.8921
40990231570175068	139.37229	-0.41591	0.22215	10.551	1.1615	0.1663
40990231570178101	139.41380	-0.36221	0.25989	10.837	1.5720	0.1804
40990373304093265	139.33025	-0.24703	0.27891	10.774	1.8176	0.3683
40990373304094208	139.34649	-0.22654	0.21814	9.863	0.8472	0.5057
40990373304094327	139.35082	-0.22401	0.21814	10.478	1.7635	0.4011
40990231570177565	139.39259	-0.37362	0.10283	9.447	1.5407	0.0642
40990235865140917	139.47916	-0.21983	0.13969	10.596	0.8532	0.174
40990235865138863	139.52824	-0.26496	0.17283	9.962	1.3845	0.9406
40990094131219343	139.58276	-0.41353	0.18554	10.919	1.9475	0.0949
40990094131224254	139.59800	-0.30041	0.05558	9.835	1.9839	0.1407
40990094131224880	139.56482	-0.28859	0.13933	9.948	0.7723	0.4146

HSC ID	ra	dec	z	$\log M_*$	$R_{\rm eff}$	$p_{\rm m}$
40990098426187510	139.59395	-0.22524	0.05477	9.092	0.8778	0.2471
40990094131221412	139.59828	-0.36293	0.25908	10.600	0.7773	0.5332
40990231570181083	139.52814	-0.29629	0.22046	10.155	1.8454	0.9324
40990098426187177	139.58925	-0.23071	0.16911	10.199	1.7163	0.3952
40990098426187178	139.58969	-0.23290	0.17006	9.278	1.7845	0.692
40990094131219637	139.60217	-0.40730	0.25960	10.253	0.8864	0.119
40990231570177462	139.52654	-0.37511	0.03884	8.596	2.5871	0.6373
40990094131223435	139.65674	-0.31598	0.05523	9.945	2.7995	0.1527
40990098426186257	139.66279	-0.24737	0.05510	9.588	1.7456	0.0677
40990098426187910	139.68622	-0.21454	0.05380	9.399	1.6844	0.0373
40990098426187544	139.69277	-0.22136	0.05473	9.138	1.2275	0.3825
40989960987231702	139.72785	-0.21283	0.15933	10.454	0.8056	0.5235
40989960987231515	139.74623	-0.21644	0.05581	11.090	6.8211	0.1679
40989956692269408	139.74818	-0.32999	0.17413	11.063	1.5110	0.1594
40989960987230167	139.75681	-0.24806	0.05567	9.199	1.3253	0.2774
40990094131220352	139.70599	-0.38582	0.17469	10.520	3.4438	0.4785
40990098426185168	139.61738	-0.26799	0.07033	8.886	3.4130	0.289
40990098426185423	139.65839	-0.26209	0.05496	9.043	1.0801	0.1324
40989956692268987	139.74785	-0.33759	0.16151	9.505	2.2432	0.3863
40989960987229392	139.83145	-0.26634	0.05420	8.782	0.6965	0.3235
40989960987231636	139.84670	-0.21330	0.03856	9.416	1.2672	0.5896
40989956692270446	139.76336	-0.30467	0.17417	10.472	0.8884	0.6909
40989960987231003	139.76701	-0.22431	0.05503	9.325	0.9885	0.3236
40989956692270922	139.76967	-0.29240	0.27289	10.770	1.4083	0.0583
40989960987231122	139.81584	-0.22731	0.13942	9.906	1.2545	0.0691
40989956692266528	139.81638	-0.39410	0.15341	10.893	3.7252	0.75
40989960987229175	139.82644	-0.27333	0.17380	10.760	1.1686	0.1625
40989956692265523	139.88435	-0.41007	0.03866	9.088	8.0841	0.272

HSC ID	ra	dec	z	$\log M_*$	$R_{\rm eff}$	$p_{\rm m}$
40989956692270559	139.88497	-0.29993	0.05418	10.125	3.9742	0.197
40989960987229682	139.79462	-0.25947	0.21480	10.197	0.6975	0.2775
40989956692271388	139.87366	-0.28046	0.21539	10.983	0.9543	0.273
40989956692268960	139.76775	-0.33960	0.05469	8.316	1.2554	0.3352
40989956692269479	139.77077	-0.32878	0.16874	9.952	1.7554	0.5687
40989956692270650	139.78343	-0.29706	0.17385	10.015	1.9099	0.4409
40989956692267556	139.78680	-0.37132	0.03869	8.890	4.0717	0.1344
40989960987230100	139.76153	-0.25006	0.05627	9.194	1.1652	0.2117
40989819253313328	139.92065	-0.36426	0.05487	10.256	8.8452	0.3876
40989819253315795	139.93223	-0.30305	0.21481	10.910	1.6754	0.1879
40989823548279259	139.96252	-0.21302	0.17378	11.334	4.0176	0.3834
40989823548279260	139.96029	-0.21245	0.17404	8.801	0.3418	0.5965
40989823548279261	139.96023	-0.21517	0.17600	9.669	0.2706	0.605
40989819253315619	139.96811	-0.30347	0.22441	10.440	1.8531	0.9363
40989823548278097	139.97048	-0.24248	0.05626	9.380	3.2151	0.1396
40995316811457893	140.00054	-0.30420	0.21524	10.829	0.7717	0.5652
40989823548277367	139.95164	-0.26127	0.17435	9.975	1.3549	0.1905
40989819253312116	139.95481	-0.39604	0.22423	10.551	2.3826	0.5204
40989823548277505	139.97226	-0.25805	0.22751	10.640	0.7802	0.331
40989819253314951	139.98407	-0.31999	0.21516	10.273	1.3294	0.1413
40989819253313745	139.98509	-0.35353	0.22444	10.991	1.5891	0.1951
40989819253315940	139.99301	-0.30305	0.21542	10.786	0.9711	0.6486
40989823548277135	139.92630	-0.26636	0.15956	9.604	2.0781	0.6569
40989819253315418	139.93082	-0.31031	0.21481	10.215	1.7257	0.4068
40989823548277506	139.96906	-0.25987	0.15943	9.739	1.8026	0.366
40989819253314327	139.97485	-0.33665	0.20311	9.946	1.2622	0.1695
40989819253313133	139.95347	-0.36951	0.21528	10.530	2.2929	0.0436
40995316811454154	140.02003	-0.36801	0.13937	9.470	2.2352	0.0749

HSC ID	ra	dec	z	$\log M_*$	$R_{\rm eff}$	$p_{\rm m}$
40995316811458217	140.07756	-0.29706	0.21566	9.822	1.0569	0.5786
40995179372498417	140.11802	-0.35773	0.18483	10.100	0.3902	0.5858
40995179372501251	140.20268	-0.28706	0.18854	10.590	1.0268	0.3627
40995316811452936	140.07947	-0.41566	0.25039	10.645	0.8890	0.2861
40995316811458155	140.08046	-0.30210	0.27027	10.685	0.7487	0.3512
40995179372498396	140.10013	-0.35889	0.25914	10.693	0.6483	0.4494
40995183667465248	140.16221	-0.21319	0.25014	10.531	1.1700	0.1054
40995316811458194	140.06694	-0.29974	0.25962	10.165	0.8776	0.4008
40995179372500021	140.17448	-0.31898	0.28833	10.284	1.4196	0.9106
40995046228511454	140.28387	-0.23105	0.06104	9.835	4.0401	0.599
40995041933543879	140.35221	-0.40958	0.15407	11.369	4.2749	0.2812
40995183667463786	140.23305	-0.24854	0.15699	10.701	1.1674	0.2173
40995183667464483	140.26647	-0.23308	0.22516	10.742	0.7891	0.4792
40995041933547314	140.29294	-0.33165	0.15263	10.517	1.7220	0.4951
40995046228511440	140.30728	-0.23044	0.05490	10.543	5.1473	0.3482
40995046228511441	140.30393	-0.22893	0.15294	9.501	2.3224	0.2706
40995046228509173	140.31536	-0.26941	0.15281	10.930	2.0415	0.9807
40995041933544073	140.32240	-0.40226	0.15345	10.571	1.7719	0.457
40995041933543901	140.33405	-0.40578	0.15473	10.677	0.9093	0.4242
40995046228510060	140.34341	-0.25634	0.18487	10.538	1.5966	0.118
40995041933544329	140.34520	-0.39826	0.15309	10.579	1.8102	0.3705
40995179372496259	140.21360	-0.41093	0.27735	11.246	0.4924	0.4952
40995183667462734	140.21843	-0.27647	0.22422	10.726	0.9637	0.3482
40995179372501601	140.22187	-0.28046	0.22465	10.189	0.6793	0.2525
40995179372498143	140.25029	-0.36671	0.18976	10.366	1.2451	0.2997
40995046228511176	140.27803	-0.23902	0.22591	10.701	0.7141	0.4973
40995046228511178	140.27909	-0.23971	0.21656	9.835	1.4159	0.4088
40995041933545618	140.29030	-0.36864	0.17408	10.335	0.8250	0.3444

HSC ID	ra	dec	z	$\log M_*$	$R_{\rm eff}$	$p_{\rm m}$
40995041933543951	140.31209	-0.40520	0.18469	10.517	2.8246	0.5566
40995046228511013	140.32690	-0.23657	0.15337	9.668	1.8503	0.2811
40995041933546878	140.30234	-0.34107	0.22677	10.439	0.7552	0.5535
40995183667462636	140.22809	-0.27542	0.21666	9.962	1.3700	0.3811
40995179372497049	140.25401	-0.39164	0.18843	9.897	1.8255	0.3875
40995041933547704	140.30389	-0.32242	0.15266	9.465	1.1199	0.776
40995041933546897	140.35683	-0.34272	0.15472	9.838	1.2252	0.4723
40995041933548868	140.27925	-0.29592	0.15700	9.643	1.5954	0.6944
40995041933547275	140.33236	-0.33117	0.15291	10.213	2.2214	0.2544
40995041933544677	140.41891	-0.38759	0.16615	9.808	1.0300	0.6106
40995046228512040	140.45922	-0.21789	0.06916	9.759	5.0792	0.5538
40994908789558674	140.48620	-0.26087	0.06922	10.288	2.7523	0.5336
40994904494598034	140.49631	-0.30137	0.15342	11.090	1.8390	0.3216
40994904494597243	140.49401	-0.31651	0.19281	10.139	0.5155	0.3714
40995046228511894	140.44373	-0.22235	0.18230	10.071	1.6820	0.1211
40994904494578739	140.47964	-0.30548	0.15369	9.948	1.4445	0.5046
40994908789559016	140.61333	-0.25496	0.05398	9.751	3.5251	0.2114
40994767055636945	140.65239	-0.40903	0.05401	11.140	10.5897	0.1753
40994767055636946	140.65136	-0.40676	0.05562	10.472	1.4530	0.5256
40994904494595727	140.58116	-0.34959	0.18139	9.749	1.0752	0.3927
40994904494595997	140.59582	-0.34528	0.28504	10.590	1.0472	0.3685
40994904494591958	140.59613	-0.41605	0.05607	9.696	2.5855	0.0507
40994904494591776	140.60279	-0.41870	0.05313	9.916	1.0216	0.4776
40994904494594918	140.60813	-0.36209	0.05568	9.497	2.0970	0.7471
40994904494599031	140.61947	-0.27992	0.14353	10.153	0.9906	0.348
40994904494592165	140.62155	-0.41116	0.05304	10.087	4.0894	0.1967
40994904494593408	140.64300	-0.39184	0.05547	10.460	6.0007	0.5427
40994904494593601	140.54693	-0.38757	0.18295	9.966	1.1095	0.3941

HSC ID	ra	dec	z	$\log M_*$	$R_{\rm eff}$	$p_{\rm m}$
40994908789559759	140.55717	-0.23903	0.27453	10.833	0.7260	0.6159
40994908789560035	140.56439	-0.23658	0.27571	11.170	2.3205	0.1299
40994908789560666	140.59068	-0.22375	0.27745	10.907	2.9552	0.4094
40994904494597689	140.60958	-0.30765	0.19611	10.457	1.4606	0.5433
40994908789558158	140.61205	-0.27396	0.28951	11.014	1.0964	0.2552
40994904494595497	140.58890	-0.35272	0.18153	10.138	2.7435	0.3937
40994908789558467	140.60758	-0.26576	0.05546	9.245	1.6596	0.8867
40994904494594404	140.61980	-0.37678	0.05420	9.126	2.4990	0.9143
40994904494592001	140.63019	-0.41303	0.04604	8.410	1.9842	0.9106
40994904494593715	140.55722	-0.38763	0.21519	9.818	1.8130	0.1734
40994908789560864	140.59743	-0.21895	0.22622	10.529	1.3853	0.5081
40994767055638938	140.71299	-0.37062	0.05941	9.678	1.8571	0.9626
40994767055636736	140.77563	-0.41382	0.05482	9.437	2.9168	0.0136
40994767055637776	140.66126	-0.38402	0.05538	9.666	0.7237	0.4903
40994767055637782	140.65789	-0.38190	0.17392	10.039	1.2647	0.2113
40994767055637349	140.66986	-0.39877	0.05550	9.170	0.3765	0.4126
40994767055620278	140.67336	-0.41678	0.05866	9.442	0.6389	0.5979
40994767055641618	140.67917	-0.30881	0.19627	10.686	0.9955	0.2057
40994767055638638	140.68149	-0.37747	0.05556	10.068	1.6404	0.7072
40994767055639530	140.68724	-0.34883	0.05826	11.022	12.6875	0.41
40994767055641291	140.68639	-0.31457	0.05426	9.565	4.4286	0.802
40994767055641446	140.70018	-0.31064	0.05793	9.529	1.5831	0.263
40994767055639496	140.70128	-0.35432	0.19628	10.051	0.7024	0.5136
40994767055637953	140.70342	-0.38888	0.19717	10.234	0.6064	0.3555
40994771350603400	140.70753	-0.27456	0.05502	9.822	1.8445	0.3643
40994767055642479	140.72044	-0.29021	0.19452	10.485	1.8960	0.5747
40994767055639700	140.72565	-0.34796	0.05623	10.198	2.0981	0.093
40994767055638033	140.73059	-0.38748	0.19711	10.525	1.2619	0.7876

HSC ID	ra	dec	z	$\log M_*$	$R_{\rm eff}$	$p_{\rm m}$
40994767055637648	140.73459	-0.39003	0.19580	10.905	1.8071	0.3343
40994767055637650	140.73701	-0.38946	0.19710	10.625	1.3275	0.6341
40994767055637649	140.74192	-0.39185	0.19688	10.522	0.6359	0.5184
40994767055637651	140.74071	-0.39323	0.05164	9.130	1.5194	0.1881
40994771350606381	140.74485	-0.21202	0.18125	10.573	0.9495	0.7166
40994767055639304	140.74981	-0.36019	0.05459	8.886	0.6670	0.3746
40994767055639399	140.75408	-0.36019	0.05689	9.901	2.8276	0.0441
40994767055638009	140.75556	-0.39246	0.05609	10.069	2.6262	0.0824
40994767055638010	140.75492	-0.38917	0.19547	9.949	1.1219	0.1838
40994767055636631	140.78945	-0.41685	0.05562	9.956	2.3909	0.3277
40994767055638916	140.70621	-0.36967	0.21477	10.488	0.4206	0.5241
40994771350605532	140.70719	-0.23141	0.19475	10.252	0.4963	0.4658
40994771350605818	140.71867	-0.22377	0.20867	10.541	0.9675	0.1258
40994767055636897	140.73987	-0.41186	0.19527	10.305	0.2405	0.609
40994771350604146	140.74095	-0.25915	0.18163	10.458	1.7811	0.5204
40994767055639349	140.70800	-0.35759	0.16667	10.681	2.8132	0.2597
40994767055637938	140.70991	-0.39014	0.19714	10.467	1.7361	0.4346
40994767055641714	140.79891	-0.30491	0.17588	9.915	1.1570	0.5422
40994767055636971	140.72051	-0.40800	0.19541	10.172	1.2291	0.2182
40994771350604000	140.74464	-0.26250	0.05716	9.161	4.3338	0.7312
40994771350605582	140.78596	-0.22720	0.18132	9.656	1.0976	0.2964
40994767055639869	140.79515	-0.35008	0.19367	9.923	1.7566	0.1144
40994767055642384	140.67356	-0.29293	0.05443	9.206	1.9569	0.1467
40994771350606270	140.73236	-0.21345	0.18147	10.443	2.4206	0.2444
40994629616683857	140.83518	-0.39711	0.05406	9.992	1.5406	0.2976
40994629616688104	140.83939	-0.30297	0.05321	9.419	1.8288	0.0774
40994633911651211	140.84316	-0.22580	0.05490	9.230	1.7344	0.1612
40994633911649825	140.90435	-0.25453	0.27710	10.996	1.5307	0.523

HSC ID	ra	dec	z	$\log M_*$	$R_{\rm eff}$	$p_{\rm m}$
40994767055625254	140.81363	-0.29938	0.15855	9.723	0.9306	0.0794
40994767055636841	140.81813	-0.41227	0.28512	10.639	1.1052	0.5269
40994633911649362	140.83657	-0.26621	0.29212	10.966	0.8058	0.352
40994629616685776	140.94627	-0.35327	0.27707	10.709	0.9404	0.5366
40994633911649513	140.86765	-0.26177	0.29148	10.728	1.1621	0.2515
40994633911650798	140.90675	-0.23459	0.28089	10.609	1.1130	0.3835
40994633911650637	140.90857	-0.23966	0.28107	10.652	0.9232	0.392
40994629616683663	140.83690	-0.40698	0.05215	8.952	2.3751	0.4242
40994629616687526	140.91474	-0.31524	0.13762	9.509	0.9148	0.1888
40994629616668332	140.92495	-0.36815	0.10710	9.315	1.3382	0.1379
40994633911650638	140.90511	-0.23907	0.28138	10.511	0.9247	0.3363
40994633911651292	140.97672	-0.21079	0.22670	10.330	0.7364	0.282
40994629616688181	140.96723	-0.30295	0.27624	10.505	0.8311	0.1898
42028149071955381	129.02496	0.11547	0.29640	11.070	1.7415	0.4111
42028144776989255	129.02863	0.01271	0.05809	9.370	3.7710	0.883
42028144776990546	129.10194	0.05148	0.27099	10.892	0.8405	0.6377
42028149071958341	129.14290	0.18837	0.13545	11.127	5.8242	0.9765
42028144776989974	129.14991	0.03445	0.19870	10.444	1.4852	0.3245
42028144776989751	129.16284	0.02715	0.14844	10.034	1.5007	0.5205
42028011633001839	129.23143	0.09189	0.19899	10.726	0.7813	0.4332
42028007338040753	129.27490	0.03802	0.16648	10.470	0.6820	0.3634
42028011633007873	129.27605	0.20794	0.20029	10.514	1.1128	0.4327
42028011633003893	129.27884	0.12891	0.28118	10.428	0.7879	0.4415
42028149071957371	129.13841	0.15940	0.05162	8.486	2.2797	0.7393
42028149071959038	129.16617	0.19706	0.17151	10.297	2.1165	0.5806
42028011633002688	129.17556	0.10475	0.19928	9.935	2.1541	0.3089
42028007338042323	129.22293	0.06666	0.28190	10.621	0.9458	0.3343
42028011633007577	129.26383	0.20030	0.26879	10.659	1.9940	0.0937

HSC ID	ra	dec	z	$\log M_*$	$R_{\rm eff}$	$p_{\rm m}$
42028011633006859	129.31766	0.18655	0.16352	11.103	2.4457	0.2021
42027869899086740	129.40912	0.05067	0.03466	9.639	5.8486	0.4425
42028011633007052	129.30210	0.18797	0.29754	9.967	1.3064	0.5551
42028007338040069	129.30523	0.02754	0.24099	11.044	4.8963	0.1166
42028007338040827	129.33189	0.03965	0.28873	10.400	0.7499	0.3631
42028011632989460	129.33389	0.20921	0.23508	10.086	0.7757	0.1197
42027869899086990	129.36910	0.05235	0.28170	11.219	1.8862	0.0761
42027869899086541	129.39190	0.04376	0.20071	10.606	2.8010	0.1108
42027874194051147	129.39354	0.19707	0.28187	10.821	1.3057	0.4654
42027869899084901	129.39964	0.00788	0.20066	10.453	0.5291	0.4555
42027874194051077	129.40567	0.18647	0.28707	10.891	1.7675	0.6682
42027874194051172	129.41503	0.19111	0.28211	10.671	1.9461	0.8355
42027874194051171	129.41705	0.19437	0.26963	11.035	0.9537	0.6236
42028007338040385	129.29445	0.03185	0.24164	10.416	0.9646	0.2181
42027874194049555	129.41313	0.15037	0.28225	10.841	1.1877	0.4419
42028011633003267	129.29324	0.11809	0.13537	9.460	1.7875	0.5649
42028007338041116	129.32774	0.04544	0.21369	10.019	1.3911	0.5903
42027869899085703	129.46090	0.02505	0.19444	9.640	0.7323	0.4076
42027869899085580	129.46857	0.02415	0.20156	11.086	3.3081	0.537
42027869899086818	129.47476	0.04847	0.11789	9.875	1.0678	0.1057
42027869899088476	129.50574	0.08507	0.08415	10.344	1.8927	0.8076
42027732460131385	129.57003	0.00910	0.10877	9.816	1.4875	0.4864
42027869899084857	129.48793	0.00673	0.16676	10.097	2.3253	0.1283
42027869899084664	129.52722	0.00201	0.23233	10.943	0.9858	0.3164
42027736755100543	129.54569	0.19568	0.16924	10.306	2.9723	0.9386
42027736755096882	129.55916	0.12288	0.05149	9.966	4.8348	0.2414
42027732460133406	129.56960	0.04935	0.21415	10.127	1.0917	0.0759
42027869899085538	129.47540	0.02250	0.16666	9.946	3.0147	0.8113

HSC ID	ra	dec	z	$\log M_*$	$R_{\rm eff}$	$p_{\rm m}$
42027869899068538	129.51419	0.02925	0.14562	9.687	1.2656	0.0981
42027874194051304	129.52809	0.19214	0.03502	8.184	3.4830	0.798
42027874194050482	129.47067	0.17422	0.28204	10.198	1.2670	0.3091
42033230018274113	129.64940	0.03676	0.07820	10.119	1.1094	0.4488
42033234313237109	129.63298	0.14455	0.26988	10.893	0.7728	0.3383
42033230018274115	129.64502	0.04144	0.27066	11.115	0.7225	0.3455
42033230018274117	129.64473	0.04078	0.07764	9.393	1.6789	0.5639
42033234313234660	129.64497	0.10049	0.16232	10.785	2.0072	0.2977
42033230018274752	129.66531	0.04811	0.07864	9.943	1.0050	0.7076
42033230018274753	129.66939	0.05320	0.26807	11.294	1.3504	0.4618
42033234313235459	129.67865	0.11468	0.16498	9.464	0.9031	0.2688
42033234313237328	129.69548	0.14863	0.26854	10.786	0.9916	0.363
42033234313238845	129.69680	0.17421	0.16452	10.610	1.0704	0.3773
42033234313238844	129.70131	0.17602	0.16318	10.759	4.0143	0.2233
42033234313238846	129.70187	0.17563	0.16268	10.852	4.1755	0.2531
42033234313239717	129.70194	0.19168	0.08414	9.699	2.1330	0.8766
42033234313240258	129.70185	0.20278	0.16112	10.338	1.7401	0.6349
42033230018271830	129.70414	0.00370	0.21398	10.919	2.0890	0.488
42033234313240134	129.70695	0.19895	0.16296	10.575	1.1426	0.4825
42033230018275302	129.71518	0.05914	0.02461	8.419	2.3012	0.723
42033230018272858	129.71512	0.02054	0.13034	9.734	2.1887	0.8314
42027732460134242	129.58591	0.06601	0.24134	10.351	0.9119	0.2113
42027736755098154	129.58771	0.15065	0.15459	10.353	1.5255	0.1207
42027732460132591	129.59002	0.03159	0.23285	10.581	0.6706	0.4549
42027736755097023	129.59080	0.12701	0.29417	10.702	1.0943	0.3033
42027736755099095	129.59867	0.17194	0.24209	11.165	3.3697	0.1218
42027736755098364	129.60136	0.15558	0.24221	10.330	0.5739	0.4222
42027732460132690	129.60140	0.03114	0.23177	10.496	0.9245	0.4977

HSC ID	ra	dec	z	$\log M_*$	$R_{\rm eff}$	$p_{\rm m}$
42027736755097523	129.62489	0.13664	0.26832	10.881	1.9938	0.6234
42033230018276255	129.67430	0.07401	0.24212	11.034	1.1366	0.3104
42033234313236212	129.67888	0.12798	0.17789	10.494	1.2327	0.3152
42033234313234448	129.67958	0.09598	0.26960	10.741	0.7974	0.3814
42033230018272687	129.69866	0.01397	0.21301	10.470	1.0137	0.4929
42033230018273562	129.70111	0.02871	0.27051	11.434	3.5982	0.1275
42033230018271829	129.70796	0.00376	0.21517	10.541	0.4985	0.54
42027736755098635	129.62875	0.15853	0.16377	10.313	2.2032	0.0968
42033234313234608	129.63197	0.09811	0.29341	10.328	1.0442	0.3428
42027736755095185	129.61876	0.09458	0.27890	10.147	1.1488	0.428
42033230018275704	129.64601	0.06452	0.29374	10.667	0.9830	0.2669
42033230018273049	129.64908	0.02035	0.07799	9.272	1.3298	0.0767
42033230018272690	129.69342	0.01509	0.15911	9.920	1.8442	0.2922
42033230018273925	129.69735	0.03465	0.27719	10.751	1.8110	0.4865
42033230018276794	129.71328	0.08802	0.19620	10.067	1.1800	0.1799
42033092579318363	129.75369	0.02813	0.15447	10.251	1.4542	0.2573
42033092579317983	129.75677	0.02159	0.13008	9.681	1.0025	0.0961
42033092579321251	129.75803	0.08476	0.13650	9.192	1.2404	0.7888
42033096874284601	129.75850	0.12114	0.16390	9.778	0.5304	0.4519
42033092579321552	129.75958	0.09025	0.04993	8.998	1.5403	0.2828
42033092579319939	129.79154	0.06035	0.29345	10.662	0.5757	0.5292
42033092579316894	129.79419	0.00604	0.13013	9.787	1.9286	0.9868
42033092579318874	129.80027	0.03943	0.26970	10.072	1.3453	0.3723
42033096874285361	129.82591	0.13884	0.15228	10.527	0.8350	0.2722
42033092579317257	129.87399	0.00915	0.15912	10.057	0.3880	0.4396
42033092579318921	129.72920	0.03649	0.26986	10.187	1.2273	0.8269
42033092579317928	129.72991	0.02186	0.27120	10.823	1.2717	0.9512
42033092579317525	129.73551	0.01350	0.21439	10.226	0.6129	0.3315

HSC ID	ra	dec	z	$\log M_*$	$R_{\rm eff}$	$p_{\rm m}$
42033092579319240	129.75968	0.04529	0.04909	8.534	0.5033	0.6263
42033096874287950	129.76208	0.17973	0.21328	10.284	1.0521	0.4857
42033092579316939	129.76313	0.00195	0.26959	10.745	1.1783	0.4076
42033096874289077	129.76570	0.19254	0.26962	10.157	0.4624	0.5553
42033092579317445	129.77823	0.01420	0.26969	10.383	0.5510	0.4719
42033096874283588	129.78713	0.10951	0.27576	10.784	1.0207	0.4074
42033096874283589	129.78842	0.11032	0.27623	10.284	0.8030	0.448
42033092579318397	129.80470	0.03018	0.24894	11.035	1.4840	0.161
42033096874284369	129.81928	0.12078	0.27547	10.976	1.3203	0.2733
42033096874287919	129.86617	0.18118	0.23435	11.008	1.0933	0.1699
42033096874287920	129.86721	0.17869	0.27131	10.826	0.7875	0.3885
42033092579318436	129.81656	0.02719	0.24977	10.562	0.7789	0.4843
42033096874288662	129.80826	0.19392	0.08424	8.752	1.7403	0.6817
42033096874285447	129.79843	0.13571	0.16110	9.717	2.5824	0.091
42033096874285821	129.84830	0.14570	0.26956	10.255	1.1323	0.323
42033096874288974	129.89809	0.19445	0.16452	9.948	1.1681	0.4744
42032959435328385	129.97916	0.14764	0.16291	10.551	1.1539	0.331
42033096874284984	129.88963	0.13109	0.15495	10.253	1.7305	0.4552
42033096874285834	129.89492	0.14828	0.27082	10.995	1.5914	0.7797
42032959435327570	129.90802	0.13485	0.26728	10.413	0.7432	0.4463
42032959435325964	129.90972	0.10088	0.27075	10.949	4.0372	0.3099
42032959435325969	129.91086	0.10430	0.27105	10.187	1.2876	0.4983
42032959435325965	129.91417	0.09818	0.26844	10.398	0.9555	0.4666
42032959435325967	129.91107	0.09798	0.26828	10.427	1.2788	0.9771
42032959435326100	129.91895	0.10086	0.27040	10.638	2.2209	0.5101
42032959435329472	129.94369	0.17319	0.26805	10.011	0.7337	0.266
42032959435331310	129.95667	0.20085	0.26984	10.659	0.4940	0.506
42032959435325908	129.97336	0.09904	0.26999	10.980	1.6520	0.9172

HSC ID	ra	dec	z	$\log M_*$	$R_{\rm eff}$	$p_{\rm m}$
42032959435330803	130.00288	0.19292	0.18002	10.451	0.6910	0.3793
42032959435327557	129.92932	0.13004	0.26922	10.102	0.8597	0.2674
42032955140348050	129.92948	0.08439	0.20427	9.554	0.9380	0.0904
42032955140360506	129.96205	0.00900	0.15295	9.785	1.1154	0.2305
42032959435328694	129.97427	0.15401	0.27444	10.317	0.9346	0.7712
42032959435328362	129.90971	0.14774	0.27182	10.290	1.9391	0.0947
42032959435326777	129.91853	0.11539	0.26550	10.458	1.8987	0.0601
42032955140361697	129.94264	0.03338	0.19054	10.078	1.6855	0.1939
42032959435326887	129.95167	0.11442	0.26943	10.247	1.4297	0.5097
42032955140363603	129.96146	0.08140	0.26944	10.078	2.4024	0.7489
42032959435326471	129.96517	0.10951	0.27835	10.550	3.2528	0.0543
42032955140361126	130.03324	0.01964	0.15448	10.032	1.3785	0.3947
42032955140363029	130.04725	0.06472	0.12942	9.959	1.1336	0.5258
42032959435329975	130.07010	0.17876	0.27095	11.468	2.4323	0.5036
42032821996375858	130.15359	0.19449	0.19072	10.488	0.9634	0.382
42032817701409480	130.16705	0.02559	0.16292	10.256	0.7719	0.2879
42032821996371082	130.17347	0.09182	0.19068	11.252	1.5541	0.5328
42032955140360486	130.02843	0.00585	0.20932	10.079	0.9765	0.2403
42032955140360630	130.05357	0.01146	0.15448	10.498	1.2351	0.578
42032955140360631	130.05402	0.01218	0.15413	9.407	4.7268	0.7827
42032959435331429	130.05751	0.20537	0.27031	10.794	0.9541	0.5382
42032955140361270	130.06369	0.02261	0.19200	10.246	0.4197	0.4645
42032821996372637	130.11673	0.13035	0.19036	10.638	1.2447	0.306
42032821996375470	130.16473	0.18647	0.19259	10.347	0.6787	0.2126
42032821996371550	130.17325	0.10394	0.26778	10.740	1.6745	0.4071
42032821996370912	130.11515	0.09470	0.23109	9.812	1.7415	0.9484
42032821996371150	130.16245	0.09665	0.06120	8.744	4.1263	0.1201
42032821996373634	130.16663	0.15008	0.02449	8.229	5.9244	0.1404

HSC ID	ra	dec	z	$\log M_*$	$R_{\rm eff}$	$p_{\rm m}$
42032959435326993	130.04327	0.11783	0.23112	10.313	1.3895	0.2138
42032817701410767	130.14978	0.05250	0.19224	10.212	2.2651	0.1352
42032821996375703	130.18144	0.19421	0.26341	10.901	0.6791	0.4968
42032821996372905	130.25642	0.13411	0.10155	10.169	3.7139	0.5201
42032817701410649	130.18376	0.05202	0.23147	10.118	1.7111	0.5525
42032817701409890	130.18838	0.03409	0.23107	10.874	2.4436	0.9062
42032817701409891	130.18723	0.03650	0.23050	9.924	0.9682	0.146
42032817701412277	130.19242	0.07926	0.16431	10.543	1.2557	0.2628
42032817701412743	130.19840	0.08816	0.26518	10.041	1.2858	0.9863
42032817701409528	130.21550	0.02676	0.16433	10.768	2.0697	0.1028
42032821996374895	130.22905	0.17682	0.07812	8.893	0.8771	0.3715
42032684557423433	130.28086	0.19525	0.10121	10.114	3.5620	0.2532
42032821996371843	130.19188	0.10962	0.11884	9.697	1.0415	0.1752
42032821996376076	130.19739	0.20513	0.26659	10.636	0.6201	0.2784
42032817701409548	130.20268	0.02775	0.16312	10.538	2.4821	0.2851
42032817701411409	130.25608	0.06383	0.26791	11.258	1.7962	0.196
42032821996372000	130.27344	0.11588	0.25592	10.587	0.6900	0.3251
42032821996375234	130.27542	0.18398	0.21262	10.485	1.3961	0.5518
42032821996373022	130.18328	0.13571	0.27761	10.824	1.5440	0.9228
42032821996373023	130.18292	0.13678	0.15462	9.075	2.1842	0.9705
42032684557419210	130.29068	0.10455	0.13412	9.495	2.1752	0.5962
42032821996372990	130.19537	0.13501	0.27736	10.391	1.7985	0.5425
42032821996371319	130.19603	0.09981	0.21537	10.751	3.7627	0.37
42032817701411492	130.20849	0.06638	0.20264	10.364	1.6954	0.1149
42032684557420918	130.30287	0.14371	0.27787	10.074	1.8490	0.9511
42032680262456409	130.33233	0.02079	0.20889	10.545	0.7250	0.3913
42032684557421886	130.36794	0.16078	0.20789	10.170	0.5553	0.482
42032684557419319	130.39653	0.10779	0.25723	10.953	0.9216	0.3155

HSC ID	ra	dec	z	$\log M_*$	$R_{\rm eff}$	$p_{\rm m}$
42032680262455771	130.44562	0.00815	0.04970	8.026	0.9880	0.1628
42032684557424218	130.45702	0.20805	0.27858	10.818	0.4980	0.4061
42032680262457768	130.45860	0.04612	0.24368	11.006	0.8452	0.3995
42032680262457732	130.46325	0.04448	0.24303	10.844	0.9607	0.2883
42032542823507713	130.46737	0.07575	0.25753	11.056	1.8053	0.3392
42032684557418716	130.41959	0.09441	0.22824	9.783	1.5530	0.2009
42032684557422299	130.44984	0.17819	0.27731	10.447	1.5242	0.4555
42032680262457870	130.33254	0.05230	0.24369	10.408	1.0985	0.4749
42032684557423509	130.37232	0.19411	0.20855	10.380	1.2038	0.366
42032684557420895	130.37857	0.14081	0.20890	10.209	1.4728	0.7174
42032680262456553	130.38646	0.02317	0.16640	10.258	2.5737	0.149
42032547118468584	130.58740	0.16151	0.07826	10.824	9.5209	0.336
42032547118466426	130.61923	0.12372	0.05089	9.503	0.9991	0.3259
42032547118466206	130.49621	0.12027	0.19962	10.569	1.2152	0.3785
42032547118470642	130.52962	0.20729	0.08550	9.539	2.8568	0.4555
42032547118466095	130.53306	0.11564	0.07796	9.242	1.8753	0.1178
42032542823507329	130.53739	0.07054	0.19960	10.777	2.1136	0.1234
42032542823506826	130.53770	0.06079	0.19986	10.744	0.6171	0.3059
42032542823503290	130.57396	0.00225	0.19984	10.645	0.8250	0.4308
42032547118467772	130.57797	0.14994	0.07890	9.295	0.5423	0.3941
42032547118465276	130.58544	0.10181	0.16265	10.851	1.4037	0.3606
42032542823507962	130.58954	0.08590	0.07650	9.579	2.9977	0.8322
42032547118466588	130.59805	0.12682	0.16269	10.614	2.7025	0.5096
42032547118466098	130.60490	0.11616	0.16303	10.790	1.7737	0.4683
42032547118466099	130.60348	0.11430	0.16189	10.536	0.6411	0.4648
42032547118466100	130.60527	0.11246	0.16221	10.118	1.1499	0.6393
42032547118465107	130.50409	0.09547	0.29264	10.617	0.5615	0.2253
42032547118467618	130.59920	0.14690	0.26015	10.479	1.1446	0.4414

HSC ID	ra	dec	z	$\log M_*$	$R_{\rm eff}$	$p_{\rm m}$
42032542823508271	130.58435	0.08631	0.14740	9.516	1.8043	0.8965
42032542823504444	130.52782	0.01753	0.16272	9.559	1.9674	0.8871
42032547118468138	130.59605	0.15630	0.15601	9.105	2.4393	0.653
42032409679517079	130.74367	0.20612	0.05033	10.538	9.1534	0.1416
42032409679516949	130.65351	0.20220	0.20804	10.395	1.1402	0.1175
42032409679512175	130.65527	0.10649	0.19110	10.831	1.2784	0.8757
42032409679515699	130.66835	0.17872	0.07796	10.226	3.5782	0.2699
42032409679511506	130.66979	0.09160	0.16213	11.066	1.4762	0.2024
42032405384550603	130.68193	0.00738	0.20007	9.931	0.6484	0.1926
42032405384554335	130.68895	0.07187	0.16128	10.163	1.4463	0.2814
42032405384551604	130.70471	0.02323	0.12790	10.577	2.4268	0.6211
42032409679515038	130.70956	0.16281	0.07820	9.714	3.2207	0.8514
42032405384555098	130.71415	0.08996	0.14754	10.827	1.5309	0.1039
42032409679513328	130.71432	0.12664	0.19994	10.049	1.4142	0.3875
42032409679515982	130.77095	0.18197	0.13403	10.065	0.9216	0.2513
42032409679514913	130.77499	0.16119	0.14214	10.184	0.8355	0.2057
42032405384552560	130.66553	0.04010	0.20063	10.539	1.9059	0.2996
42032409679516806	130.66768	0.19828	0.26962	10.557	0.9918	0.2371
42032405384552273	130.67975	0.03547	0.24419	10.711	0.8184	0.517
42032405384552238	130.71936	0.03330	0.11383	9.921	2.5341	0.1638
42032409679516222	130.68815	0.18716	0.26941	9.991	2.0519	0.5978
42032272240561534	130.86113	0.14137	0.10950	9.399	2.1712	0.0511
42032272240560322	130.91181	0.11752	0.08609	9.956	3.5276	0.1567
42032409679511854	130.79748	0.09728	0.07836	9.090	1.5875	0.5399
42032272240564686	130.84346	0.20036	0.15546	10.439	1.0255	0.3675
42032272240560796	130.86095	0.12921	0.16135	10.013	1.8231	0.4571
42032267945598942	130.91362	0.05413	0.12787	10.583	2.2593	0.1378
42032272240559454	130.92606	0.10204	0.14775	10.259	0.6887	0.3451

HSC ID	ra	dec	z	$\log M_*$	$R_{\rm eff}$	$p_{\rm m}$
42032272240561045	130.86582	0.13247	0.19998	10.278	0.6802	0.3905
42032267945598646	130.88721	0.04817	0.22921	10.393	0.7493	0.2539
42032272240564182	130.89701	0.18822	0.19235	10.462	1.5202	0.3081
42032409679517100	130.83120	0.20599	0.05050	8.961	3.5552	0.3558
42032405384552181	130.83686	0.03215	0.21268	9.806	1.1071	0.4517
42032272240561473	130.85441	0.13841	0.19933	10.157	1.9560	0.4269
42032267945596697	130.97271	0.01384	0.15478	10.788	4.0647	0.4423
42032267945598883	130.97920	0.05341	0.22935	10.703	1.0072	0.4848
42032134801607726	131.03630	0.16991	0.07782	9.440	1.7390	0.5518
42032134801604697	131.06681	0.09621	0.20621	10.346	1.3529	0.4631
42032134801605558	131.07481	0.11803	0.20659	10.234	1.9922	0.7038
42032272240562537	130.94768	0.15923	0.15109	9.998	1.2311	0.0731
42032272240563246	131.01375	0.17364	0.26877	10.645	0.6564	0.5565
42032134801608783	131.03262	0.19374	0.16102	10.177	0.5388	0.3768
42032272240562676	130.95235	0.16183	0.15096	9.487	1.3663	0.1917
42037632359748908	131.16683	0.15245	0.07671	10.144	0.8678	0.561
42037632359748568	131.17084	0.14521	0.07600	9.026	0.8818	0.1555
42037632359746439	131.17357	0.10867	0.11914	10.307	2.1571	0.9885
42037490625832808	131.21711	0.07244	0.22947	9.927	0.9677	0.2636
42037628064783506	131.12934	0.07340	0.29122	10.572	1.1359	0.5611
42037632359748485	131.14924	0.14344	0.24032	10.336	0.4718	0.3727
42037628064781551	131.19576	0.03824	0.14514	9.581	1.0686	0.2857
42032134801605117	131.08144	0.10804	0.20627	9.931	2.1222	0.4507
42032130506645365	131.08671	0.05556	0.29075	10.506	1.2344	0.3554
42037632359746786	131.12986	0.11135	0.08632	8.964	3.4182	0.9049
42037628064783406	131.19837	0.07001	0.19748	9.567	2.3022	0.7968
42037490625831472	131.30600	0.04823	0.07760	10.183	0.9833	0.294
42037490625833294	131.25100	0.08057	0.19740	10.244	1.6049	0.6945

HSC ID	ra	dec	z	$\log M_*$	$R_{\rm eff}$	$p_{\rm m}$
42037494920795732	131.25809	0.20202	0.28022	10.819	0.6677	0.5787
42037494920790795	131.35667	0.11996	0.13400	10.155	3.1882	0.408
42037357481838670	131.40864	0.11442	0.18971	10.121	0.8386	0.2729
42037357481839879	131.40992	0.13289	0.05203	8.578	1.5674	0.8864
42037357481838567	131.43788	0.11174	0.21530	10.526	0.5905	0.3764
42037357481842713	131.45046	0.18029	0.15518	10.461	1.4449	0.2589
42037357481842892	131.48279	0.18321	0.16246	10.215	3.5513	0.8023
42037357481837486	131.48695	0.09606	0.25571	11.117	1.7560	0.835
42037490625832205	131.38513	0.06318	0.18930	10.164	1.1274	0.352
42037353186879294	131.42342	0.08254	0.19677	9.973	0.4786	0.4035
42037357481839404	131.47836	0.12746	0.27869	10.880	0.9127	0.5159
42037357481841143	131.47899	0.15269	0.27889	10.795	1.1344	0.2478
42037357481837740	131.48136	0.09532	0.26475	10.844	0.8653	0.2995
42037353186877782	131.50015	0.05259	0.26444	10.845	2.0424	0.2188
42037353186879174	131.40874	0.08120	0.19620	9.517	1.3916	0.4304
42037357481837689	131.43907	0.09499	0.25886	10.472	1.8430	0.4409
42037357481839440	131.39356	0.12728	0.25875	9.845	0.9811	0.688
42037357481843196	131.46718	0.18494	0.21614	10.106	1.8112	0.3712
42037353186877292	131.52509	0.04941	0.14479	9.243	0.6339	0.4021
42037357481843932	131.52657	0.20069	0.12904	9.838	1.5558	0.426
42037357481839762	131.55634	0.13657	0.19648	10.440	1.2082	0.5505
42037215747919397	131.67019	0.05858	0.06951	9.128	1.0558	0.106
42037353186878578	131.55675	0.06928	0.26836	10.702	0.6509	0.4156
42037357481843448	131.56424	0.19448	0.15907	9.557	2.6444	0.9462
42037357481843353	131.56993	0.19138	0.15867	9.664	0.8567	0.3681
42037215747918937	131.69323	0.04722	0.19605	10.729	0.9061	0.2414
42037220042889006	131.75286	0.19926	0.13641	10.061	0.6816	0.4348
42037215747919281	131.75822	0.05855	0.15971	10.078	1.1175	0.4878

HSC ID	ra	dec	z	$\log M_*$	$R_{\rm eff}$	$p_{\rm m}$
42037215747919282	131.75641	0.05677	0.15970	9.661	1.2934	0.4348
42037082603931573	131.80349	0.15259	0.10254	9.287	1.6539	0.8409
42037215747917408	131.70084	0.00887	0.25678	10.736	1.2785	0.517
42037215747917756	131.71961	0.01726	0.25636	10.877	1.0957	0.2461
42037082603930850	131.80051	0.13949	0.22399	10.130	1.2584	0.5505
42037078308971228	131.84982	0.02136	0.16522	10.662	0.8677	0.6723
42037078308970229	131.85339	0.00697	0.16554	10.232	1.1827	0.3421
42037082603932308	131.87053	0.17296	0.09677	10.026	3.9551	0.7162
42037082603929744	131.87230	0.11753	0.17782	9.966	0.7362	0.3833
42037082603929745	131.87388	0.11888	0.17852	11.102	2.1473	0.7986
42037082603931071	131.87570	0.14467	0.17924	10.733	1.2487	0.3189
42037078308975108	131.94238	0.08432	0.09667	10.766	2.2742	0.1508
42037078308971538	131.83489	0.03237	0.25721	10.793	0.8006	0.4335
42037078308971724	131.84445	0.03055	0.16509	9.834	1.6814	0.4359
42037082603931904	131.85826	0.16076	0.19337	9.547	1.0358	0.3568
42036945164981116	131.96974	0.18593	0.27581	10.272	1.4175	0.0533
42036945164981661	131.97650	0.19814	0.16511	9.397	0.5898	0.1842
42036940870019169	132.00321	0.04696	0.16615	10.084	0.5769	0.2287
42036940870016520	132.02368	0.00244	0.17855	9.881	0.7357	0.498
42036945164980599	132.06153	0.17399	0.15965	9.527	1.2461	0.5767
42036945164982292	131.99837	0.20955	0.27630	10.595	0.6092	0.4157
42036940870019899	132.02093	0.06441	0.10146	9.196	0.8158	0.1313
42036945164980868	132.06725	0.18060	0.27498	10.608	0.4767	0.5122
42036945164978059	132.09323	0.12034	0.29408	10.841	1.4264	0.3
42036945164977594	132.10045	0.11218	0.28953	10.947	0.9245	0.4391
42036945164961882	132.08641	0.13934	0.19347	9.643	0.9833	0.0966
42036945164978896	132.11280	0.13603	0.19885	10.326	1.9207	0.4264
42036803431061013	132.20987	0.04472	0.22172	9.961	0.8640	0.6097

HSC ID	ra	dec	z	$\log M_*$	$R_{\rm eff}$	$p_{\rm m}$
42036807726026703	132.22625	0.15635	0.11745	10.126	1.7845	0.3376

Table 3.3: The first thousand rows of the merger probability catalog, which will be made publicly available. The columns are, from left to right: HSC ID, right ascension, declination, redshift, log stellar mass, effective radii in arcseconds, merger probability.

We plot a histogram of the merger probabilities of the SDSS and GAMA galaxies in Fig. 3.10. We see that the outputted probabilities are diverse in range, with the most galaxies being assigned ”unconfident” labels, with the peak being between 0.1 - 0.5 for the SDSS galaxies and 0.3 - 0.5 for the GAMA galaxies. This location of the peak is similar to that found in the simulation predictions in the previous Section, but differs from the probabilities found by transfer learning in Ackermann et al. (2018); Ferreira et al. (2020), where very clear probabilities both for mergers and non-mergers were favored. A possible explanation for the difference in distribution between our results and previous works, i.e., the peak in the 0.1 - 0.6 merger probability range, is the inclusion of the substantial number of mini mergers in our TNG training sample. We will be able to examine the effect of these mini mergers upon the completion of the images in Bottrell et al. (2023), as we will have many more major and minor mergers to fine-tune our model with. Many galaxies with similar appearances as the true mini mergers used in the fine-tuning process could be assigned ”unconfident” merger probablities in this range, whether they be merging or non-merging in ground truth. However, we also note the secondary peak at higher merger probability (> 0.9), meaning many mergers are guveb confident merger probabilities. This is consistent with the above mentioned works, and also allows for a large ”confident” merger sample for science purposes.

We show examples of galaxies within various merger probability bins in our predicted samples in Figures 3.11 through 3.14. We find that in the low merger probability bins (merger probabilities $0 - 0.3$, Fig. 3.11), our model correctly identifies likely stellar overlaps and projections as non-mergers, as well as a diverse appearance of non-mergers, similar to the correctly identified non-mergers in the simulation data. On the high merger probability end (merger probabilities > 0.8), similar to as seen in the simulation data, the model can predict mergers with diverse appearances, including clear interacting pairs and late or early stage mergers with disturbances.

As further validation, we confirm our model's ability to differentiate between projections and physically connected pairs in observational images. For each galaxy within our two samples that has a neighbor within a 30 kpc physical aperture, we calculate the line-of-sight velocity offset between the galaxy and its neighbor by $\Delta v = c\Delta z/(1 + z_{\rm target})$. We plot the merger probability distribution of these galaxies, binned by the line-of-sight velocity offset with its neighbor, or in the case of galaxies with multiple neighbors the minimum line-of-sight velocity offset, in Fig. 3.15. We find that pairs with offset $\Delta v < 500 {\rm kms}^{-1}$ makes up the greatest fraction of galaxies pairs with merger probability >0.8, and as the velocity offset increases, a greater distribution of galaxies are given unclear to lower merger probabilities (merger probability <0.5). Of the galaxies with both a high merger probability and offset, while a fraction of which may be projections, there are also likely to be true mergers that coincidentally have a projection. In particular, there may be post-merger galaxies that are not a pair but still have high merger probability. Based on our simulation results in Fig. 3.3b, our model identifies 1 post-merger galaxy for every 2 pre-merger galaxies. Following these results, a fraction of galaxies with $\Delta v > 500 {\rm kms}^{-1}$ and high merger probabilities in Fig. 3.15 are likely to be post-mergers.

3.5.2 Comparison with previous methods

We conduct one final validation by comparing this method with previous merger identification methods, specifically the multi-step identification method conducted in Chapter 2. We make merger predictions on the 298 SDSS-MaNGA galaxies we identified in Chapter 2 using our fine-tuned model. Figure 3.16 shows the merger probability distribution for these galaxies.

We find that 100 of 298 galaxies are given a merger probability > 0.8, and 174 have merger probability > 0.5, indicating just under half of the mergers are given merger probability < 0.5. We attribute this partially to the use of SDSS images, which are of lower resolution compared to HSC-SSP, and are also qualitatively different in terms of noise.

3.5.3 Merger sample selection for science

The results from simulation data show that a complete binary split, or in other words a merger probability > 0.5 is a merger and < 0.5 is a non-merger, gives a precision that is $\sim$ 80%. However, the merger probability distribution for both observation and simulation results show that many galaxies lie in a range between merger probability 0.2 – 0.6. As such, while the merger probabilities we found can be sufficiently useful to investigate trends between merger probability and physical properties, conducting studies adopting a complete binary split may suffer from contamination of "unconfident" galaxies. We can see from Fig. 3.13 that there are many unclear galaxies in the probability range 0.5 – 0.8 that may or may not be real mergers; thus, using galaxies in this range may contaminate both merger and non-merger samples, which will affect results in merger related sciences.

We plot the merger fraction of our two samples as a function of merger probability in Fig. 3.17. We compare our results with previous works calculating the merger fraction in similar redshift ranges, both in observations and simulations (Lotz et al., 2011; Cotini et al., 2013; Pearson et al., 2019; Kim et al., 2021; Nevin et al., 2023). We find that our merger fractions, in most cases, become statistically consistent with these works if we consider "confident" classifications (merger probability > 0.8) as our threshold, with the threshold indicated by the dotted vertical line. However, we note that despite the statistical consistency there are likely to be contaminants regardless of threshold.

We will not set a definite, arbitrary threshold to define a merger in the catalog to be released; instead, we will just provide the merger probabilities for every galaxy, as shown in Table 3.3[1], and users can determine their thresholds. However, we recommend that a "confident" threshold (merger probability > 0.8) is used to determine a merger sample.

[1]The full version of Table 3.3 is available in electronic format the CDS via anonymous ftp to cdsarc.cds.unistra.fr (130.79.128.5) or via https://cdsarc.cds.unistra.fr/cgi-bin/qcat?J/A+A/

3.6 Merger galaxy properties

In this section, we use merger probabilities obtained using our model to investigate the relationship between galaxy mergers and local galaxy environments. We evaluate the merger probability distribution in differing environmental density bins for the various environmental parameters. We also investigate the relationship between galaxy merging and environment in TNG simulations, and look for any agreements between observations and simulations.

3.6.1 Environmental overdensities as a function of merger probability

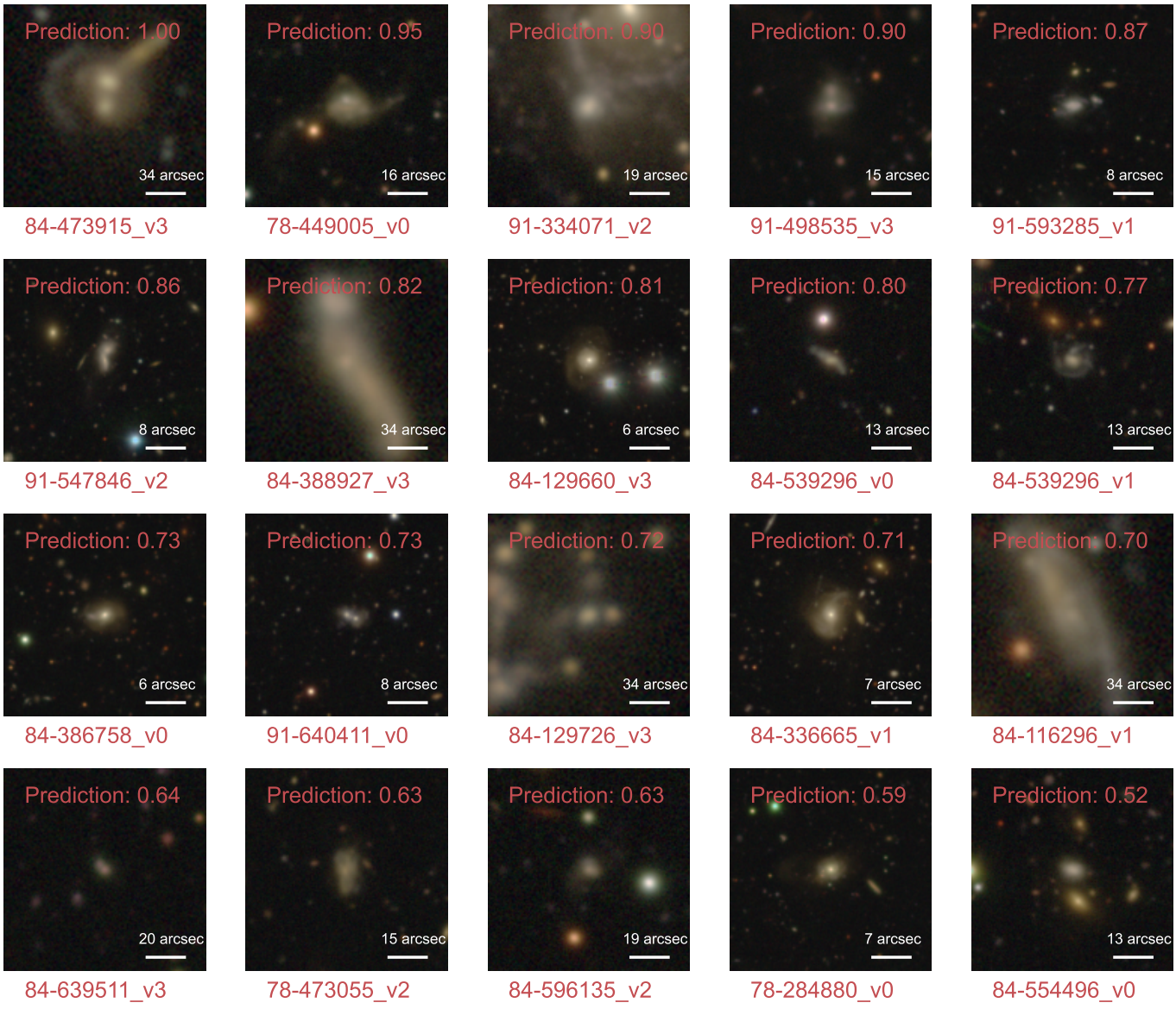

Fig. 3.6: 20 randomly drawn examples of true positive classifications (merger probability > 0.5) from the 10 test sets, in descending order, with the probabilities indicated in the image, and the identification of the galaxy indicated below the image in the format [snapshot]-[ID]_[viewing angle]. The model seems to be able to identify various merger features, including close companions and merger remnants such as rings.

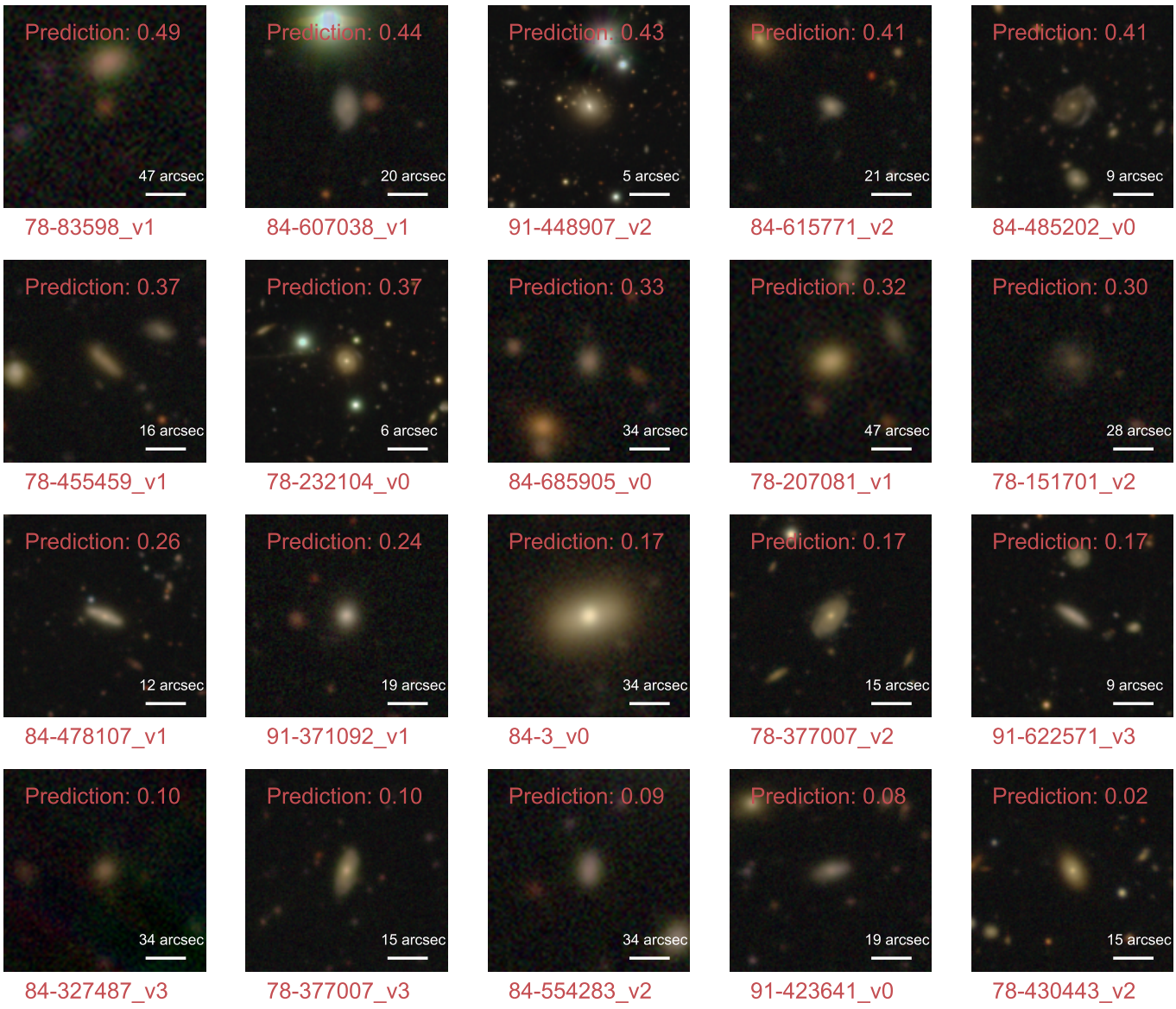

Fig. 3.7: Same as Fig. 3.6 but for true negatives. The model seems to be able to correctly identify some projections/overlaps as non-interacting. More importantly, a diverse appearance of non-mergers are correctly identified.

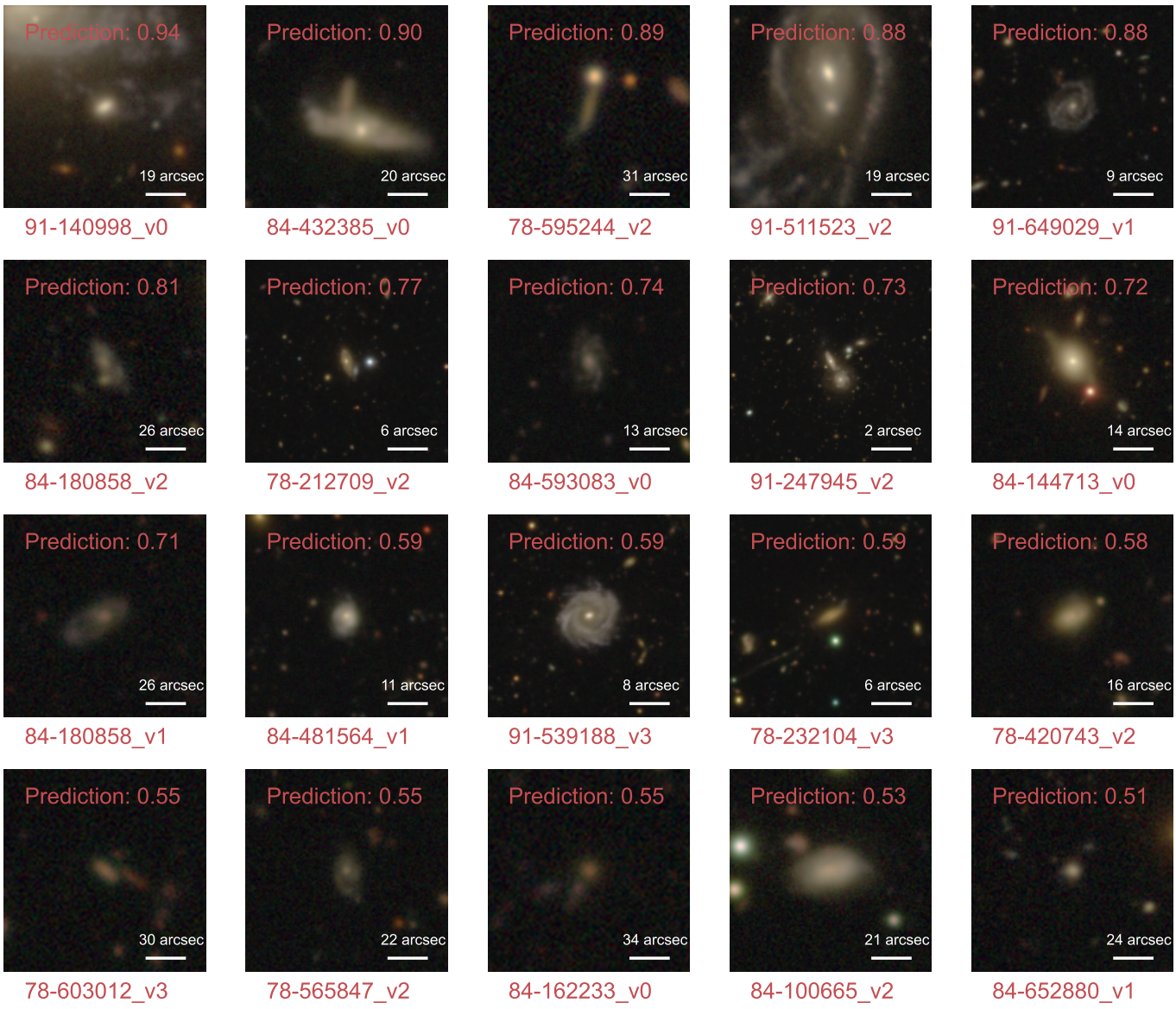

Fig. 3.8: Same as Fig. 3.6 but for false positives. Some close overlaps are incorrectly classified as a merging. Such galaxies, such as 84-432385_v2 with a merger probability of 0.90, would also likely be classified as mergers by human visual identification.

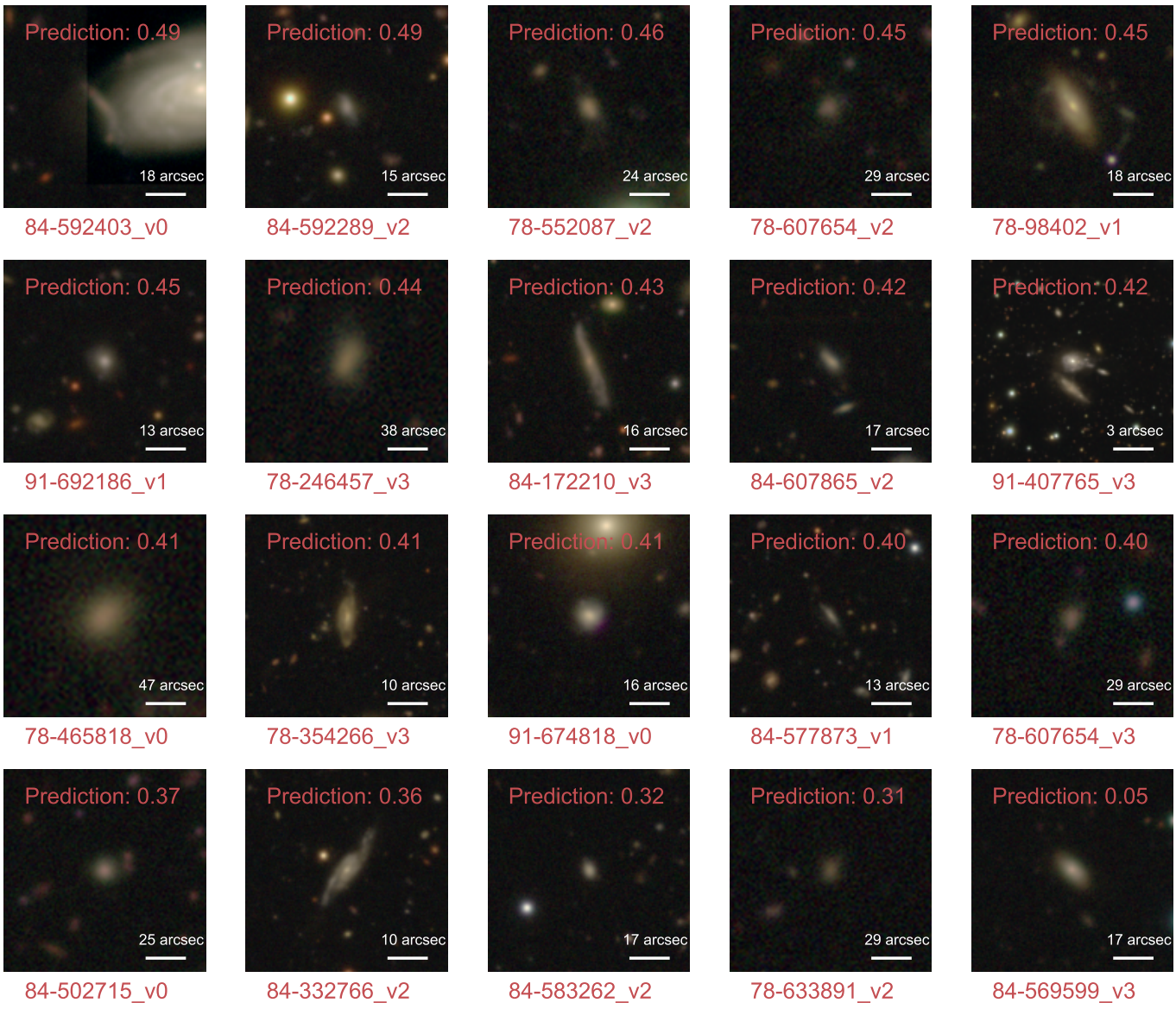

Fig. 3.9: Same as Fig. 3.6 but for false negatives. Many galaxies with lower probabilities, especially those in the bottom two rows are minor or mini mergers with the most recent/next merger close to the 0.5 Gyr threshold for merger selection.

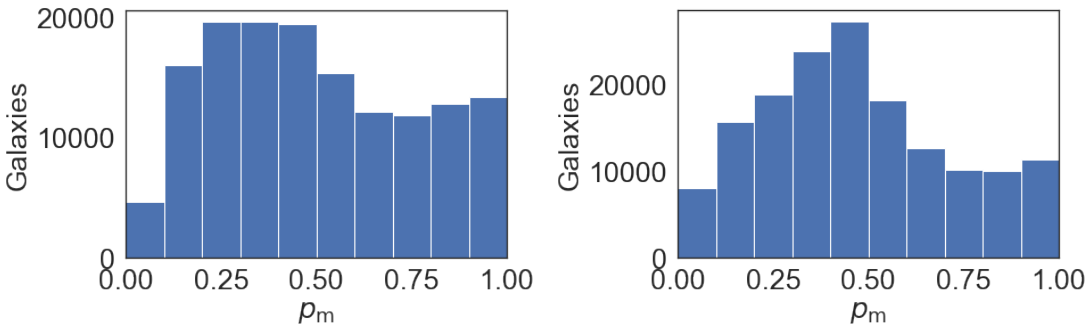

Fig. 3.10: Merger probability distributions for HSC-SDSS (upper) and HSC-GAMA (lower) cross-matched galaxies predicted using our fine-tuned model. Note that in both cases, more galaxies lie in an unclear range (merger probability $0.2 - 0.5$) for non-mergers than "confident" non-mergers (merger probability $0 - 0.1$). However, we find that many of the mergers identified are confident (merger probability > 0.8).

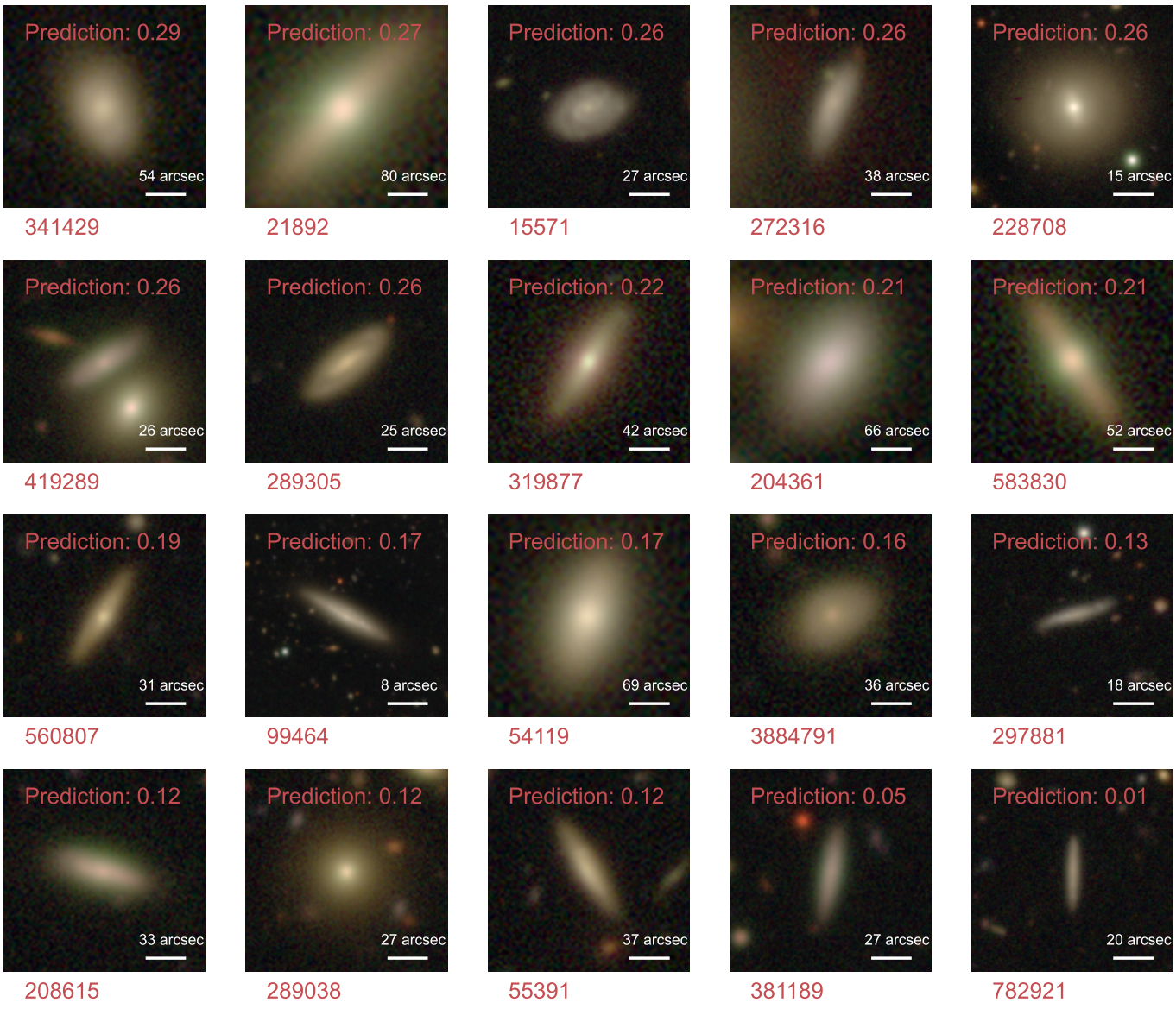

Fig. 3.11: 20 randomly drawn examples of GAMA galaxies with a merger probability < 0.3, with merger probabilities in descending order. The merger probabilities are indicated in the image and the GAMA ID below the image.

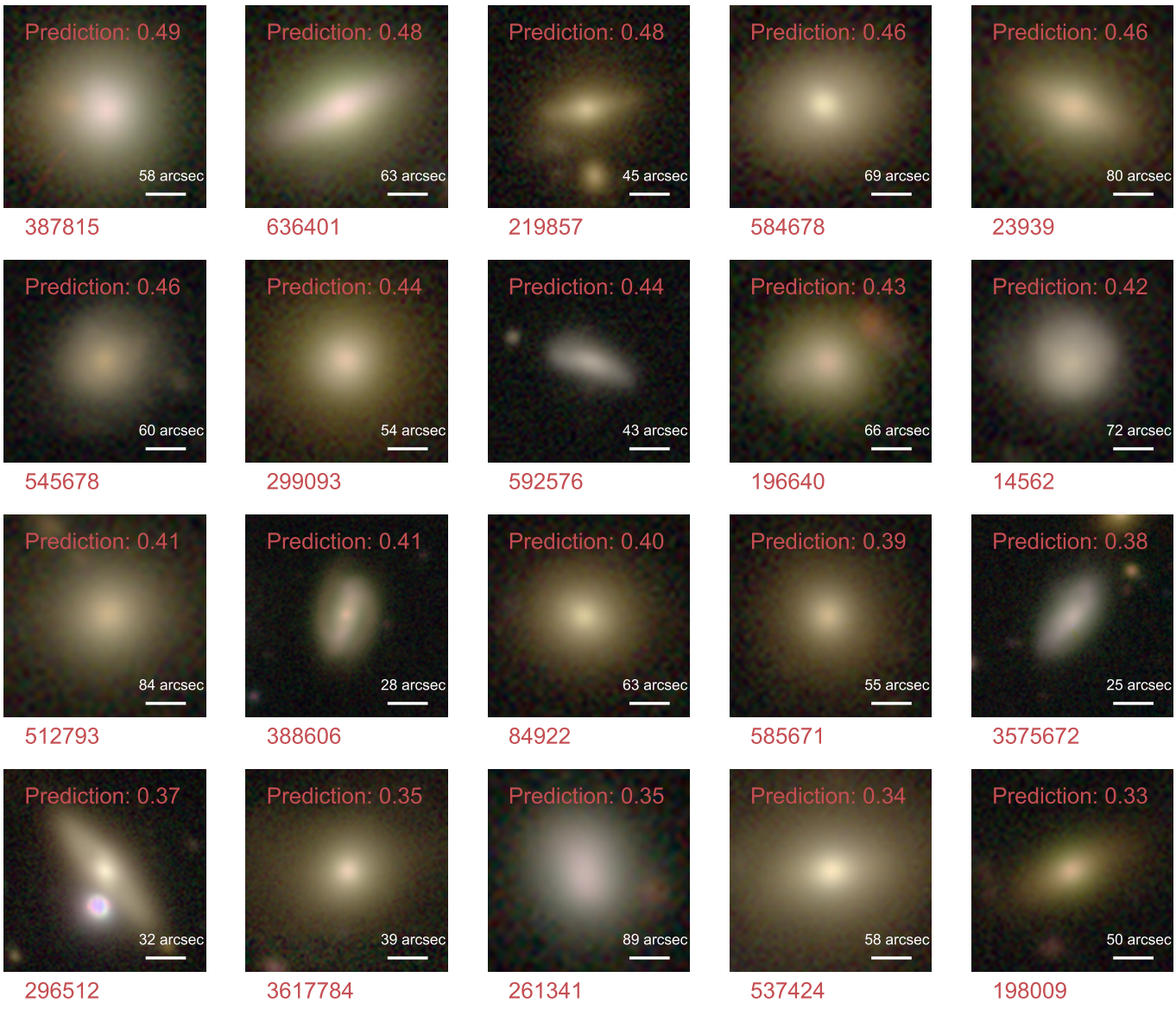

Fig. 3.12: Same as Fig. 3.11 but for merger probability > 0.3 and < 0.5.

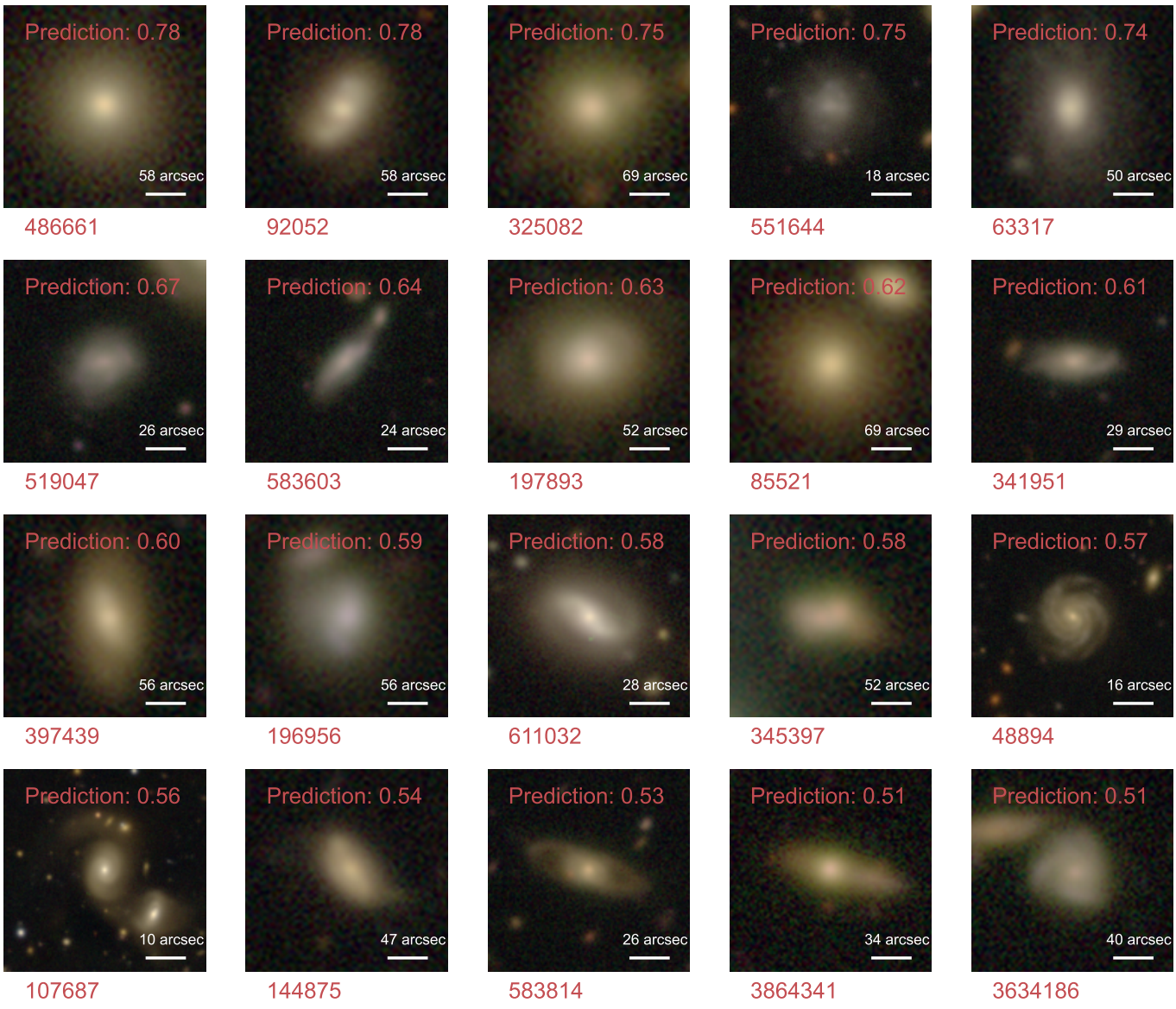

Fig. 3.13: Same as Fig. 3.11 but for merger probability > 0.5 and < 0.8.

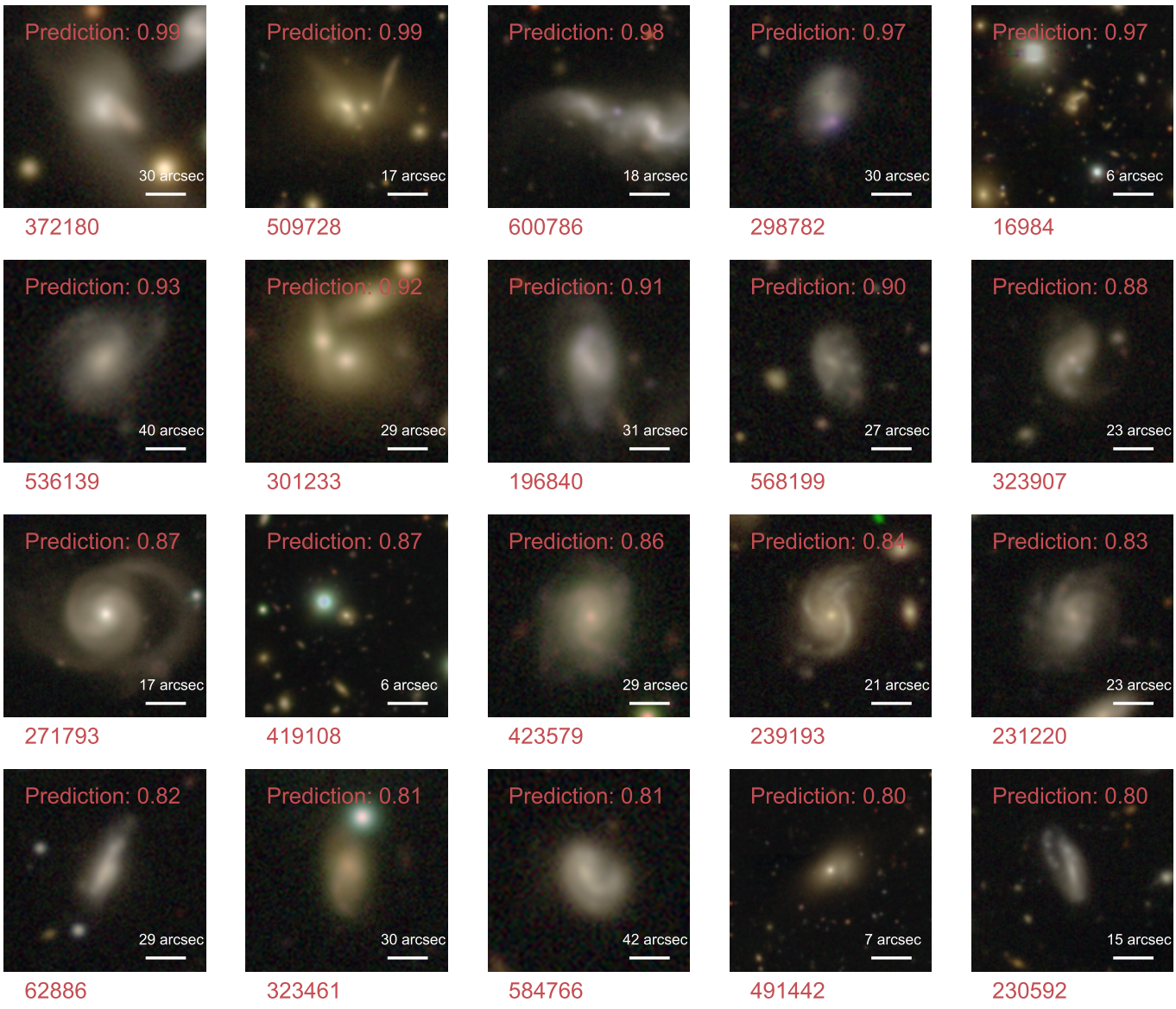

Fig. 3.14: Same as Fig. 3.11 but for merger probability > 0.8.

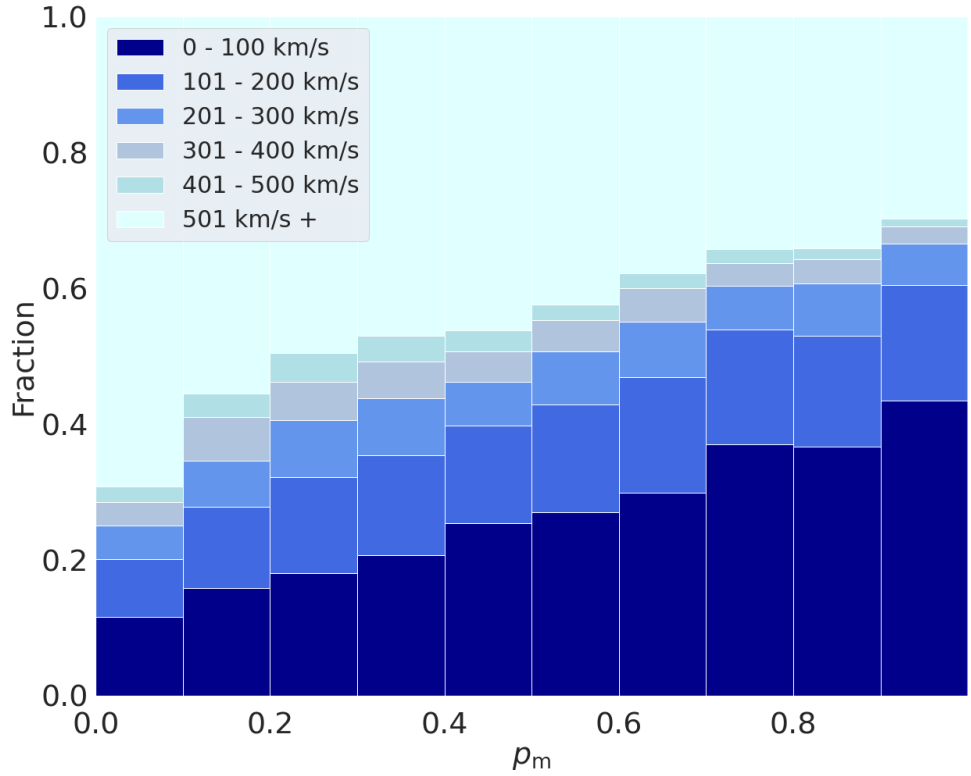

Fig. 3.15: Merger probability distributions for galaxies with a spectroscopically identified pair within a 30 kpc radius aperture, binned by velocity difference of the pair. The vertical axis represents the fraction of galaxies in each merger probability bin belonging to each velocity difference bin. We find that the fraction of smaller velocity difference galaxy pairs increases monotonically with merger probability bin.

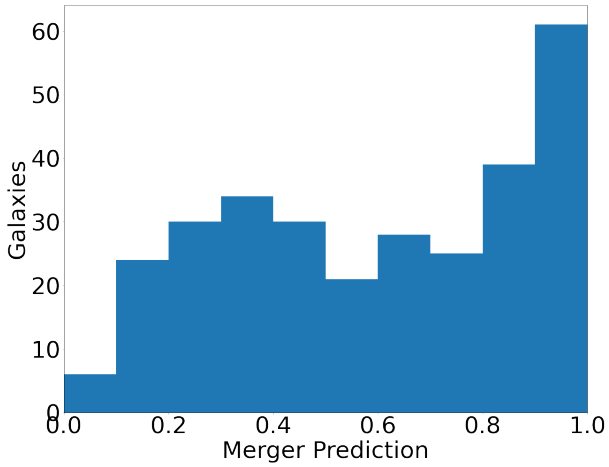

Fig. 3.16: Merger probability distributions of the SDSS-MaNGA mergers used in the investigation in Chapter 2 predicted using our fine-tuned mode. We find that the peak of the distribution is confident (merger probability > 0.8), consisting of 100 of 298 galaxies. 174 of 298 galaxies have a merger probability > 0.5.

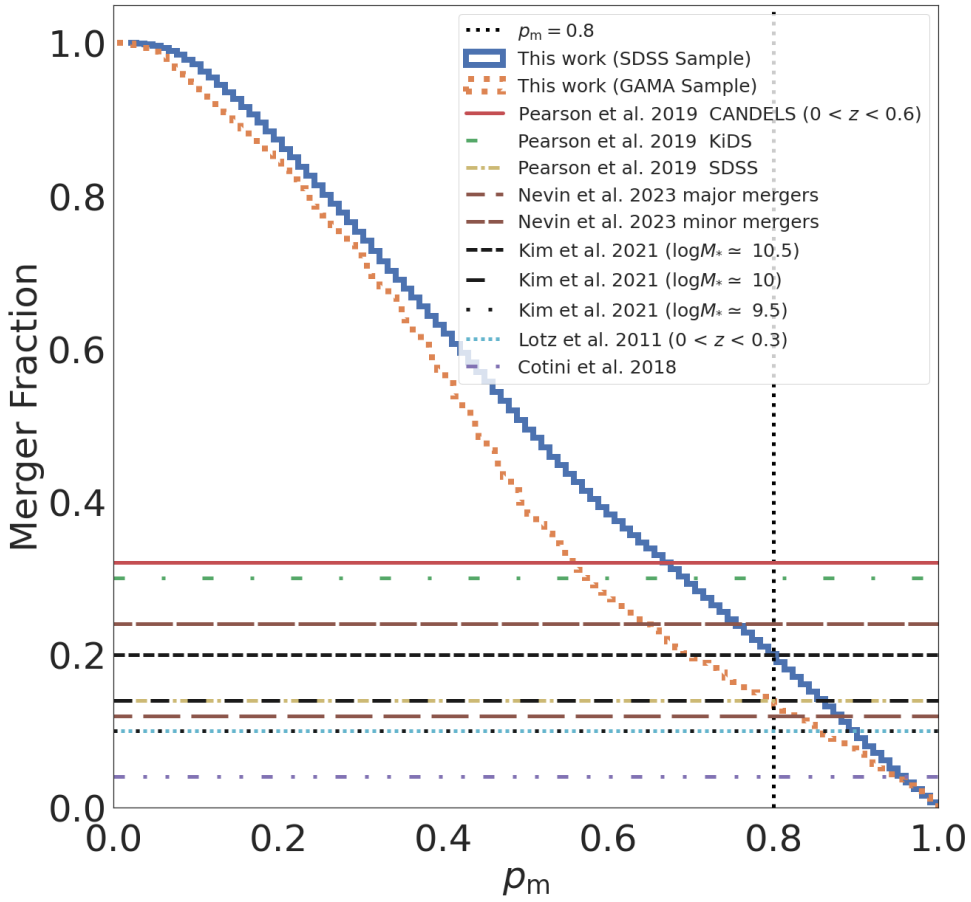

Fig. 3.17: Merger fraction as a function of merger probability for our two samples. The black vertical dotted line indicates the "confident" merger probability threshold of 0.8. We also plot the merger fractions found in Pearson et al. (2019, red, green, and yellow lines), Nevin et al. (2023, brown lines), Kim et al. (2021, black lines), Lotz et al. (2011, light blue dotted line), and Cotini et al. (2013, purple line). We find that our merger fraction matches those of previous studies at increased merger probabilities.

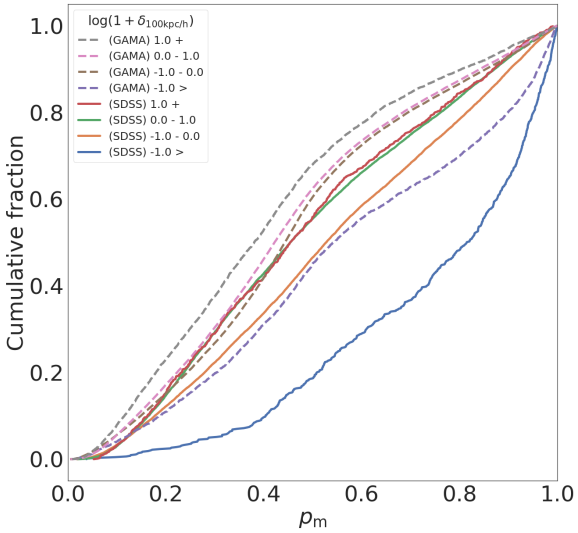
log(1 + $\delta_{100kpc/h}$)
(GAMA) 1.0 +
(GAMA) 0.0 - 1.0
(GAMA) -1.0 - 0.0
(GAMA) -1.0 >
(SDSS) 1.0 +
(SDSS) 0.0 - 1.0
(SDSS) -1.0 - 0.0
(SDSS) -1.0 >
Cumulative fraction
p_m

(a)

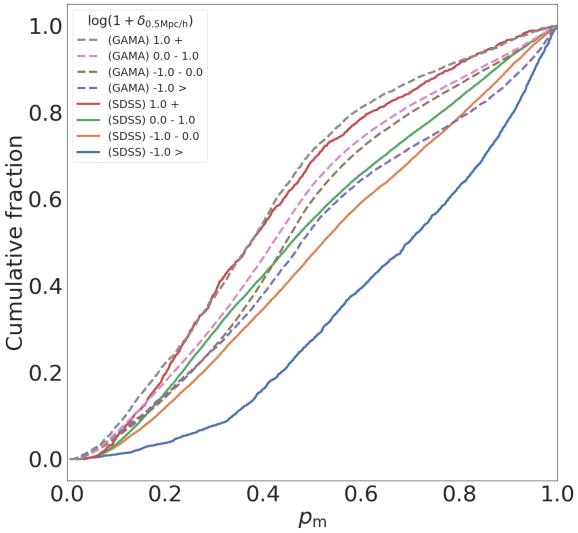
log(1 + $\delta_{0.5Mpc/h}$)
(GAMA) 1.0 +
(GAMA) 0.0 - 1.0
(GAMA) -1.0 - 0.0
(GAMA) -1.0 >
(SDSS) 1.0 +
(SDSS) 0.0 - 1.0
(SDSS) -1.0 - 0.0
(SDSS) -1.0 >
Cumulative fraction
p_m

(b)

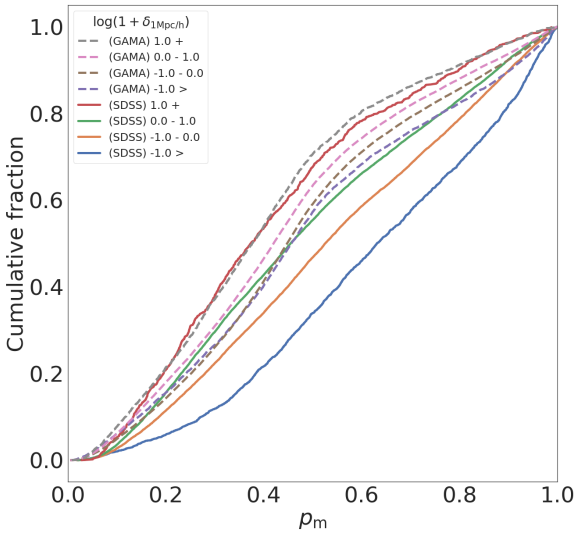
log(1 + $\delta_{1Mpc/h}$)
(GAMA) 1.0 +
(GAMA) 0.0 - 1.0
(GAMA) -1.0 - 0.0
(GAMA) -1.0 >
(SDSS) 1.0 +
(SDSS) 0.0 - 1.0
(SDSS) -1.0 - 0.0
(SDSS) -1.0 >
Cumulative fraction
p_m

(c)

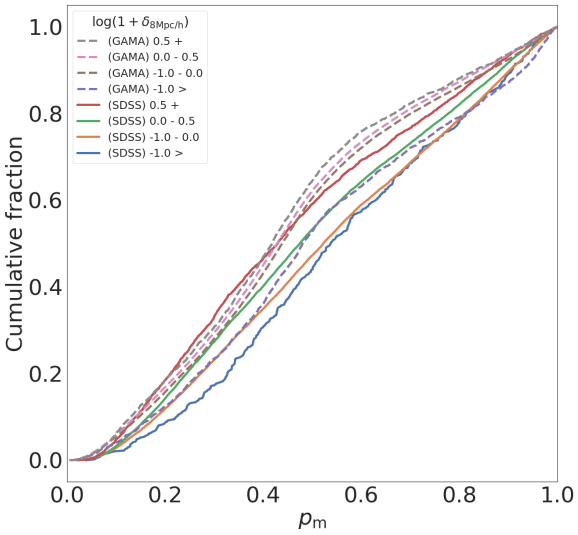
log(1 + $\delta_{8Mpc/h}$)
(GAMA) 0.5 +
(GAMA) 0.0 - 0.5
(GAMA) -1.0 - 0.0
(GAMA) -1.0 >
(SDSS) 0.5 +
(SDSS) 0.0 - 0.5
(SDSS) -1.0 - 0.0
(SDSS) -1.0 >
Cumulative fraction
p_m

(d)

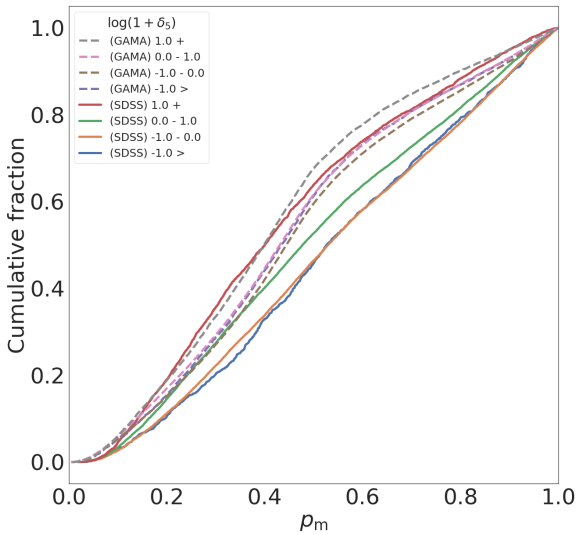
log(1 + δ_5)
(GAMA) 1.0 +
(GAMA) 0.0 - 1.0
(GAMA) -1.0 - 0.0
(GAMA) -1.0 >
(SDSS) 1.0 +
(SDSS) 0.0 - 1.0
(SDSS) -1.0 - 0.0
(SDSS) -1.0 >
Cumulative fraction
p_m

(e)

Fig. 3.19: Cumulative distribution curves of merger probabilities of HSC galaxies cross-matched with GAMA (dotted lines) and SDSS (solid lines) predicted by our fine-tuned model, for environmental densities at differing apertures. Each curve represents a different environmental density bin. The gradients of these curves show that in lower density environments, there are more higher merger probability galaxies, and in higher density environments, there are more galaxies with lower merger probabilities. This trend holds true for each parameter investigated. The trend also holds qualitatively between the SDSS and GAMA samples. The environmental parameters are as follows, and we also indicate the KS test statistic between the densest and least dense regions in each figure as reference. *Upper left panel* **a)** : $0.1h^{-1}$ Mpc stellar mass overdensity $\log(1 + \delta_{0.1\mathrm{Mpc}/h})$, KS test (SDSS) statistic: 0.394, KS test (GAMA) statistic: 0.238. *Upper right panel* **b)** : $0.5h^{-1}$ Mpc stellar mass overdensity $\log(1 + \delta_{0.5\mathrm{Mpc}/h})$, KS test (SDSS) statistic: 0.417, KS test (GAMA) statistic: 0.184. *Middle left panel* **c)** : $1h^{-1}$ Mpc stellar mass overdensity $\log(1 + \delta_{1\mathrm{Mpc}/h})$, KS test (SDSS) statistic: 0.341, KS test (GAMA) statistic: 0.143. *Middle right panel* **d)** : $8h^{-1}$ Mpc stellar mass overdensity $\log(1 + \delta_{8\mathrm{Mpc}/h})$, KS test (SDSS) statistic: 0.183, KS test (GAMA) statistic: 0.127. *Bottom panel* **e)** : Fifth nearest neighbor mass overdensity, KS test (SDSS) statistic: 0.191,
KS test (GAMA) statistic: 0.069.

Figure 3.19 shows the cumulative distributions of merger probability in bins of various environment metrics described in Section 3.4. The distributions are split into separate density bins, depending on the scale of the parameter used.

The upper left panel of Fig. 3.19 shows the sensitivity of merger probability to environmental mass overdensities at 0.1 h^{-1}Mpc scales (0.2 h^{-1}Mpc aperture, centered on the target galaxy). The upper right panel shows the same at 0.5 h^{-1}Mpc scales (1 h^{-1}Mpc aperture). The middle left panel shows the same at 1 h^{-1}Mpc scales (2 h^{-1}Mpc aperture). The middle right panel shows the same at 8 h^{-1}Mpc scales (16 h^{-1}Mpc aperture). The bottom panel shows the sensitivity of merger probability to environmental mass overdensities within the radii of the target galaxy's fifth nearest neighbor. From blue to red, the curves show the cumulative distributions of merger probability in increasingly mass-overdense environments.

We find a clear difference in the distribution curves and histograms between the most mass-underdense ($\log(1 + \delta_x) < -1.0$) and most mass-overdense ($\log(1 + \delta_x) > 1.0$) environments, with a similar trend holding across all five environmental parameters investigated. In each panel, we find that the most mass-underdense environments contain the largest number of galaxies with high merger probability, as seen by the blue curve in each panel. This is the most pronounced in the blue curves in the upper left (0.5 h^{-1}Mpc) and upper right (1 h^{-1}Mpc) panels, but still qualitatively hold true in the bottom two panels (8 h^{-1}Mpc and fifth nearest neighbor scale).

Conversely, we find that the most mass-overdense environments contain the largest number of galaxies with low merger probability, as seen by the red curves.

In mass-overdense environments ($\log(1+\delta_x) > 0.0$), we find that galaxies with a lower merger probability tend to be in this environment, as seen by the red and green curves. For lower density environments ($\log(1+\delta_x) < 0.0$), we find that the opposite holds true, that higher-merger-probability galaxies tend to be in mass-underdense environments, shown by the blue and orange curves. We also find that these trends, in general, qualitatively hold true regardless of stellar mass of the target galaxy, as shown in Fig. 3.20 to 3.24. In most figures, the most mass-overdense regions have more galaxies with low merger probability, and high-merger-probability galaxies are more likely to lie in mass-underdense regions. We note that the terms mass-overdense and -underdense do not necessarily refer to group members and non-group members, and we find no differences when investigating these qualitative trends separately for group and non-group members. Further, as the stellar mass overdensities have a strong correlation with halo mass (Yesuf, 2022), these trends also appear at differing halo mass scales.

These results are consistent with the findings of works such as Ghigna et al. (1998), Lin et al. (2010) and Alonso et al. (2012). These works, with environments computed at similar scales, suggest that mergers and merging pairs are more likely to happen in less dense environments. In addition, spectroscopic pair matching methods with strict spectroscopic cuts are more likely to produce results similar to our findings (Ellison et al., 2010).

However, we also note that these results contradict with the suggestion that galaxy interactions are associated with intermediate to higher density regions, where galaxies have close companions and neighbors (Darg et al., 2010a; Jian et al., 2012). For example, Darg et al. (2010a) found that at the $\log(1+\delta_{2h^{-1}\mathrm{Mpc}})$ scale, even though both mergers and non-mergers peak in an intermediate environment, mergers occupy a slightly denser environment, which differs from our findings. We discuss possible reasons in Section 3.7.

3.6.2 Comparison with simulation data

Figures 3.25 through 3.31 show the cumulative histograms of environmental distributions of a total of 244,722 TNG50 and TNG100 mergers and non-mergers between snapshots 59 and

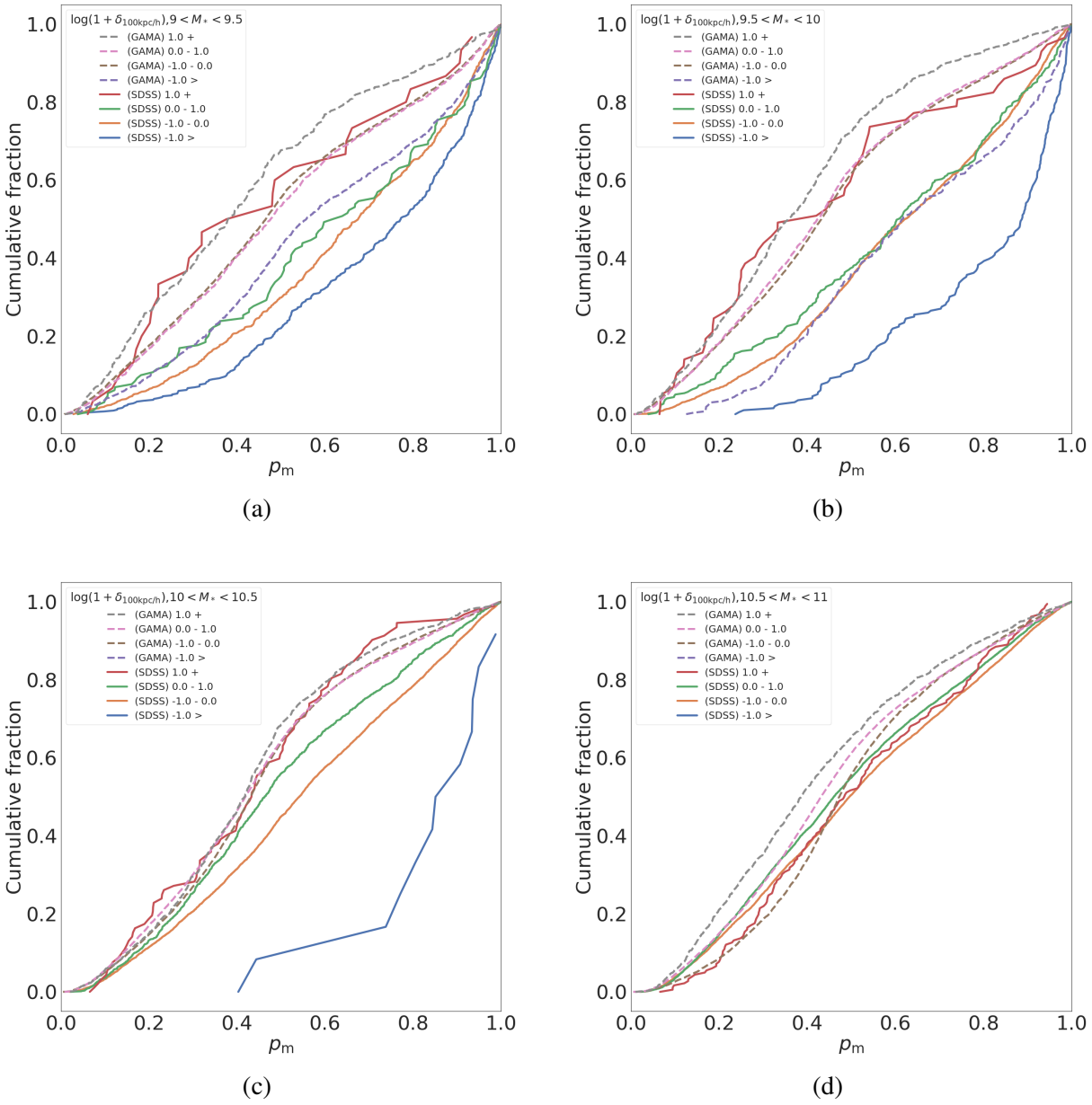

Fig. 3.20: Cumulative distribution curves of merger probabilities of HSC galaxies cross-matched with GAMA (dotted lines) and SDSS (solid lines) predicted by our fine-tuned model, similar to Fig. 3.19, but separated into different mass bins. The KS test statistic between the most underdense and most overdense environments are also indicated for each subplot, with p-values available if ¿ 0.05. Calculated for a 100 kpc radius aperture, in the following mass bins. $9 < \log(M_*) < 9.5$ (*upper left panel*): KS test (SDSS) statistic: 0.432, KS test (GAMA) statistic: 0.263. $9.5 < \log(M_*) < 10$ (*upper right panel*): KS test (SDSS) statistic: 0.601, KS test (GAMA) statistic: 0.378. $10 < \log(M_*) < 10.5$ (*lower left panel*: KS test (SDSS) statistic: 0.757, KS test (GAMA) statistic: 0.053. $10.5 < \log(M_*) < 11$ (*lower right panel*): KS test (SDSS) statistic: 0.064 p-value: 0.430, KS test (GAMA) statistic: 0.192.

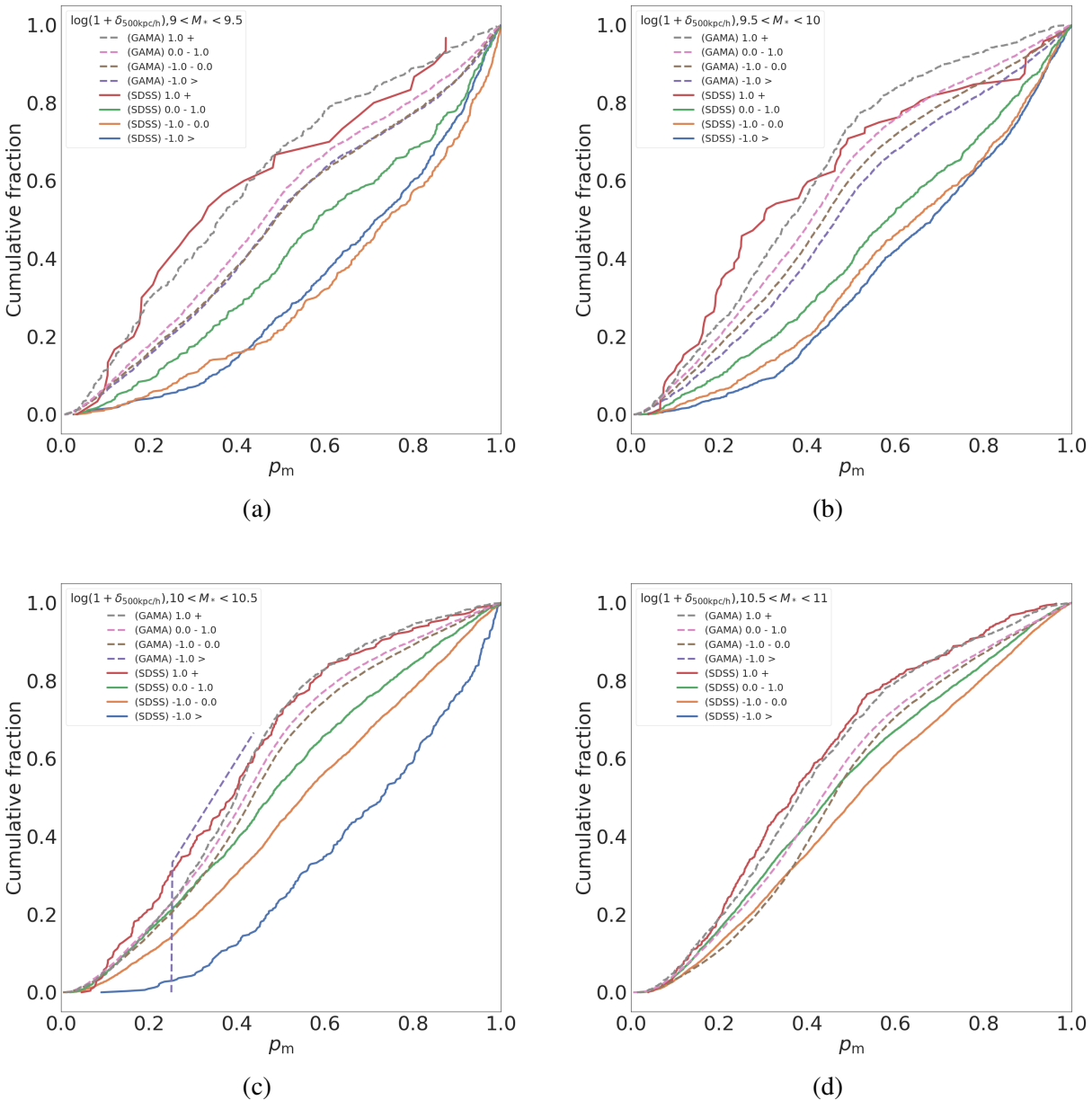

Fig. 3.21: Same as Fig. 3.20 but for a 500 kpc radius aperture. $9 < \log(M_*) < 9.5$ (*upper left panel*): KS test (SDSS) statistic: 0.483, KS test (GAMA) statistic: 0.190. $9.5 < \log(M_*) < 10$ (*upper right panel*): KS test (SDSS) statistic: 0.455, KS test (GAMA) statistic: 0.193. $10 < \log(M_*) < 10.5$ (*lower left panel*): KS test (SDSS) statistic: 0.492, KS test (GAMA) statistic: 0.434, p-value: 0.503. $10.5 < \log(M_*) < 11$ (*lower right panel*) KS test (SDSS) statistic: 0.233, KS test (GAMA) statistic: 0.159.

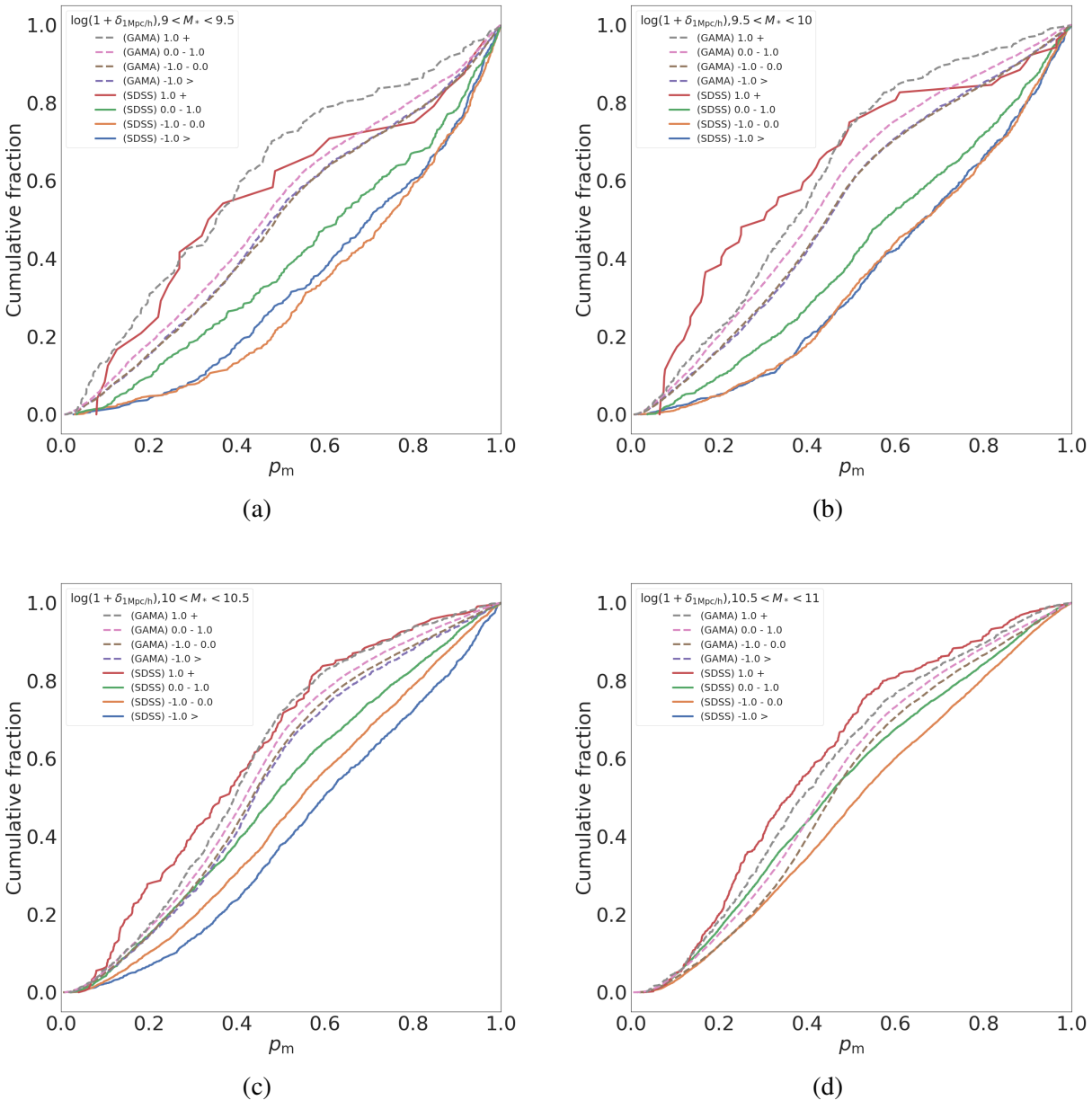

Fig. 3.22: Same as Fig. 3.20 but for a 1 Mpc radius aperture. $9 < \log(M_*) < 9.5$ (*upper left panel*): KS test (SDSS) statistic: 0.436, KS test (GAMA) statistic: 0.211. $9.5 < \log(M_*) < 10$ (*upper right panel*): KS test (SDSS) statistic: 0.473, KS test (GAMA) statistic: 0.156. $10 < \log(M_*) < 10.5$ (*lower left panel*): KS test (SDSS) statistic: 0.352, KS test (GAMA) statistic: 0.113. $10.5 < \log(M_*) < 11$ (*lower right panel*): KS test (SDSS) statistic: 0.241, KS test (GAMA) statistic: 0.137.

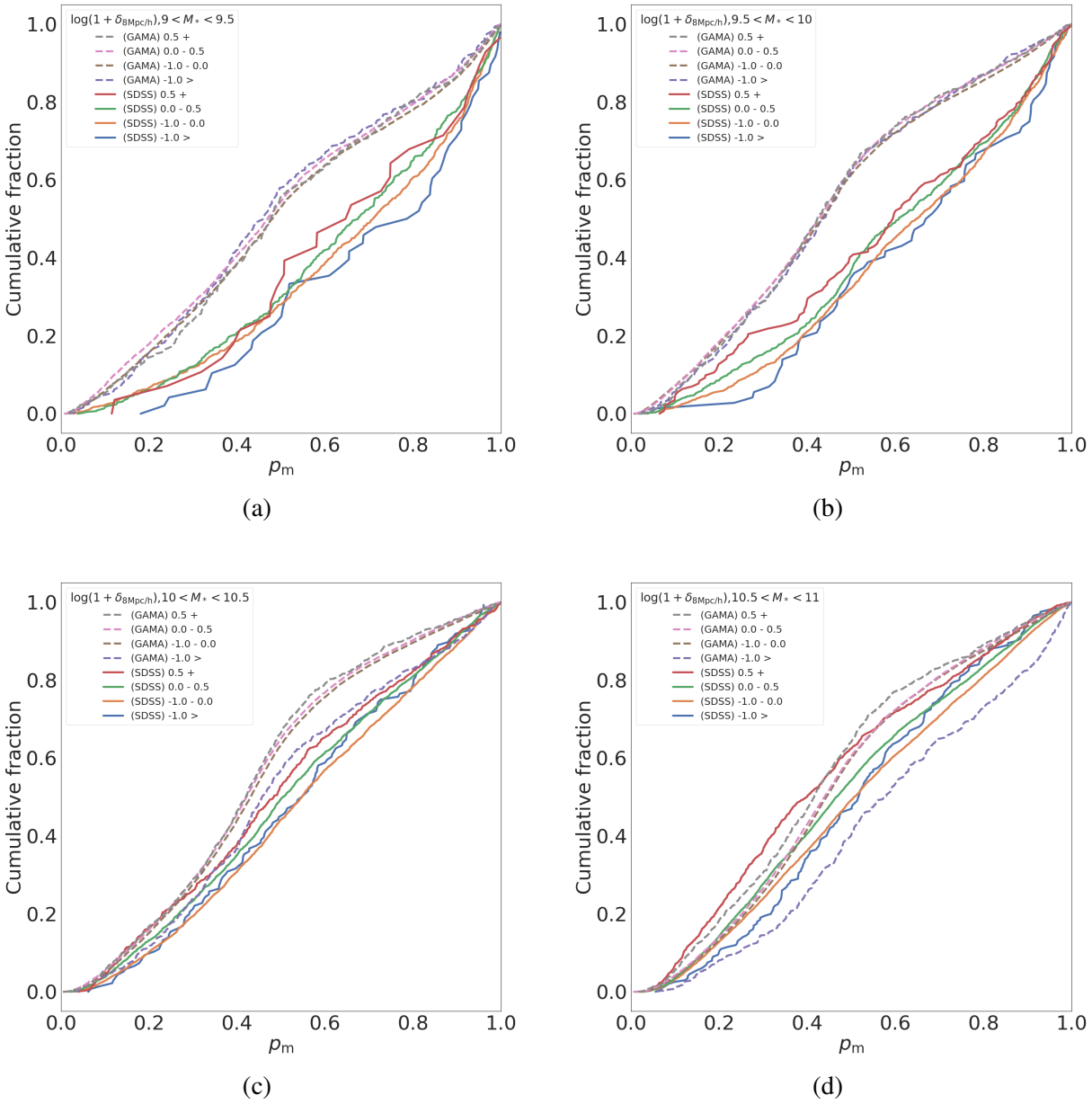

Fig. 3.23: Same as Fig. 3.20 but for a 8 Mpc radius aperture. $9 < \log(M_*) < 9.5$ (*upper left panel*): KS test (SDSS) statistic: 0.193, p-value: 0.459, KS test (GAMA) statistic: 0.053, p-value: 0.767. $9.5 < \log(M_*) < 10$ (*upper right panel*): KS test (SDSS) statistic: 0.170, p-value: 0.111, KS test (GAMA) statistic: 0.036, p-value: 0.822. $10 < \log(M_*) < 10.5$ (*lower left panel*): KS test (SDSS) statistic: 0.107, p-value: 0.143, KS test (GAMA) statistic: 0.125, p-value: 7.059×10^{-7}. $10.5 < \log(M_*) < 11$ (*lower right panel*): KS test (SDSS) statistic: 0.200, KS test (GAMA) statistic: 0.255.

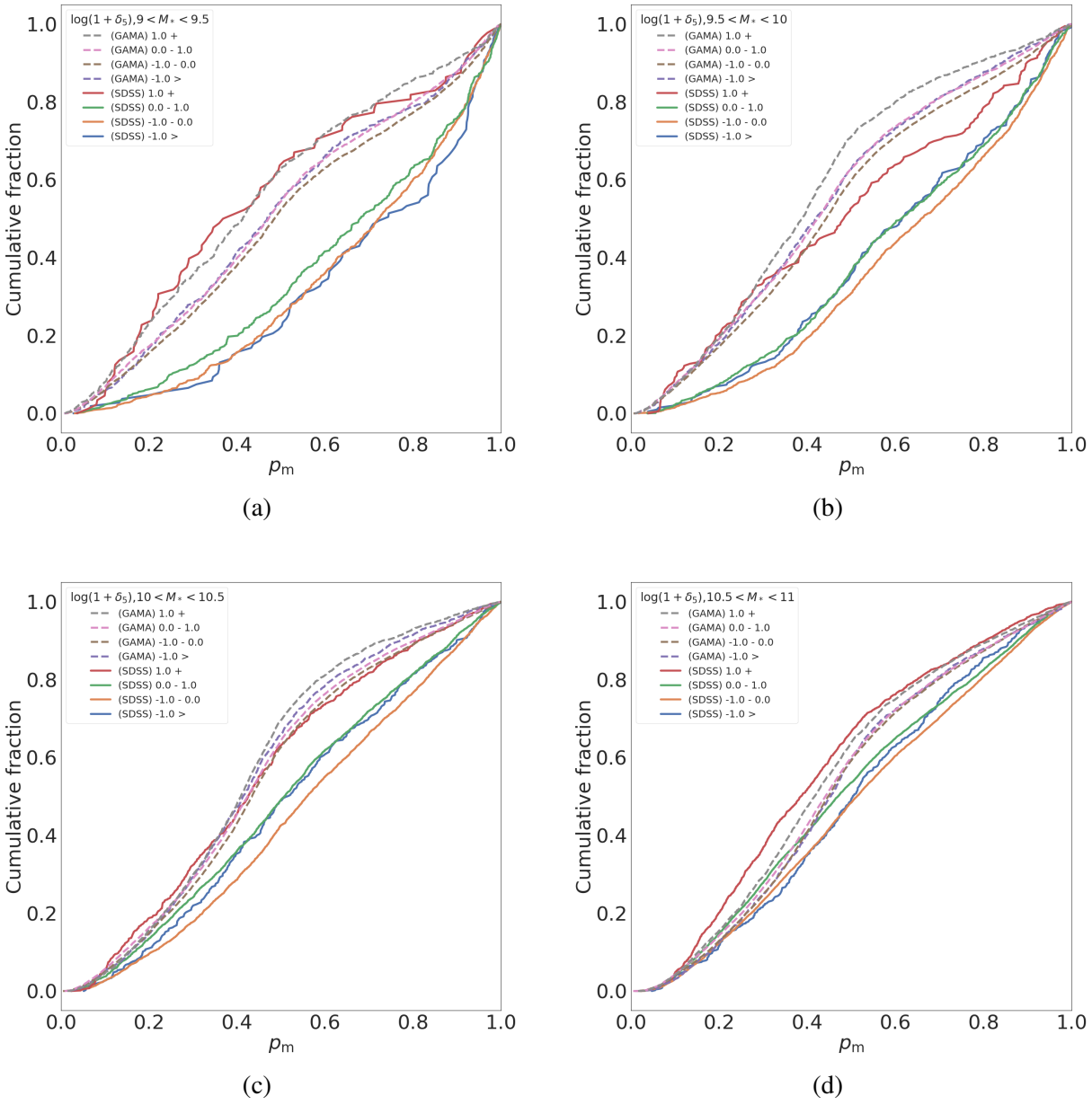

Fig. 3.24: Same as Fig. 3.20 but for an aperture of radius up to the fifth nearest neighbor. $9 < \log(M_*) < 9.5$ (*upper left panel*): KS test (SDSS) statistic: 0.423, KS test (GAMA) statistic: 0.094. $9.5 < \log(M_*) < 10$ (*upper right panel*): KS test (SDSS) statistic: 0.220, KS test (GAMA) statistic: 0.091. $10 < \log(M_*) < 10.5$ (*lower left panel*): KS test (SDSS) statistic: 0.152, KS test (GAMA) statistic: 0.037, p-value: 0.045. $10.5 < \log(M_*) < 11$ (*lower right panel*): KS test (SDSS) statistic: 0.190, KS test (GAMA) statistic: 0.075.

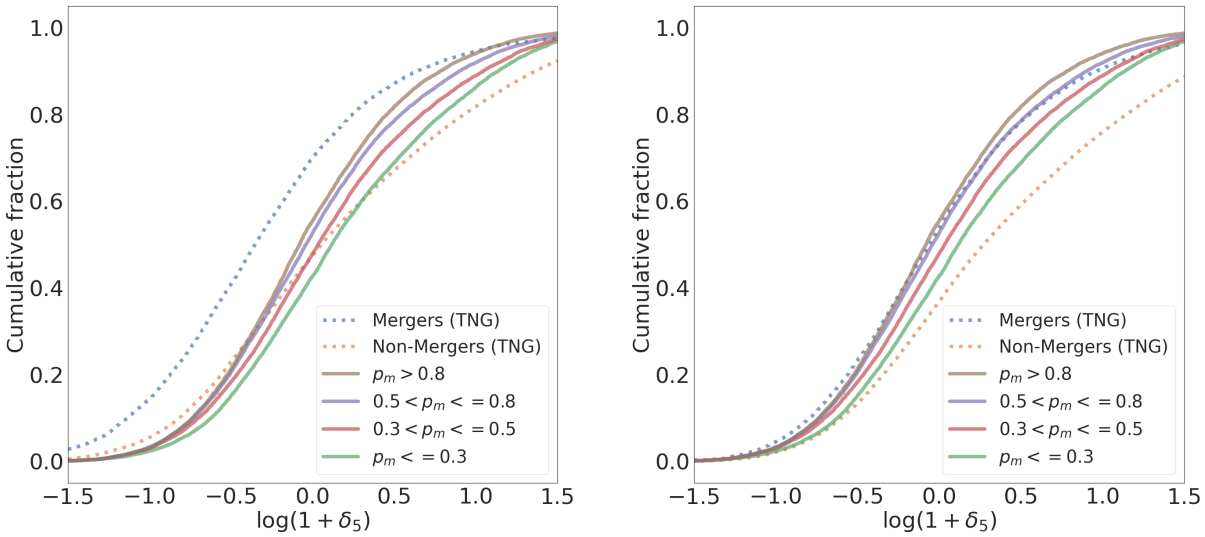

(a) (b)

Fig. 3.25: Environment distribution cumulative histograms of the environmental densities within a spherical volume including the fifth nearest neighbor to the target galaxy, for TNG50 and TNG100 mergers and non-mergers. From left to right: a) environmental mass densities taking into account companions with mass ratio >1:4 (major companions), and b) environmental mass densities taking into account companions with mass ratio >1:10 (major and minor companions). We also make the histograms for the observational data visible as reference where available, indicated by the dotted lines. KS test statistics between simulation mergers and non-mergers, as well as between confident mergers (merger probability >0.8) and non-mergers (merger probability <0.3) are indicated. Major companions (*left panel*): KS test (Simulation) statistic: 0.226, KS test (Observation) statistic: 0.131. Major and minor companions (*right panel*): KS test (Simulation) statistic: 0.194, KS test (Observation) statistic: 0.131.

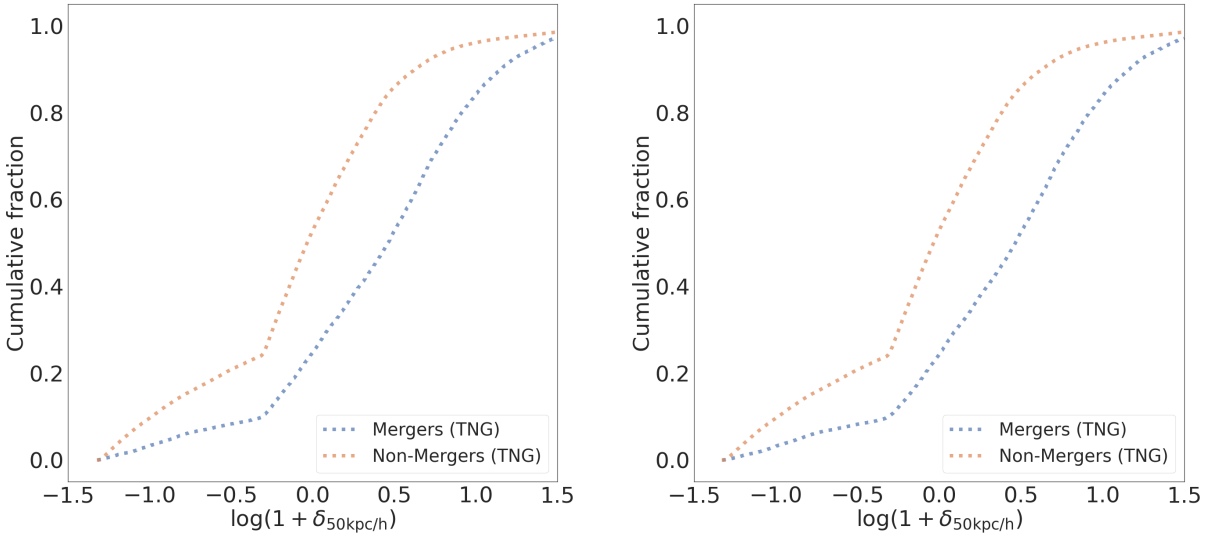

(a) (b)

Fig. 3.26: Same as Fig. 3.25, but for stellar mass overdensities within a 50 kpc radii spherical volume. Major companions (*left panel*): KS test (Simulation) statistic: 0.348. Major and minor companions (*right panel*): KS test (Simulation) statistic: 0.353.

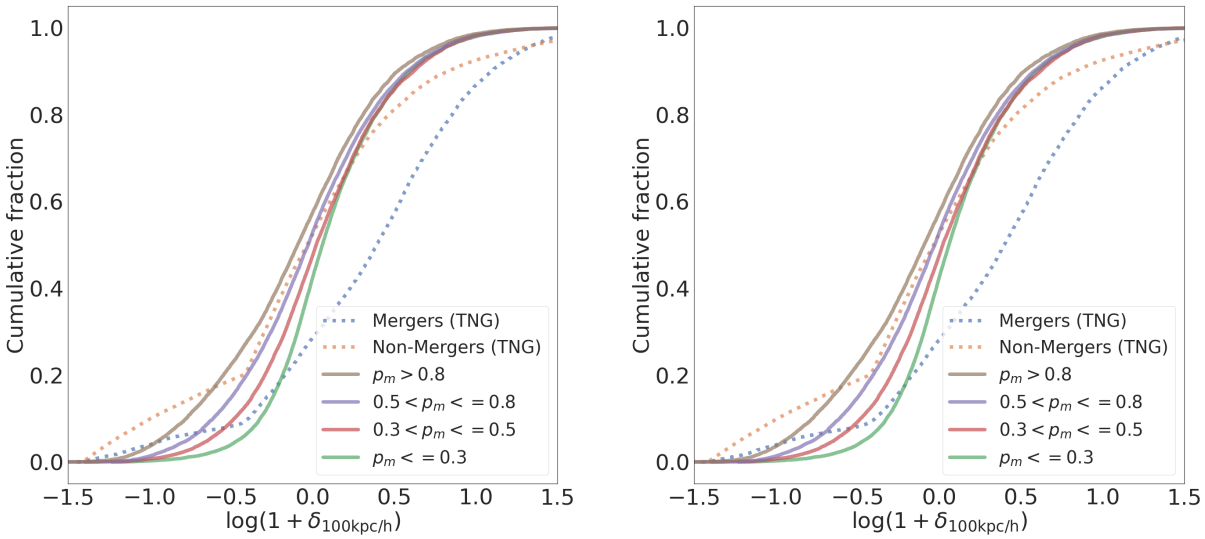

(a) (b)

Fig. 3.27: Same as Fig. 3.25, but for stellar mass overdensities within a 100 kpc radii spherical volume. Observational data are available for this parameter. Major companions (*left panel*): KS test (Simulation) statistic: 0.285, KS test (Observation) statistic: 0.231. Major and minor companions (*right panel*): KS test (Simulation) statistic: 0.260, KS test (Observation) statistic: 0.231.

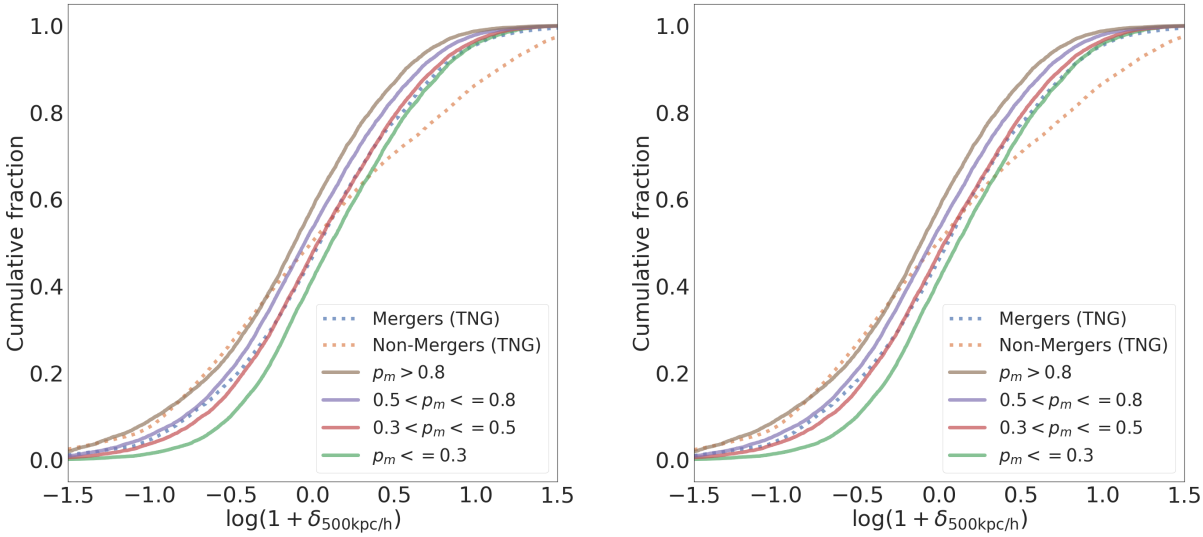

(a) (b)

Fig. 3.28: Same as Fig. 3.25, but for stellar mass overdensities within a 500 kpc radii spherical volume. Observational data are available for this parameter. Major companions (*left panel*): KS test (Simulation) statistic: 0.108, KS test (Observation) statistic: 0.171. Major and minor companions (*right panel*): KS test (Simulation) statistic: 0.100, KS test (Observation) statistic: 0.171.

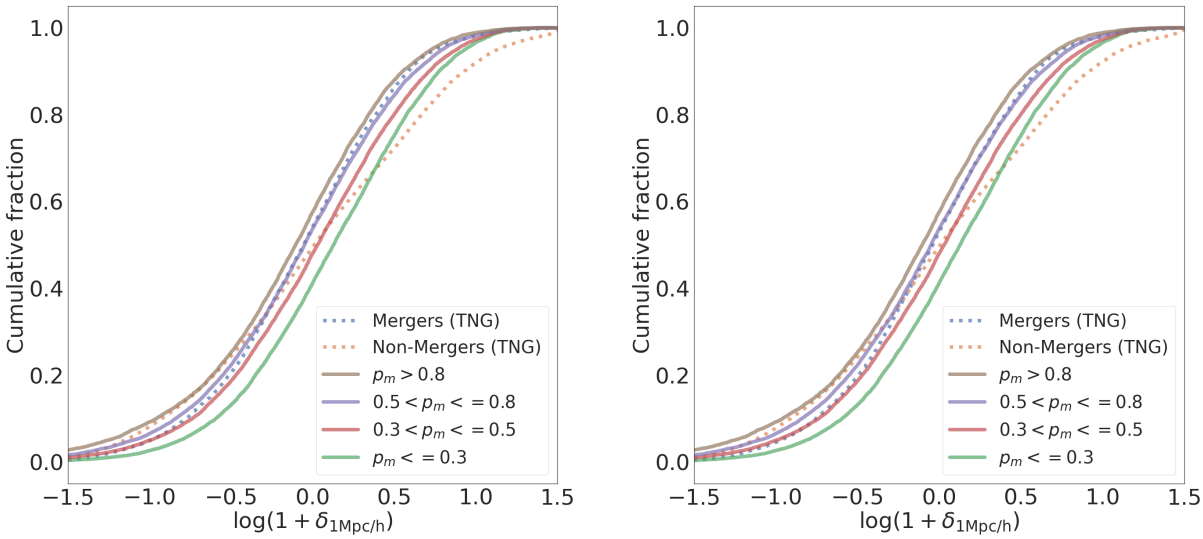

(a) (b)

Fig. 3.29: Same as Fig. 3.25, but for stellar mass overdensities within a 1 Mpc radii spherical volume. Observational data are available for this parameter. Major companions (*left panel*): KS test (Simulation) statistic: 0.140, KS test (Observation) statistic: 0.168. Major and minor companions (*right panel*): KS test (Simulation) statistic: 0.129, KS test (Observation) statistic: 0.168.

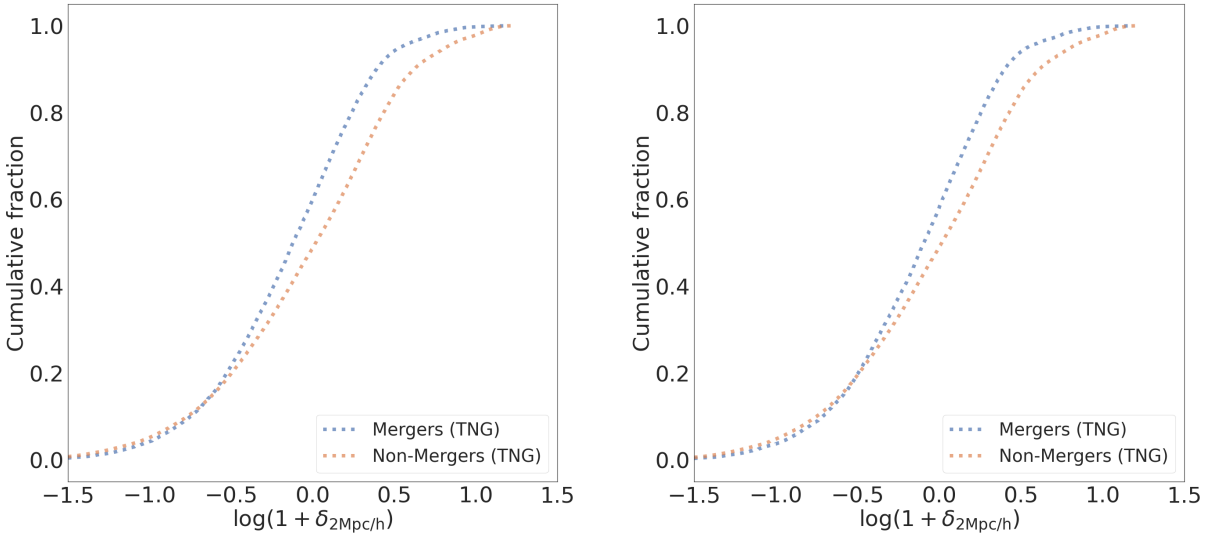

(a) (b)

Fig. 3.30: Same as Fig. 3.25, but for stellar mass overdensities within a 2 Mpc radii spherical volume. Major companions (*left panel*): KS test (Simulation) statistic: 0.147. Major and minor companions (*right panel*): KS test (Simulation) statistic: 0.131.

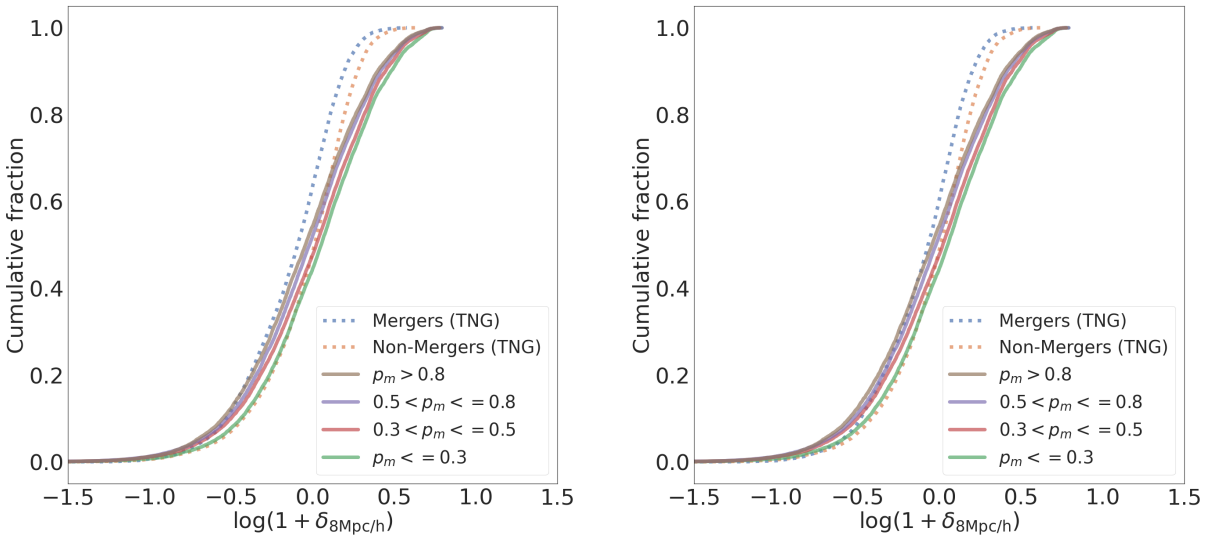

(a) (b)

Fig. 3.31: Same as Fig. 3.25, but for stellar mass overdensities within a 8 Mpc radii spherical volume. Observational data are available for this parameter. Major companions (*left panel*): KS test (Simulation) statistic: 0.153,KS test (Observation) statistic: 0.102. Major and minor companions (*right panel*): KS test (Simulation) statistic: 0.123, KS test (Observation) statistic: 0.102.

99 (redshifts $0.7 > z > 0.1$), grouped by redshift, further split into two subfigures, with the left figure accounting for companions with mass ratio >1:4 (major companions) and the right figure accounting for companions with mass ratio >1:10 (major and minor companions), for each parameter. The mergers and non-mergers were selected using the same timescale criteria used in creating the fine-tuning data-set for Zoobot, for a total of 17,877 mergers and 226,895 non-mergers. The environmental parameters used – the stellar mass overdensities within a spherical volume with radii of 0.05, 0.1, 0.5, 1, 2, and 8 h^{-1}Mpc as well as within the radii of the fifth nearest neighbor – are similar to the observations and were calculated through computations similar to those used for the environmental parameters of the observations in Section 3.4. We also make the environmental distributions from the SDSS observations visible where the data are available: the density within the 0.1 h^{-1}Mpc, 0.5 h^{-1}Mpc, 1 h^{-1}Mpc, 8 h^{-1}Mpc radii spherical volume, and the radii of the fifth nearest neighbor. We split the observational data in four different merger probability bins, with p_m <0.3, 0.3<p_m<0.5, 0.5<p_m<0.8, and 0.8<p_m.

We find two differing trends in the simulational data, depending on the scale of the environmental density parameter. For the environmental density parameters of the scale of 0.5 h^{-1}Mpc and larger, and for fifth nearest neighbor environments, a greater fraction of mergers lie in mass-underdense environments, and a greater fraction of non-mergers lie in mass-overdense environments, indicating a similar trend as that seen with the predictions from observational data, as the fraction of mergers in lower density environments increases with increasing merger probability bin. We also find that there are very little to no mergers found in the densest environments for each of these parameters. We also find that these trends are, in general, not sensitive to mass ratio, and hold true for all investigated redshift bins up to $z = 0.7$. As such, we have a consistency in the relationship between galaxy mergers and environmental densities between observations and simulations at equivalent scales.

Conversely, we find that the above trend is reversed for the environmental density parameters within the spherical volume of 0.05 and 0.1 h^{-1}Mpc, found in Fig. 3.26 and Fig. 3.27, respectively. That is, at these scales, we find that the majority of non-mergers are in the lowest density environments, as shown by the brown, red, and orange lines, and mergers are found in denser environments, as shown by the blue, green, and purple lines. These trends are also not sensitive

to mass ratio or redshift. However, this reversal does not occur in the observational data, as shown in Fig. 3.27. While the behavior of the low merger environment curves show a steeper gradient in underdense regions ($0.5 < \log(1 + \delta_x) < 0.0$), the trend is qualitatively similar as the larger scales. Further investigation is required on the inconsistency between the observations and simulations at this scale, particularly as they are consistent at larger scales. We plan to investigate this in future works.

3.7 Discussion

Based on our merger probabilities and subsequent analysis in the previous section, our investigation finds that at the scales of 0.5 h^{-1} Mpc and greater, or close to the cluster scale and larger, merger galaxies are more prevalent in lower density environments, and higher density environments have a lower merger incidence, with this trend found both in observations and simulations. At the 0.1 h^{-1}Mpc and lower scales, or close to the galaxy scale, there are more non-mergers in lower density environments in the simulations; however, this reversal does not occur in our observational data.

Previous studies that have investigated the environmental dependence of merger activity have found varying results, with some works finding a greater merger fraction in higher density environments (Jian et al., 2012), and others finding merger fraction peaks in intermediate environments (Perez et al., 2009), and others finding that mergers are more likely to occur in lower density environments (Ghigna et al., 1998). We have results showing that the merger prevalence can be increased at both mass-overdense and -underdense environments, with the trend differing depending on the scale of the environmental parameter.

In the richest environments, such as in the center of clusters, velocity dispersions are high, at scales of $\sim$ 1000 km s^{-1} (Struble & Rood, 1999). At these speeds, galaxy-galaxy interactions are likely to be elastic encounters, and mergers and infall are less likely to occur (Kuntschner et al., 2002). Such encounters can strip the gas required to fuel star formation events (Gunn & Gott, 1972), and hence be a catalyst for dynamical evolution in cluster galaxies, but the final product of the interaction will likely not be a merger, resulting in lower merger incidence. As such, while

higher density regions can have an increased pair fraction, but a lowered merger fraction (Lin et al., 2010). Conversely, in lower density environments, accretion and merger events can occur more frequently.

At a smaller scale, such as in the galaxy scale, over 90% of non-merger galaxies are found in lower density environments, and higher density environments are mostly populated with mergers. At this scale, galaxies are likely to be at closer projected separation with its neighbors compared to at greater scales, and hence be part of a merger. As a result, higher densities at this scale means there is a greater likelihood of a neighbor being a physically connected merger, resulting in the reversal of the trend from the larger scales.

We suggest a possible reason for any disagreements with previous works, particularly in higher density environments, to be attributed to the difference in merger sample selection techniques. For example, Darg et al. (2010a), a work based on visual identification of mergers, finds that while both mergers and non-mergers peak in intermediate density environments, mergers occupy slightly denser environments than non-mergers. However, Ellison et al. (2010), a work using spectroscopic pair selection, finds that a significant fraction of galaxy pairs are in higher density environments, but they also suggest that lower density environments are where mergers are likely to occur, a suggestion that is consistent with our results.

Different merger sample selection methods will lead to different merger samples, some with very little overlap (De Propris et al., 2007), and as such, trends in physical properties such as environment may differ. Additionally, some methods may be susceptible to overestimation of merger galaxies and contamination.

Spectroscopic pair matching methods can contaminate merger samples with interlopers. In high velocity dispersion environments, using the line-of-sight velocities as a proxy for three-dimensional velocities has limitations, and is strongly affected by interlopers (Saro et al., 2013), and galaxies may be considered merging pairs even if they are not physically connected. As such, merger catalogs created using these methods can overestimate the merger fraction.

Similarly, image-based classification techniques can also be contaminated with stellar and galactic chance projections, in both visual identification (Darg et al., 2010a,b; Pearson et al., 2019) and quantitative morphologies (De Propris et al., 2007). In visual identification, the lack

of complete information for objects could lead to projected galaxy pairs and galaxy-star pairs to be incorrectly classified as mergers. Such projections and galaxy-star pairs can also pose difficulties when conducting studies with quantitative morphologies such as asymmetries. The source extraction algorithms used may incorrectly deblend galaxy images containing projections, leading to highly asymmetric non-mergers. Contaminations from projections are likely to be more frequent in higher density environments.

Moreover, we note that our environment parameters discriminate by mass-overdense and -underdense regions, with no specification on group or cluster membership. While number-overdense environments, such as groups and clusters, do have evidence of merger activity, particularly at z >1 (Lemaux et al., 2012; Tomczak et al., 2017; Liu et al., 2023), our parameters focus on the masses of these environments. In mass-overdense environments, as our figures do show, there are still galaxies with high merger probabilities to be found. These galaxies are likely dry merger systems occurring in groups or cluster environments, particularly important for the formation of early-type brightest cluster galaxies (BCGs) in cluster centers (Mulchaey et al., 2006; Rines et al., 2007; McIntosh et al., 2008; Tran et al., 2008; Liu et al., 2009; Lin et al., 2010; Burke & Collins, 2013; Lidman et al., 2013; Ascaso et al., 2014). However, at redshift z <1, many BCGs have finished their growth, and while there are BCGs that continue their growth through mergers at these redshifts, such cases are a minority (Collins et al., 2009; Stott et al., 2010, 2011; Liu et al., 2015; Runge & Yan, 2018). Further, in the most mass-overdense environments, at z <1, merger activity is suppressed due to increased velocity dispersions (Pipino et al., 2014), leading to a lower merger fraction in these environments. In mass-underdense environments, such as in field environments, or the outskirts of clusters and groups, the likelihood of finding a merger increases (Ghigna et al., 1998; Oh et al., 2019). This is also found at higher redshifts, both in the field (Delahaye et al., 2017) and in outskirt (Koulouridis & Bartalucci, 2019) regions. As such, the fraction of mergers in mass-underdense regions should be greater than that in mass-overdense regions, which is consistent with our results.

Our environmental trends, particularly the decreased fraction of mergers in higher density environments, show that our morphology-based classification model is likely able to differentiate and give low merger probabilities to images of interlopers, or in other words non-merging pairs

in higher density environments, an issue that needs corrections in both spectroscopy-based and image-based classification methods. We note that our environmental trends on observational data may harbor an implicit bias due to the morphology-density relation (Dressler, 1980). The high velocity encounters in higher density environments can strip gas in galaxies, leading to visual morphologies exhibiting more smoother, spheroidal features. As such, galaxies in higher density environments are less likely to exhibit the tidal features that are present in mergers, resulting in such galaxies to be assigned low merger probabilities by our morphology-based merger identification model. However, we suggest that such a bias can be mitigated. First, the findings in Darg et al. (2010a), based on visual classification, suggest that mergers are more likely found in higher density environments, which contradicts what is found in comsmological n-body and hydrodynamical simulations. As the implicit biases due to the morphology density relation can be overlooked by visual classification studies, we suggest that a similar overlook is possible in our work. Second, the ground truth merger selection in our fine-tuning process is based on the time to the closest merger event, and is not be biased to any environments and morphlogies.

Investigations on the physical properties of the merger galaxies, such as projected separation and relative velocity differences with their neighbors, as well as colors, star formation rates and morphologies, are planned in future works, to determine if there are any environmental dependences on the properties of the mergers themselves in addition to merger incidence.

3.8 Conclusion

In this work, we take a deep learning based approach for merger classification in Subaru HSC-SSP. We fine-tune the pretrained model Zoobot using synthetic HSC images of galaxies in the Illustris TNG simulations, then make predictions using the fine-tuned model on a sample of galaxies in HSC-SSP S21A wide cross-matched with SDSS and GAMA. We find that the fine-tuning approach can achieve accuracies comparable to previous merger classification studies using simulational data, at a 76% accuracy, as well as 80% completion and precision. We achieved these results requiring a far smaller sample size than previous studies, sufficing with

$\sim 10^3$ training samples of each class. We also find that our morphology-based model is able to correctly predict both mergers and non-mergers of diverse appearances, mergers of differing mass ratios and stages, and can also distinguish to a degree between projections and true merging pairs. The merger rate found by our model is consistent with those of previous works if we adopt a "confident" threshold.

We have made the merger catalog we produced in this work publicly available. We plan to classify all of HSC-SSP in the future and make the results publicly available as well.

Further, we studied the relationship between merger activity and multi-scale galaxy environments in both the simulation data of TNG and the observational data of HSC-SSP, and compared our results. We find two trends in the simulation data, and one trend in the observational data. Both sets of data are in agreement that at scales of 0.5 h^{-1}Mpc and larger, merger galaxies favor mass-underdense environments, and non-mergers favor mass-overdense environments. However, below these scales, the simulation data finds that non-merger galaxies are most prevalent in mass-underdense environments, and mass-overdense environments favor mergers. In future works, we plan to investigate in both observations and simulations where the reversal in trend occurs, as well as the galaxy properties of the mergers themselves. For example, we plan to investigate the connection between mergers, environment, and star formation. This investigation will give us insight on whether environment plays a role in the enhancement of star formation rate in interacting galaxy systems. We also will search for further methods to improve the Zoobot fine-tuning model, such as increasing the number of training images, either through inclusion of other TNG simulation synthetic images, such as TNG100, or inclusion of more snapshots. We also will look to compare the performance of our synthetic image-fine-tuned model to that of an observation image-fine-tuned model, where merger labels from the HSC morphology catalogue GALAXY CRUISE (Tanaka et al., 2023) will be used.

Chapter 4

The impact of galaxy mergers on AGN activity

Preliminary version of a paper currently in writing, tentative title "*The connection between mergers and AGN activity in the Subaru HSC-SSP*", by Kiyoaki Christopher Omori, Connor Bottrell, Mike Walmsley, Tsutomu T. Takeuchi, and others, to be submitted to Astronomy & Astrophysics.

The gas inflows associated with galaxy mergers is considered to fuel supermassive blackhole (SMBH) growth and subsequent fueling of AGNs. However, the connection between merger activity and AGN activity is contested, and investigations are required to confirm whether or not merger activity is a dominant pathway for AGN ignition.nIn this work, we compare merger incidences and AGN incidences for galaxies in the Subaru HSC-SSP, with the aim of investigating the connection between merger activity and AGN activity.We identify mergers in the Subaru HSC-SSP through a fine-tuned version of the deep learning representation model Zoobot, pretrained on citizen science votes on Galaxy Zoo DeCALS images. Zoobot was fine-tuned using synthetic HSC-SSP images from the TNG50 simulations, then used to find merger probabilities in observational images of the HSC-SSP. The AGNs are identified through SED fitting. The spectra is passed through SED fitting code PROSPECT, which can decompose between galaxy and AGN flux contribution of the SED. Galaxies with a flux contribution fraction $f_{\mathrm{AGN}} > 0.1$. We find that merger incidence does not significantly increase among AGNs compared to non-AGNs,

meaning that mergers are not necessarily the cause of AGN activity. However, we also find a slight increase in AGN incidence among mergers, indicating that mergers are more likely to be AGN hosts than non-mergers.

4.1 Introduction

Almost all massive galaxies host a central supermassive blackhole (SMBH, Kormendy & Richstone (1995); Kormendy & Ho (2013)). SMBHs can grow through accretion events. When material infalls onto the accretion disk surrounding a SMBH, a large amount of energy is released as radiation observable over a wide range of wavelengths. Galaxies with this bright central emission are called an active galactic nuclei (AGN) host.

One of the avenues that is considered to be associated with such infall and the subsequent ignition of AGNs is the process of galaxy interactions and mergers (Di Matteo et al., 2005; Hopkins et al., 2008b). When multiple galaxies interact and merge, strong gravitational torques will result due to tidally induced stellar bars. The torques will pull gaseous content towards the central regions of galaxies, causing rapid accretion onto SMBHs, and subsequent triggering of AGN activity. The end stage of mergers, when coalescence occurs, is also a site of AGN activity, as there is an additional inflow of gas towards the central regions.

While simulational data has shown that merger activity is an efficient pathway for SMBH growth, the relationship between merger activity and AGN activity is still under debate in observation-based investigations. A number of studies have found that the fraction of AGN hosts is higher among galaxies with merger-like morphologies and close galaxy pairs compared to non-mergers (Ellison et al., 2011; Silverman et al., 2011; Lackner et al., 2014; Satyapal et al., 2014; Weston et al., 2017; Goulding et al., 2018). Similarly, a number of studies have found that AGNs are more likely to reside in merging systems. (Treister et al., 2012; Santini et al., 2012; Kocevski et al., 2015; Ellison et al., 2019). However, a large number of studies have questioned the connection between mergers and AGNs (Grogin et al., 2005; Gabor et al., 2009; Cisternas et al., 2011; Kocevski et al., 2012; Villforth et al., 2014; Mechtley et al., 2016; Gao et al., 2020; Silva et al., 2021). Some works have concluded that only the most luminous AGNs are driven by

merger activity (Urrutia et al., 2008; Treister et al., 2012; Menci et al., 2014; Glikman et al., 2015; Hong et al., 2015; Weigel et al., 2018; McAlpine et al., 2020), but even those conclusions have been contested by other studies (Hewlett et al., 2017; Villforth et al., 2017).

One possible reason for the variety of conflicting results is the identification method, for both mergers and AGN hosts. Mergers can be identified through a variety of methods. Some studies identify mergers based on spectroscopic close pair matching (Ellison et al., 2011; Silverman et al., 2011). Others use image-based classification, such as non-parametric summary statistics based on the galaxy morphologies (Goulding et al., 2018), or pure visual classification (Urrutia et al., 2008; Cisternas et al., 2011; Satyapal et al., 2014). Each of these methods have varying sensitivities to varying stages of mergers. Spectroscopic pair identification is sensitive towards early stage mergers, but fails to recognize post-coalescence or late stage mergers, as such mergers only have single galaxy statistics. The use of summary statistics can identify many early stage and post-coalescence mergers, but may fail in other signatures and are highly sensitive to galaxy physical properties such as gas content (Lotz et al., 2008). With regards to AGN identification, there also exists a wide variety of identification methods. Some studies use emission line diagnostics (BPT diagrams, Baldwin et al. (1981)), others use colour-selection (Donley et al., 2012), X-Ray selection (Marchesi et al., 2016), or radio selection (Marchesi et al., 2016). Each of these methods can identify AGNs at varying stages of its lifetime (Sanders et al., 1988), or with different physical properties, which can lead to widely varying selections (Juneau et al., 2013; Trump et al., 2015) Further, the timescale of AGN and merger activities can lead to difficult results. The timescale of AGN activity is typically about 10^5 years (Schawinski et al., 2015). This is far shorter compared to the observability timescale of merger signatures, which can last from 0.2 to several Gyr (Lotz et al., 2008, 2010b,a). As such, it is likely that in observational studies that a large portion of identified mergers are either before or after the AGN phase of the merger process.

In this work, we identify galaxies from the multi-tiered, wide-field, multi-band imaging survey Hyper Suprime-Cam Subaru Strategic Program (HSC-SSP; Aihara et al. (2018)). Mergers are identified from optical images using a machine-learning based method, in the form of fine-tuning. We fine-tune the pre-trained model Zoobot (Walmsley et al., 2023) using observation-realistic

synthetic galaxy images from the TNG simulations. This method allows for a very time and human-resource efficient identification process over several thousand galaxies. This method is able to diversely identify merger galaxies at varying merger stages and mass ratios. AGNs are identified using SED fitting covering from the NIR to UV. This method can recover a large fraction of AGNs identified using other methods such as emission line diagnostics and X-ray identification. We combine the two methods that diversely identify mergers and AGNs to investigate the relation between merger activity and AGN activity.

This paper is structured as follows. Section 4.2 highlights our sample and criteria for merger and AGN selection. Section 4.3 shows our results, and Section 4.4 discusses them. We conclude our work in Section 4.5.

4.2 Sample Selection

In this work, we use galaxies from the multi-tiered, wide-field, multi-band imaging survey HSC-SSP, which is observed using the Subaru 8.2 m telescope on Manuakea in Hawaii. Further details about the HSC-SSP survey, the instrumentation used, and its various techniques are available in Aihara et al. (2018) and other relevant papers (Bosch et al., 2018; Miyazaki et al., 2018; Komiyama et al., 2018; Furusawa et al., 2018). We use the HSC-SSP due to its wide field of observation and high depth and resolution of its ground-based imaging. In the layer used in this work, the Wide Layer, the HSC-SSP covers about 600 deg^2 of the sky in five broad band filters (*grizy*), with observations from 330 nights coadded, and with a width of $r \approx 26$ mags (5σ, point source). These properties will provide us with high quality imaging data of a high number of galaxies to make merger predictions on.

Observational images from HSC-SSP Wide Public Data Release 3 (Aihara et al., 2022) are used. To ensure spectroscopic redshifts, as the photometric redshifts from the HSC-SSP has errors, the HSC sample is cross-matched with the Galaxy And Mass Assembly Data Release 4 (GAMA DR4, Driver et al., 2022). The galaxies lie in redshift $z = 0.01 - 0.35$, have a stellar mass range within M_* $3 \times 10^9 - 3 \times 10^{11} M_\odot$, and a magnitude range of $r < 19.8$. Stellar masses are obtained using the SED fitting code MAGPHYS (Driver et al., 2018). To select a merger sample and AGN

sample for this work, we refer to the following methods, respectively.

4.2.1 Merger probabilities

We perform merger classification of HSC-SSP galaxies through fine-tuning of the publicly available pretrained model Zoobot (Walmsley et al., 2023). Zoobot can be fine-tuned for use in galaxy morphology classification problems. The model is pretrained using data and labels from Galaxy Zoo DECaLS (Walmsley et al., 2022a), a project where galaxy images from the deep, low-redshift Dark Energy Camera Legacy Survey (DECaLS Dey et al., 2019) are given classifications through citizen science. The use of DECaLS images offers improved imaging quality compared to previous citizen science-based models, and enables for fainter and lower surface brightness merger features.

The fine-tuning technique involves using an initially trained model, in this case Zoobot, and adapting the model for the task in question, in this case merger classification. From the initial model, weights, and representations, the uppermost, or 'head' layer, is removed, and weights and representations from the remainder of the model frozen. Then, a new 'head' model, with outputs tendered for the new task, is added, and the new model is trained for the new task. Detailed descriptions of the methods used in GZ DECaLS and Zoobot are available in Walmsley et al. (2022a), Walmsley et al. (2022b), and Walmsley et al. (2023).

For this study, we use the fine-tuned model featured in Omori et al. (2023). In this work, Zoobot is fine-tuned using observation realistic mock images of simulations from Bottrell et al. (2023). In Bottrell et al. (2023), galaxy simulational data from the TNG simulations (Springel et al., 2018; Pillepich et al., 2018a; Naiman et al., 2018; Nelson et al., 2018; Marinacci et al., 2018) is passed through the Monte Carlo Radiative transfer code SKIRT (Camps & Baes, 2020) into idealized images, before being processed into HSC realistic images. Details are available in Bottrell et al. (2023). The fine-tuning is conducted using images of ~1200 mergers and non-mergers. The fine-tuned model is able to differentiate between mergers and chance projections, and can also correctly classify mergers at various mass ratios and merger stages. Using the fine-tuned model, merger predictions are made on ~ 150,000 galaxies in GAMA DR4. Further details on the fine-tuned model and its performance are available in Omori et al. (2023). With the fine-tuned

model, predictions are made on *gri* images of HSC-SSP galaxies. Images are cutout first with a size encompassing $10 \times R_{\rm eff}$, then re-sized to 300×300 pixels. For each input image, our model will output a merger probability between 0 and 1, with 0 indicating non-merger and 1 indicating a merger.

4.2.2 AGN probabilities

AGN host galaxies in the GAMA catalog are identified using the SED fitting code PROSPECT (Robotham et al., 2020). Photometry identified in Davies et al. (2021) is put through PROSPECT. PROSPECT uses a Bruzual & Charlot stellar library (Bruzual & Charlot, 2003) and Chabrier initial mass function (Chabrier, 2003) to model stellar components. The model consists of a two-component description of the interstellar medium, a dust component attenuating emission from all stars, and a birth cloud attenuating emission from young stars. Details about PROSPECT are available in Robotham et al. (2020), and further details regarding galaxy modeling are available in Thorne et al. (2021, 2022).

For AGN modeling, the Fritz et al. (2006) AGN model is used, as it can fit MIR excess and the larger wavelength coverage in the ultraviolet allows for greater constraint of AGN parameters. The Fritz model is able to account sufficiently for the contribution from the galaxy as well as from the AGN torus. Various AGN implementations and their contributions to the overall galaxy SED can be accounted for by the Fritz model. Details about the fitting process are explained in Thorne et al. (2021, 2022).

AGNs and non-AGNs are classified based on the value $f_{\rm AGN}$, which is the fraction of flux within $5 - 20\mu$m contributed by the AGN component. This value is calculated after the best fit total and AGN component SEDs are fit.

For this work, we select mergers by adopting the 'confident' merger cutoff used in Omori et al. (2023), being a merger probability ¿ 0.8. Non-mergers are selected from galaxies with merger probability ¡ 0.3. These two cutoffs decrease the probability of contamination in our samples. We select AGN hosts by adopting an AGN cutoff used in Thorne et al. (2022), with galaxies with $f_{\rm AGN}$ ¿ 0.1 being considered an AGN host. For each AGN, we select a non-AGN with similar stellar mass, redshift, and star formation rate. Similarly, for each merger, we select a non-merger

with with similar stellar mass, redshift and star formation rate. We show 20 examples each of AGN-mergers, AGN-non-mergers, non-AGN-mergers, and non-AGN-non-mergers in Fig. 4.1 to Fig. 4.4.

4.3 Results

In this section, we conducted multiple tests on the connection between merger activity and AGN activity. As indicated previously, mergers are selected based on Omori et al. (2023) merger probabilities, with mergers being galaxies with merger probability ¿ 0.8, and non-mergers being galaxies with merger probability ¡ 0.3. AGN hosts are selected based on Thorne et al. (2022), with galaxies with $f_{\rm AGN}$ ¿ 0.1 being considered an AGN host, and all others being considered a non-AGN.

We first studied whether AGNs hosts have an increased merger fraction. Figure 4.5 shows a comparison of merger probability distribution between our AGN and non-AGN samples. While we find that the number of low merger probability ($p_{\rm m} < 0.3$) galaxies is higher among non-AGNs, and higher merger probability ($p_{\rm m} > 0.5$) galaxies is higher among AGNs, the KS-test does not reject the null hypothesis. As such, we find that there is not a significant increase in merger incidence among AGNs compared to non-AGNs. These results are aligned with studies that find that AGNs are not necessarily induced by mergers (Grogin et al., 2005; Gabor et al., 2009; Cisternas et al., 2011; Kocevski et al., 2012; Villforth et al., 2014; Mechtley et al., 2016; Gao et al., 2020; Silva et al., 2021).

We next investigated whether or not mergers can be a trigger for AGN activity. We plot the distribution of $f_{\rm AGN}$ between the merger and non-merger samples in Fig. 4.6. We find that while the number of galaxies is highest among non-AGNs by a significant margin for both mergers and non-mergers, the KS-test rejects the null hypothesis. We find a slight increase of AGN incidence among merger galaxies, which align with studies that find an AGN excess in mergers (Treister et al., 2012; Santini et al., 2012; Kocevski et al., 2015; Ellison et al., 2019).

4.4 Discussion

Our results show that merger incidence does not have a notable difference between AGN and non-AGN samples, but AGN incidence does have a notable difference between mergers and non-mergers. The lack of difference of merger distributions between AGNs and non-AGNs means that in our current merger and AGN selection criteria, AGNs are not necessarily merger

driven, and there are other processes driving AGN formation. These results are consistent with those of Grogin et al. (2005); Gabor et al. (2009); Cisternas et al. (2011); Kocevski et al. (2012); Villforth et al. (2014); Mechtley et al. (2016); Gao et al. (2020); Silva et al. (2021), which question the role of merger activity in AGN activity. However, while the overall fraction of mergers hosting AGNs is a minority, the increase in AGN incidence among mergers indicate that mergers are more likely to harbour AGNs than non-mergers, which align with Treister et al. (2012); Santini et al. (2012); Kocevski et al. (2015); Ellison et al. (2019).

The mixed results compared with previous studies likely is due to the selection method of both mergers and AGNs. The merger selection method used in Omori et al. (2023) is able to identify mergers diversely. First, the Omori et al. (2023). model is able to classify merger galaxies at varying stages, such as in the pre-merger and post-merger stage. This will result in many mergers before or after the AGN phase of the merger process, to be included in our sample. In addition, mergers that are less likely to induce AGNs, such as dry mergers (Silva et al., 2021), are likely to be identified by the model. Further decomposition of the merger sample will be required to gain a better understanding of the role of mergers in AGN activity. For example, many of the previously mentioned studies finding a merger-AGN connection are focused on major mergers, so limiting our merger sample to major mergers may alter our results. However, the impact of major mergers on AGN activity, even for gas-rich mergers, has also been questioned (Marian et al., 2019).

With regards to AGNs, the selection criteria in Thorne et al. (2022) was based on the $f_{\rm AGN}$ value, or the AGN flux contribution fraction. This method is found to recover AGNs identified using other methods, such as X-ray selection, color selection, and emission line diagnostics, at varying levels. As such, the diverse AGN selection will likely include a large fraction of AGNs that ignited by activity other than mergers, such as gas cloud accretion activity (Maccagni et al., 2014). Similar to decomposition of the merger sample, a decomposition of the AGN sample is required to understand whether or not there exists a particular property of AGNs linked to merger activity. For example, radio-loud AGNs are considered to be linked to merger activity (Chiaberge et al., 2015), so if we can separate our merger sample only to those with radio detections, we may find different results.

Finally, we attribute a lack of connection between mergers and AGNs to the timescale difference between merger activity and AGN activity, as mentioned in the introduction. The timescale of AGN activity, at 10^5 years (Schawinski et al., 2015), is afar shorter and is only a small fraction of the timescale of merger activity, which can last from 0.2 to several Gyr (Lotz et al., 2008, 2010b,a). Our fine-tuned model can diversely identify mergers, particularly giving high merger probabilities to early stage mergers, which are not yet at the AGN stage of the merger process. As such, merger-AGN connections are not found at the timescale of our merger sample. Limiting the merger sample to only those that are at the AGN formation timescale of the merger process may alter our results.

4.5 Conclusions

In this work, we investigate the relationship between merger activity and AGN activity by comparing the merger probability and AGN flux contribution in HSC-SSP and GAMA cross-matched galaxies. Merger probabilities were obtained using a CNN fine-tuned using observation realistic images of the TNG simulations. AGN flux contributions were obtained using the SED fitting code PROSPECT.

Our main findings include the following:

1. We compared the merger probability distribution between AGN hosts and non-AGN hosts, and found that there is no significant difference in distribution, indicating a lack of merger excess among AGN hosts. This is likely due to the AGN selection.

2. We also compared the AGN flux contribution $f_{\rm AGN}$ distribution between mergers and non-mergers. While there are still the most merging and non-merging systems that are not AGN hosts, the KS-test showed that the distributions are different, and that AGN incidence is slightly higher among mergers. Mergers are more likely to host AGNs than non-mergers.

Further decomposition of the AGN and merger samples will be required to understand if there is a dependence on other physical properties on the merger-AGN relation. Future works will investigate dependences on properties such as stellar mass, AGN luminosity, and environment.

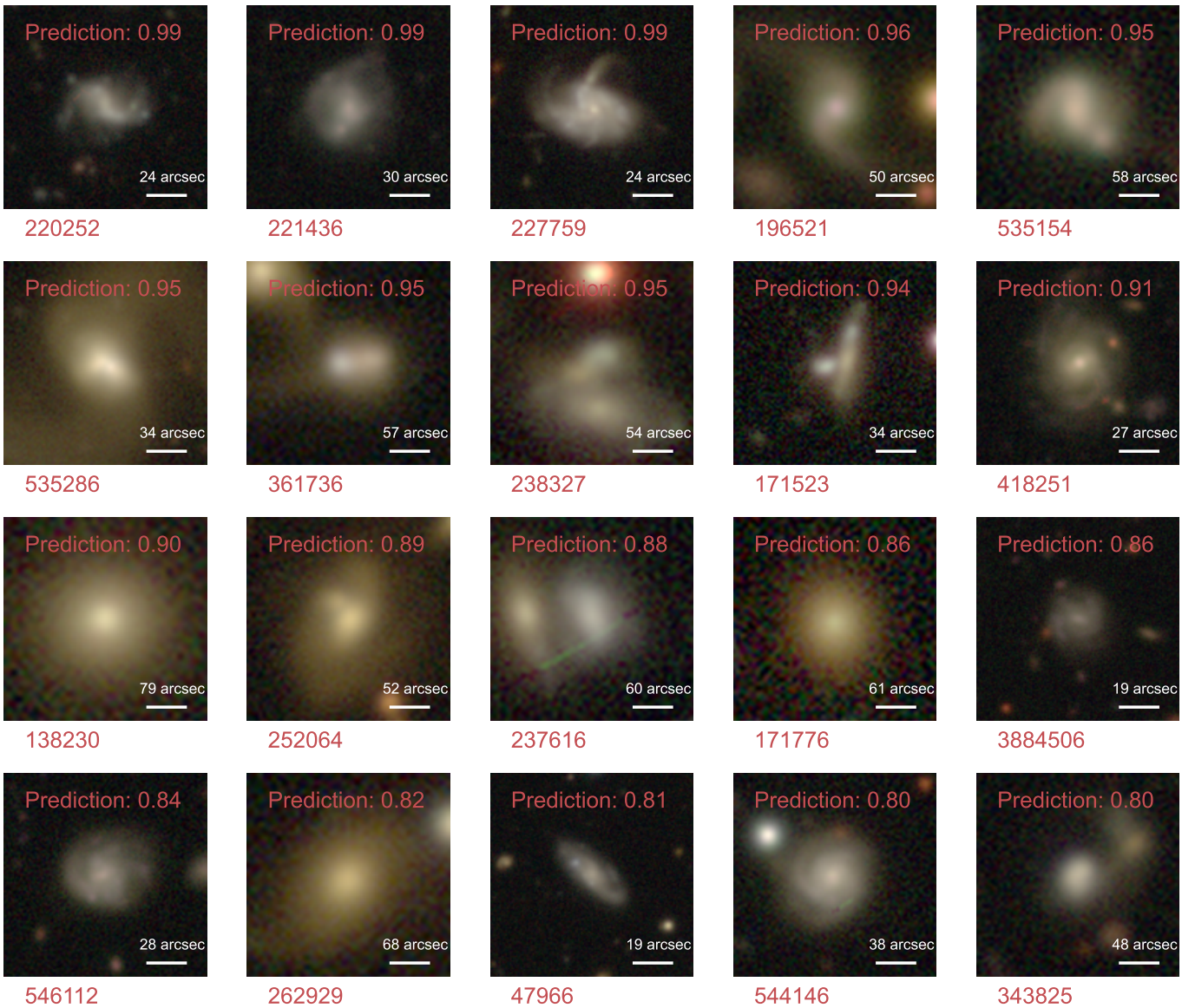

Fig. 4.1: 20 randomly drawn examples of AGN hosts (f_{AGN} ¿ 0.1) that are also mergers (merger probability > 0.8), with merger probabilities in descending order, with the probabilities indicated in the image, and the identification of the galaxy indicated below with its GAMA CATA ID.

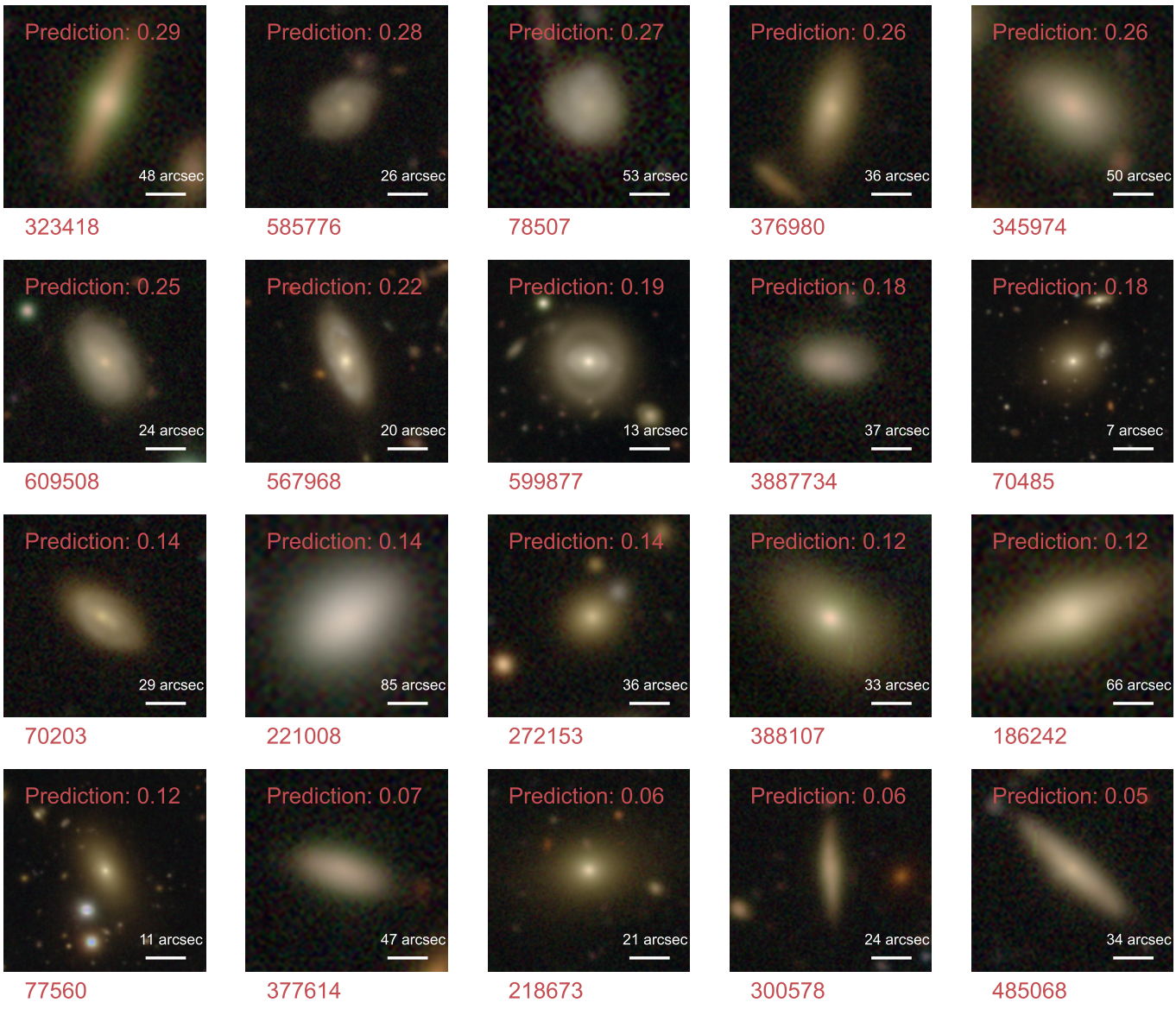

Fig. 4.2: Same as Fig. 4.1 but for AGNs that are non-mergers (merger probability < 0.3).

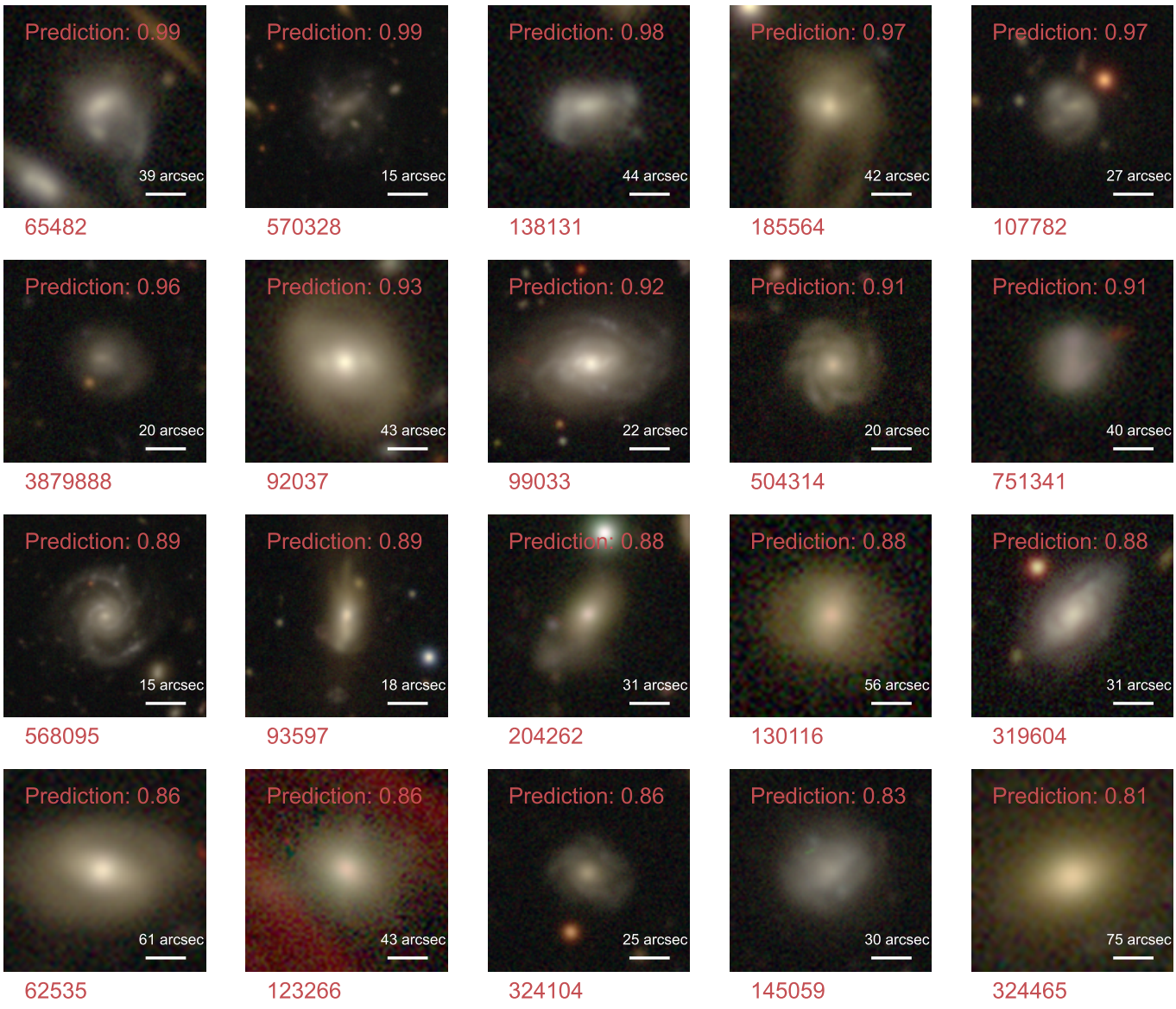

Fig. 4.3: Same as Fig. 4.1 but for mergers that are not AGN hosts ($f_{\rm AGN} \leq 0.1$).

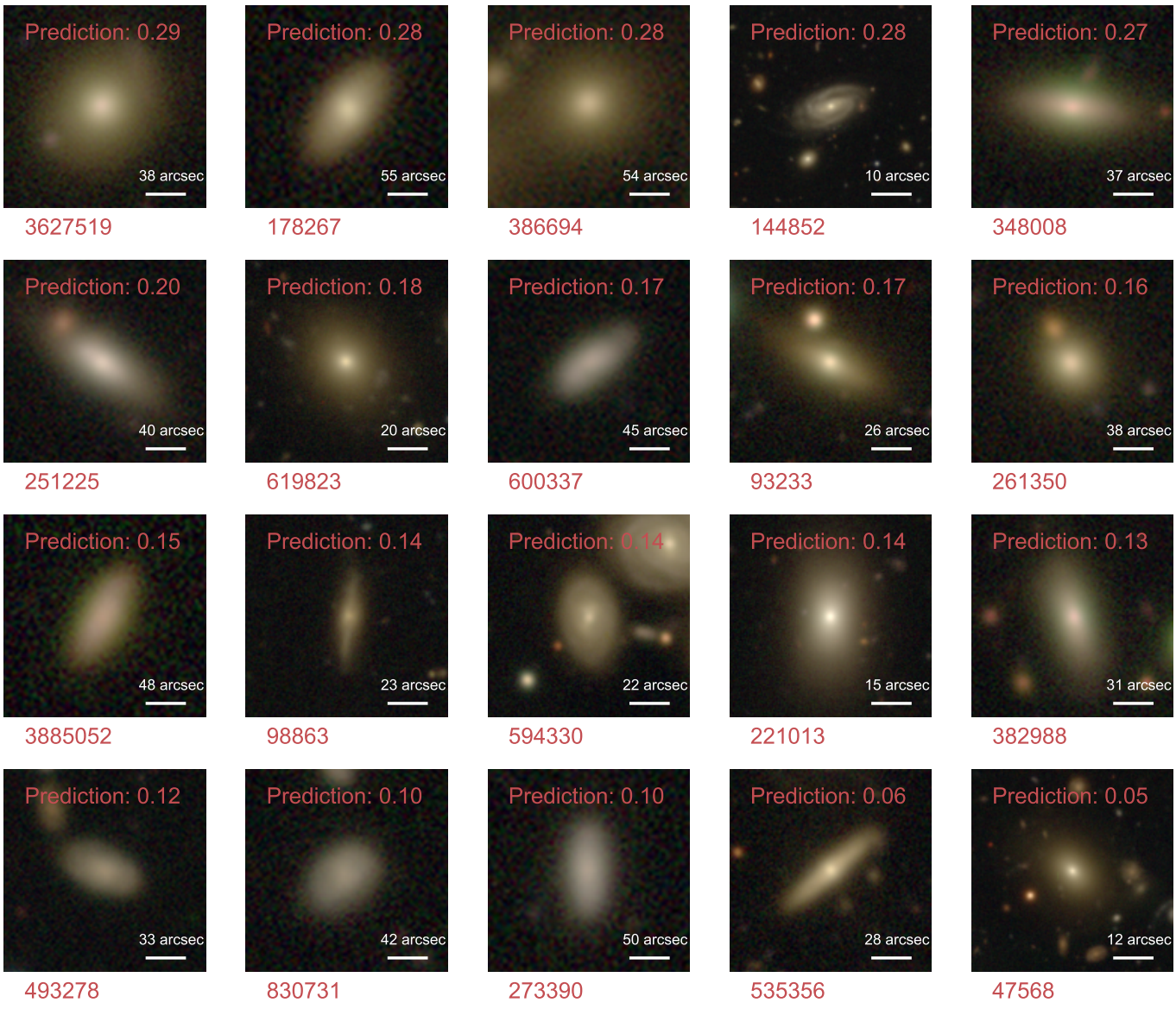

Fig. 4.4: Same as Fig. 4.1 but for non-mergers that are not AGN hosts.

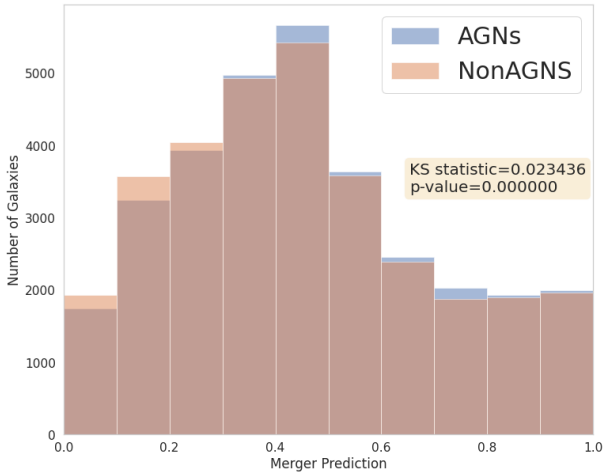

Fig. 4.5: Distributions of merger probabilities identified using the Omori et al. (2023) model for the AGN (blue) and non-AGN (orange) samples. The KS statistic and p-value are indicated in the yellow box. We find that there is little difference between merger probability distribution between AGNs and non-AGNs.

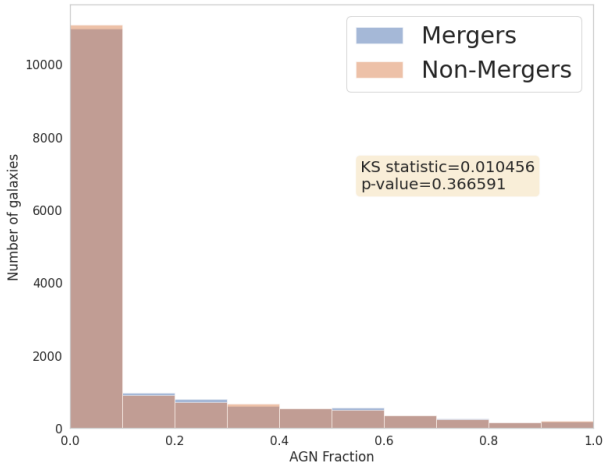

Fig. 4.6: Distributions of AGN fractions identified using PROSPECT for the merger (blue, $p_{\rm m} > 0.8$) and non-merger (orange, $p_{\rm m} < 0.8$) samples. The KS statistic and p-value are indicated in the yellow box. We find that the null hypothesis is rejected by the KS-test. While a large number of both merger and non-mergers do not have AGNs, the AGN fraction is increased among merger galaxies.

Chapter 5

Conclusions

Galaxy mergers are a very fundamental and important process when discussing galaxy evolution. In the currently accepted ΛCDM framework for structure formation, large scale structures are considered to evolve through hierarchical growth. In the context of galaxies, one such avenue of hierarchical growth is through galaxy mergers. As such, in order to understand the evolution of galaxies, it is necessary to understand galaxy mergers and their associated processes, such as star formation, chemical evolution, and AGN activity. However, our understanding of the role that mergers can play within galaxy evolution and associated processes is still heavily contested.

One main reason for the disagreements in theories lies in galaxy merger identification methods. In order to conduct studies that can enrich our understanding of galaxy mergers, a method to accurately identify mergers, with high completeness and precision, must be employed. Various methods have been used in a variety of studies, with all methods having their own strengths and limitations. No matter the method, due to the wide variety of merger galaxies, the removal of interlopers whilst simultaneously achieving a high completeness is is a complex task.

In this thesis, we approach merger identification in large-scale galaxy surveys through various methods, and use the merger samples identified through these methods to conduct merger-related studies. Chapter 2 is a version of , and Chapter 3 is an expanded version of . Our methods and associated studies are summarized as follows.

5.1 Merger Identification Methods

The first method used in this thesis, introduced in Chapter 2, combines the use of spatially resolved kinematics and optical images. These two items are complementary to each other. The spatially resolved kinematics can reveal merger signatures, such as gaseous and stellar disturbances, that may not be seen in optical images. On the contrary, the optical images can confirm or rule out some kinematic disturbances, such as those caused by foreground stellar objects. However, this method had many shortcomings. Integral field spectroscopy is required for spatially resolved kinematics, which is observationally expensive and severely limits the surveys and sample sizes that can be used. Further, it has been found that the inclusion of spatially resolved kinematics only marginally increases merger identification accuracy, and the trade-off between the marginal improvement and observational, time, and human resource costs required for this method must be carefully considered.

The second method used in this thesis, introduced in Chapter 3, is machine-learning based. The use of machine learning models, such as convolutional neural networks, has become increasingly common for morphological classification in present day galaxy surveys, as conventional methods have become unrealistic due to the increasing survey sizes. However, these methods are not without their limitations, mostly attributed to the images used in training the models, highlighted in Section 1.3.4. To overcome these limitations, we employ a transfer-learning based method, where a model pretrained on deep galaxy images is fine-tuned using observation-realistic synthetic images of TNG simulations. The resulting model is able to identify mergers at varying stages and mass ratios, and can differentiate between true mergers and chance projections. This model will be used to make merger predictions for a large amount of HSC-SSP galaxies, and the predictions will be the baseline for merger investigations in the HSC-SSP.

5.2 Merger Galaxy Studies

Using the various merger selection methods, I conducted a number of studies on galaxy mergers in relation to galaxy properties. These were conducted to investigate the role of galaxy mergers on galaxy evolution and related processes.

In Chapter 2, mergers from MaNGA selected through a combination of visual classification and spatially resolved stellar kinematics were used to investigate the relation of mergers on the mass-metallicity relation (MZR) at the spatially resolved scale. I found that the spatially resolved MZR in merger galaxies has a bimodal distribution, with one peak aligning with the MZR of the entire MaNGA sample, and the other showing a diluted metallicity. Through the use of spatial information, I found that the diluted region belonged to the central region of close galaxy pairs. This indicates that when galaxies come close to coalescence, the gas flows as a result of mergers inflows towards the circumnuclear regions of the host galaxy, and metallicity dilution occurs.

In Chapter 3, mergers from HSC-SSP selected through a fine-tuning based machine learning were used to investigate the impact of environment on galaxy merger incidence. I found that in observational data, mass underdense regions have the highest merger incidence, and mass underdense regions have the lowest merger incidence. The finding that mass underdense regions favour merger activity gives a new viewpoint on a long-standing debate and possible misconception on where mergers occur in the low redshift ($z < 0.3$) Universe. However, in simulational data I found that below a certain aperture radius, mass overdense regions become a site for mergers. As this turnaround was not visible in the observations, further investigations are required.

In Chapter 4, mergers from HSC-SSP selected through the same model as the previous chapter, alongside AGNs selected using full SED fitting, are used to investigate the relationship between mergers, AGNs, and environment. I found that there is little difference in merger probability distribution between AGNs and non-AGNs, and likewise little difference in AGN fraction (AGN flux contribution to entire galaxy flux) between mergers and non-mergers. As both merger and AGN selection methods are meant to include a variety of mergers and AGNs, the samples likely include many non-AGN mergers and AGNs that are not merger-driven. I results show that AGNs are not necessarily merger driven, and further investigations will be required to understand on the properties of mergers that can drive AGN activity.

5.3 Future Prospects

This collection of works require future prospects to enrich our understanding of galaxy mergers. I write down some examples of potential future steps of this work.

① Creation of a merger catalogue for entire HSC-SSP footprint

In the current stage, predictions for approximately 300,000 galaxies from HSC-SSP S21A, with SDSS and GAMA footprint overlaps, have been made. In the immediate future, I plan to use my fine-tuned model to make merger predictions on the remainder of HSC-SSP S21A, and make the probabilities publicly available. This merger probability catalogue is anticipated to be one of the largest of its kind, including over 50 million galaxies. The predictions made on the high resolution images of the HSC-SSP, combined with the large number of samples used, will allow for further merger galaxy studies, both by myself and by the public.

② Spectroscopic observations and the HSC-PFS

Spectroscopic information was intensively used in Chapter 2 for SDSS-MaNGA galaxies to investigate chemical evolution in mergers, as spatially resolved spectroscopic information was available throughout the entire MaNGA footprint. However, in our investigations using the HSC-SSP, investigations using spectroscopic observations was limited to galaxies with GAMA or SDSS overlaps. The introduction of the Hyper Suprime-Cam Prime Focus Spectrograph (HSC-PFS, Wang et al. (2014); Tamura et al. (2016)) will provide us with spectroscopic observations of a much larger footprint of the HSC-SSP, allowing us to conduct investigations at greater resolutions and with larger sample sizes. The observations made with the HSC-PFS will enable in-depth studies of star formation histories of merging systems.

③ Multiwavelength approach for merger investigations

The investigations conducted in this thesis are done using optical wavelength observations of SDSS and HSC. Adding information from observations at other wavelengths will allow us to draw a more complete picture of mergers and related processes. For example, gas properties, such as resolved gas properties and gas mass, can be found through observations at other wavelengths such as radio observations for HI gas or infrared for CO gas. Having access to such properties will enrich our understanding of the role of gas in mergers and associated processes.

④ Expansion into higher redshifts

The investigations conducted in this thesis are at very low redshifts, with the SDSS MaNGA work at $z < 0.15$ and the HSC-SSP work at $z < 0.3$. The conclusions of this work may not necessarily hold true at higher redshifts. For example, at higher redshifts (e.g. $z > 2$), mergers are an important driver of galaxy evolution in protocluster (overdense) regions (Liu et al., 2023). In addition, investigating scaling relations, such as the MZR, for mergers and non-mergers at both high and low redshifts will give us a greater understanding of the redshift evolution of the processes and the role of mergers. However, identification of mergers becomes more difficult as redshift increases, as the faint merger signatures will become increasingly undetectable, and machine learning models will likely have greater difficulties with high redshift merger identification. We will require a method to robustly identify mergers to conduct high-z merger investigations.

Bibliography

Abdurro'uf, Accetta, K., Aerts, C., et al. 2022, ApJS, 259, 35, doi: 10.3847/1538-4365/ac4414

Ackermann, S., Schawinski, K., Zhang, C., Weigel, A. K., & Turp, M. D. 2018, MNRAS, 479, 415–425, doi: 10.1093/mnras/sty1398

Aihara, H., Armstrong, R., Bickerton, S., et al. 2018, PASJ, 70, S8, doi: 10.1093/pasj/psx081

Aihara, H., AlSayyad, Y., Ando, M., et al. 2022, PASJ, 74, 247, doi: 10.1093/pasj/psab122

Alonso, S., Mesa, V., Padilla, N., & Lambas, D. G. 2012, A&A, 539, A46, doi: 10.1051/0004-6361/201117901

Ascaso, B., Lemaux, B. C., Lubin, L. M., et al. 2014, MNRAS, 442, 589, doi: 10.1093/mnras/stu877

Bacon, R., Copin, Y., Monnet, G., et al. 2001, MNRAS, 326, 23–35, doi: 10.1046/j.1365-8711.2001.04612.x

Baldwin, J. A., Phillips, M. M., & Terlevich, R. 1981, PASP, 93, 5, doi: 10.1086/130766

Balogh, M. L., Morris, S. L., Yee, H. K. C., Carlberg, R. G., & Ellingson, E. 1999, ApJ, 527, 54, doi: 10.1086/308056

Banerji, M., Lahav, O., Lintott, C. J., et al. 2010, MNRAS, 406, 342, doi: 10.1111/j.1365-2966.2010.16713.x

Barnes, J. E. 2004, MNRAS, 350, 798, doi: 10.1111/j.1365-2966.2004.07725.x

Barnes, J. E., & Hernquist, L. 1992, ARA&A, 30, 705, doi: 10.1146/annurev.aa.30.090192.003421

Barnes, J. E., & Hernquist, L. E. 1991, ApJ, 370, L65, doi: 10.1086/185978

Barrera-Ballesteros, J. K., García-Lorenzo, B., Falcón-Barroso, J., et al. 2015, A&A, 582, A21, doi: 10.1051/0004-6361/201424935

Barrera-Ballesteros, J. K., Heckman, T. M., Zhu, G. B., et al. 2016, MNRAS, 463, 2513, doi: 10.1093/mnras/stw1984

Barton, E. J., Geller, M. J., & Kenyon, S. J. 2000, ApJ, 530, 660, doi: 10.1086/308392

Beckman, J., Carretero, C., & Vazdekis, A. 2008, Chinese Journal of Astronomy and Astrophysics Supplement, 8, 77

Bédorf, J., & Portegies Zwart, S. 2013, MNRAS, 431, 767, doi: 10.1093/mnras/stt208

Bender, R., & Surma, P. 1992, A&A, 258, 250

Berg, T. A. M., Simard, L., Mendel, T. J., & Ellison, S. L. 2014, MNRAS, 440, L66, doi: 10.1093/mnrasl/slu026

Bershady, M. A., Jangren, A., & Conselice, C. J. 2000, AJ, 119, 2645, doi: 10.1086/301386

Bertola, F., Buson, L. M., & Zeilinger, W. W. 1992, ApJ, 401, L79, doi: 10.1086/186675

Bickley, R. W., Ellison, S. L., Patton, D. R., et al. 2022, MNRAS, 514, 3294, doi: 10.1093/mnras/stac1500

Bickley, R. W., Bottrell, C., Hani, M. H., et al. 2021, MNRAS, 504, 372, doi: 10.1093/mnras/stab806

Blanton, M. R., Bershady, M. A., Abolfathi, B., et al. 2017, AJ, 154, 28, doi: 10.3847/1538-3881/aa7567

Blumenthal, G. R., Faber, S. M., Primack, J. R., & Rees, M. J. 1984, Nature, 311, 517, doi: 10.1038/311517a0

Blumenthal, K. A., & Barnes, J. E. 2018, MNRAS, 479, 3952, doi: 10.1093/mnras/sty1605

Blumenthal, K. A., Moreno, J., Barnes, J. E., et al. 2020, MNRAS, 492, 2075, doi: 10.1093/mnras/stz3472

Bosch, J., Armstrong, R., Bickerton, S., et al. 2018, PASJ, 70, S5, doi: 10.1093/pasj/psx080

Bottrell, C., Hani, M. H., Teimoorinia, H., Patton, D. R., & Ellison, S. L. 2022, MNRAS, 511, 100, doi: 10.1093/mnras/stab3717

Bottrell, C., Simard, L., Mendel, J. T., & Ellison, S. L. 2019a, MNRAS, 486, 390, doi: 10.1093/mnras/stz855

Bottrell, C., Hani, M. H., Teimoorinia, H., et al. 2019b, MNRAS, 490, 5390, doi: 10.1093/mnras/stz2934

Bottrell, C., Yesuf, H. M., Popping, G., et al. 2023, MNRAS, doi: 10.1093/mnras/stad2971

Bruzual, G., & Charlot, S. 2003, MNRAS, 344, 1000, doi: 10.1046/j.1365-8711.2003.06897.x

Bruzual A., G. 1983, ApJ, 273, 105, doi: 10.1086/161352

Bundy, K., Bershady, M. A., Law, D. R., et al. 2015, ApJ, 798, 7, doi: 10.1088/0004-637X/798/1/7

Burke, C., & Collins, C. A. 2013, MNRAS, 434, 2856, doi: 10.1093/mnras/stt1192

Burkey, J. M., Keel, W. C., Windhorst, R. A., & Franklin, B. E. 1994, ApJ, 429, L13, doi: 10.1086/187402

Bustamante, S., Ellison, S. L., Patton, D. R., & Sparre, M. 2020, MNRAS, 494, 3469, doi: 10.1093/mnras/staa1025

Bustamante, S., Sparre, M., Springel, V., & Grand, R. J. J. 2018, MNRAS, 479, 3381, doi: 10.1093/mnras/sty1692

Camps, P., & Baes, M. 2020, Astronomy and Computing, 31, 100381, doi: 10.1016/j.ascom.2020.100381

Cappellari, M. 2017, MNRAS, 466, 798, doi: 10.1093/mnras/stw3020

Cappellari, M., & Copin, Y. 2003, MNRAS, 342, 345, doi: 10.1046/j.1365-8711.2003.06541.x

Cappellari, M., Emsellem, E., Krajnović, D., et al. 2011, MNRAS, 413, 813–836, doi: 10.1111/j.1365-2966.2010.18174.x

Carlberg, R. G., Pritchet, C. J., & Infante, L. 1994, ApJ, 435, 540, doi: 10.1086/174835

Cavanagh, M. K., Bekki, K., & Groves, B. A. 2023, MNRAS, 520, 5885, doi: 10.1093/mnras/stad476

Chabrier, G. 2003, PASP, 115, 763, doi: 10.1086/376392

Chen, Y.-M., Kauffmann, G., Tremonti, C. A., et al. 2012, MNRAS, 421, 314, doi: 10.1111/j.1365-2966.2011.20306.x

Cheng, T.-Y., Conselice, C. J., Aragón-Salamanca, A., et al. 2021, MNRAS, 507, 4425, doi: 10.1093/mnras/stab2142

Chiaberge, M., Gilli, R., Lotz, J. M., & Norman, C. 2015, ApJ, 806, 147, doi: 10.1088/0004-637X/806/2/147

Cid Fernandes, R., Stasińska, G., Schlickmann, M. S., et al. 2010, MNRAS, 403, 1036, doi: 10.1111/j.1365-2966.2009.16185.x

Ćiprijanović, A., Snyder, G. F., Nord, B., & Peek, J. E. G. 2020, Astronomy and Computing, 32, 100390, doi: 10.1016/j.ascom.2020.100390

Ćiprijanović, A., Kafkes, D., Downey, K., et al. 2021, MNRAS, 506, 677, doi: 10.1093/mnras/stab1677

Cisternas, M., Jahnke, K., Inskip, K. J., et al. 2011, ApJ, 726, 57, doi: 10.1088/0004-637X/726/2/57

Coccato, L., Morelli, L., Corsini, E. M., et al. 2011, MNRAS, 412, L113–L117, doi: 10.1111/j.1745-3933.2011.01016.x

Coccato, L., Morelli, L., Pizzella, A., et al. 2012, A&A, 549, A3, doi: 10.1051/0004-6361/201220460

Collins, C. A., Stott, J. P., Hilton, M., et al. 2009, Nature, 458, 603, doi: 10.1038/nature07865

Conselice, C. J. 2003, ApJS, 147, 1, doi: 10.1086/375001

Conselice, C. J., Bershady, M. A., & Jangren, A. 2000, ApJ, 529, 886, doi: 10.1086/308300

Cortijo-Ferrero, C., González Delgado, R. M., Pérez, E., et al. 2017, MNRAS, 467, 3898, doi: 10.1093/mnras/stx383

Cotini, S., Ripamonti, E., Caccianiga, A., et al. 2013, MNRAS, 431, 2661, doi: 10.1093/mnras/stt358

Crocker, A. F., Jeong, H., Komugi, S., et al. 2009, MNRAS, 393, 1255–1264, doi: 10.1111/j.1365-2966.2008.14295.x

Crocker, A. F., Jeong, H., Komugi, S., et al. 2009, MNRAS, 393, 1255, doi: 10.1111/j.1365-2966.2008.14295.x

Darg, D. W., Kaviraj, S., Lintott, C. J., et al. 2010, MNRAS, 401, 1043–1056, doi: 10.1111/j.1365-2966.2009.15686.x

Darg, D. W., Kaviraj, S., Lintott, C. J., et al. 2010a, MNRAS, 401, 1552, doi: 10.1111/j.1365-2966.2009.15786.x

—. 2010b, MNRAS, 401, 1043, doi: 10.1111/j.1365-2966.2009.15686.x

Davies, L. J. M., Thorne, J. E., Robotham, A. S. G., et al. 2021, MNRAS, 506, 256, doi: 10.1093/mnras/stab1601

Davies, R. L., Kuntschner, H., Emsellem, E., et al. 2001, ApJ, 548, L33–L36, doi: 10.1086/318930

De Propris, R., Conselice, C. J., Liske, J., et al. 2007, ApJ, 666, 212, doi: 10.1086/520488

De Propris, R., Liske, J., Driver, S. P., Allen, P. D., & Cross, N. J. G. 2005, AJ, 130, 1516, doi: 10.1086/433169

Delahaye, A. G., Webb, T. M. A., Nantais, J., et al. 2017, ApJ, 843, 126, doi: 10.3847/1538-4357/aa756a

Dey, A., Schlegel, D. J., Lang, D., et al. 2019, AJ, 157, 168, doi: 10.3847/1538-3881/ab089d

Di Matteo, T., Springel, V., & Hernquist, L. 2005, Nature, 433, 604, doi: 10.1038/nature03335

Dieleman, S., Willett, K. W., & Dambre, J. 2015, MNRAS, 450, 1441, doi: 10.1093/mnras/stv632

Domínguez Sánchez, H., Huertas-Company, M., Bernardi, M., Tuccillo, D., & Fischer, J. L. 2018, MNRAS, 476, 3661, doi: 10.1093/mnras/sty338

Domínguez Sánchez, H., Margalef, B., Bernardi, M., & Huertas-Company, M. 2022, MNRAS, 509, 4024, doi: 10.1093/mnras/stab3089

Domínguez Sánchez, H., Huertas-Company, M., Bernardi, M., et al. 2019, MNRAS, 484, 93, doi: 10.1093/mnras/sty3497

Donley, J. L., Koekemoer, A. M., Brusa, M., et al. 2012, ApJ, 748, 142, doi: 10.1088/0004-637X/748/2/142

Dressler, A. 1980, ApJ, 236, 351, doi: 10.1086/157753

Driver, S. P., Andrews, S. K., da Cunha, E., et al. 2018, MNRAS, 475, 2891, doi: 10.1093/mnras/stx2728

Driver, S. P., Bellstedt, S., Robotham, A. S. G., et al. 2022, MNRAS, 513, 439, doi: 10.1093/mnras/stac472

Duncan, K., Conselice, C. J., Mundy, C., et al. 2019, ApJ, 876, 110, doi: 10.3847/1538-4357/ab148a

Edmunds, M. G., & Pagel, B. E. J. 1984, MNRAS, 211, 507, doi: 10.1093/mnras/211.3.507

Ellison, S. L., Patton, D. R., & Hickox, R. C. 2015, MNRAS, 451, L35, doi: 10.1093/mnrasl/slv061

Ellison, S. L., Patton, D. R., Mendel, J. T., & Scudder, J. M. 2011, MNRAS, 418, 2043, doi: 10.1111/j.1365-2966.2011.19624.x

Ellison, S. L., Patton, D. R., Simard, L., & McConnachie, A. W. 2008, AJ, 135, 1877, doi: 10.1088/0004-6256/135/5/1877

Ellison, S. L., Patton, D. R., Simard, L., et al. 2010, MNRAS, 407, 1514, doi: 10.1111/j.1365-2966.2010.17076.x

Ellison, S. L., Viswanathan, A., Patton, D. R., et al. 2019, MNRAS, 487, 2491, doi: 10.1093/mnras/stz1431

Fakhouri, O., & Ma, C.-P. 2009, MNRAS, 394, 1825, doi: 10.1111/j.1365-2966.2009.14480.x

Ferreira, L., Conselice, C. J., Duncan, K., et al. 2020, ApJ, 895, 115, doi: 10.3847/1538-4357/ab8f9b

Ferreira, L., Conselice, C. J., Kuchner, U., & Tohill, C.-B. 2022, ApJ, 931, 34, doi: 10.3847/1538-4357/ac66ea

Fischer, J. L., Domínguez Sánchez, H., & Bernardi, M. 2019, MNRAS, 483, 2057, doi: 10.1093/mnras/sty3135

Foster, C., Hopkins, A. M., Gunawardhana, M., et al. 2012, A&A, 547, A79, doi: 10.1051/0004-6361/201220050

Fritz, J., Franceschini, A., & Hatziminaoglou, E. 2006, MNRAS, 366, 767, doi: 10.1111/j.1365-2966.2006.09866.x

Furusawa, H., Koike, M., Takata, T., et al. 2018, PASJ, 70, S3, doi: 10.1093/pasj/psx079

Gabor, J. M., Impey, C. D., Jahnke, K., et al. 2009, ApJ, 691, 705, doi: 10.1088/0004-637X/691/1/705

Gao, F., Wang, L., Pearson, W. J., et al. 2020, A&A, 637, A94, doi: 10.1051/0004-6361/201937178

García-Benito, R., Zibetti, S., Sánchez, S. F., et al. 2015, A&A, 576, A135, doi: 10.1051/0004-6361/201425080

Garduño, L. E., Lara-López, M. A., López-Cruz, O., et al. 2021, MNRAS, 501, 2969, doi: 10.1093/mnras/staa3799

Gharat, S., & Dandawate, Y. 2022, MNRAS, 511, 5120, doi: 10.1093/mnras/stac457

Ghigna, S., Moore, B., Governato, F., et al. 1998, MNRAS, 300, 146, doi: 10.1046/j.1365-8711.1998.01918.x

Ghosh, A., Urry, C. M., Wang, Z., et al. 2020, ApJ, 895, 112, doi: 10.3847/1538-4357/ab8a47

Glikman, E., Simmons, B., Mailly, M., et al. 2015, ApJ, 806, 218, doi: 10.1088/0004-637X/806/2/218

Goddard, D., Thomas, D., Maraston, C., et al. 2017, MNRAS, 466, 4731, doi: 10.1093/mnras/stw3371

Goto, T., Nichol, R. C., Okamura, S., et al. 2003, PASJ, 55, 771, doi: 10.1093/pasj/55.4.771

Goulding, A. D., Greene, J. E., Bezanson, R., et al. 2018, PASJ, 70, S37, doi: 10.1093/pasj/psx135

Greenawalt, B., Walterbos, R. A. M., Thilker, D., & Hoopes, C. G. 1998, ApJ, 506, 135, doi: 10.1086/306232

Grogin, N. A., Conselice, C. J., Chatzichristou, E., et al. 2005, ApJ, 627, L97, doi: 10.1086/432256

Groves, B., Dopita, M. A., Sutherland, R. S., et al. 2008, ApJS, 176, 438, doi: 10.1086/528711

Grønnow, A. E., Finlator, K., & Christensen, L. 2015, MNRAS, 451, 4005, doi: 10.1093/mnras/stv1232

Gunn, J. E., & Gott, J. Richard, I. 1972, ApJ, 176, 1, doi: 10.1086/151605

Gunn, J. E., Siegmund, W. A., Mannery, E. J., et al. 2006, AJ, 131, 2332, doi: 10.1086/500975

Guseva, N. G., Papaderos, P., Meyer, H. T., Izotov, Y. I., & Fricke, K. J. 2009, A&A, 505, 63, doi: 10.1051/0004-6361/200912414

Guzmán-Ortega, A., Rodriguez-Gomez, V., Snyder, G. F., Chamberlain, K., & Hernquist, L. 2023, MNRAS, 519, 4920, doi: 10.1093/mnras/stac3334

He, K., Zhang, X., Ren, S., & Sun, J. 2015, in 2015 IEEE International Conference on Computer Vision (ICCV), 1026–1034, doi: 10.1109/ICCV.2015.123

Hernquist, L. 1989, Nature, 340, 687, doi: 10.1038/340687a0

—. 1992, ApJ, 400, 460, doi: 10.1086/172009

Hester, J. A., & Tasitsiomi, A. 2010, ApJ, 715, 342, doi: 10.1088/0004-637X/715/1/342

Hewlett, T., Villforth, C., Wild, V., et al. 2017, MNRAS, 470, 755, doi: 10.1093/mnras/stx997

Holincheck, A. J., Wallin, J. F., Borne, K., et al. 2016, MNRAS, 459, 720, doi: 10.1093/mnras/stw649

Hong, J., Im, M., Kim, M., & Ho, L. C. 2015, ApJ, 804, 34, doi: 10.1088/0004-637X/804/1/34

Hoopes, C. G., & Walterbos, R. A. M. 2003, ApJ, 586, 902, doi: 10.1086/367954

Hoopes, C. G., Walterbos, R. A. M., & Greenwalt, B. E. 1996, AJ, 112, 1429, doi: 10.1086/118111

Hopkins, P. F., Cox, T. J., Hernquist, L., et al. 2013, MNRAS, 430, 1901, doi: 10.1093/mnras/stt017

Hopkins, P. F., Cox, T. J., Kereš, D., & Hernquist, L. 2008a, ApJS, 175, 390, doi: 10.1086/524363

Hopkins, P. F., Hernquist, L., Cox, T. J., & Kereš, D. 2008b, ApJS, 175, 356, doi: 10.1086/524362

Hopkins, P. F., & Quataert, E. 2010, MNRAS, 407, 1529, doi: 10.1111/j.1365-2966.2010.17064.x

Huertas-Company, M., & Lanusse, F. 2023, PASA, 40, e001, doi: 10.1017/pasa.2022.55

Huertas-Company, M., Gravet, R., Cabrera-Vives, G., et al. 2015, A&AS, 221, 8, doi: 10.1088/0067-0049/221/1/8

Iono, D., Yun, M. S., & Mihos, J. C. 2004, ApJ, 616, 199, doi: 10.1086/424797

Jacobs, C., Collett, T., Glazebrook, K., et al. 2019, MNRAS, 484, 5330, doi: 10.1093/mnras/stz272

Jesseit, R., Naab, T., Peletier, R. F., & Burkert, A. 2007, MNRAS, 376, 997, doi: 10.1111/j.1365-2966.2007.11524.x

Jian, H.-Y., Lin, L., & Chiueh, T. 2012, ApJ, 754, 26, doi: 10.1088/0004-637X/754/1/26

Jin, Y., Chen, Y., Shi, Y., et al. 2016, MNRAS, 463, 913–926, doi: 10.1093/mnras/stw2055

Juneau, S., Dickinson, M., Bournaud, F., et al. 2013, ApJ, 764, 176, doi: 10.1088/0004-637X/764/2/176

Katkov, I. Y., Sil'chenko, O. K., Chilingarian, I. V., Uklein, R. I., & Egorov, O. V. 2016, MNRAS, 461, 2068–2076, doi: 10.1093/mnras/stw1452

Kauffmann, G., Heckman, T. M., Simon White, D. M., et al. 2003, MNRAS, 341, 33–53, doi: 10.1046/j.1365-8711.2003.06291.x

Kawanomoto, S., Uraguchi, F., Komiyama, Y., et al. 2018, PASJ, 70, 66, doi: 10.1093/pasj/psy056

Keel, W. C., Kennicutt, R. C., J., Hummel, E., & van der Hulst, J. M. 1985, AJ, 90, 708, doi: 10.1086/113779

Kepner, J. V. 1999, ApJ, 520, 59, doi: 10.1086/307419

Kewley, L. J., Groves, B., Kauffmann, G., & Heckman, T. 2006, MNRAS, 372, 961, doi: 10.1111/j.1365-2966.2006.10859.x

Kim, E., Hwang, H. S., Jeong, W.-S., et al. 2021, MNRAS, 507, 3113, doi: 10.1093/mnras/stab2090

Kitzbichler, M. G., & White, S. D. M. 2008, MNRAS, 391, 1489, doi: 10.1111/j.1365-2966.2008.13873.x

Kitzbichler, M. G., & White, S. D. M. 2008, MNRAS, 391, 1489–1498, doi: 10.1111/j.1365-2966.2008.13873.x

Kocevski, D. D., Faber, S. M., Mozena, M., et al. 2012, ApJ, 744, 148, doi: 10.1088/0004-637X/744/2/148

Kocevski, D. D., Brightman, M., Nandra, K., et al. 2015, ApJ, 814, 104, doi: 10.1088/0004-637X/814/2/104

Komiyama, Y., Obuchi, Y., Nakaya, H., et al. 2018, PASJ, 70, S2, doi: 10.1093/pasj/psx069

Kormendy, J., & Ho, L. C. 2013, ARA&A, 51, 511, doi: 10.1146/annurev-astro-082708-101811

Kormendy, J., & Richstone, D. 1995, ARA&A, 33, 581, doi: 10.1146/annurev.aa.33.090195.003053

Koss, M., Mushotzky, R., Veilleux, S., & Winter, L. 2010, ApJ, 716, L125, doi: 10.1088/2041-8205/716/2/L125

Koulouridis, E., & Bartalucci, I. 2019, A&A, 623, L10, doi: 10.1051/0004-6361/201935082

Krajnović, D., Emsellem, E., Cappellari, M., et al. 2011, MNRAS, 414, 2923, doi: 10.1111/j.1365-2966.2011.18560.x

Krajnović, D., Emsellem, E., Cappellari, M., et al. 2011, MNRAS, 414, 2923, doi: 10.1111/j.1365-2966.2011.18560.x

Krizhevsky, A., Sutskever, I., & Hinton, G. E. 2017, Commun. ACM, 60, 84–90, doi: 10.1145/3065386

Kuntschner, H., Smith, R. J., Colless, M., et al. 2002, MNRAS, 337, 172, doi: 10.1046/j.1365-8711.2002.05897.x

Lacey, C., & Cole, S. 1994, MNRAS, 271, 676, doi: 10.1093/mnras/271.3.676

Lackner, C. N., Silverman, J. D., Salvato, M., et al. 2014, AJ, 148, 137, doi: 10.1088/0004-6256/148/6/137

Lang, M., Holley-Bockelmann, K., & Sinha, M. 2014, ApJ, 790, L33, doi: 10.1088/2041-8205/790/2/L33

Law, D. R., Cherinka, B., Yan, R., et al. 2016, AJ, 152, 83, doi: 10.3847/0004-6256/152/4/83

Lemaux, B. C., Gal, R. R., Lubin, L. M., et al. 2012, ApJ, 745, 106, doi: 10.1088/0004-637X/745/2/106

Lequeux, J., Peimbert, M., Rayo, J. F., Serrano, A., & Torres-Peimbert, S. 1979, A&A, 500, 145

Li, S.-l., Shi, Y., Bizyaev, D., et al. 2019, arXiv e-prints, arXiv:1912.04522. https://arxiv.org/abs/astro-ph.GA/1912.04522

Lidman, C., Iacobuta, G., Bauer, A. E., et al. 2013, MNRAS, 433, 825, doi: 10.1093/mnras/stt777

Lin, L., Koo, D. C., Willmer, C. N. A., et al. 2004, ApJ, 617, L9, doi: 10.1086/427183

Lin, L., Cooper, M. C., Jian, H.-Y., et al. 2010, ApJ, 718, 1158, doi: 10.1088/0004-637X/718/2/1158

Lin, L., Hsieh, B.-C., Pan, H.-A., et al. 2019, ApJ, 872, 50, doi: 10.3847/1538-4357/aafa84

Lintott, C., Schawinski, K., Bamford, S., et al. 2011, MNRAS, 410, 166, doi: 10.1111/j.1365-2966.2010.17432.x

Lintott, C. J., Schawinski, K., Slosar, A., et al. 2008, MNRAS, 389, 1179, doi: 10.1111/j.1365-2966.2008.13689.x

Liu, F. S., Lei, F. J., Meng, X. M., & Jiang, D. F. 2015, MNRAS, 447, 1491, doi: 10.1093/mnras/stu2543

Liu, F. S., Mao, S., Deng, Z. G., Xia, X. Y., & Wen, Z. L. 2009, MNRAS, 396, 2003, doi: 10.1111/j.1365-2966.2009.14907.x

Liu, S., Zheng, X. Z., Shi, D. D., et al. 2023, MNRAS, 523, 2422, doi: 10.1093/mnras/stad1543

Lotz, J. M., Jonsson, P., Cox, T. J., et al. 2011, ApJ, 742, 103, doi: 10.1088/0004-637X/742/2/103

Lotz, J. M., Jonsson, P., Cox, T. J., & Primack, J. R. 2008, MNRAS, 391, 1137, doi: 10.1111/j.1365-2966.2008.14004.x

—. 2010a, MNRAS, 404, 590, doi: 10.1111/j.1365-2966.2010.16269.x

—. 2010b, MNRAS, 404, 575, doi: 10.1111/j.1365-2966.2010.16268.x

Lotz, J. M., Primack, J., & Madau, P. 2004, AJ, 128, 163, doi: 10.1086/421849

Maccagni, F. M., Morganti, R., Oosterloo, T. A., & Mahony, E. K. 2014, A&A, 571, A67, doi: 10.1051/0004-6361/201424334

Madsen, G. J., Reynolds, R. J., & Haffner, L. M. 2006, ApJ, 652, 401, doi: 10.1086/508441

Mannucci, F., Cresci, G., Maiolino, R., Marconi, A., & Gnerucci, A. 2010, MNRAS, 408, 2115–2127, doi: 10.1111/j.1365-2966.2010.17291.x

Mantha, K. B., McIntosh, D. H., Ciaschi, C. P., et al. 2019, MNRAS, 486, 2643, doi: 10.1093/mnras/stz872

Marchesi, S., Civano, F., Elvis, M., et al. 2016, ApJ, 817, 34, doi: 10.3847/0004-637X/817/1/34

Marian, V., Jahnke, K., Mechtley, M., et al. 2019, ApJ, 882, 141, doi: 10.3847/1538-4357/ab385b

Marinacci, F., Vogelsberger, M., Pakmor, R., et al. 2018, MNRAS, 480, 5113, doi: 10.1093/mnras/sty2206

Marino, R. A., Rosales-Ortega, F. F., Sánchez, S. F., et al. 2013, A&A, 559, A114, doi: 10.1051/0004-6361/201321956

Martin, G., Kaviraj, S., Devriendt, J. E. G., Dubois, Y., & Pichon, C. 2018, MNRAS, 480, 2266, doi: 10.1093/mnras/sty1936

Matteo, T. D., Springel, V., & Hernquist, L. 2005, Nature, 433, 604, doi: 10.1038/nature03335

McAlpine, S., Harrison, C. M., Rosario, D. J., et al. 2020, MNRAS, 494, 5713, doi: 10.1093/mnras/staa1123

McClure-Griffiths, N. M., Pisano, D. J., Calabretta, M. R., et al. 2009, ApJS, 181, 398, doi: 10.1088/0067-0049/181/2/398

McDermid, R. M., Alatalo, K., Blitz, L., et al. 2015, MNRAS, 448, 3484–3513, doi: 10.1093/mnras/stv105

McIntosh, D. H., Guo, Y., Hertzberg, J., et al. 2008, MNRAS, 388, 1537, doi: 10.1111/j.1365-2966.2008.13531.x

Mechtley, M., Jahnke, K., Windhorst, R. A., et al. 2016, ApJ, 830, 156, doi: 10.3847/0004-637X/830/2/156

Menci, N., Gatti, M., Fiore, F., & Lamastra, A. 2014, A&A, 569, A37, doi: 10.1051/0004-6361/201424217

Michel-Dansac, L., Lambas, D. G., Alonso, M. S., & Tissera, P. 2008, MNRAS, 386, L82, doi: 10.1111/j.1745-3933.2008.00466.x

Mihos, J. C., & Hernquist, L. 1996, ApJ, 464, 641, doi: 10.1086/177353

Miyazaki, S., Komiyama, Y., Kawanomoto, S., et al. 2018, PASJ, 70, S1, doi: 10.1093/pasj/psx063

Montuori, M., Di Matteo, P., Lehnert, M. D., Combes, F., & Semelin, B. 2010, A&A, 518, A56, doi: 10.1051/0004-6361/201014304

Morales-Vargas, A., Torres-Papaqui, J. P., Rosales-Ortega, F. F., et al. 2020, MNRAS, 499, 4370, doi: 10.1093/mnras/staa2833

Moran, S. M., Heckman, T. M., Kauffmann, G., et al. 2012, ApJ, 745, 66, doi: 10.1088/0004-637X/745/1/66

Moreno, J., Torrey, P., Ellison, S. L., et al. 2015, MNRAS, 448, 1107, doi: 10.1093/mnras/stv094

Mulchaey, J. S., Lubin, L. M., Fassnacht, C., Rosati, P., & Jeltema, T. E. 2006, ApJ, 646, 133, doi: 10.1086/504790

Naab, T., & Burkert, A. 2001, in Astronomical Society of the Pacific Conference Series, Vol. 249, The Central Kiloparsec of Starbursts and AGN: The La Palma Connection, ed. J. H. Knapen, J. E. Beckman, I. Shlosman, & T. J. Mahoney, 735. https://arxiv.org/abs/astro-ph/0110374

Naab, T., & Burkert, A. 2003, ApJ, 597, 893, doi: 10.1086/378581

Naiman, J. P., Pillepich, A., Springel, V., et al. 2018, MNRAS, 477, 1206, doi: 10.1093/mnras/sty618

Nair, P. B., & Abraham, R. G. 2010, VizieR Online Data Catalog, J/ApJS/186/427

Nedelchev, B., Coccato, L., Corsini, E. M., et al. 2019, A&A, 623, A87, doi: 10.1051/0004-6361/201832840

Negroponte, J., & White, S. D. M. 1983, MNRAS, 205, 1009, doi: 10.1093/mnras/205.4.1009

Nelson, D., Pillepich, A., Springel, V., et al. 2018, MNRAS, 475, 624, doi: 10.1093/mnras/stx3040

—. 2019, MNRAS, 490, 3234, doi: 10.1093/mnras/stz2306

Nevin, R., Blecha, L., Comerford, J., & Greene, J. 2019, ApJ, 872, 76, doi: 10.3847/1538-4357/aafd34

Nevin, R., Blecha, L., Comerford, J., et al. 2023, MNRAS, 522, 1, doi: 10.1093/mnras/stad911

Nevin, R., Blecha, L., Comerford, J., et al. 2021, ApJ, 912, 45, doi: 10.3847/1538-4357/abe2a9

Noeske, K. G., Weiner, B. J., Faber, S. M., et al. 2007, ApJ, 660, L43, doi: 10.1086/517926

Oh, S., Kim, K., Lee, J. H., et al. 2019, MNRAS, 488, 4169, doi: 10.1093/mnras/stz1920

Omori, K. C., Bottrell, C., Walmsley, M., et al. 2023, Galaxy mergers in Subaru HSC-SSP: a deep representation learning approach for identification and the role of environment on merger incidence. https://arxiv.org/abs/2309.15539

Parikh, T., Thomas, D., Maraston, C., et al. 2018, MNRAS, 477, 3954, doi: 10.1093/mnras/sty785

Patton, D. R., Carlberg, R. G., Marzke, R. O., et al. 2000, ApJ, 536, 153–172, doi: 10.1086/308907

Patton, D. R., Ellison, S. L., Simard, L., McConnachie, A. W., & Mendel, J. T. 2011, MNRAS, 412, 591, doi: 10.1111/j.1365-2966.2010.17932.x

Patton, D. R., Pritchet, C. J., Yee, H. K. C., Ellingson, E., & Carlberg, R. G. 1997, ApJ, 475, 29–42, doi: 10.1086/303535

Patton, D. R., Torrey, P., Ellison, S. L., Mendel, J. T., & Scudder, J. M. 2013, MNRAS, 433, L59, doi: 10.1093/mnrasl/slt058

Pearson, W. J., Wang, L., Trayford, J. W., Petrillo, C. E., & van der Tak, F. F. S. 2019, A&A, 626, A49, doi: 10.1051/0004-6361/201935355

Pearson, W. J., Wang, L., Alpaslan, M., et al. 2019, A&A, 631, A51, doi: 10.1051/0004-6361/201936337

Pearson, W. J., Wang, L., Alpaslan, M., et al. 2019, A&A, 631, A51, doi: 10.1051/0004-6361/201936337

Pearson, W. J., Suelves, L. E., Ho, S. C. C., et al. 2022, A&A, 661, A52, doi: 10.1051/0004-6361/202141013

Peebles, P. J. E. 1982, ApJ, 263, L1, doi: 10.1086/183911

Penoyre, Z., Moster, B. P., Sijacki, D., & Genel, S. 2017, MNRAS, 468, 3883, doi: 10.1093/mnras/stx762

Perez, J., Michel-Dansac, L., & Tissera, P. B. 2011, MNRAS, 417, 580, doi: 10.1111/j.1365-2966.2011.19300.x

Perez, J., Tissera, P. B., Padilla, N. D., Alonso, S., & García Lambas, D. 2009, Boletin de la Asociacion Argentina de Astronomia La Plata Argentina, 52, 225

Pillepich, A., Nelson, D., Hernquist, L., et al. 2018a, MNRAS, 475, 648, doi: 10.1093/mnras/stx3112

Pillepich, A., Springel, V., Nelson, D., et al. 2018b, MNRAS, 473, 4077, doi: 10.1093/mnras/stx2656

Pillepich, A., Nelson, D., Springel, V., et al. 2019, MNRAS, 490, 3196, doi: 10.1093/mnras/stz2338

Pilyugin, L. S. 2001, A&A, 374, 412, doi: 10.1051/0004-6361:20010732

Pipino, A., Cibinel, A., Tacchella, S., et al. 2014, ApJ, 797, 127, doi: 10.1088/0004-637X/797/2/127

Popping, G., Pillepich, A., Calistro Rivera, G., et al. 2022, MNRAS, 510, 3321, doi: 10.1093/mnras/stab3312

Press, W. H., & Schechter, P. 1974, ApJ, 187, 425, doi: 10.1086/152650

Rémy-Ruyer, A., Madden, S. C., Galliano, F., et al. 2014, A&A, 563, A31, doi: 10.1051/0004-6361/201322803

Reynolds, R. J. 1985, ApJ, 294, 256, doi: 10.1086/163294

—. 1987, ApJ, 323, 118, doi: 10.1086/165811

Rines, K., Finn, R., & Vikhlinin, A. 2007, ApJ, 665, L9, doi: 10.1086/521102

Robotham, A. S. G., Bellstedt, S., Lagos, C. d. P., et al. 2020, MNRAS, 495, 905, doi: 10.1093/mnras/staa1116

Robotham, A. S. G., Liske, J., Driver, S. P., et al. 2013, MNRAS, 431, 167–193, doi: 10.1093/mnras/stt156

Robotham, A. S. G., Driver, S. P., Davies, L. J. M., et al. 2014, MNRAS, 444, 3986, doi: 10.1093/mnras/stu1604

Rodrigues, M., Puech, M., Flores, H., Hammer, F., & Pirzkal, N. 2018, MNRAS, 475, 5133, doi: 10.1093/mnras/sty098

Rodriguez-Gomez, V., Pillepich, A., Sales, L. V., et al. 2016, MNRAS, 458, 2371, doi: 10.1093/mnras/stw456

Rosales-Ortega, F. F., Sánchez, S. F., Iglesias-Páramo, J., et al. 2012, ApJ, 756, L31, doi: 10.1088/2041-8205/756/2/L31

Rose, C., Kartaltepe, J. S., Snyder, G. F., et al. 2023, ApJ, 942, 54, doi: 10.3847/1538-4357/ac9f10

Rowlands, K., Heckman, T., Wild, V., et al. 2018, MNRAS, 480, 2544, doi: 10.1093/mnras/sty1916

Runge, J., & Yan, H. 2018, ApJ, 853, 47, doi: 10.3847/1538-4357/aaa020

Rupke, D. S. N., Kewley, L. J., & Barnes, J. E. 2010, ApJ, 710, L156–L160, doi: 10.1088/2041-8205/710/2/l156

Saitoh, T. R., Daisaka, H., Kokubo, E., et al. 2009, PASJ, 61, 481, doi: 10.1093/pasj/61.3.481

Salim, S., Boquien, M., & Lee, J. C. 2018, ApJ, 859, 11, doi: 10.3847/1538-4357/aabf3c

Salim, S., Lee, J. C., Janowiecki, S., et al. 2016, ApJS, 227, 2, doi: 10.3847/0067-0049/227/1/2

Sánchez, S. F., Rosales-Ortega, F. F., Jungwiert, B., et al. 2013, A&A, 554, A58, doi: 10.1051/0004-6361/201220669

Sánchez-Blázquez, P., Peletier, R. F., Jiménez-Vicente, J., et al. 2006, MNRAS, 371, 703, doi: 10.1111/j.1365-2966.2006.10699.x

Sanders, D. B., & Mirabel, I. F. 1996, ARA&A, 34, 749, doi: 10.1146/annurev.astro.34.1.749

Sanders, D. B., Soifer, B. T., Elias, J. H., et al. 1988, ApJ, 325, 74, doi: 10.1086/165983

Santini, P., Rosario, D. J., Shao, L., et al. 2012, A&A, 540, A109, doi: 10.1051/0004-6361/201118266

Saro, A., Mohr, J. J., Bazin, G., & Dolag, K. 2013, ApJ, 772, 47, doi: 10.1088/0004-637X/772/1/47

Satyapal, S., Ellison, S. L., McAlpine, W., et al. 2014, MNRAS, 441, 1297, doi: 10.1093/mnras/stu650

Schawinski, K., Koss, M., Berney, S., & Sartori, L. F. 2015, MNRAS, 451, 2517, doi: 10.1093/mnras/stv1136

Schulz, S., Popping, G., Pillepich, A., et al. 2020, MNRAS, 497, 4773, doi: 10.1093/mnras/staa1900

Scudder, J. M., Ellison, S. L., Torrey, P., Patton, D. R., & Mendel, J. T. 2012, MNRAS, 426, 549, doi: 10.1111/j.1365-2966.2012.21749.x

Shields, G. A. 1990, ARA&A, 28, 525, doi: 10.1146/annurev.aa.28.090190.002521

Silva, A., Marchesini, D., Silverman, J. D., et al. 2021, ApJ, 909, 124, doi: 10.3847/1538-4357/abdbb1

Silverman, J. D., Kampczyk, P., Jahnke, K., et al. 2011, ApJ, 743, 2, doi: 10.1088/0004-637X/743/1/2

Skillman, E. D., Kennicutt, R. C., & Hodge, P. W. 1989, ApJ, 347, 875, doi: 10.1086/168178

Smirnov, N. V. 1939, Bulletin Moscow University, 2, 3

Snyder, G. F., Rodriguez-Gomez, V., Lotz, J. M., et al. 2019, MNRAS, 486, 3702, doi: 10.1093/mnras/stz1059

Soares, D. S. L. 2007, AJ, 134, 71, doi: 10.1086/518240

Sol Alonso, M., Michel-Dansac, L., & Lambas, D. G. 2010, A&A, 514, A57, doi: 10.1051/0004-6361/200912814

Somerville, R. S., & Davé, R. 2015, ARA&A, 53, 51, doi: 10.1146/annurev-astro-082812-140951

Sparre, M., & Springel, V. 2016, MNRAS, 462, 2418, doi: 10.1093/mnras/stw1793

Springel, V. 2010, MNRAS, 401, 791, doi: 10.1111/j.1365-2966.2009.15715.x

Springel, V., Pakmor, R., Pillepich, A., et al. 2018, MNRAS, 475, 676, doi: 10.1093/mnras/stx3304

Stott, J. P., Collins, C. A., Burke, C., Hamilton-Morris, V., & Smith, G. P. 2011, MNRAS, 414, 445, doi: 10.1111/j.1365-2966.2011.18404.x

Stott, J. P., Collins, C. A., Sahlén, M., et al. 2010, ApJ, 718, 23, doi: 10.1088/0004-637X/718/1/23

Struble, M. F., & Rood, H. J. 1999, ApJS, 125, 35, doi: 10.1086/313274

Tamura, N., Takato, N., Shimono, A., et al. 2016, in Society of Photo-Optical Instrumentation Engineers (SPIE) Conference Series, Vol. 9908, Ground-based and Airborne Instrumentation for Astronomy VI, ed. C. J. Evans, L. Simard, & H. Takami, 99081M, doi: 10.1117/12.2232103

Tanaka, M., Koike, M., Naito, S., et al. 2023, PASJ, 75, 986, doi: 10.1093/pasj/psad055

Taylor, P., Federrath, C., & Kobayashi, C. 2018, MNRAS, 479, 141–152, doi: 10.1093/mnras/sty1439

Thibert, N., Sawicki, M., Goulding, A., et al. 2021, Research Notes of the American Astronomical Society, 5, 144, doi: 10.3847/2515-5172/ac0911

Thorne, J. E., Robotham, A. S. G., Davies, L. J. M., et al. 2021, MNRAS, 505, 540, doi: 10.1093/mnras/stab1294

—. 2022, MNRAS, 509, 4940, doi: 10.1093/mnras/stab3208

Thorp, M. D., Bluck, A. F. L., Ellison, S. L., et al. 2021, MNRAS, 507, 886, doi: 10.1093/mnras/stab2201

Thorp, M. D., Ellison, S. L., Simard, L., Sánchez, S. F., & Antonio, B. 2019, MNRAS, 482, L55, doi: 10.1093/mnrasl/sly185

Tomczak, A. R., Lemaux, B. C., Lubin, L. M., et al. 2017, MNRAS, 472, 3512, doi: 10.1093/mnras/stx2245

Toomre, A. 1977, in Evolution of Galaxies and Stellar Populations, ed. B. M. Tinsley & D. C. Larson, Richard B. Gehret, 401

Toomre, A., & Toomre, J. 1972, ApJ, 178, 623, doi: 10.1086/151823

Torrey, P., Cox, T. J., Kewley, L., & Hernquist, L. 2012, ApJ, 746, 108, doi: 10.1088/0004-637X/746/1/108

Tran, K.-V. H., Moustakas, J., Gonzalez, A. H., et al. 2008, ApJ, 683, L17, doi: 10.1086/591422

Treister, E., Schawinski, K., Urry, C. M., & Simmons, B. D. 2012, ApJ, 758, L39, doi: 10.1088/2041-8205/758/2/L39

Tremonti, C. A., Heckman, T. M., Kauffmann, G., et al. 2004, ApJ, 613, 898, doi: 10.1086/423264

Trump, J. R., Sun, M., Zeimann, G. R., et al. 2015, ApJ, 811, 26, doi: 10.1088/0004-637X/811/1/26

Tsatsi, A., Macciò, A. V., van de Ven, G., & Moster, B. P. 2015, ApJ, 802, L3, doi: 10.1088/2041-8205/802/1/l3

Urrutia, T., Lacy, M., & Becker, R. H. 2008, ApJ, 674, 80, doi: 10.1086/523959

Vila-Costas, M. B., & Edmunds, M. G. 1992, MNRAS, 259, 121, doi: 10.1093/mnras/259.1.121

Vilchez, J. M., Pagel, B. E. J., Diaz, A. I., Terlevich, E., & Edmunds, M. G. 1988, MNRAS, 235, 633, doi: 10.1093/mnras/235.3.633

Villforth, C., Hamann, F., Rosario, D. J., et al. 2014, MNRAS, 439, 3342, doi: 10.1093/mnras/stu173

Villforth, C., Hamilton, T., Pawlik, M. M., et al. 2017, MNRAS, 466, 812, doi: 10.1093/mnras/stw3037

Voges, E. S., & Walterbos, R. A. M. 2006, ApJ, 644, L29, doi: 10.1086/505575

Wake, D. A., Bundy, K., Diamond-Stanic, A. M., et al. 2017, AJ, 154, 86, doi: 10.3847/1538-3881/aa7ecc

Walmsley, M., Ferguson, A. M. N., Mann, R. G., & Lintott, C. J. 2019, MNRAS, 483, 2968, doi: 10.1093/mnras/sty3232

Walmsley, M., Lintott, C., Géron, T., et al. 2022a, MNRAS, 509, 3966, doi: 10.1093/mnras/stab2093

Walmsley, M., Scaife, A. M. M., Lintott, C., et al. 2022b, MNRAS, 513, 1581, doi: 10.1093/mnras/stac525

Walmsley, M., Allen, C., Aussel, B., et al. 2023, Journal of Open Source Software, 8, 5312, doi: 10.21105/joss.05312

Walterbos, R. A. M., & Braun, R. 1994, ApJ, 431, 156, doi: 10.1086/174475

Wang, S.-Y., Braun, D. F., Schwochert, M. A., et al. 2014, in Society of Photo-Optical Instrumentation Engineers (SPIE) Conference Series, Vol. 9147, Ground-based and Airborne Instrumentation for Astronomy V, ed. S. K. Ramsay, I. S. McLean, & H. Takami, 91475Q, doi: 10.1117/12.2057247

Weigel, A. K., Schawinski, K., Treister, E., Trakhtenbrot, B., & Sanders, D. B. 2018, MNRAS, 476, 2308, doi: 10.1093/mnras/sty383

Weigel, A. K., Schawinski, K., Caplar, N., et al. 2017, ApJ, 845, 145, doi: 10.3847/1538-4357/aa8097

Weinberger, R., Springel, V., Hernquist, L., et al. 2017, MNRAS, 465, 3291, doi: 10.1093/mnras/stw2944

Westfall, K. B., Cappellari, M., Bershady, M. A., et al. 2019, AJ, 158, 231, doi: 10.3847/1538-3881/ab44a2

Westfall, K. B., Cappellari, M., Bershady, M. A., et al. 2019, AJ, 158, 231, doi: 10.3847/1538-3881/ab44a2

Weston, M. E., McIntosh, D. H., Brodwin, M., et al. 2017, MNRAS, 464, 3882, doi: 10.1093/mnras/stw2620

White, S. D. M., & Frenk, C. S. 1991, ApJ, 379, 52, doi: 10.1086/170483

White, S. D. M., & Rees, M. J. 1978, MNRAS, 183, 341, doi: 10.1093/mnras/183.3.341

Wilkinson, D. M., Maraston, C., Goddard, D., Thomas, D., & Parikh, T. 2017, MNRAS, 472, 4297, doi: 10.1093/mnras/stx2215

Wilkinson, S., Ellison, S. L., Bottrell, C., et al. 2022, MNRAS, 516, 4354, doi: 10.1093/mnras/stac1962

Willett, K. W., Lintott, C. J., Bamford, S. P., et al. 2013, MNRAS, 435, 2835, doi: 10.1093/mnras/stt1458

Woods, D., Fahlman, G. G., & Richer, H. B. 1995, ApJ, 454, 32, doi: 10.1086/176461

Worthey, G., Faber, S. M., Gonzalez, J. J., & Burstein, D. 1994, ApJS, 94, 687, doi: 10.1086/192087

Wu, W., & Keel, W. C. 1998, AJ, 116, 1513, doi: 10.1086/300526

Yan, R., Bundy, K., Law, D. R., et al. 2016, AJ, 152, 197, doi: 10.3847/0004-6256/152/6/197

Yee, H. K. C., & Ellingson, E. 1995, ApJ, 445, 37, doi: 10.1086/175670

Yesuf, H. M. 2022, ApJ, 936, 124, doi: 10.3847/1538-4357/ac83b0

York, D. G., Adelman, J., Anderson, John E., J., et al. 2000, AJ, 120, 1579, doi: 10.1086/301513

Yu, X., Shi, Y., Chen, Y., et al. 2019, MNRAS, 486, 4463–4472, doi: 10.1093/mnras/stz1146

Zepf, S. E., & Koo, D. C. 1989, ApJ, 337, 34, doi: 10.1086/167085

Zhang, K., Yan, R., Bundy, K., et al. 2017, MNRAS, 466, 3217, doi: 10.1093/mnras/stw3308

Zhu, X.-P., Dai, J.-M., Bian, C.-J., et al. 2019, Ap&SS, 364, 55, doi: 10.1007/s10509-019-3540-1

Appendix A

Appendix A

Here, we present a reference work, where we use kinematic identification for galaxies with a kinematically disturbed core (KDC).

A.1 Introduction

A.1.1 Kinematics as an indicator

Galaxy interactions are commonly associated with disturbances in galaxy kinematics. In interacting galaxies, we expect to find complex and disturbed kinematics, such as asymmetries and distortions in both the stellar and gaseous velocity fields (Jesseit et al., 2007). These kinematic indicators can be present in galaxies that have been classified as non-merging by morphological/image based classification methods (e.g. Barrera-Ballesteros et al., 2015). By investigating the spatially resolved stellar and gaseous properties of galaxies that show disturbances in their kinematics, we can develop an understanding of the interaction processes that took place during the galaxy's existence and paint a picture of its formation and evolutionary pathways; however, there have been a number of limitations, mainly related to observational equipment, that have made studies of such properties difficult. Single fiber surveys such as SDSS are limited to the central region of the galaxy, and they cannot paint a picture of the behaviour of the entire galaxy. Similarly, long-slit surveys also have limitations, because while they are able to spatially resolve a target galaxy, it is limited to an elongated region. Recent advances in integral field

spectroscopy have given us access to spatially resolved data which will help us identify and analyse galaxies and their properties. In addition, these advancements have made the mapping of galaxies extending to their outer regions possible, allowing for a more thorough understanding of the galaxy. For example, projects such as SAURON (Bacon et al., 2001) and ATLAS3D (Cappellari et al., 2011) have been successful at spatially resolving local early type galaxies out to 1 effective radius. In this paper, we use data from the integral field spectroscopy survey MaNGA (Mapping Nearby Galaxies at Apache Point Observatory, Bundy et al. 2015) to search for and analyse interacting galaxies. In comparison to the projects above, the MaNGA survey can map out effective information out to 1.5 effective radius for two-thirds of its sample and 2.5 effective radius for one third of its sample (Yan et al., 2016), which allows for coverage of the majority of light as well as the observations of properties such as gradients at galaxy outskirts and accretion events in galaxy outskirts. MaNGA also has a larger number of galaxies observed over a wider wavelength range compared to the above surveys. By identifying a large number of galaxies as interacting/non-interacting through kinematics and investigating their properties, we hope to develop a new galaxy classification method that will increase our understanding of galaxy interactions.

A.2 Method

The integral field spectroscopic survey MaNGA is one of the three core projects of Sloan Digital Sky Survey IV (SDSS-IV, Blanton et al. 2017). It uses the 2.5 meter telescope at the Apache Point Observatory (Gunn et al., 2006). MaNGA aims to map and acquire spatially resolved spectroscopic observations of 10,000 local galaxies, in a redshift range of $0.01 < z < 0.15$, and at an average redshift of 0.037 (Law et al., 2016) by 2020. MaNGA spectra cover a wavelength range of 3,600Å–10,000Å, at a resolution of R $\sim$ 2,000.

The MaNGA target selection is optimized in such a way that galaxies are selected based on only their SDSS *i*-band absolute magnitude and redshift, and the sample is unbiased based on their sizes or environments. The methodology and extensive efforts taken for this optimisation are highlighted in Wake et al. (2017). We used data from SDSS Data Release 16, which includes

[1]https://www.sdss.org/dr16/manga/manga-data/data-access/

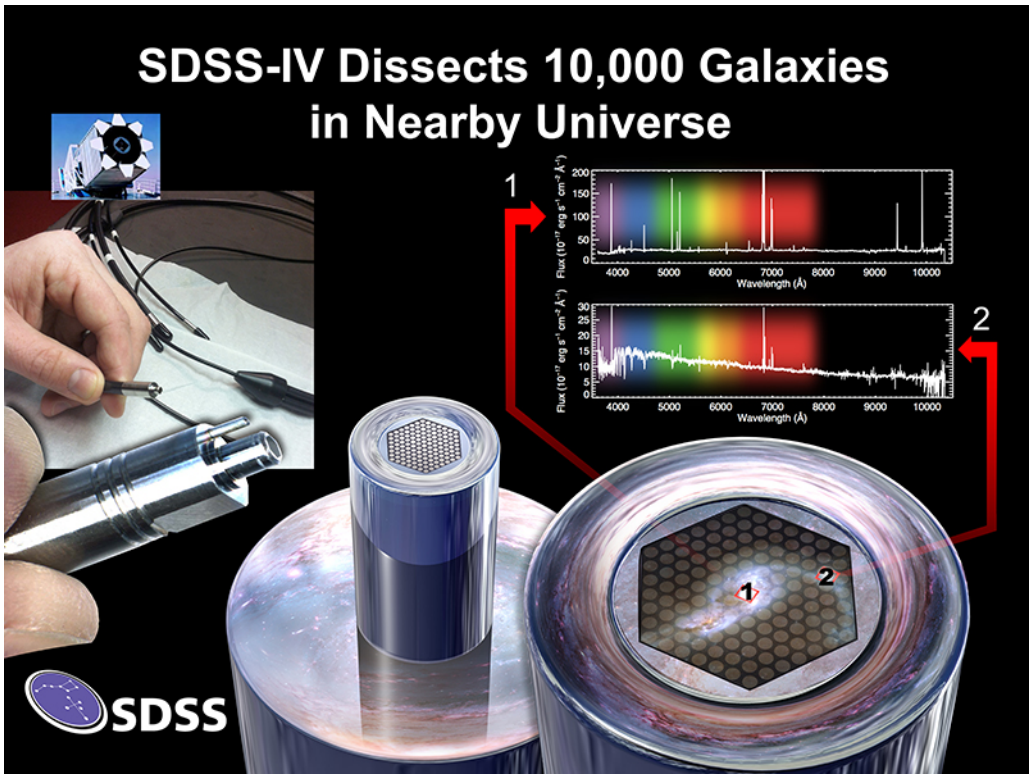

Fig. A.1: An illustration of how the array of fibers allows for spatially resolved spectroscopic observations in MaNGA. The telescope is shown in the top left.[1]

4675 unique MaNGA galaxies. We selected our galaxy sample from our DR16 data by visual classification of 2D galaxy kinematic maps provided by MaNGA. Of the 4,675 galaxies above, we were able to obtain kinematic maps of 4,671 galaxies. As stated in Sect. 1, we expect to find complex and disturbed stellar kinematics in interacting galaxies, such as asymmetries, tidal tails and bridges. While some of these features are also observable through optical images, there is a surface brightness dependence, and occasionally cannot be seen through images alone. Investigation of kinematic maps allows us to observe such features even under surface brightness limitations. We investigated the stellar velocity maps of MaNGA galaxies and selected galaxies with visually asymmetric stellar velocity maps. An example of symmetric and asymmetric stellar kinematic maps are in Figure A.2.

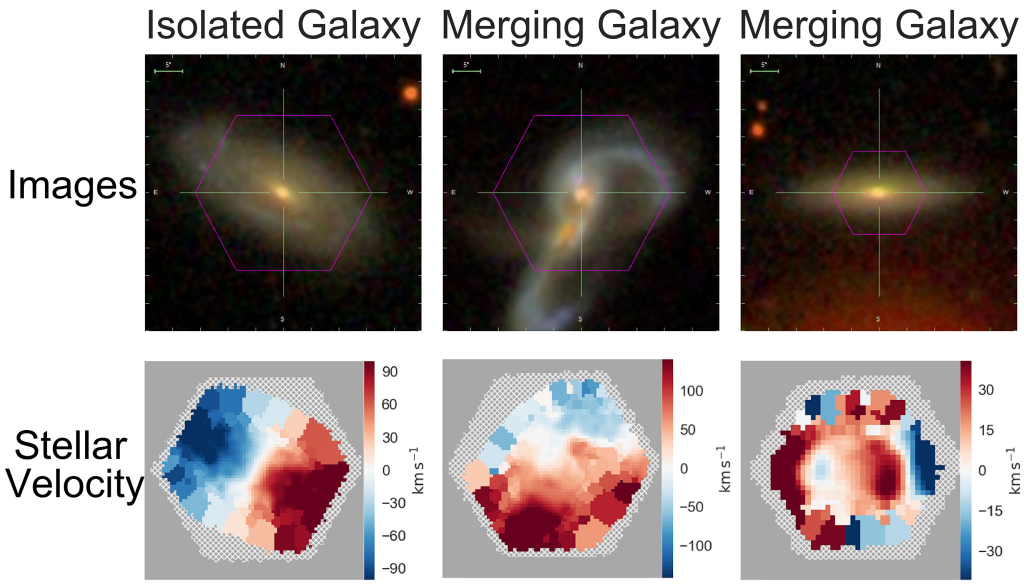

Fig. A.2: Examples of galaxies with their corresponding stellar velocity maps. The upper row shows galaxy optical images, and the lower row the stellar kinematic maps, in units of km s^{-1}.[2]

After the first identification process, we narrowed down our sample through investigation of SDSS optical images. We divided the galaxies into two sub-samples: **a)** Galaxies with secondaries and **b)** isolated galaxies. Examples of isolated and galaxies with secondaries, in addition to their kinematics, are shown in Figure A.3.

[2]https://www.sdss.org/press-releases/dont-judge-a-galaxy-by-its-cover-astronomers-develop-new-tool-to-find-merging-galaxies/

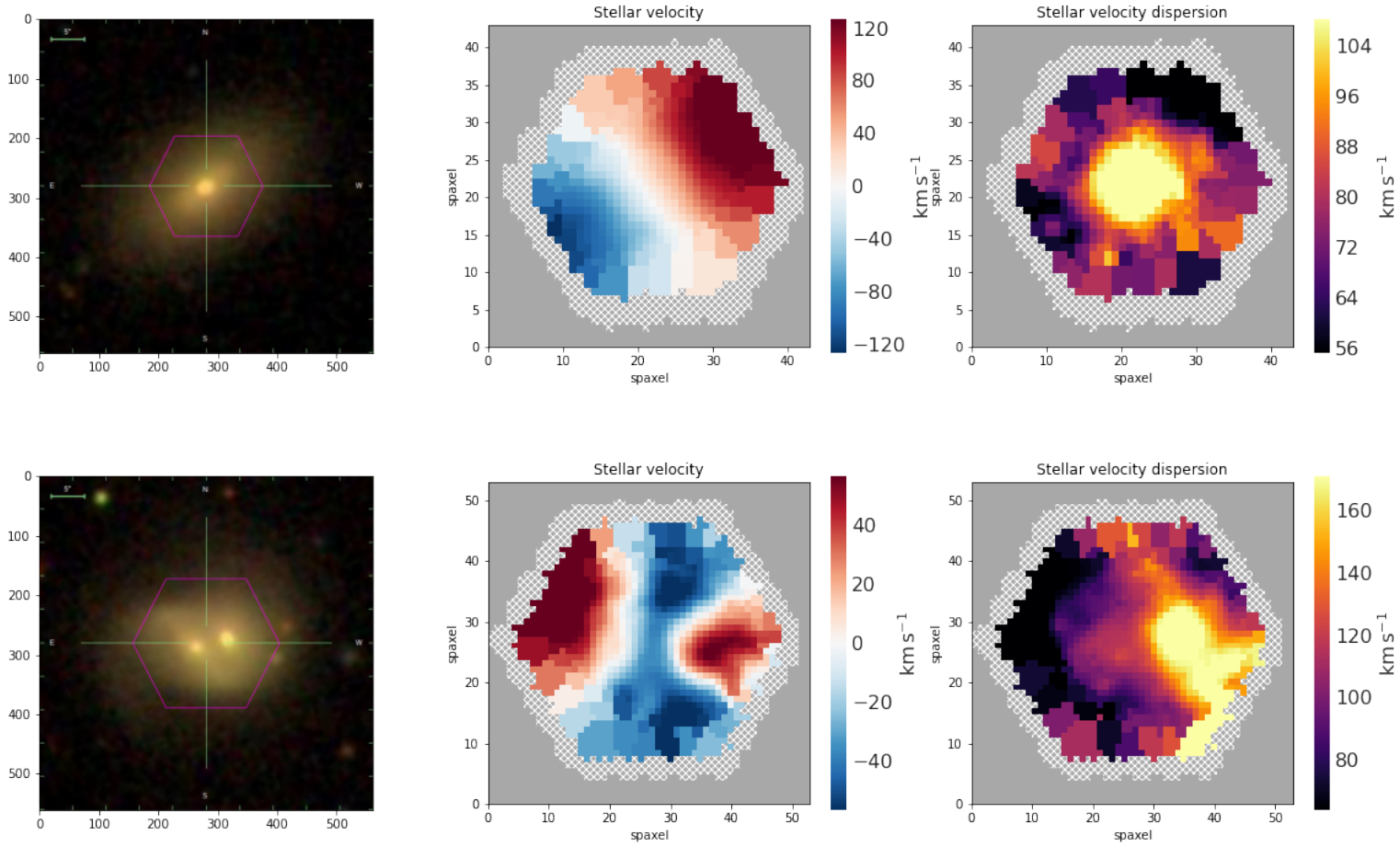

Fig. A.3: Examples of an isolated galaxy (top), and a galaxy with a secondary (bottom), with their stellar velocity and stellar velocity dispersion maps.

We were left with a sample of 786 galaxies with secondaries and 783 isolated galaxies. A simple graphic flowchart of our process is highlighted in Fig. A.4.

Of the isolated galaxies, we further identified galaxies with a counter-rotating core. Of a broader group of galaxies with a kinematically distinct stellar core (KDC), which are galaxies with a rotational misalignment between the core and main body of > 30 deg (Krajnović et al., 2011), galaxies with a counter-rotating core have a core and main body rotating in opposite directions (= 180 deg). Such a feature is thought to be a relic of an external gas accretion event (Bertola et al., 1992). A significant amount of angular momentum is required to change the orientation of the co-rotating gas, and external processes, for example, a major merger (e.g. Bender &

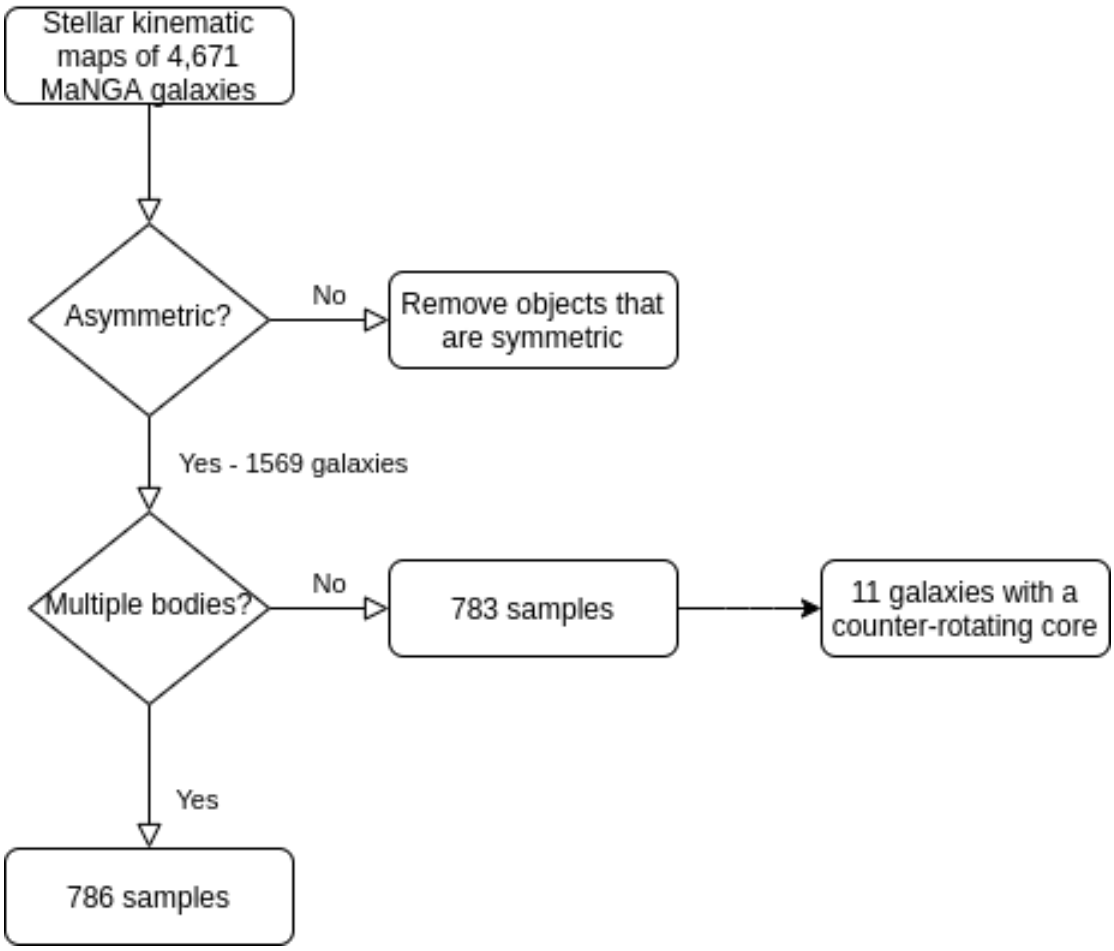

Fig. A.4: A simplified flowchart of our identification process.

Surma, 1992; Barnes & Hernquist, 1991), are more likely to provide this angular momentum than an internal one. We considered galaxies to have counter-rotating cores if their stellar velocity maps **a)** had a rotational misalignment between the inner and outer galactic regions and **b)** the misalignment was large enough such that the inner and outer regions were rotating in opposite directions, as in the core and main body were counter-rotating with respect to each other (= 180 deg). Of the stellar velocity maps of 4671 of 4675 MaNGA galaxies, and identified eleven galaxies with a kinematically distinct core in their stellar maps. Of these eleven galaxies, we used the spatially resolved BPT diagrams (Baldwin et al., 1981) to identify three galaxies as star-forming (SF), five as AGN-hosting, two non-classified, and one ambiguous. We investigate the spatially resolved kinematics, stellar population properties and star formation histories of these galaxies. Table A.1 shows our galaxy sample.

We plan to subdivide and conduct investigations on the other asymmetric isolated galaxies in a later study.

A.3 Data Analysis

We conducted two studies for this work. The first part of this work involves the investigation of galaxies with a counter-rotating core, where we looked at the physical properties of the eleven galaxies found in the previous section. The second part of this work revolves around the development of a classification mechanism for interacting galaxies using kinematic indicators. We write here the methods used to obtain the stellar kinematics of the MaNGA galaxies, as well as the galaxy physical properties used in the analysis of the galaxies with a counter-rotating core. For the first part of our work, we focused on investigating the spatially resolved **a)** stellar and gaseous kinematics, **b)** stellar population properties and **c)** star formation histories of our sample. By investigating **a)**, we can check for consistency with previous works that suggest galaxies that have undergone an external accretion event are likely to have misaligned stellar and gaseous kinematics (Bertola et al., 1992). We investigated **b)** to understand the process via which the counter-rotating core may have formed. We investigated **c)** to check if the galaxy had recently experienced a star formation episode, and if so, where it occurred.

Plate-IFU **(a)**	z **(b)**	M_* **(c)**	R_e **(d)**	Age **(e)**	Type **(f)**	p_m (GZ) **(g)**	p_m (DL) **(h)**
8143-3702	0.025	6.384×10^9	4.454	0.852	AGN	0	0.140
8155-3702	0.023	1.111×10^{10}	3.516	0.553	AGN	0	0.225
8606-3702	0.024	1.596×10^{10}	8.042	N/A	AGN	0	0.563
8989-9101	0.033	2.318×10^{10}	7.961	0.814	AGN	0	0.552
8995-3703	0.055	2.174×10^{10}	3.178	0.976	AGN	0.049	0.908
8615-1902	0.020	5.974×10^9	3.679	0.775	SF	0.018	0.168
9027-3703	0.021	2.443×10^9	4.904	0.335	SF	0	0.132
9872-3701	0.020	5.556×10^9	3.849	0.743	SF	0	0.167
8143-1902	0.041	7.967×10^9	1.901	0.984	unclassified	0	0.135
8335-1901	0.055	2.174×10^{10}	3.178	0.976	unclassified	0	0.223
9027-1902	0.022	3.657×10^9	2.253	0.8958	ambiguous	0	0.164

Table A.1: List of galaxy sample. Column **(a)**: MaNGA plate-ifu identification; column **(b)**: redshift; column **(c)**: galaxy stellar mass, given in $M_\odot$; column **(d)**: elliptical Petrosian 50 percent light radius given in arcsec; column **(e)**: age, given in Gyr, from Goddard et al. (2017), estimated with 1-sigma errors for a central 3-arcsecond aperture and for an elliptical radius of one effective radius R_e; column **(f)**: galaxy classification from spatially resolved BPT diagram; column **(g)**: merger probability in Darg et al. (2010); column **(h)**: merger probability given in Fischer et al. (2019).

A.3.1 Stellar and gas kinematics

The kinematic maps of both stellar and ionized gas were obtained from the output of the data analysis pipeline (DAP) in MaNGA (Westfall et al., 2019). The DAP bins adjacent spaxels using the Voronoi binning method of Cappellari & Copin (2003), and the spectra of these spaxels are stacked and averaged to meet he target minimum signal-to-noise (S/N) ratio to obtain accurate stellar kinematics, which in this case is 10. The stellar continuum of each binned spectra was fitted using the penalized pixel-fitting (pPXF) method by Cappellari (2017) and hierarchically clustered MILES templates (MILES-HC, MILES stellar library: Sánchez-Blázquez et al. 2006). The stellar kinematic information (velocity and velocity dispersion) was obtained through this fitting process. Once the fitting is finished, emission line analysis is conducted. Emission line measurements were made in two ways, both from emission line moments and Gaussian emission-models, and they provided us with best-fit continuum models and fluxes and equivalent widths of emission lines. These measurements also give us the information on the velocity and velocity dispersion, σ. For this work, we utilised Hα (6564 Å) emission lines to investigate gaseous kinematics.

A.3.2 Stellar population properties

To obtain the stellar population properties, such as metallicity and age, we referred to the MaNGA FIREFLY Value Added Catalogue (Goddard et al. 2017; Parikh et al. 2018, hereafter MaNGA FIREFLY VAC), which provides spatially resolved stellar population properties for MaNGA galaxies. The MaNGA FIREFLY VAC used the full spectral fitting code FIREFLY (**F**itting **I**te**R**ativ**E**ly for **F**or **L**ikelihood Anal**Y**sis, Wilkinson et al. 2017) to obtain the stellar population properties. FIREFLY is a χ^2 minimisation fitting code that best fits a spectral energy distribution (SED) with a linear combination of simple stellar populations (SSPs). The best-fit combination provided us with light and mass-weighted ages log (Gyr) and metallicities $[Z/H]$. This code is applied to the spatially resolved spectra of MaNGA galaxies to give us spatially resolved properties and gradients. Details on how the ages and metallicities were obtained from spectra are written in Goddard et al. (2017) and references within. FIREFLY is applied to spectra binned using the Voronoi method with a minimum S/N of 10 per pixel. The on-sky position of each bin

(relative to the galactic center) was used to obtain the effective radius of each bin, and gradients were measured using least-squares linear regression for data points out to $1.5R_e$. Details on FIREFLY are available in Wilkinson et al. (2017); Goddard et al. (2017); Parikh et al. (2018).

A.3.3 Star formation histories

To investigate the star formation history of the galaxies with a counter-rotating core, we use the D_n4000 versus $H\delta_A$ diagnostic diagram developed by Kauffmann et al. (2003). This diagnostic is based on two spectral indices, the 4000 Å break and the strength of the Hδ absorption line. The combination of these two indices can tell us about the recent star formation history of galaxies. The two indices are inversely correlated. Galaxies with recent star formation activity have a weaker D_n4000 value and deeper $H\delta_A$ absorption index.

The 4000 Å break is seen due to the accumulation of multiple spectral lines in a narrow wavelength region. This is due to two factors, one being the lack of hot blue stars, and the other being metals in the stellar atmosphere absorbing high energy radiation. Old stellar populations have a large 4000 Å break, and young stellar populations a small one. The D_n4000 index is a parameter defined by Bruzual A. (1983) as the ratio of the average flux density F_ν in the bands 3750–3950 and 4050–4250 Å.

Strong Hδ absorption lines are an indicator of recently ceased starburst activity, with no star formation in the last 0.1–1 Gyr (Goto et al., 2003). The stellar population is dominated by A stars, which have a stronger Hδ absorption than O and B stars. The $H\delta_A$ index is defined as the equivalent width of the Hδ absorption feature in the bandpass 4083–4122 Å.

These indices were available in spatially resolved form for MaNGA galaxies in the MaNGA FIREFLY VAC. For the D_n4000 index, MaNGA FIREFLY VAC uses a narrower continuum band than defined by Bruzual A. (1983), that is, 3850–3950 and 4000–4100 Å, which was introduced by Balogh et al. (1999) to calculate the index. We therefore followed their method and adopted that for this work. For $H\delta_A$, MaNGA FIREFLY VAC calculates this index using Equation (2) of Worthey et al. (1994):

$$EW = \int_{\lambda_1}^{\lambda_2} \left(1 - \frac{F_{I\lambda}}{F_{C\lambda}}\right) \tag{A.1}$$

where $F_{I\lambda}$ is the flux per unit wavelength in the index passband, $F_{C\lambda}$ the straight-line continuum flux in the index passband, and λ_1 and λ_2 the wavelength range.

The D_n4000–Hδ_A plane introduced by Kauffmann et al. (2003) is a very powerful diagnostic to estimate star formation activity in a galaxy over the past 1–2 Gyr. In addition, the two indices are largely insensitive to dust attenuation, which can increase the chance of inaccuracies. Whereas Kauffmann et al. (2003) used this plane to identify whether or not a galaxy as a whole has had recent star formation, we use this plane on the spatially resolved indices of each galaxy in our sample to examine if and where the galaxy has experienced recent star forming activity.

A.4 Results

A.4.1 Results - Galaxies with a counter-rotating core

In the following sections, we discuss our findings with regards to the stellar and gaseous kinematics, stellar population properties and star formation histories of the eleven galaxies with a counter-rotating core.

Stellar and gaseous properties

Figure A.5 shows the SDSS optical images, and Figure A.6 shows the kinematic maps of our entire galaxy sample. From left to right in Figure A.6, the columns show the MaNGA plate-IFU identification, the stellar velocity, stellar σ, Hα velocity, and Hα σ maps. We find that most of our samples have a decoupling between the stellar and gaseous velocity maps. While the stellar velocity maps show the feature of a KDC, such a feature is absent from most of the gaseous velocity maps.

We also investigated the rotational direction of the stars and gas, and we noted the differences. The three star-forming galaxies and one of the AGN-hosting galaxies show that the rotational direction of gas was opposite to that of the main stellar body, that is, the gas co-rotates with respect to the KDC of these galaxies. The four remaining AGNs show that the rotational direction of the gas was the same as that of the main stellar body, meaning the gas counter-rotates with respect to the KDC of these galaxies. Of the two unclassified galaxies, the gas is co-rotating with

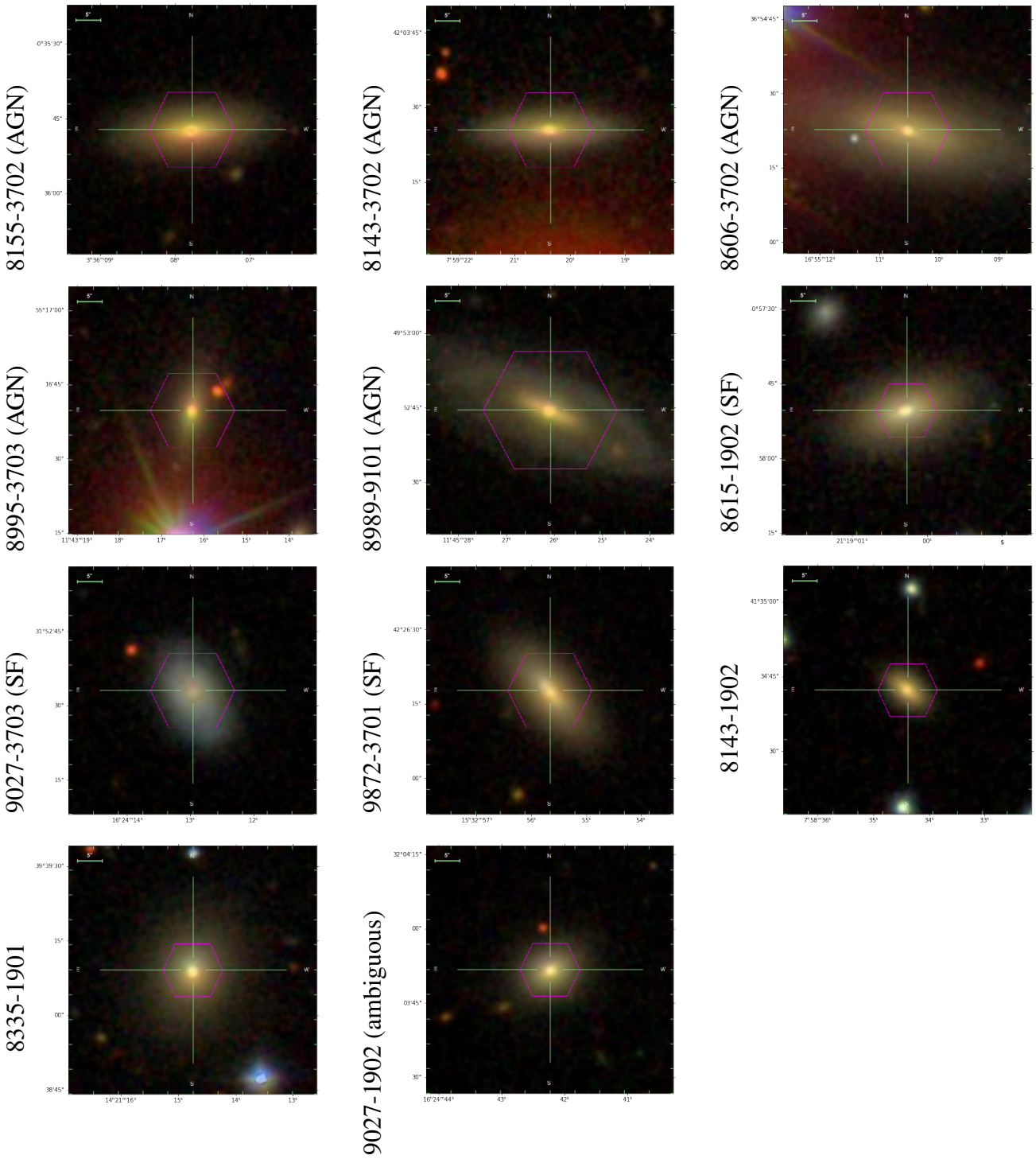

Fig. A.5: SDSS optical images of the galaxies sampled in this work. The magenta hexagons indicate the surveyed area of the galaxy.

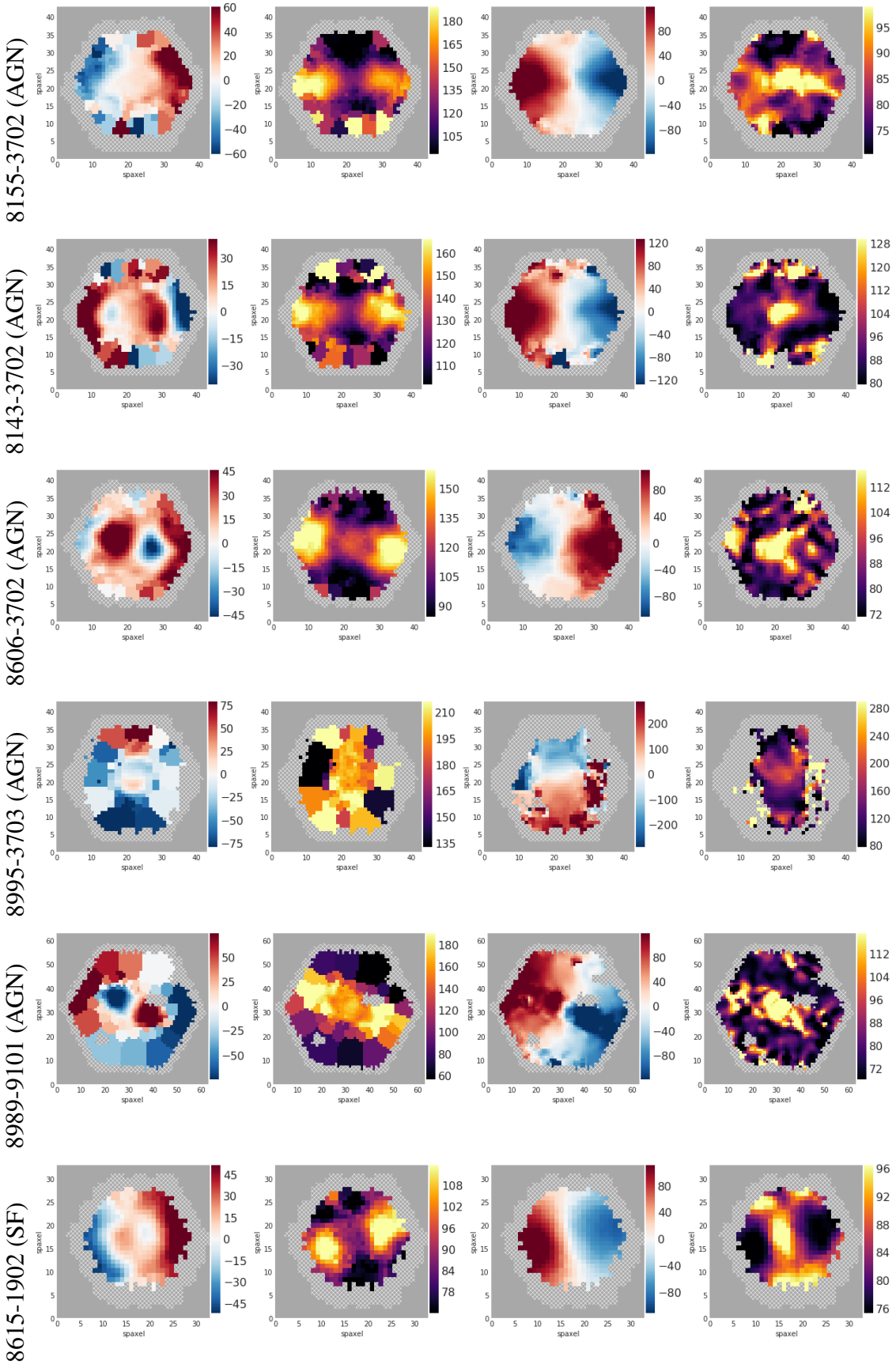

Fig. A.6: Kinematic maps for our galaxy sample. The first column shows the MaNGA plate-ifu identification, the second the line-of-sight stellar velocity (km s^{-1}), third the line-of-sight stellar velocity dispersion (km s^{-1}), the fourth the line-of-sight Hα velocity (km s^{-1}), and the fifth the line-of-sight Hα velocity dispersion (km s^{-1}). In the maps, 1 spaxel = 0.5 arcsec.

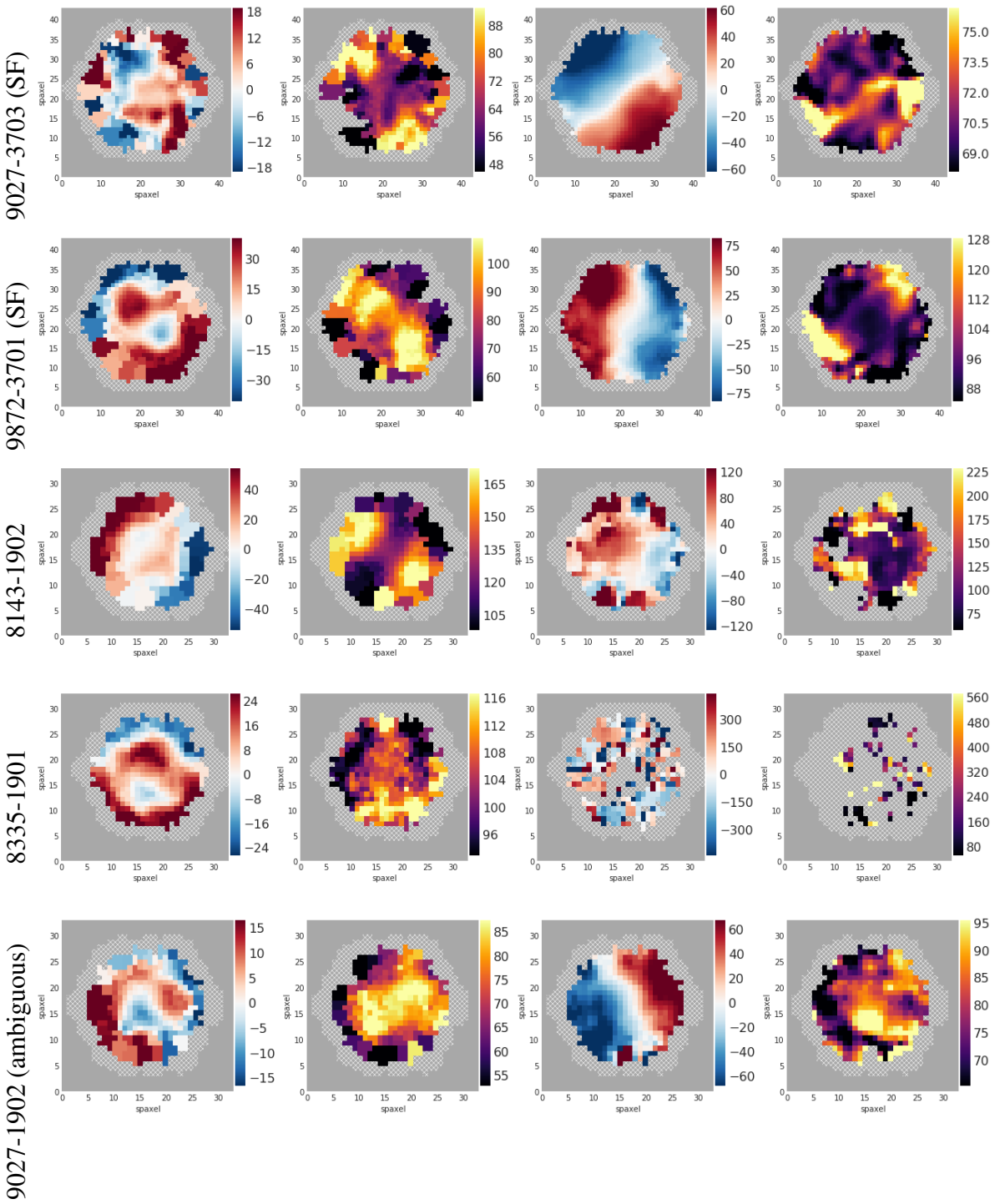

Fig. A.6: Continued.

the main body in 8143–1902. 8335–1901 does not have sufficient measurements to make any statement. Ambiguous galaxy 9027-1902 has gas co-rotating with the KDC.

Looking at the velocity dispersion maps, we find that many of the galaxies show two distinct peaks in the stellar σ maps, which decoupled with the Hα σ maps. These two peaks have previously been referred to as "2-σ galaxies" (Krajnović et al., 2011), with the two peaks in the stellar velocity dispersion maps lying off-centered symmetrically along the major axis of the galaxy. The Hα σ maps show varying behaviour, with the star-forming galaxies showing peaks close to perpendicular to the stellar σ, and the AGN galaxies showing a central peak. The two unclassified galaxies lack sufficient data to allow us to make any statement about their Hα σ maps. The ambiguous galaxy has a slightly off-centered peak.

Stellar population properties

Plate-IFU	Age Gradient	Age Gradient Zeropoint	Metallicity Gradient	Metallicity Gradient Zeropoint
8143-3702 (AGN)	0.013±0.013	0.832	-0.152±0.027	0.114
8155-3702 (AGN)	0.016±0.071	0.629	-0.159±0.012	0.114
8606-3702 (AGN)	0.058±0.005	0.811	-0.245±0.142	0.157
8989-9101 (AGN)	-0.108±0.028	1.003	-0.110±0.079	0.079
8995-3703 (AGN)	-0.044±0.030	1.023	0.073±0.027	-0.198
8615-1902 (starforming)	0.179±0.005	0.516	0.079±0.070	-0.242
9027-3703 (starforming)	-0.209±0.052	0.650	0.040±0.049	-0.267
9872-3701 (starforming)	0.259±0.032	0.369	-0.049±0.011	-0.098
8143-1902 (unclassified)	0.028±0.021	0.905	-0.048±0.017	0.133
8335-1901 (unclassified)	0.121±0.024	0.649	-0.109±0.008	0.109
9027-1902 (ambiguous)	0.078±0.030	0.787	-0.142±0.014	-0.089

Table A.2: Stellar population gradients given for our galaxy sample within 1.5 R_e, obtained from the MaNGA FIREFLY VAC.

Table A.2 shows the age and metallicity gradients of our sample, with both values provided from the MaNGA FIREFLY VAC, obtained by linearly fitting the data points with 1.5 R_e. Figure A.7 graphs the gradients. Figure A.8 shows the spatially resolved age and metallicity maps of our sample. The left diagram shows the ages, and the right the metallicities. Our results show that

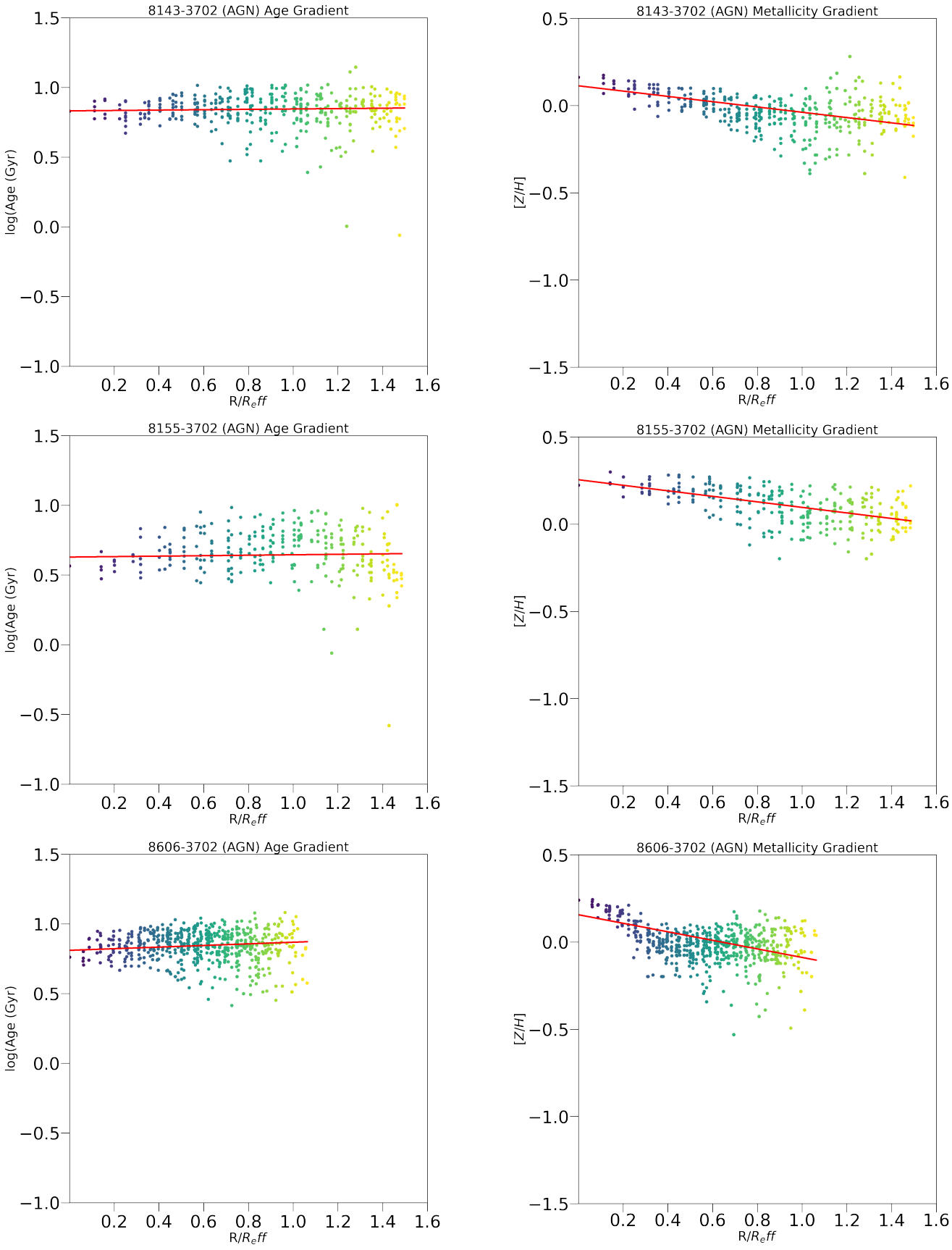

Fig. A.7: The age (in units of log(Age(Gyr))). and metallicity (in units of [Z/H]) gradients of our sample. The first column shows the age gradients, and the second the metallicity gradients. The red lines indicate the best fit gradients from the MaNGA FIREFLY VAC, obtained within 1.5 R_e.

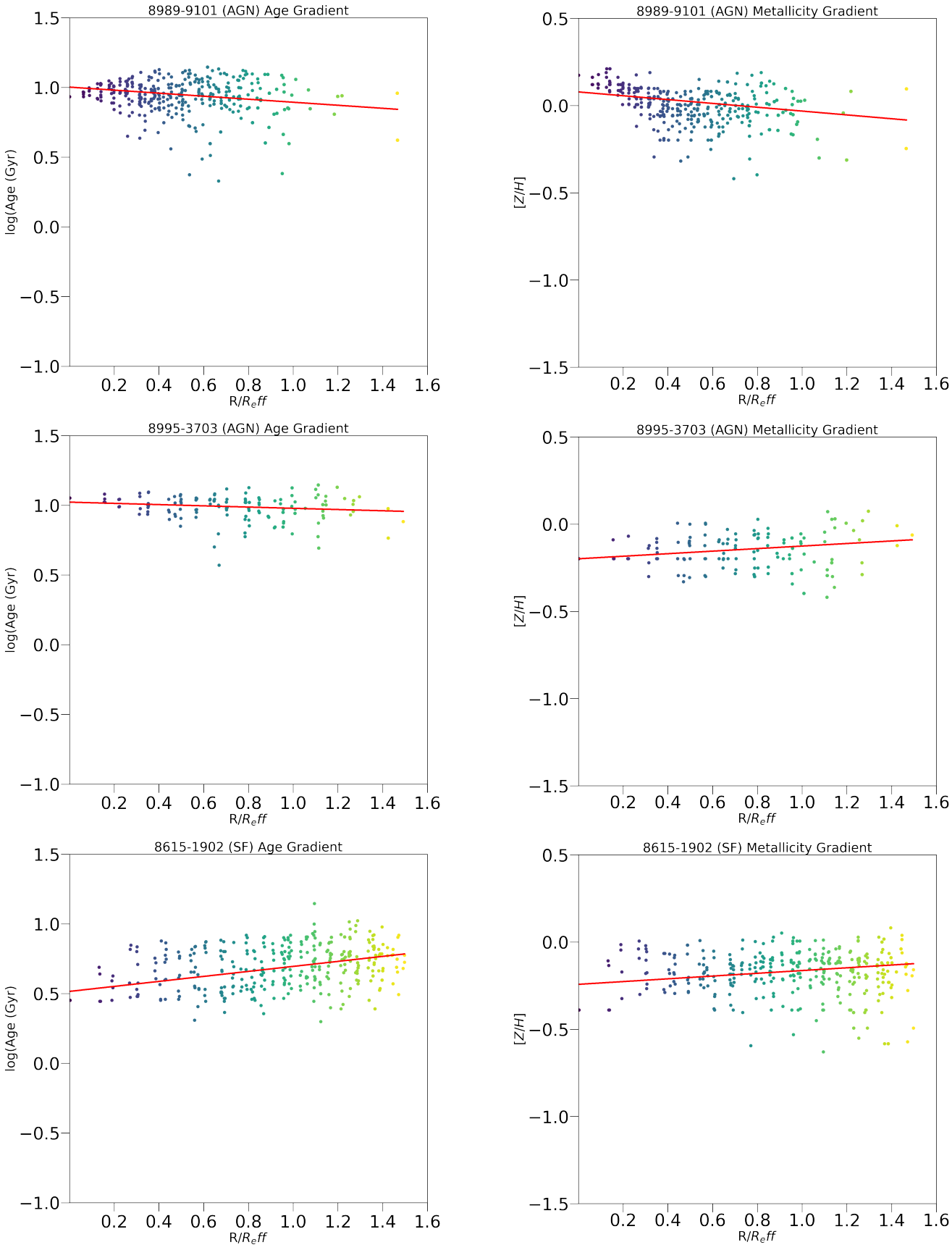

Fig. A.7: Continued.

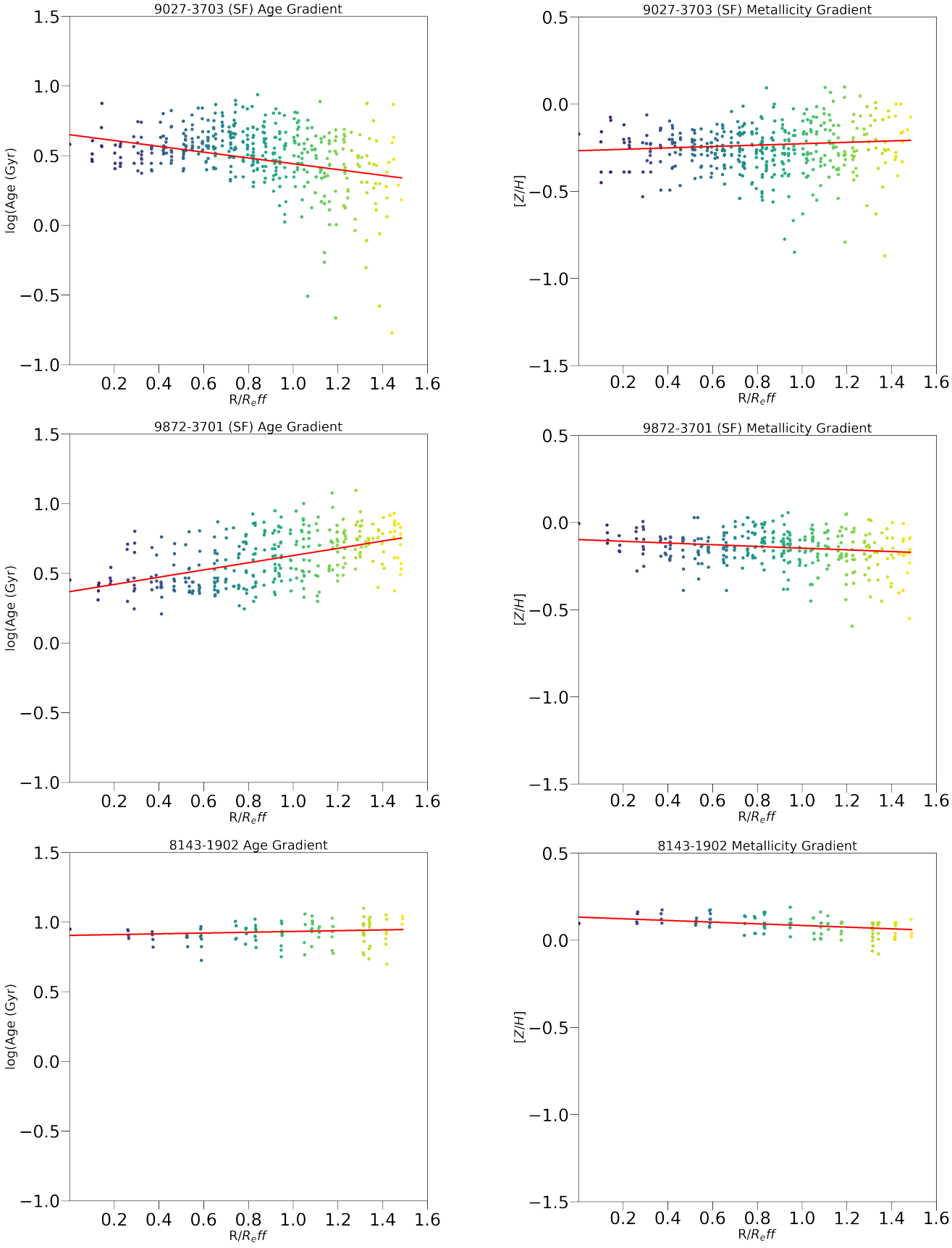

Fig. A.7: Continued.

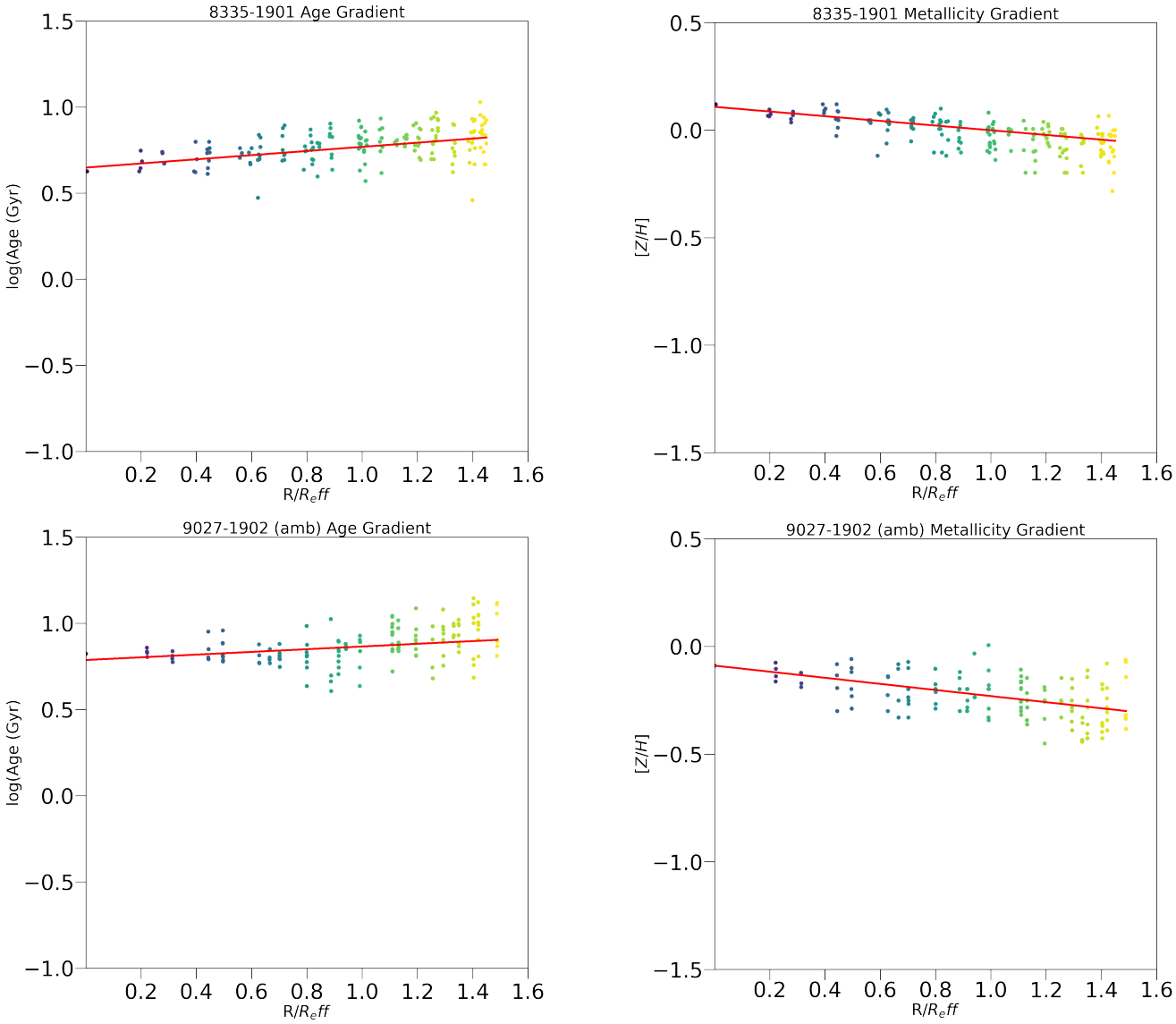

Fig. A.7: Continued.

in the AGN-hosting galaxies, the ages show relatively shallow gradients compared to the star-forming galaxies, and the metallicities show more steep gradients in the AGN hosts compared to the star-forming galaxies. Two of the three star-forming galaxies, 9872–3701 and 8615–1902, show positive gradients, while 9027–3702 has a negative gradient. The two unclassified galaxies have positive age and negative metallicity gradients, however 8143–1902 has shallower gradients compared to 8335–1901. The ambiguous galaxy show gradient steepnesses similar to those of the AGN hosts.

Star Formation Histories

Figure A.9 shows the spatially resolved D_n4000 and $H\delta_A$ distributions of our sample. From left to right, the columns show the D_n4000 and $H\delta_A$ maps. Figure A.10 shows the D_n4000 versus $H\delta_A$ plane plotted with their radial profiles. Our results show that two of the three star-forming galaxies, 9872–3701 and 8615–1902, show distinctly different behaviour compared to the rest of the sample.

We see that 9872–3701 and 8615–1902 have increasing D_n4000 radially outward, with the core showing $D_n4000 < 1.5$, indicating young stellar populations in the core compared to the outskirts. The rest of the sample show D_n4000 decreasing radially outward, with the core having $D_n4000 > 1.5$, denoting old stellar populations. The outskirts of the AGN-hosting galaxies show younger stellar populations.

We also see that 9027–3703 and 8615-1902 have a high $H\delta_A$ in the core region, and lower values in the outskirts. This indicates that recent star formation occurred in the galaxy core. The rest of the sample show opposing behaviour, with the outskirts displaying a higher $H\delta_A$ than the core. However, the outskirts mostly display a lower value than the cores of the star-forming galaxies. Looking at $H\delta_A$ plotted as a function of D_n4000 in Figure A.10, we can see that the radial gradient for 9027–3703 and 8615–1902 shows a decrease in $H\delta_A$/increase in D_n4000 radially outward, which is opposite to the rest of the sample. The unclassified and ambiguous galaxies do not show much of a gradient in their distributions.

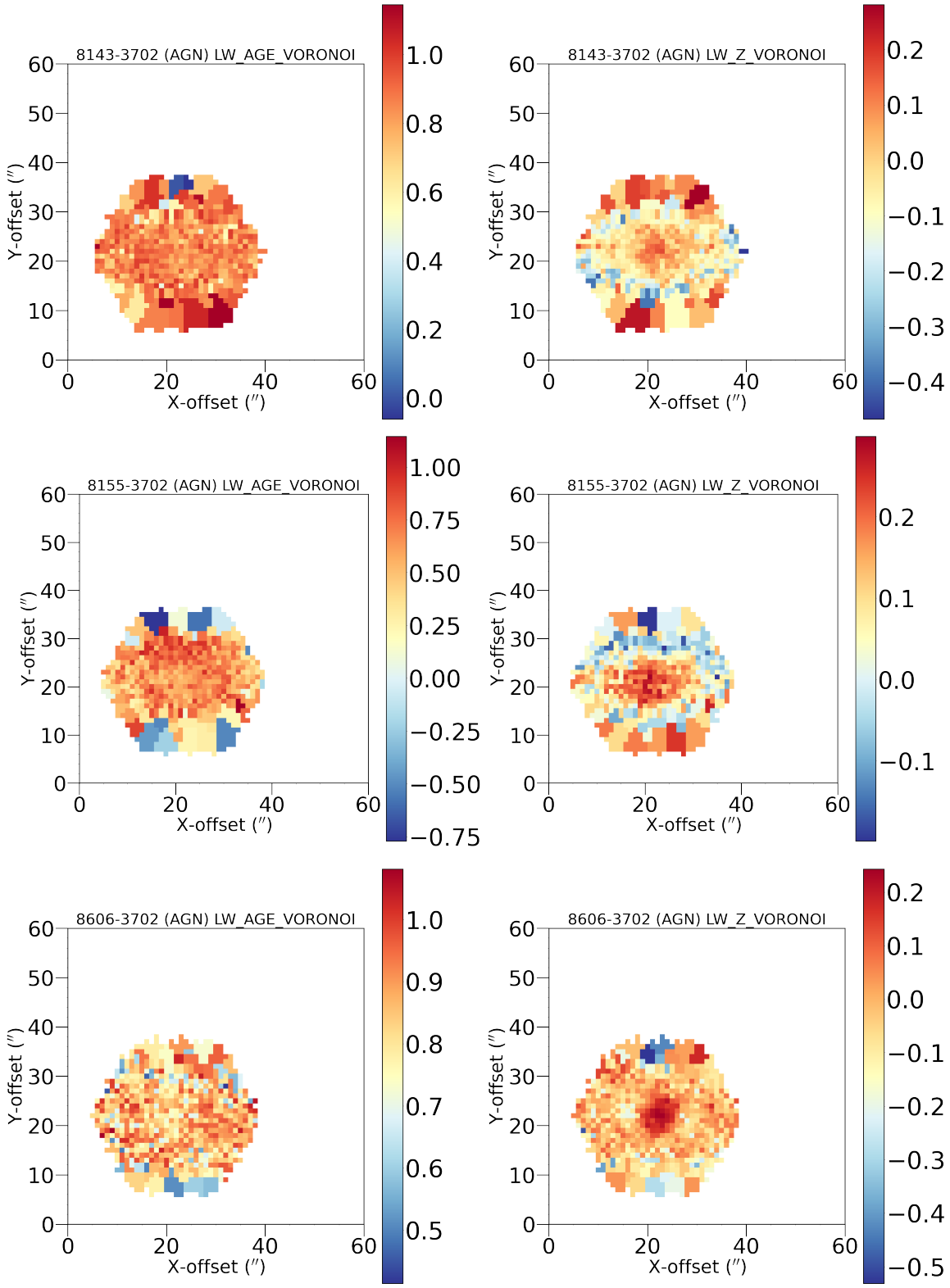

Fig. A.8: The spatially resolved age (in units of log(Age(Gyr))). and metallicity (in units of [Z/H]) distributions of our sample. The first column shows the spatially resolved age distribution, and the second the spatially resolved metallicity distribution.

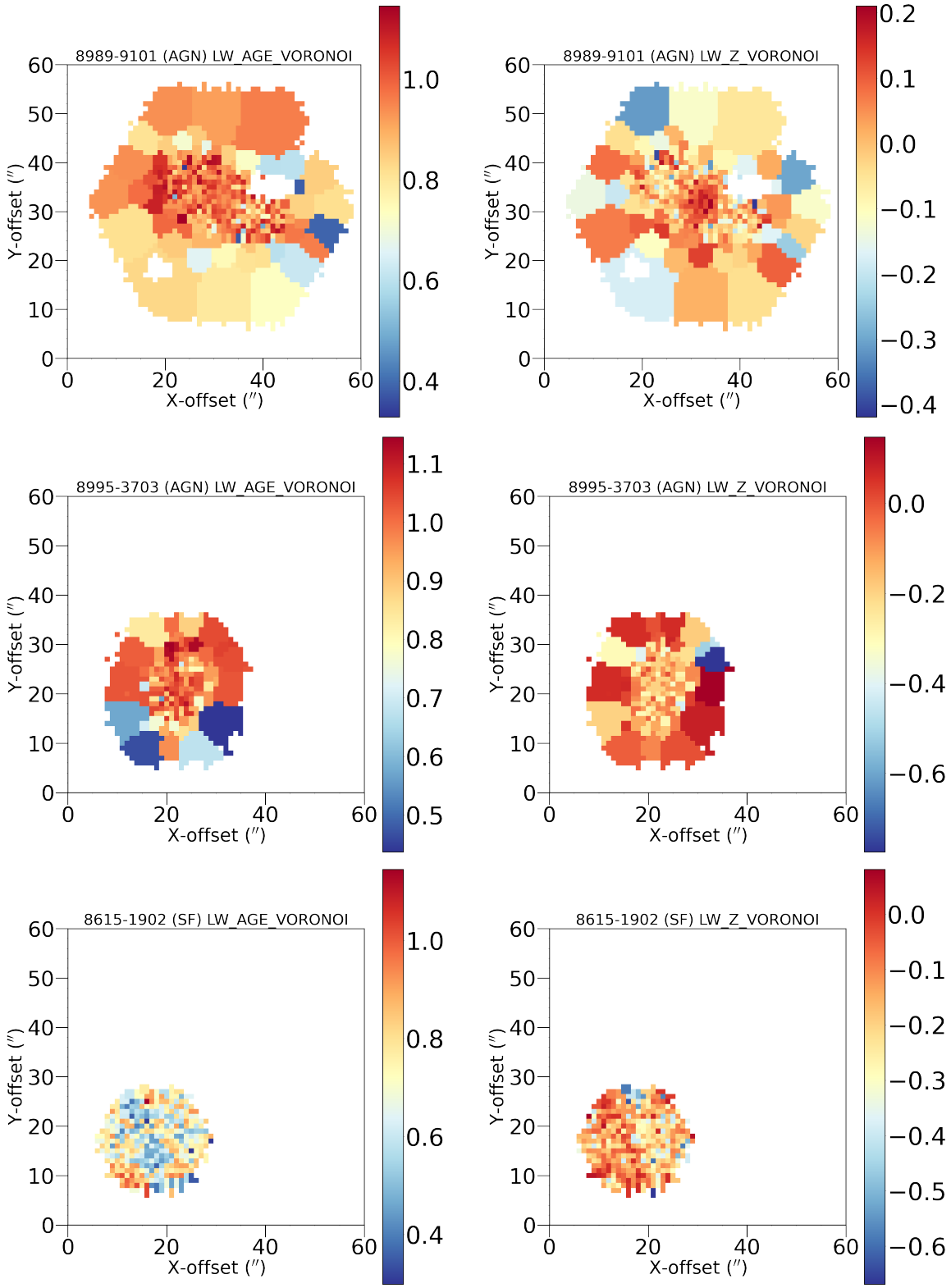

Fig. A.8: Continued.

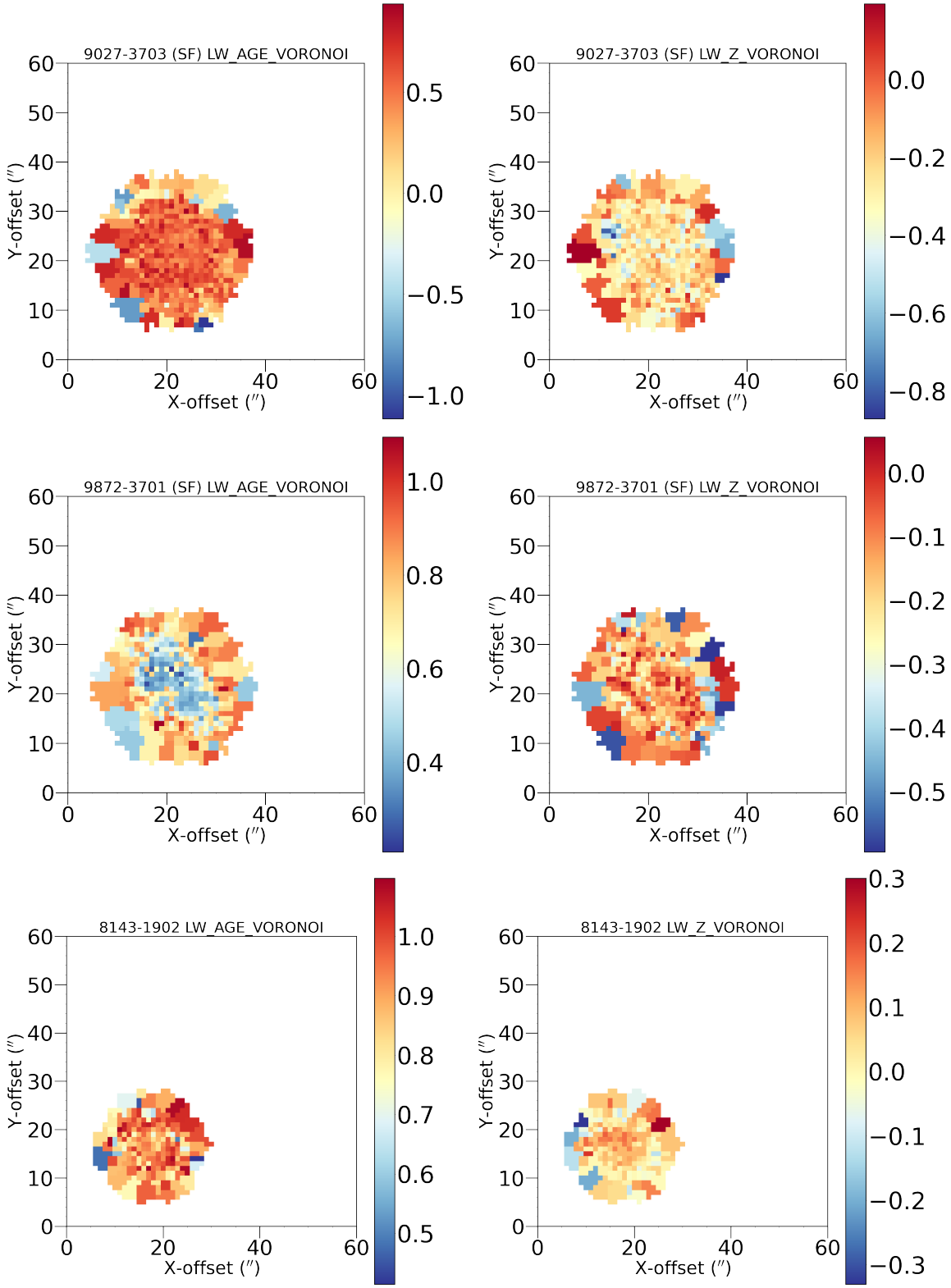

Fig. A.8: Continued.

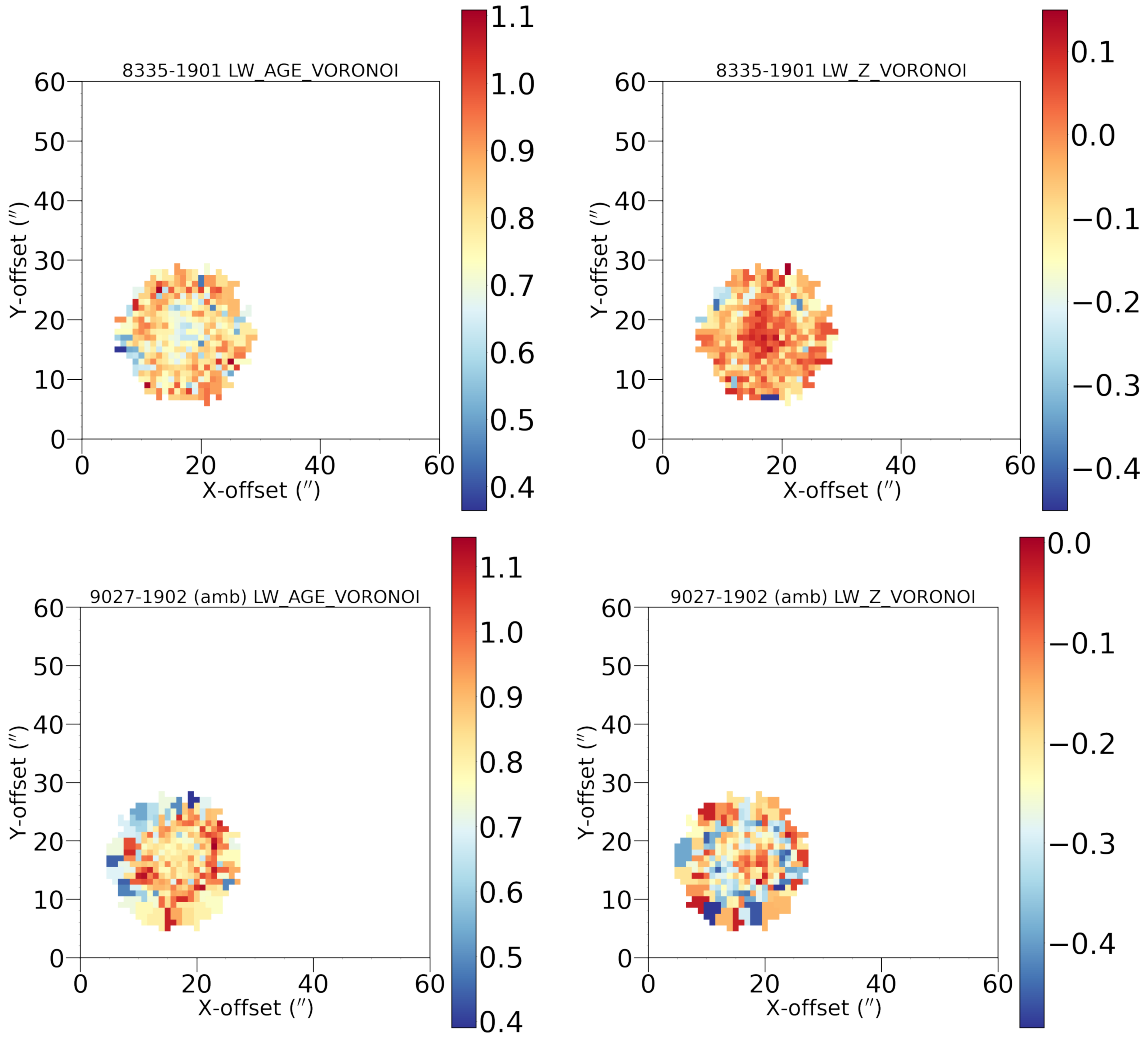

Fig. A.8: Continued.

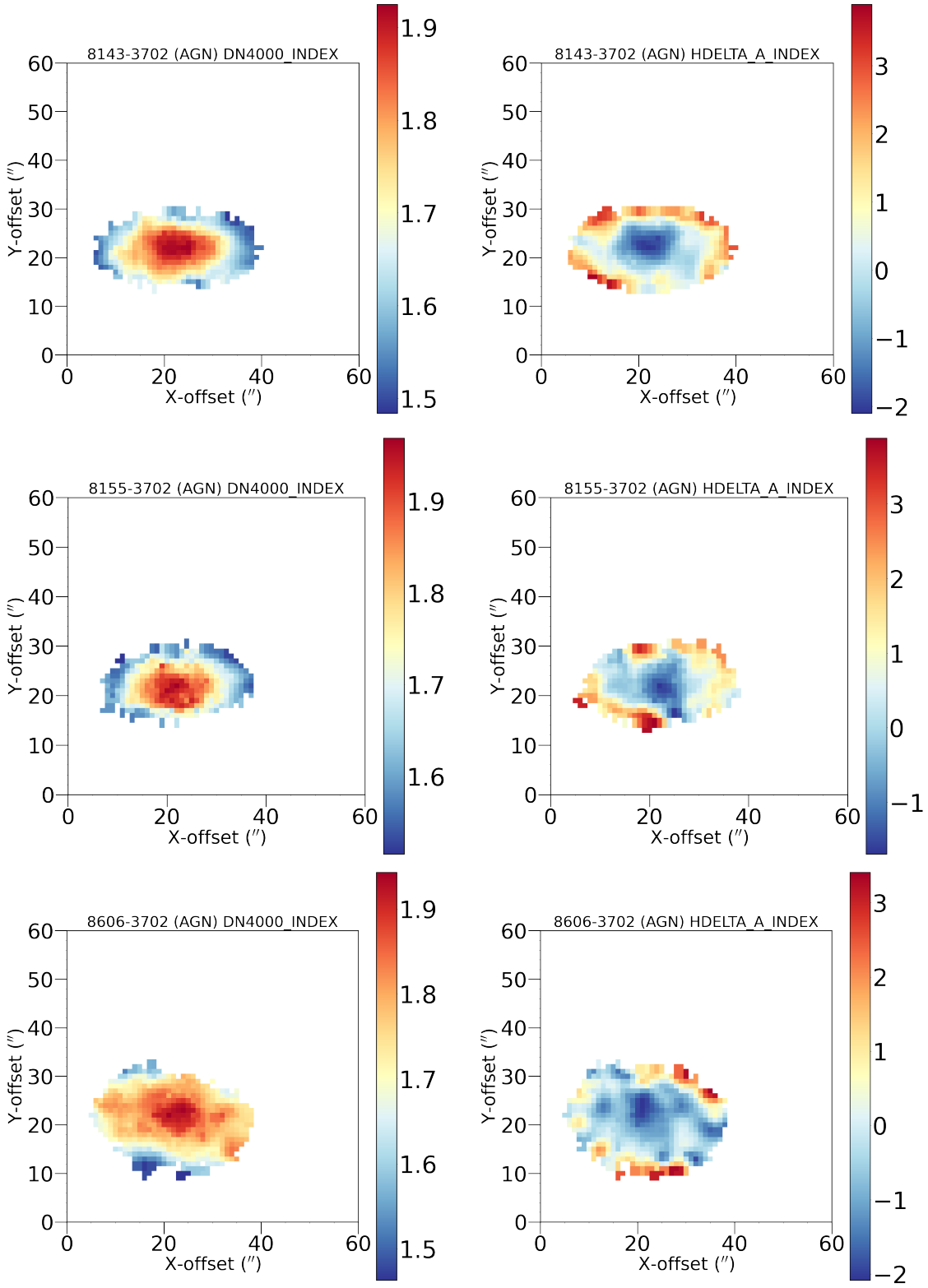

Fig. A.9: The spatially resolved D_n4000 and Hδ_A distributions of our sample. The first column shows the spatially resolved D_n4000 distribution, and the second the spatially resolved Hδ_A distribution.

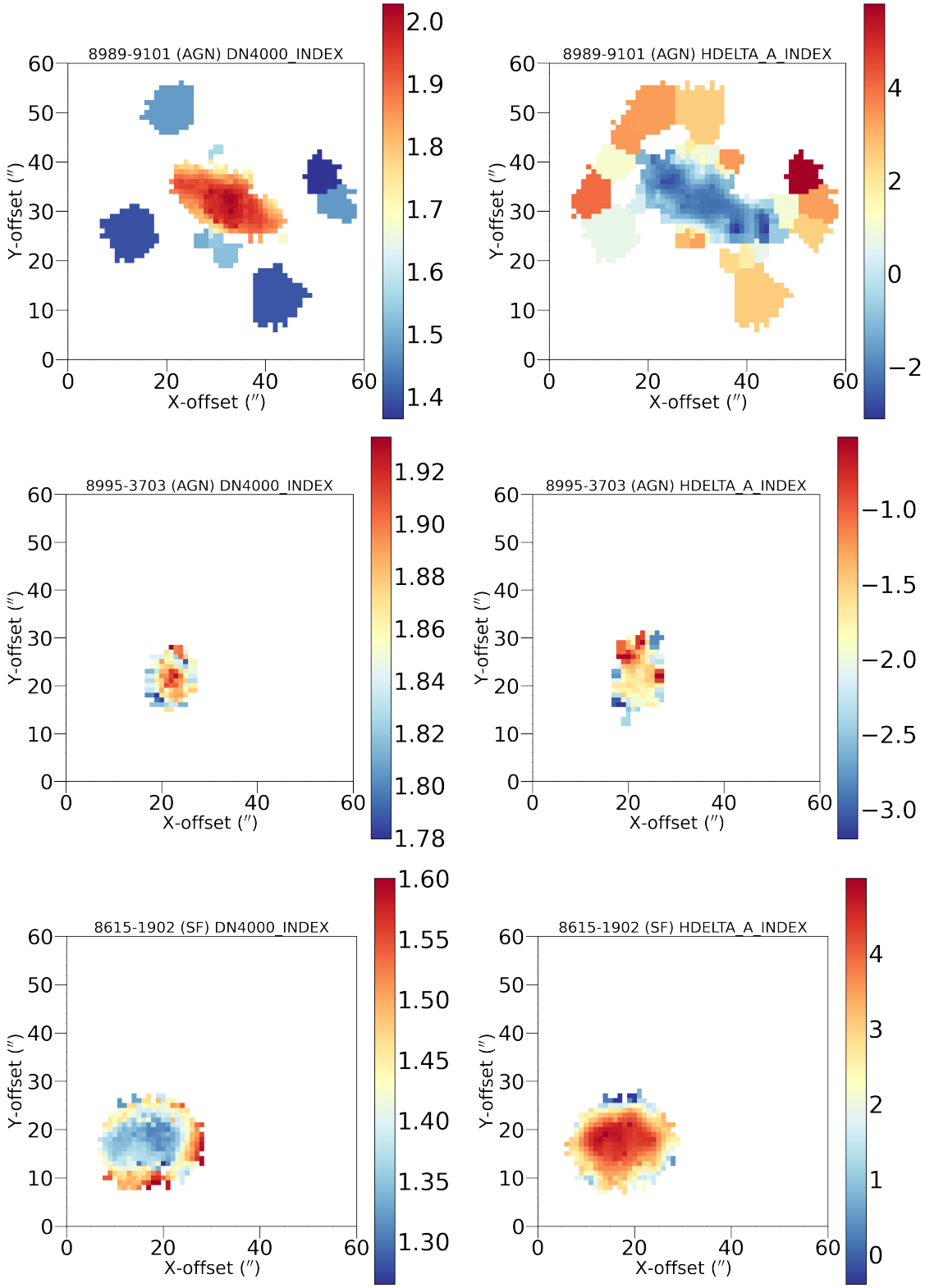

Fig. A.9: Continued.

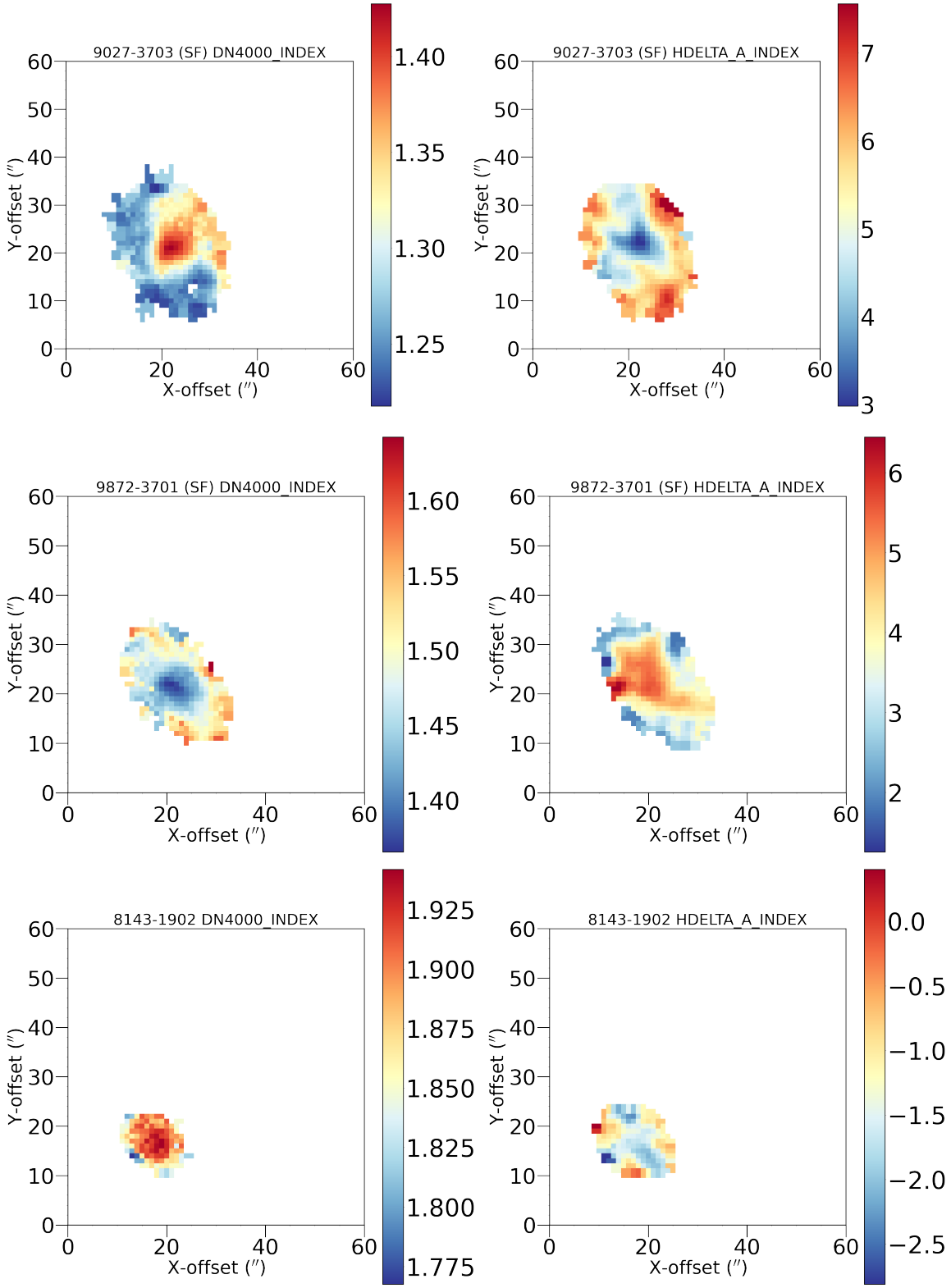

Fig. A.9: Continued.

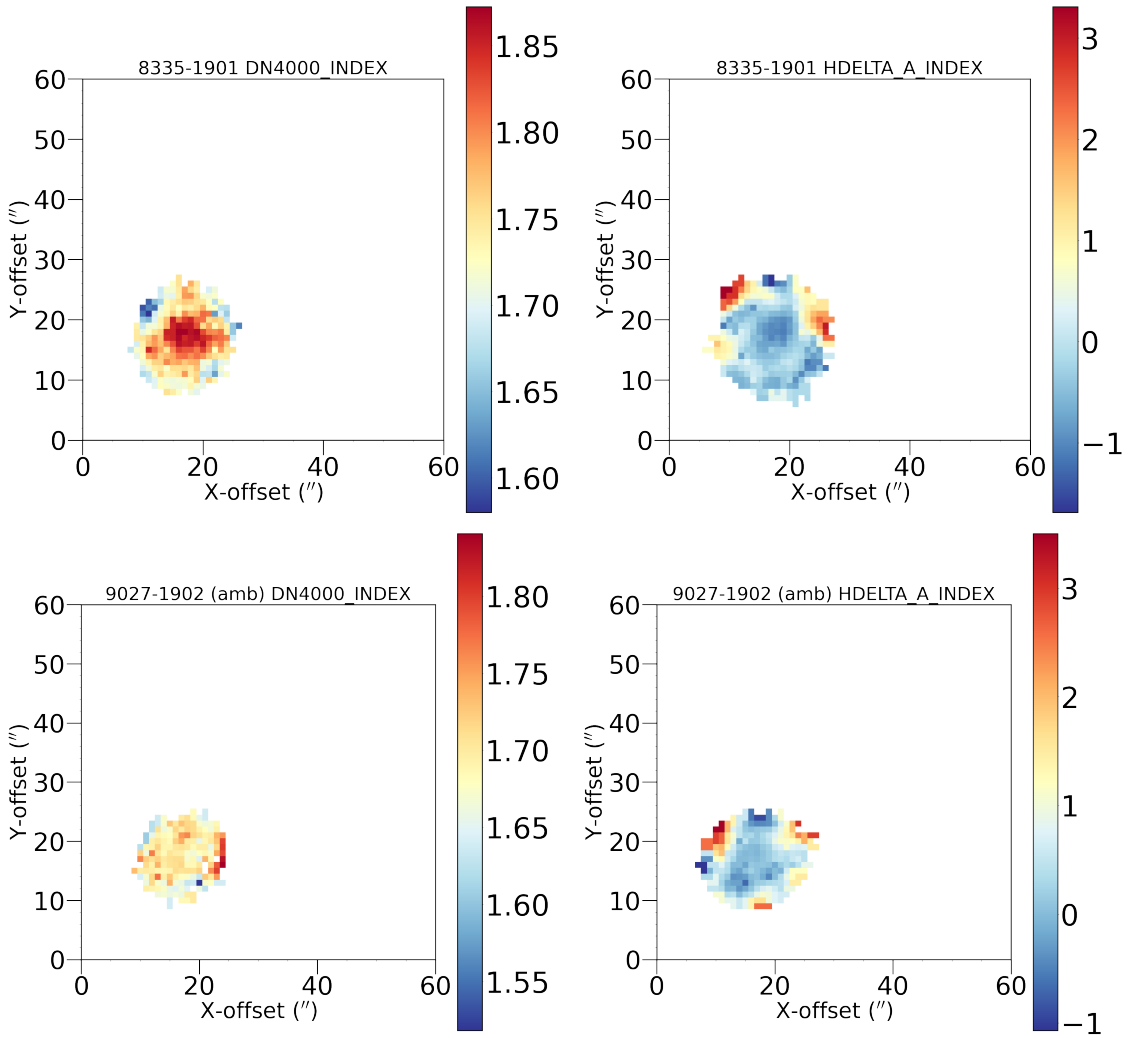

Fig. A.9: Continued.

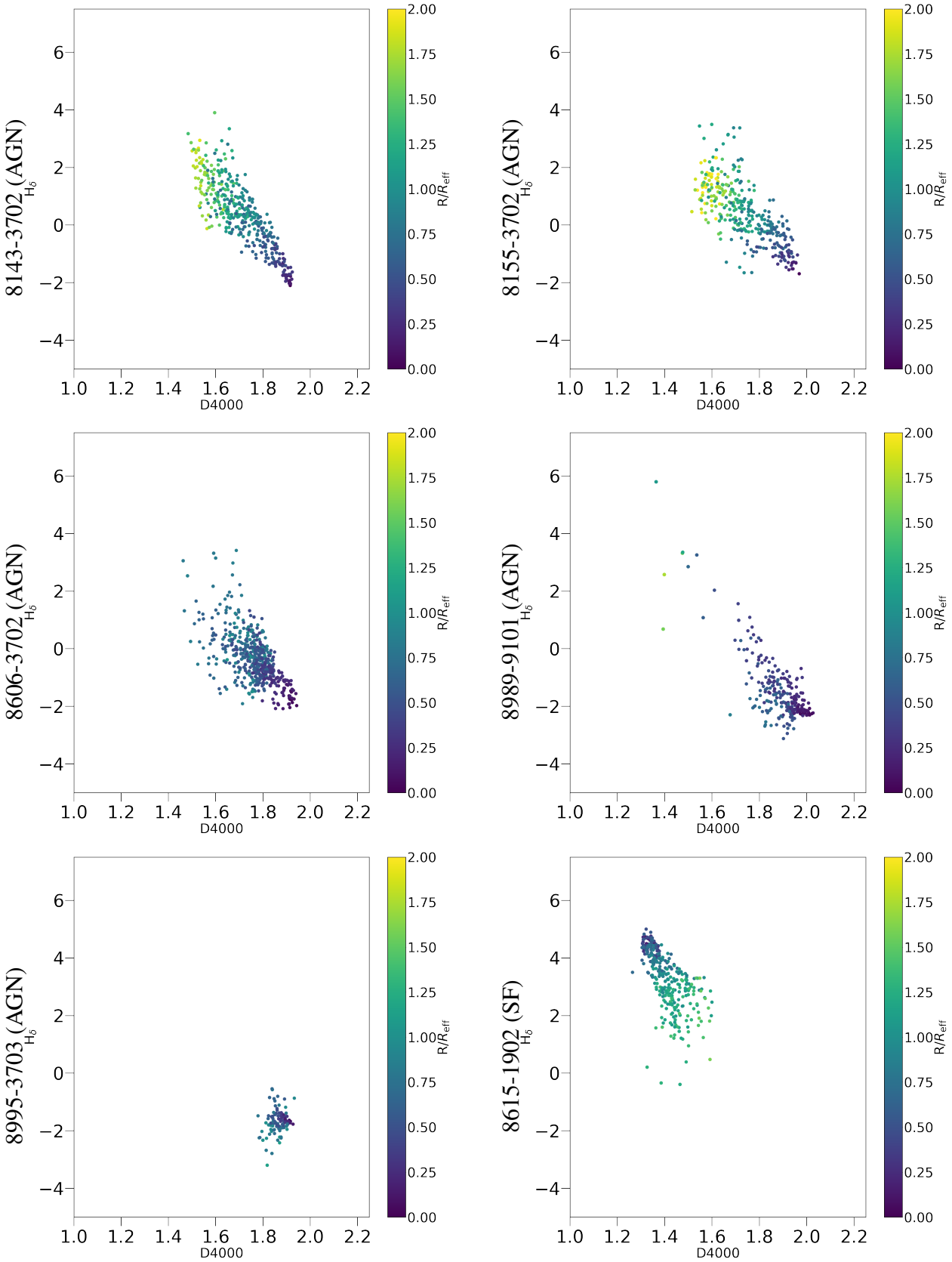

Fig. A.10: The Kauffmann et al. (2003) diagnostic, or D_n4000 as a function of $H\delta_A$, colour coded by effective radius of our sample. Two galaxies are shown per row.

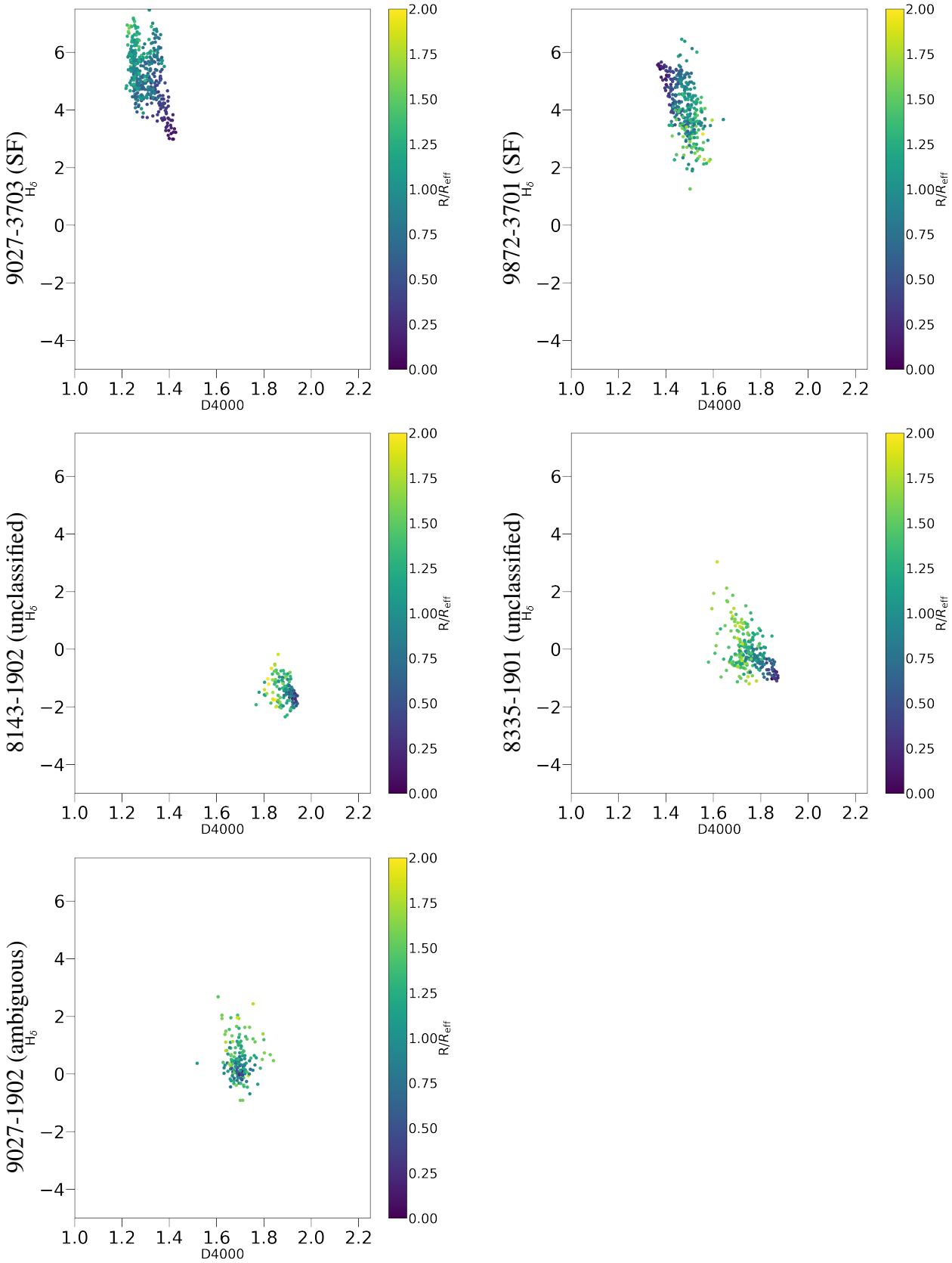

Fig. A.10: Continued.

A.4.2 Results - Identification of interacting galaxies using galaxy kinematics

For the galaxy pairs we obtained in 2.3, we investigated whether the galaxies were indeed interacting or not. This determination was made through a number of criteria:

- We visually confirmed that the secondary object was indeed a galaxy, and not a stellar object. An example of a stellar object contaminating the kinematic map is shown in Figure (figure).
- The secondary object did not have a significant redshift difference, as in they are indeed physically bound. For many of the pairs, we did not have a spectroscopic redshift for both objects, and had to rely on photometric redshifts. We considered the objects physically bound if the pairs were within either the cutoff defined by Kitzbichler & White (2008) for photometric redshifts or Patton et al. (2000) for spectroscopic redshifts.
- We also investigated the stellar velocity dispersion maps. We expected to find an increased velocity dispersion in the areas of or close to the interaction.
- Even if multiple photometric or spectroscopic redshifts were not available, if the galaxy had merger indicators such as multiple cores, bridges, tidal tails, etc., they were included in the sample.

After applying these cuts, we were left with 298 potential pairs out of the initial list of 786 candidates.

Physical properties of narrowed down sample

To check if there were any trends in galaxies that fit our classification, we plotted the stellar mass-star formation rate relation, also known as the 'star-forming main sequence' (Noeske et al., 2007) of our sample. Figure A.11 shows the relation. The stellar mass was obtained through the MaNGA FIREFLY VAC, and the star formation rate from the MaNGA DAP.
We also compared the stellar mass distribution of our sample to that of the entire MaNGA sample, and MaNGA galaxies considered merging by Darg et al. (2010), showin A.12. We find that our

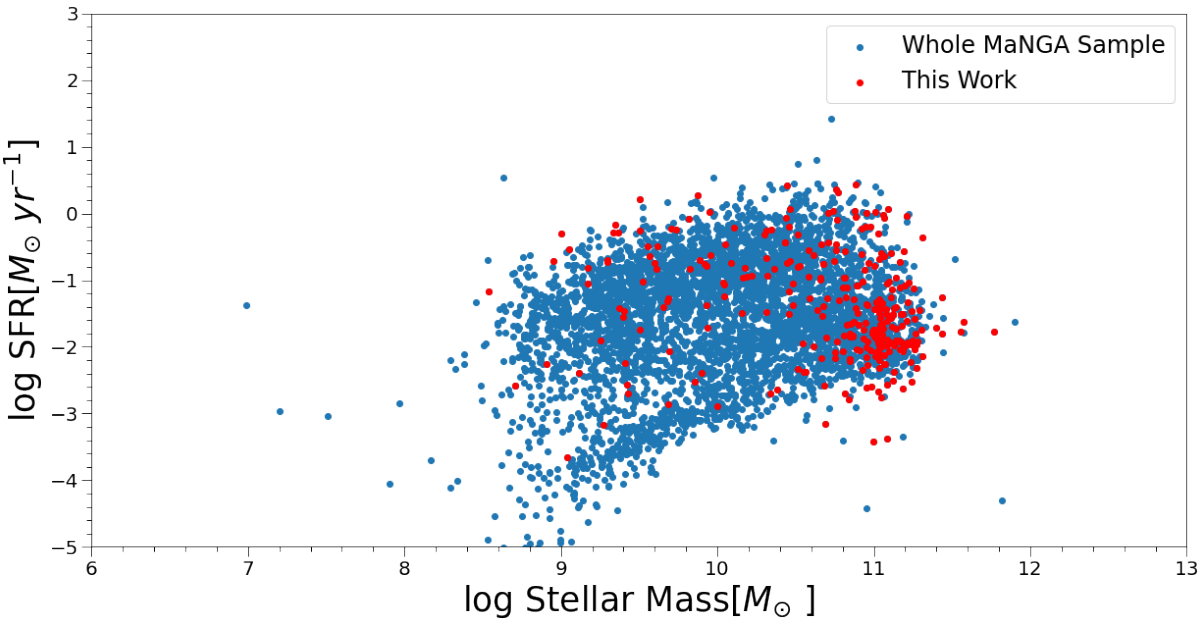

Fig. A.11: The M_*–SFR plot of our sample overplotted on the entire MaNGA sample. Our work is plotted in red, and the MaNGA sample in blue.

method tends more towards higher stellar masses than Darg et al. (2010).

A.5 Discussion

The properties of kinematically misaligned or decoupled galaxies have been studied using MaNGA data in several works, such as Jin et al. (2016) and Li et al. (2019). However, these works do not focus specifically on the properties of galaxies with a KDC or galaxies with a counter-rotating core.

We investigate the spatially resolved kinematics, stellar population properties, and star formation histories of galaxies with a counter-rotating core. Specifically, these galaxies fall under 2-σ galaxies. We find that the stars and gas of these galaxies are decoupled, and the nature of decoupling differed depending on if the galaxy was identified as SF or an AGN host. We find that the recent star formation history of these galaxies also differed based on their identification. Due to our small sample size of only five AGN galaxies, three SF, two unclassified and one ambiguous, these observed properties may not be a trend but simply individual special cases. We hope to conduct this analysis on a greater sample size in future works so that we can make

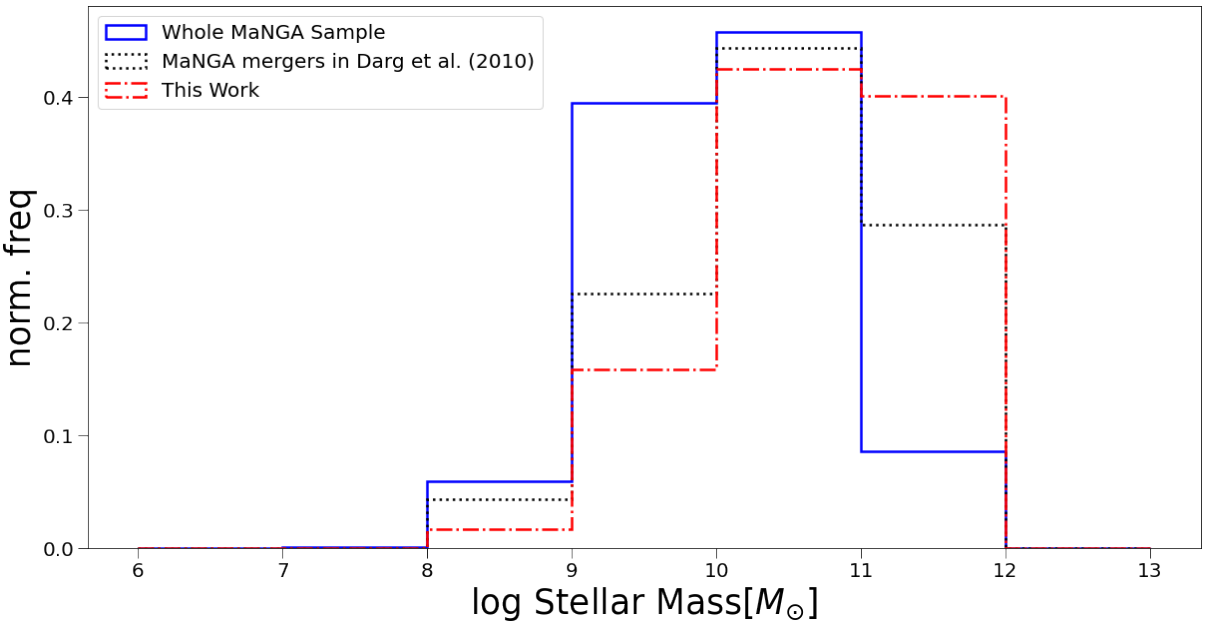

Fig. A.12: Stellar mass distributions of **a)** our work (blue), **b)** the whole MaNGA survey, and **c)** MaNGA galaxies classified merging by Darg et al. (2010).

definitive conclusions.

Finally, we will briefly discuss how the use of galaxy kinematics can help us identify interacting galaxies with better accuracy than visually based methods.

A.5.1 Kinematic properties

We find that galaxies with a counter-rotating stellar core do not show a similar property in their gas kinematics, i.e. the gaseous velocity maps show no kinematically distinct core. There are multiple possible explanations as to why the gaseous kinematics are as such.

A large kinematic misalignment, such as KDCs, is said to be a relic of an external accretion event, such as a galaxy merger (e.g. Bender & Surma, 1992; Barnes & Hernquist, 1991). When such an event occurs, the accreted material flow towards the centre of the galaxy with an angular momentum different from the main body of the galaxy. The fate of this accreted material may explain why the gas does not show a distinct core. There are a number of explanations as to what happened to the gas. Much of the accreted gas associated with the KDC may be consumed by a merger-induced star formation event that had ceased at the time of observation, leaving no

kinematically decoupled gas in the core (Taylor et al., 2018). Another possible explanation is the difference in collisionless/collisional nature of stellar and gaseous systems (Crocker et al., 2009) in interacting galaxies. In the timescale of galaxy interactions and mergers, stars are collisionless, and hence two systems of counter-rotating stars can co-exist in the same galaxy. However, because gaseous systems are collisional, one of the two systems must dominate over the other.

We also find that the rotational direction of the KDC differs depending on if the galaxy is classified as a SF galaxy or AGN host. For the AGN-hosting galaxies, the stars of the KDC are counter-rotating with respect to the gaseous main body of the galaxy, and the gas and stars of the main body are co-rotating. The SF galaxies, on the other hand, have counter-rotating stars and gas, with the KDC co-rotating with the gaseous body. A possible explanation for the SF galaxies having a counter-rotating gaseous body is that the accreted counter-rotating gas is still present in the galaxy as the dominant system and is contributing to current star formation. Once the accreted counter-rotating gas has been consumed and the star formation ceased, the co-rotating gas dominates, leaving us with observations as the ones seen in the AGN hosts and unclassified galaxy 8143–1902. The ambiguous galaxy demonstrates a rotational behaviour similar to that of the SF galaxies; however, we cannot make any definite statement because it is a single galaxy.

With the velocity dispersion (σ) maps, we find that the stellar and gaseous σ maps show peaks in different locations, with the stellar σ maps having two peaks; however, such property is not seen in the gaseous σ map. This '2-σ' feature is known to appear in the remnants of major mergers, as shown in simulation works such as Tsatsi et al. (2015). The origins of these peaks are considered to be from gas accretion (see Krajnović et al., 2011) or from merger events (see Crocker et al., 2009).

The gas σ maps show differing properties, with four of the five AGN-hosts and the ambiguous galaxy seemingly showing central peaks, and all of the SF galaxies showing peaks perpendicular to the stellar velocity, with two of three showing no central peak.The stellar-gaseous decoupling shown in the AGN galaxies can be explained via the same process as the velocity maps. Since gaseous systems are collisional, the gaseous kinematics of either the accreted gas or the galaxy experiencing accretion must dominate.

The gaseous velocity dispersion distribution in the SF galaxies is distinctly different from those in the galaxies classified as AGN hosting and ambiguous. Among the three galaxies, two do not exhibit a central peak in the gaseous velocity maps. All three galaxies show symmetrical peaks in the outer regions, along the minor axis. The lack of a peak in the central region differs from the distribution of gaseous velocity dispersions of SF galaxies investigated in previous works studying MaNGA galaxies such as Yu et al. (2019), even with effects such as beam smearing taken into account. We also considered the possibility that these peaks coincide with local star formation. However, as shown from the Hα flux diagrams in Fig. A.13, the locations of active star formation do not coincide with the peaks. As the peaks lie in the outer regions, we also looked into the local spectra of the areas where the peaks exist in order to check if the peaks are a result of errors or of a poor fit to intrinsic emission lines, which may be a consequence of noise or complex dynamics in the gas. However, the peaks do not coincide with regions of high error, which are masked in Fig. A.6. With regard to the fits to emission lines, as we can see from the spectra of the peak Hα regions in Fig. A.14, the Hα emission lines do not seem to have poor Gaussian fits for two of the three galaxies. 9872–3701 may be a result of a poor fit. The source of this lack of central peak is not well understood, and we plan to discuss it in our future work.

A.5.2 Stellar population properties

To understand more about the KDC in each galaxy in our sample, we investigated the spatially resolved stellar population properties, namely the spatially resolved ages and metallicities of the KDC and the surrounding main body of the galaxy, as well as the gradients of these properties. Similar to the kinematics, we find that the gradients differ depending on whether the galaxy is classified as an AGN host or SF.

Age gradients

The steepness of the age gradients differ based on the BPT classification of the galaxies. The galaxies classified as AGN and the one ambiguous galaxy have shallow light-weighted age gradients compared to the SF classified galaxies. These shallow gradients are similar to the average gradients of early-type galaxies surveyed in the MaNGA survey such as Goddard et al.

(2017), which showed relatively shallow age gradients for early-type galaxies regardless of mass bin.

Two of the three SF galaxies, 9872–3701 and 8615–1902, show positive age gradients, whereas the third, 9027–3703, shows a negative age gradient. These gradients are more significant than the ones found in the AGN-hosts. These gradients are not consistent with the age gradients found in Goddard et al. (2017). However, the SDSS morphological classification for 9027–3703 is a spiral galaxy; in such a case, the gradient is consistent with those of late-type galaxies in Goddard et al. (2017)

The two unclassified galaxies both show positive gradients; however, 8143–1902 shows a shallow gradient similar to that of the AGN hosts, whereas 8335–1901 shows a steeper gradient, much like two of the three SF galaxies. Because there are only two samples, we hope future studies will give us more samples from which we can formulate a statement on.

Metallicity gradients

Similar to the age gradients, the metallicity gradients show different properties depending on their classification.

Four of the five AGN host galaxies have greater than solar metallicity in the core region, and has a relatively sharp negative metallicity gradient compared to the SF galaxies. This demonstrated gradient is consistent with those shown in previous MaNGA works such as Goddard et al. (2017). These works suggest an 'outside-in' formation scenario, where the outer region forms stars first, then the core forms younger, metal-rich stars later. However, this scenario contradicts our findings in the age gradients. The three SF galaxies show no distinct metallicity gradient. The unclassified galaxies both show negative gradients; however, much like their age gradients, 8143–1902 shows a shallower gradient compared to 8335–1901. Whereas 8143–1902 shows a similar age gradient to that of AGN hosts, the metallicity gradient is shallower compared to them, and are also inconsistent with those shown in works such as Goddard et al. (2017). On the other hand, 8335–1901 shows a steep age gradient similar to that of SF galaxies in our sample, however the metallicity gradient is not consistent with them. Again, these are only two samples, so we cannot make any statements as to whether or not there is a trend. There is a clear difference

in the age and metallicity gradients between the AGN host galaxies and SF galaxies, but the gradients of individual galaxies do not give us a complete picture of their formation scenarios. This discussion will be for a later paper.

Star formation histories

We discuss here the spatially resolved star formation histories of our sample using the using the D_n4000 versus $H\delta_A$ diagnostic diagram developed by Kauffmann et al. (2003).

The AGN-hosting galaxies show a gradient where the galaxy is dominated by older stellar populations as indicated by their D_n4000 values, and the stellar population tends to get younger radially outwards. The lack of young stellar populations in the central regions is consistent with our findings in the kinematic maps, because they indicate no recent star formation. These galaxies exhibit an inside-out quenching star formation history, with the outer regions showing the most recent star formation. The SF galaxy 9072–3702 also shows a gradient where the stellar populations get younger radially outwards. However, the D_n4000 values indicate that the galaxy has experienced recent star formation, which is consistent with our findings in the kinematic maps.

All three SF galaxies are dominated by young stellar populations, as indicated by the galaxies being dominated by spaxels with $D_n4000 > 1.5$. The radial gradients for two of the three galaxies, 9027–3703 and 8615–1902, indicate that the most recent star formation occurred in the core. The gaseous velocity maps show that the gas is counter-rotating with the main stellar body. It is possible that the accreted counter-rotating gas, which is the dominating system for SF galaxies, is still present and forming stars. We will require a larger number of samples to investigate whether or not the radial gradients of the star formation history differ depending on if the galaxy is SF or an AGN host. We hope to find more SF galaxies with a counter-rotating core in future studies so that we can make a definitive statement.

The two unclassified galaxies show stellar populations getting younger radially outwards, with the galaxy being dominated by older stellar populations, exhibiting inside-out quenching similar to the AGN host galaxies.

The ambiguous galaxy does not show a gradient that follow outside-in or inside-out scenarios.

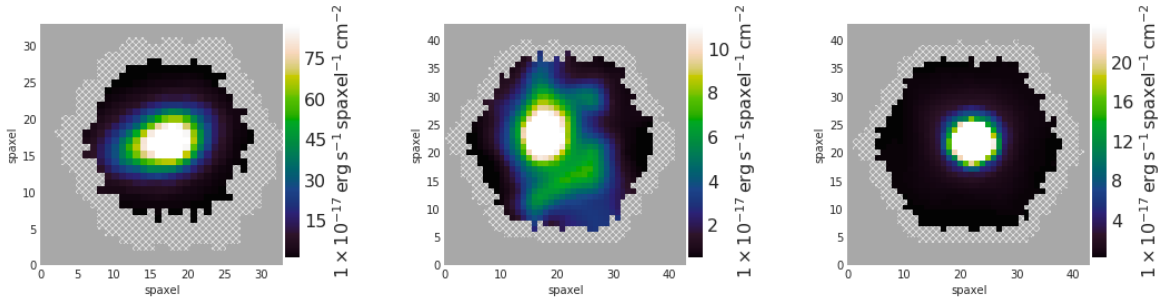

Fig. A.13: The Hα flux diagrams for the three star-forming galaxies. From left to right, 8615–1902, 9027–3703, 9872–3701.

Comparison with previous studies of 2-σ galaxies

We have compared our findings in stellar population properties with previous works studying KDCs and 2-σ galaxies. The AGN-hosting galaxies show shallow age gradients, and four of the five galaxies show relatively sharp negative metallicity gradients. These results are similar to those found in works studying NGC 448 (e.g. Katkov et al., 2016; Nedelchev et al., 2019), which suggest rapid outside-in star formation. However, the diagnostic diagram indicates an opposing scenario, because the indicators of the most recent star formation lie in the outer region.

For the SF galaxies, two of the three galaxies, 9872–3701 and 8615–1902, show a relatively sharp positive age gradient, with the youngest stars in the core regions, and a shallower metallicity gradient compared to the AGN hosts. The stellar age gradients are consistent with the radial profiles obtained using the Kauffmann diagnostic, where the same two galaxies show the youngest stars in the inner regions and 9027–3703 shows the youngest stars in the outer regions. The positive gradients are similar to what was seen in previous studies such as Coccato et al. (2011) and Coccato et al. (2012); however, the shallow metallicity gradients do not seem to match what was found in these studies.

Conducting spectral decomposition on the main and counter-rotating components may tell us more about the radial profiles of each component, as well as their star formation histories. This discussion will be for a later paper.

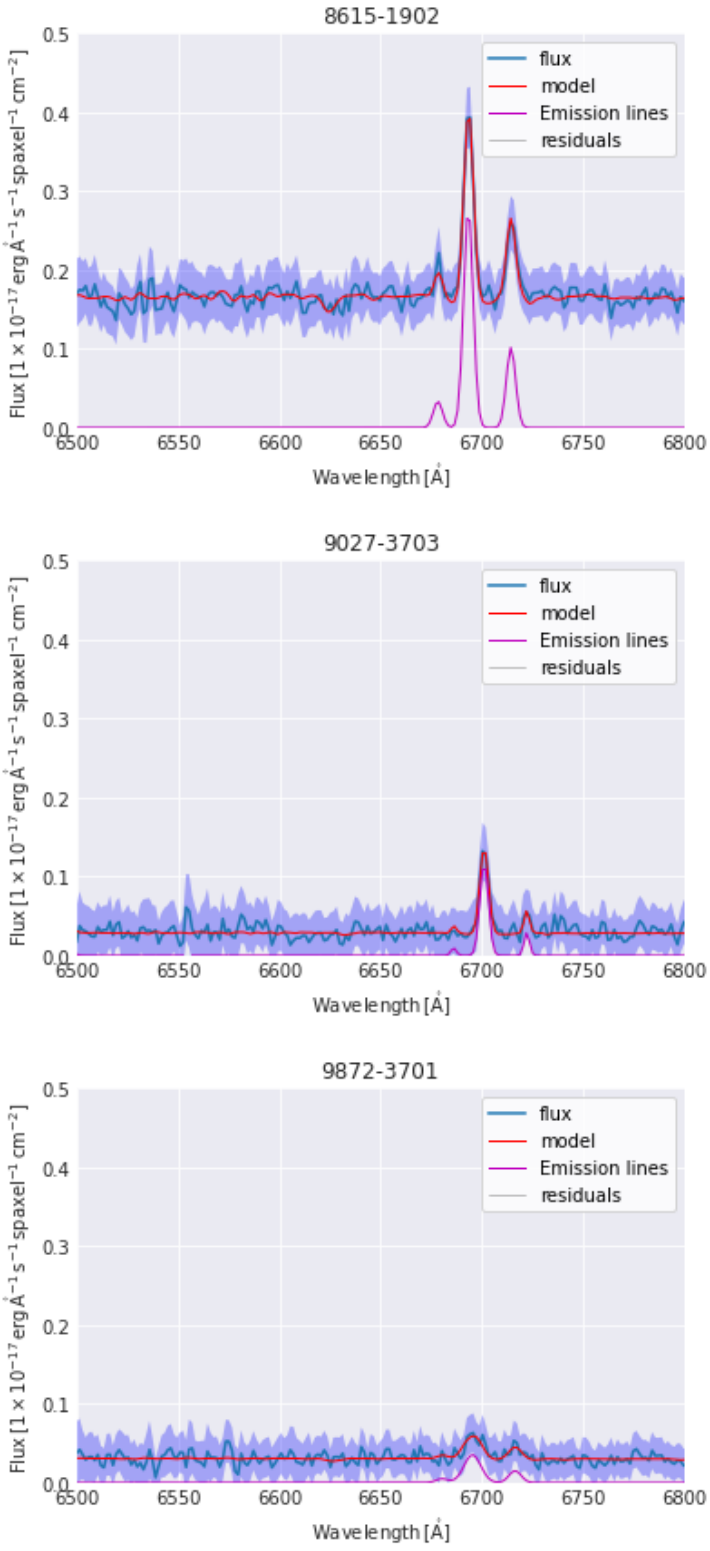

Fig. A.14: The Hα emission line region spectra of the Hα emission line peak spaxels for the three star-forming galaxies. From left to right, 8615–1902, 9027–3703, 9872–3701.

Comparison with galaxies without a counter-rotating core

We compared the results of our sample to AGN-hosting and SF galaxies without a counter-rotating core. The star formation histories of both AGN-hosting and SF galaxies without a counter-rotating core show a radial gradient where the core has an older stellar population compared to the outside regions. As both AGN-hosting and SF galaxies without a counter-rotating core, and AGN-hosting galaxies with a counter-rotating core exhibit similar radial gradients that support inside-out quenching of star formation, it may be feasible to say that the SF galaxies with a counter-rotating core have a distinct star formation pathway, and the star formation history on its own cannot distinguish a galaxy with a counter-rotating core from a galaxy without one. These results are consistent with previous studies such as Davies et al. (2001) and McDermid et al. (2015), with the former finding that the core and main body of KDC galaxies have a similar formation history (i.e. indistinguishable from non-KDC galaxies), and the latter finding that kinematics alone do not place a large constraint on evolutionary pathways. Galaxies observed in the MaNGA survey have a higher percentage of inside-out quenching compared to outside-in quenching (Lin et al., 2019), so the distribution of star formation histories of our sample may be due to sampling bias.

A.5.3 Using kinematics to identify interacting galaxies

Here we discuss the prospects of using spatially resolved kinematic data as a method to identify interacting galaxies and its advantages over conventional optical image-based classification methods.

Counter-rotating galaxies

For our counter-rotating galaxy sample, in Table A.1, we can see that the majority of galaxies identified as having a KDC have been identified as non-interacting galaxies by multiple optical image-based classification catalogues. Nine galaxies in our sample had 0 merger probability based on Galaxy Zoo data. The two galaxies with non-0 merger probabilities also did not have a high enough p_m value to be considered a merger. Deep learning techniques also did not classify these galaxies as likely to be merger galaxies. The only galaxy with a p_m at a high enough

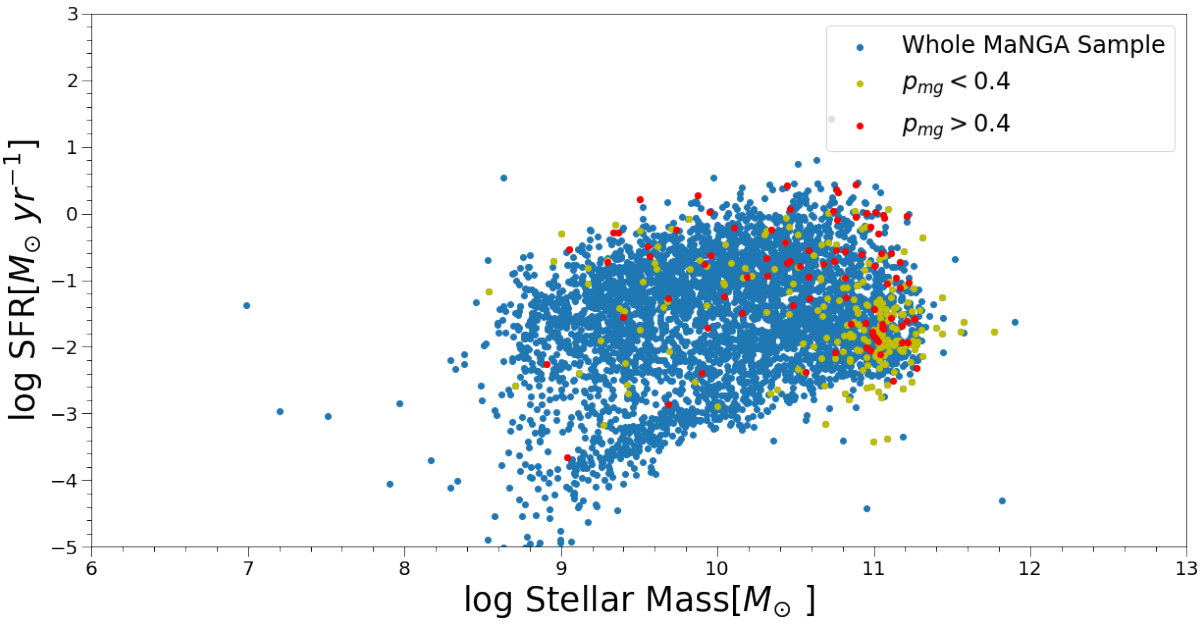

Fig. A.15: The star-forming main sequence plot of our sample overplotted on the entire MaNGA sample, with our sample further divided into galaxies considered merging/non-merging by the Galaxy Zoo. Samples considered merging by the Galaxy Zoo are plotted in red, non-merging in yellow, and the MaNGA sample in blue.

value to be confidently classified as a merger is 8995–3703, but this classification is likely due to contamination from a non-galaxy object in the optical image. These galaxies may be recent post-merger galaxies, and optical image-based classification methods, whether they be visual inspection or machine learning, are susceptible to incorrectly classify them.

Paired sample

Of our kinematically identified sample of pairs, 209 galaxies were in disagreement with the Galaxy Zoo project. To investigate what types of galaxies our in disagreement, we applied the Galaxy Zoo merger values to our main sequence diagram in Figure A.15.

Our comparison with the Galaxy Zoo shows that kinematic classification can correctly classify a wide range of galaxies that were classified merging and non-merging by visual classification alone. Additionally, this wide range of star formation rates is in agreement with works such as Pearson et al. (2019) which state that interacting galaxies do not necessarily have a larger star formation rate than non-interacting galaxies. Interacting galaxies can include dry mergers, where

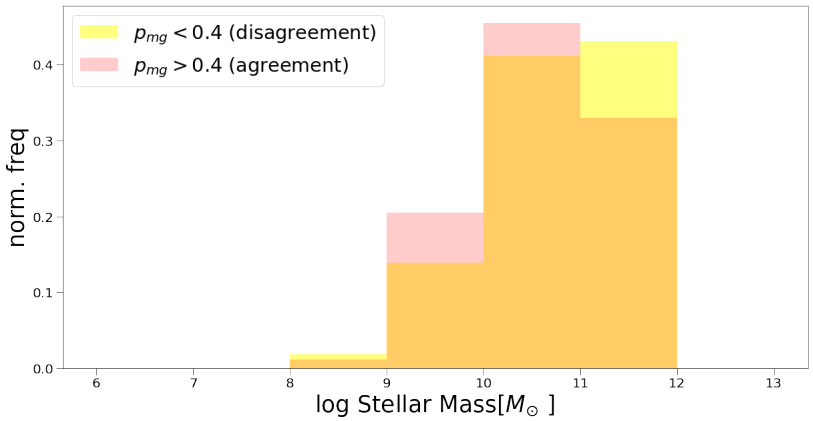

(a) Stellar mass

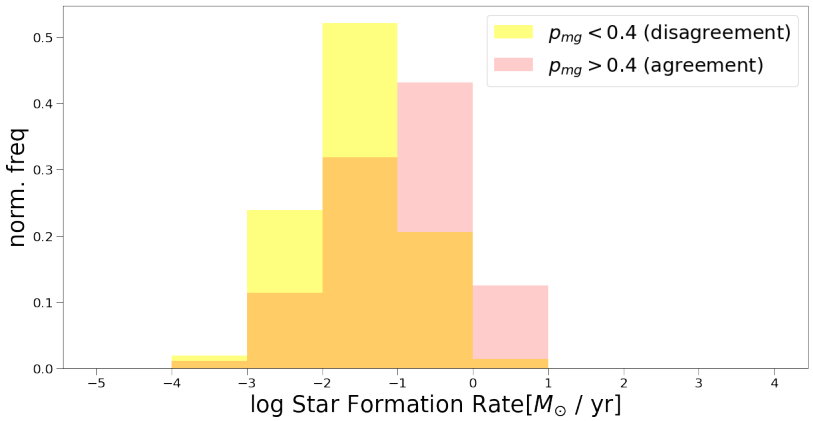

(b) SFR

Fig. A.16: Stellar mass and star formation rate distributions of our sample, divided into classified as merging (agreement/red) or non-merging (disagreement/yellow) by the Galaxy Zoo.

star formation is not active, and our sample likely includes such galaxies.

We used the two-sample Kolmogorov-Smirnov test (KS-test; Smirnov (1939)), to compare the distribution of the objects in agreement and disagreement, with the null hypothesis that the two distributions are the same being rejected at level $\alpha = 0.05$, if the KS-test statistic $D_{N,M} > \mathrm{Crit}_{N,M}$, with $\mathrm{Crit}_{N,M} = c(\alpha)\sqrt{\frac{n+m}{nm}}$, where $c\alpha = 1.224$ for $\alpha = 0.05$. The results are shown in Table A.3. We find that there was a difference in distribution for agreements and disagreements in SFR based on our KS-test result for lower SFR, particularly in the $\log \mathrm{SFR} < -2 M_\odot \mathrm{yr}^{-1}$ region, which can be seen in Fig. A.16 These galaxies are most likely dry mergers which show kinematic indicators of interaction but lack visual merger tracers.

There were also galaxies that were classified merging by Galaxy Zoo that had regular kinematics,

Property	KS-test statistic $D_{N,M}$	Critical value $\text{Crit}_{N,M}$	p-value
$\log M_*$	0.153	0.155	0.097
log SFR	0.341	0.155	6.363e−6

Table A.3: KS-test results for our sample classified by the Galaxy Zoo.

which we will explain in the next Section.

We also compared our results to the MaNGA Morphology Deep Learning DR15 catalog (Fischer et al., 2019) in Fig. A.17, and the distributions in Fig. A.18.

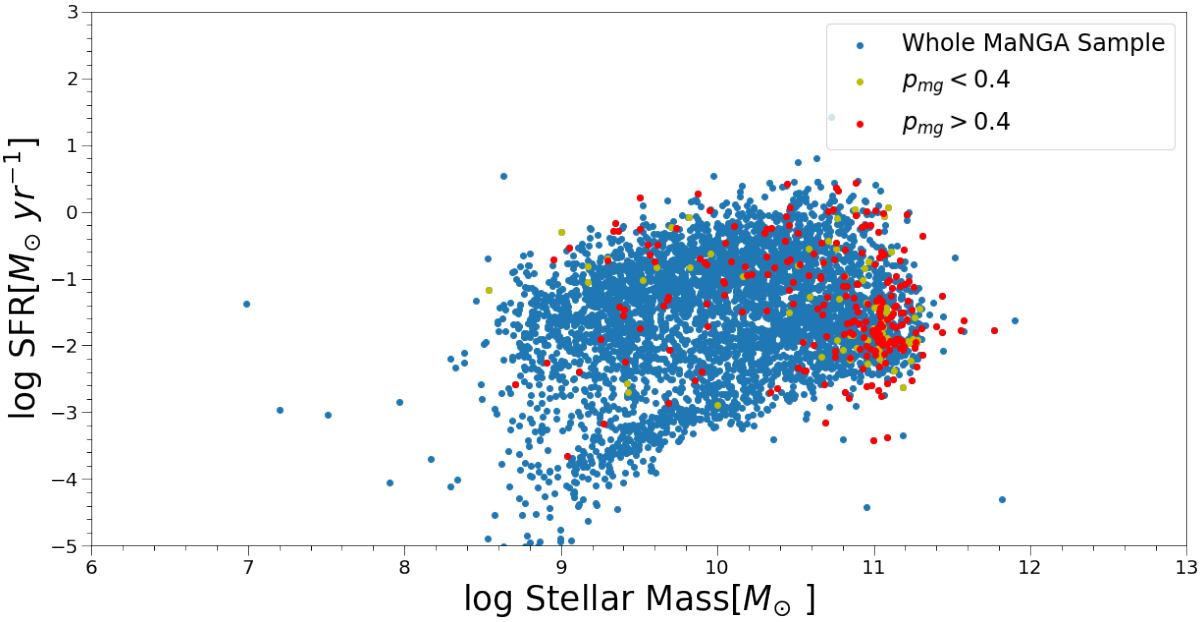

Fig. A.17: The M_*–SFR plot of our sample overplotted on the entire MaNGA sample, with our sample further divided into galaxies considered merging/non-merging by Fischer et al. (2019). Samples considered merging by the work are plotted in red, non-merging in yellow, and the MaNGA sample in blue.

Of the 298 galaxies classified as interacting using our method, 69 galaxies were not classified as interacting by Fischer et al. (2019). Based on our KS-test results in Table A.4, we could not find any noticeable trend in disagreements. We also found that there were a large number of galaxies classified as interacting by the Deep Learning catalogue that we did not. Some were misclassifications which we will highlight in the following section, however there were many false positives which included secondary galaxies at differing redshifts ($\delta z > 0.5$) and stellar

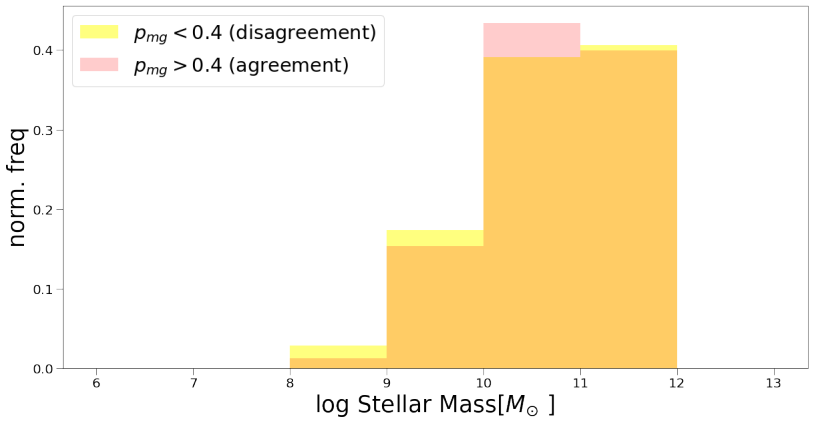

(a) Stellar mass

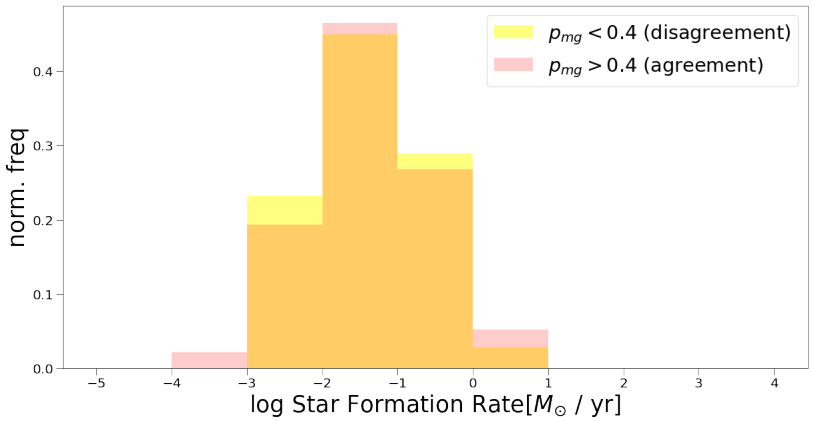

(b) SFR

Fig. A.18: Stellar mass and star formation rate distributions of our sample, divided into classified as merging (agreement/red) or non-merging (disagreement/yellow) by the Fischer et al. (2019).

objects.

Misclassifications

In Figure A.19, we show examples of true positive, true negative, false positive and false negative galaxies classified as interacting/non-interacting by using kinematics. As it can be seen in the false negative in the figure, we had a number of galaxies that have their merger signatures outside of the field of view misclassified as false negative. These galaxies had high merging probabilities in both Galaxy Zoo and Deep Learning catalogues, and can be confirmed as mergers visually. For example, the false negative example (bottom right) of A.19, 8439–6104 is very likely to be a merger, with a p_m of 0.93 given by the Galaxy Zoo and 0.99 given by Deep Learning catalogues.

Property	KS-test statistic $D_{N,M}$	Critical value $\text{Crit}_{N,M}$	p-value
$\log M_*$	0.098	0.168	0.648
log SFR	0.099	0.168	0.636

Table A.4: KS-test results for our sample classified by the Fischer et al. (2019).

However, as it had regular kinematics, meaning it had symmetric velocity maps, we did not consider it as a candidate for interacting galaxies during the kinematic identification process, so we did not do any visual confirmation.

With regards to the false positives, the initial kinematic identification process is very prone to misclassifications, as evidenced by the 786 galaxies with secondaries, of which over half were not considered interacting. The kinematic maps alone cannot distinguish between stellar objects and galaxies. This issue can be addressed by the additional visual confirmation that we have conducted. The kinematic identification process also has a difficulty distinguishing between close pairs and overlaps at differing redshifts ($\delta z > 0.05$). This issue can be addressed if complete photometric or spectroscopic information is available for both sources. Nonetheless, the use of kinematics alone is problematic when doing identification and classification, and should be combined with other indicators. Meanwhile, there are a large number of isolated galaxies with no close neighbours with irregular kinematics. We plan to investigate the origin of these distortions in later works. It is possible that these galaxies are very late stage mergers or merger remnants, or the distortions originate from internal events.

A.6 Conclusion

We visually identified interacting galaxies using kinematics indicators such as asymmetries using two-dimensional galaxy kinematics.

Galaxies with a counter-rotating core

Of the sample, we selected galaxies with a kinematically distinct stellar core (KDC) that are also counter-rotating, and analysed their spatially resolved kinematic properties, stellar population

properties and star formation histories. We discovered that these properties may differ depending on whether the galaxies were classified SF or AGN by their spatially resolved BPT diagrams. Our main findings include the following:

- The rotational orientation of the galaxy main body and gas differ for SF and AGN galaxies. SF galaxies have counter-rotating stellar main bodies and gases, meaning the counter-rotating core was co-rotating with gas. AGN galaxies have co-rotating stellar main bodies and gases, so the core was counter-rotating with the main body and gas.

- The stellar velocity dispersion maps indicate that galaxies with a counter-rotating core are '2-σ' galaxies, which show two off-centred symmetrical peaks aligned with the major axis. The stellar σ maps and gaseous σ maps are decoupled for both SF and AGN galaxies. The SF galaxies show peaks along the minor axis in the gaseous σ maps, and AGN galaxies show a central peak.

- The age and metallicity gradients of the AGN host galaxies are similar to those of the average of the field sample of MaNGA galaxies. However, the gradients observed in the SF galaxies show gradients that are not similar to the average. The AGN galaxies show similar gradients to those of other $2-\sigma$ galaxies studied in previous works, whereas the SF galaxies did not.

- Stellar populations of the sample indicated an inside-out quenching star formation history for most of the galaxies. Two of the the SF galaxies showed different behaviour, with the core having a younger population compared to the outskirts.

Based on our results, we can see that even though all of our galaxies can be seen as ones with counter-rotating cores, there is a distinct difference in their properties, which may depend on their ionisation source (AGN host or SF). While the AGN hosts show properties similar to those found in previous works, the SF galaxies show properties not necessarily consistent with previous works. However, due to a small sample size, we cannot make any definitive statements. This difference may be an indicator of the evolutionary stage the galaxy is in of a merger/accretion process. The SF galaxies are in an earlier stage of merger/accretion, where the galaxy has

accreted gas with a distinct angular momentum and is forming stars, most recently in the core region, with the same angular momentum as the gas. The AGN host galaxies are in a later stage of merger/accretion, where the accreted external gas has been consumed by star formation activity, leaving only the gas from the initial galaxy. On the other hand, the stars with the same angular momentum as the gas have not yet relaxed, and they have retained their kinematic information. The galaxy has undergone inside-out quenching, possibly as a result of AGN feedback.

Due to the above reasons, in future studies, instead of investigating these galaxies with a counter-rotating core as 'SF' or 'AGN hosts', it may be more feasible to conduct investigations with the consideration that galaxies with a counter-rotating core fall under a single evolutionary timeline, and the BPT classifications are an indicator of evolutionary stage. However, due to the small sample size, we cannot make a solid conclusion, and an increased sample size and further studies will be required to solidify this statement. Future SDSS data releases expect over 10,000 unique MaNGA targets, so we anticipate a greater number of galaxies with a counter-rotating core on which to conduct this investigation on, allowing us to draw stronger conclusions.

Galaxy classification using kinematic indicators

By using both kinematic maps and galaxy optical images, we were able to correctly classify a wider range of galaxies that were previously considered not interacting by classification methods that only used optical images. Our results show that by combining spatially resolved kinematic data with other indicators, we can correctly classify a large number of galaxies that have been previously misclassified.

In future works, we look to investigate other spatially resolved kinematic and physical properties to assist in classifying interacting galaxies, and develop an accurate classification mechanism. For example, our visual inspection mainly focused on the symmetry/asymmetry of the galaxy velocity i.e. how the galaxy was rotating. We did not inspect the actual rotational speed of the galaxy, which can hold information about its star formation and merger history (Penoyre et al., 2017). We also plan to incorporate and combine the non-parametric indicators stated in Sect. 1, such as in Nevin et al. (2019), so galaxies at various stages of interaction can be accounted for. While human-dependent methods for such a mechanism would be highly time- and human-

resources consuming, machine learning techniques would help in reducing this issue. By having a complex neural network identify and detect various merger features in the kinematic data, optical images and galaxy physical properties, we may be able to develop an efficient, physically motivated interacting galaxy classification mechanism.

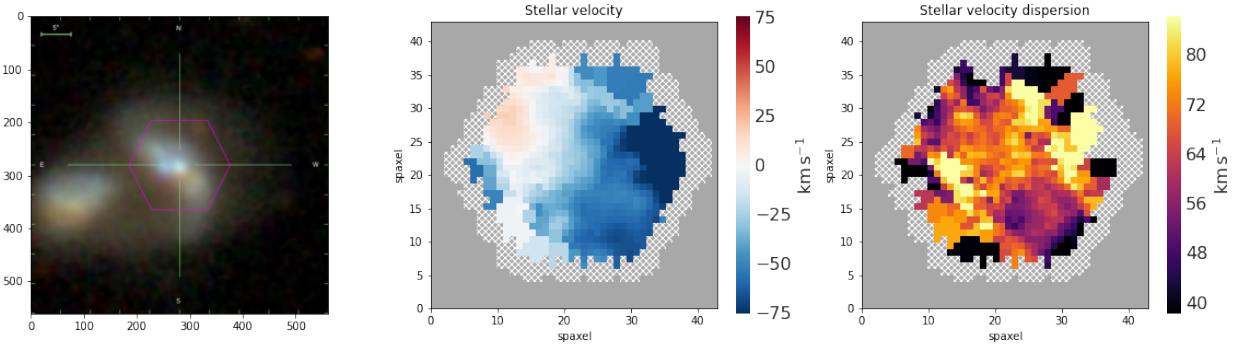

(a) True positive

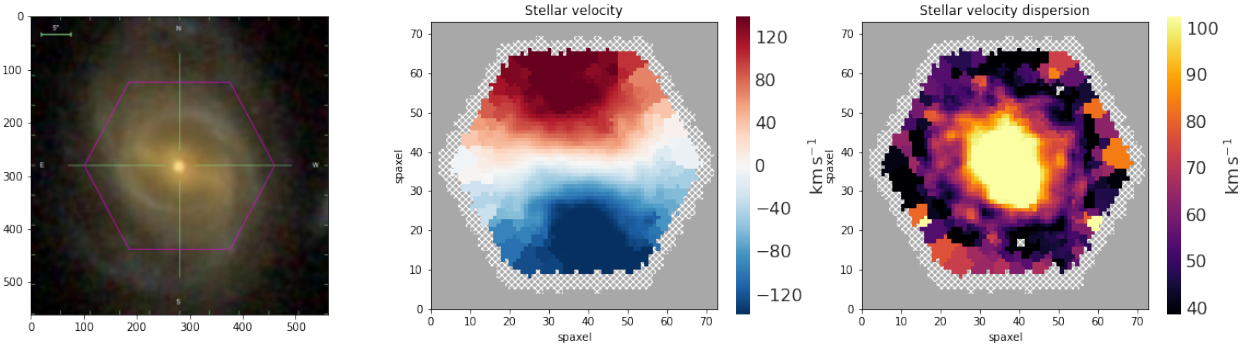

(b) True negative

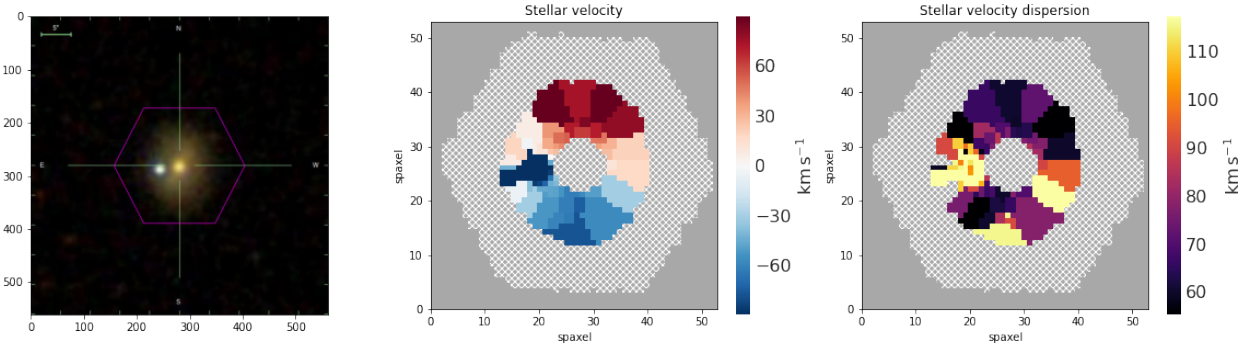

(c) False positive

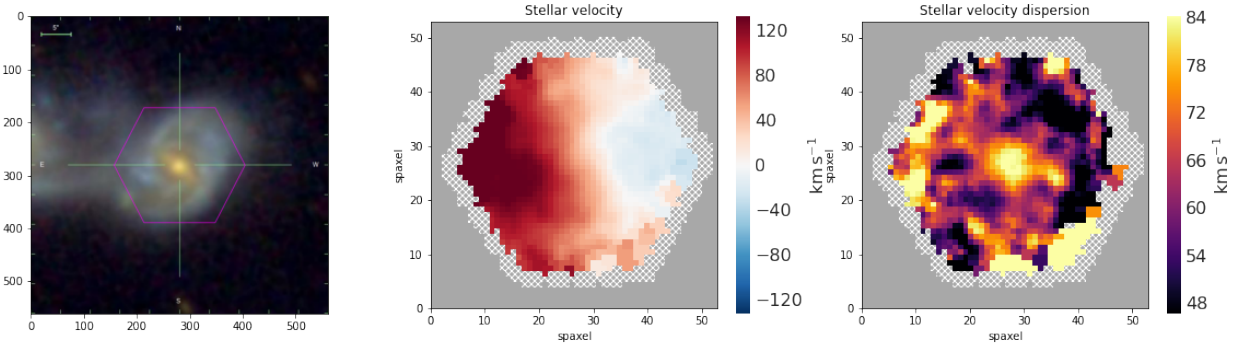

(d) False negative

Fig. A.19: Examples of true positive, true negative, false positive, false negative galaxies with their kinematic maps.